Universidad de Jaén

Evolución petrológica y geoquímica de rodingitas durante la subducción y deshidratación de rocas mantélicas

(Complejo Nevado-Filábride, SE de España):
implicaciones para el funcionamiento de una zona de subducción

Petrological and geochemical evolution of rodingites during subduction and dehydration of enclosing mantle rocks

(Nevado-Filábride Complex, SE Spain):
implications for subduction zones processes

Casto Laborda López

Escuela de Doctorado

Doctorado en Ciencia y
Tecnología de la Tierra y
del Medio Ambiente

EPSL
Escuela Politécnica Superior de Linares

CENTRO DE ESTUDIOS
AVANZADOS EN
CIENCIAS DE LA TIERRA
UNIVERSIDAD DE JAÉN

Tesis Doctoral, 2019

Universidad de Jaén
Escuela de Doctorado

TESIS DOCTORAL

●

Evolución petrológica y geoquímica de rodingitas durante la subducción y deshidratación de rocas mantélicas (Complejo Nevado-Filábride, SE de España): implicaciones para el funcionamiento de una zona de subducción

PRESENTADA POR:
Casto Laborda López

DIRIGIDA POR:
Vicente López Sánchez-Vizcaíno
Claudio Marchesi

JAÉN, 10 de abril de 2019

Universidad de Jaén

Departamento de Geología

Centro de Estudios Avanzados
en Ciencias de la Tierra

Programa de Doctorado en Ciencia
y Tecnología de la Tierra

Evolución petrológica y geoquímica de rodingitas durante la subducción y deshidratación de rocas mantélicas (Complejo Nevado-Filábride, SE de España): implicaciones para el funcionamiento de una zona de subducción

…

Petrological and geochemical evolution of rodingites during subduction and dehydration of enclosing mantle rocks (Nevado-Filábride Complex, SE Spain): implications for subduction zones processes

Memoria de Tesis presentada por Casto Laborda López para optar al grado de Doctor por la Universidad de Jaén, con mención de Doctorado Internacional.

Esta Tesis Doctoral ha sido dirigida por el Dr. Vicente López Sánchez-Vizcaíno (Departamento de Geología y Centro de Estudios Avanzados en Ciencias de la Tierra, Escuela Politécnica Superior de Linares, Universidad de Jaén) y el Dr. Claudio Marchesi (Departamento de Mineralogía y Petrología, IACT-CSIC, Facultad de Ciencias, Universidad de Granada).

Jaén, abril de 2019

Visto Bueno de los Directores:

LOPEZ SANCHEZ
VIZCAINO
VICENTE AGUSTIN
- 30526653H

Firmado digitalmente por LOPEZ SANCHEZ
VIZCAINO VICENTE AGUSTIN - 30526653H
Nombre de reconocimiento (DN): c=ES,
serialNumber=IDCES-30526653H,
givenName=VICENTE AGUSTIN, sn=LOPEZ
SANCHEZ VIZCAINO, cn=LOPEZ SANCHEZ
VIZCAINO VICENTE AGUSTIN - 30526653H
Fecha: 2019.04.09 21:45:05 +02'00'

Vicente López Sánchez Vizcaíno

MARCHESI
CLAUDIO -
X4521281X

Firmato digitalmente da MARCHESI
CLAUDIO - X4521281X
ND: c=ES, serialNumber=X4521281X,
sn=MARCHESI, givenName=CLAUDIO,
cn=MARCHESI CLAUDIO - X4521281X
Data: 2019.04.09 21:18:33 +02'00'

Claudio Marchesi

LABORDA
LOPEZ CASTO
- 23292237E

Firmado digitalmente
por LABORDA LOPEZ
CASTO - 23292237E
Fecha: 2019.04.09
20:03:09 +02'00'

El Doctorando
Casto Laborda López

Funding: Research presented in this Ph.D. Thesis has been funded by the predoctoral FPI grant BES-2013-065336, bound to research grant CGL2012-32067 from “Dirección General de Investigación Científica y Técnica”. I also acknowledge funding from “Agencia Estatal de Investigación”, under grant CGL2016-75224-R, and from the “Junta de Andalucía” research grant P12-RNM-3141 and research groups RNM-145 and RNM-374. My research stay in Durham University was funded by a grant from “Programa de Ayudas a la Movilidad Predoctoral (MINECO); 2014”. My stay at Instituto Andaluz de Ciencias de la Tierra (IACT; CSIC-UGR) for sample preparation and analytical work was possible thanks to “Unidad Asociada del Departamento de Geología de la UJA con IACT-CSIC”. This research and the research infrastructures at the IACT have benefited from funding from the European Social Fund and the European Regional Development Fund.

Μεταμόρφωσις

A mis padres, a mi familia y a mis amigos

El Cerro del Almirez:

del fuego al agua
del agua al fuego
y de ahí
al cielo.

El hilo, la piedra y el laberinto.

Resumen

El Cerro del Almirez (Cordilleras Béticas, sur de España) es un terreno metamórfico subducido y posteriormente exhumado en el que se preserva de forma excepcional la transición entre serpentinitas con antigorita y harzburgitas con clorita. Esta transición registra la reacción de desestabilización de antigorita en serpentinitas en condiciones de alta presión (~ 16–19 kbar) y temperatura (~ 650 °C). Tres tipos de budines de metarrodingitas con tamaño variable están encajados en las rocas ultramáficas del Cerro del Almirez, rodeados por bordes de reacción metasomáticos.

El tipo 1, metarrodingitas con grandita (granate + clorita + diópsido + titanita ± magnetita ± ilmenita), aflora principalmente en el dominio de las serpentinitas con antigorita y presenta tres generaciones de granate. La primera generación (Grt-1), rica en grosularia, se formó durante la rodingitización de fondo oceánico (<2 kbar, ~ 150–325 °C, ~ tampón FMQ). Durante la subducción, el crecimiento alterno de dos generaciones más de granate, el Grt-2b (más rico en andradita y piralspita que el Grt-1) y el Grt-3 (mucho más rico en andradita que el anterior), refleja el cambio entre condiciones metamórficas tamponadas internamente por la composición de la roca en el primer caso (> 10 kbar, ~ 350–650 °C, ~ tampón FMQ), y por los eventos de afluencia de fluidos oxidantes externos en el segundo (fO_2 ~ tampón HM). Estos fluidos oxidantes se liberaron de las serpentinitas encajantes por la desestabilización de la brucita u otras reacciones previas a la desestabilización final de la antigorita.

El tipo 2, metarrodingitas con epidota (epidota + diópsido + titanita ± granate), se formó por la transformación del tipo 1, y es la metarrodingita más abundante en el dominio de las harzburgitas con clorita. Este tipo de metarrodingitas se formó por la variación de los potenciales químicos de SiO_2 (aumento de −884 a −860 kJ/mol) y CaO (disminución de −708 a −725 kJ/mol) provocados por el gran influjo de fluidos con carácter oxidante generados durante la reacción de ruptura de la antigorita a alta presión en las rocas ultramáficas. La formación de una nueva generación de granate (Grt-4) rico en piraslpita y grandita en estas metarrodingitas marca el reequilibrio progresivo de los granates con los nuevos valores de las variables intensivas. El último tipo de metarrodingitas, el tipo 3, metarrodingitas con piralspita (granate + epidota + anfíbol + clorita ± diópsido + rutilo), se formó a partir de las del tipo 2 y sólo aparece encajado en las harzburgitas con clorita. En las metarrodingitas de tipo 3 se han podido determinar las condiciones máximas del metamorfismo (16–19 kbar, 660–684 °C). La transformación

en metarrodingitas con piralspita está marcada por la cristalización de una última generación de granate (Grt-5) junto con la recristalización del diópsido en anfíbol tremolítico, ambos procesos debidos a la disminución en la fugacidad del oxígeno (fO_2), el descenso de μCaO (de −726 a −735 kJ/mol) y el aumento del μMgO (de −630 a −626 kJ/mol) que venían ocurriendo desde la formación del Grt-4. Este cambio en los potenciales químicos estuvo inducido por la interacción química de la metarrodingita con los bordes metasomáticos de reacción. Los diferentes valores de la razón Fe^{3+}/Fe_{Total} en las serpentinitas con antigorita, las harzburgitas con clorita, los bordes de reacción y los tres tipos de metarrodingitas, reflejan un estado de oxidación altamente heterogéneo para este conjunto de materiales durante la subducción. Por lo tanto, reservorios fuertemente oxidados, tales como las metarrodingitas, pueden ser transferidos hacia el manto profundo en zonas de subducción.

Las metarrodingitas del Cerro del Almirez experimentaron múltiples cambios composicionales durante su evolución desde la formación de las rodingitas en el fondo oceánico, pasando por la evolución metamórfica prograda hasta alcanzar las condiciones de desestabilización de la antigorita y deshidratación de las serpentinitas, y la exhumación final. Durante su completa rodingitización en el fondo oceánico, los protolitos basálticos y doleríticos de las metarrodingitas con grandita sufrieron una pérdida de metales alcalinos (Na, K, Cs y Rb) y de Si, Ba, Pb y Sr, junto a un enriquecimiento concomitante en Ca. Estos cambios composicionales ocurrieron en unas condiciones altamente reductoras de los fluidos que procedían de la serpentinización de las rocas ultramáficas encajantes. Por el contrario, las concentraciones de tierras raras (REE) en roca total preservaron su patrón ígneo tras la rodingitización. Estos elementos se redistribuyeron, no obstante, en las nuevas asociaciones metasomáticas dominadas por el granate grandítico rico en grosularia (Grt-1), clorita y diópsido. En el fondo oceánico y durante la subducción, el fuerte gradiente de los potenciales químicos de Mg, Ca y Al en el contacto serpentinita-rodingita desencadenó, por medio de un metasomatismo difusivo, la transformación de las partes externas de la rodingita en un *black-wall* muy rico en clorita, y de la serpentinita adyacente en rocas constituidas por diópsido - clorita (± olivino). Estas litologías heredaron el patrón de roca total de los elementos del grupo del platino de sus correspondientes protolitos. Por otro lado, sus contenidos heterogéneos en REE reflejan grados de alteración metasomática diferentes dependiendo de su cercanía o lejanía al contacto original entre la rodingita y la serpentinita.

Durante la subducción, la abundancia de clorita en los bordes de reacción metasomáticos favoreció su cizallamiento y provocó la mezcla mecánica ocasional entre estas rocas y las metarrodingitas. Durante la subducción, las metarrodingitas interactuaron con fluidos oxidantes liberados por las serpentinitas encajantes formando el Grt-3 rico en andradita y con altas relaciones MREE/HREE. Estos fluidos también provocaron la removilización de Re, mientras que las LREE y el Th quedaron retenidos en las allanitas accesorias. La transformación de las metarrodingitas con grandita a metarrodingitas con epidota provocó la liberación de Ca, Mn, Pt y Pd en los fluidos oxidantes y, por el contrario, la captación de Si, Sr, Pb, Ba ± Eu, que quedaron alojados preferencialmente en la epidota y, en menor medida, en el diópsido.

Las metarrodingitas con piralspita se formaron en las condiciones de máxima presión y temperatura por ruptura de la epidota, liberando los elementos retenidos previamente en esta fase mineral (Ca, Sr y Pb). Finalmente, todos los tipos de metarrodingitas experimentaron grados variables de anfibolitización retrógrada inducida por fluidos derivados de metasedimentos externos, provocando su empobrecimiento en Ca y el enriquecimiento en Mg, Ba y álcalis (Na, K, Cs y Rb).

Las variaciones geoquímicas descritas reflejan el intercambio de elementos mayores y trazas entre las diferentes litologías (serpentinitas, metarrodingitas y metasedimentos) en una losa de subducción o en el canal de subducción (limite losa-manto). Las rodingitas pueden influir en el estado redox y en los patrones composicionales de los fluidos liberados desde la placa que subduce, especialmente a través de la oxidación del hierro, el fraccionamiento de Sr, Pb y Ba por la epidota, y la liberación de Ca, Re, Pt y Pd en los fluidos. Este flujo de metales preciosos a través de fluidos derivados de metarrodingitas puede producir magmas de arco particularmente adecuados para generar depósitos de minerales con interés económico. Además, el alto contenido en Ca de estos fluidos puede inducir metasomatismo y refertilización en el manto del sub-arco. Por último, el reciclaje profundo de metarrodingitas residuales en el manto astenosférico convectivo puede producir reservorios ricos en Ca que se asemejen a las fuentes de los basaltos de islas oceánicas (OIB).

Palabras clave: Cerro del Almirez, subducción, rodingita, deshidratación de serpentinitas, fluido, fugacidad del oxígeno, elementos del grupo del platino.

Abstract

The transition between antigorite-serpentinite and chlorite-harzburgite in the Cerro del Almirez ultramafic massif (Betic Cordillera, southern Spain) exceptionally marks in the field the front of antigorite breakdown at high pressure (~16–19 kbar) and temperature (~650 °C) in paleosubducted serpentinite. These ultramafic lithologies enclose three types of metarodingite boudins of variable size surrounded by metasomatic, chlorite-rich reaction rims.

Type 1 Grandite-metarodingite (garnet + chlorite + diopside + titanite ± magnetite ± ilmenite) mainly crops out in the antigorite-serpentinite domain and has three generations of garnet. Grossular-rich Grt-1 formed during rodingitization at the seafloor (<2 kbar, ~150–325 °C, ~FMQ buffer). During subduction, the alternating growth of Grt-2b (richer in andradite and pyralspite components than Grt-1) and Grt-3 (very rich in andradite component) reflects the change from internally buffered metamorphic conditions (>10 kbar, ~350–650 °C, ~FMQ buffer) to influx events of oxidizing fluids (fO_2 ~HM buffer) released by brucite and partial antigorite breakdowns in host serpentinite.

Type 2 Epidote-metarodingite (epidote + diopside + titanite ± garnet) derives from Type 1 and is the most abundant metarodingite type enclosed in dehydrated chlorite-harzburgite. Type 2 formed by increasing μSiO_2 (from −884 to −860 kJ/mol) and decreasing μCaO (from −708 to −725 kJ/mol) triggered by the flux of high amounts of oxidizing fluids during the high-P antigorite breakdown in serpentinite. The growth of Grt-4, with low-grandite and high-pyralspite components, in Type 2 metarodingite accounts for progressive re-equilibration of garnet with changing intensive variables.

Type 3 Pyralspite-metarodingite (garnet + epidote + amphibole + chlorite ± diopside + rutile) crops out in the chlorite-harzburgite domain and formed at peak metamorphic conditions (16–19 kbar, 660–684 °C) from Type 2 metarodingite. This transformation caused the growth of a last generation of pyralspite-rich garnet (Grt-5) and the recrystallization of diopside into tremolitic amphibole at decreasing fO_2 and μCaO (from −726 to −735 kJ/mol) and increasing μMgO (from −630 to −626 kJ/mol) due to chemical mixing between metarodingite and reaction rims. The different bulk Fe^{3+}/Fe_{Total} ratios of antigorite-serpentinite and chlorite-harzburgite, and of the three metarodingite types,

reflect the highly heterogeneous oxidation state of the subducting slab and likely point to the transfer of localized oxidized reservoirs, such as metarodingites, into the deep mantle.

Multiple compositional changes affected the Cerro del Almirez rodingites during their metamorphic evolution, from rodingitization on the seafloor to dehydration of host subducted antigorite serpentinites at peak metamorphic conditions. Basaltic and doleritic protoliths of Grandite-metarodingites lost alkaline metals (Na, K, Cs and Rb), Si, Ba, Pb and Sr, and gained Ca through intense seafloor rodingitization by highly reducing fluids reacting with host serpentinites. Rare earth elements (REE) in whole-rocks, conversely, preserved their igneous signature during rodingitization and were incorporated into the new metamorphic assemblage dominated by granditic garnet (Grt-1), chlorite and diopside. At the ocean floor and during subduction, the strong gradient of chemical potentials of Mg, Ca and Al at the serpentinite-rodingite interface triggered the transformation of metarodingites to metasomatic chlorite-blackwalls and of serpentinites to chlorite (± olivine)-diopside rims. These transitional lithologies inherited the platinum-group element signature of their protoliths, while their heterogeneous REE contents reflect different grades of metasomatism at different distance from the original rodingite-serpentinite contact.

During subduction, abundant chlorite favoured shearing of metasomatic rims and physical mixing with metarodingites or between the metasomatic rims themselves. Subducting Grandite-metarodingites interacted with fluids released by brucite and partial antigorite breakdowns in serpentinites, leading to oxidation of iron and precipitation of new andraditic garnet (Grt-3) with high MREE/HREE ratios. These oxidizing fluids from serpentinites also mobilized Re, while LREE and Th were retained in accessory allanite. Strong fluxing of fluids produced by antigorite breakdown in serpentinites promoted the transformation of Grandite- to Epidote-metarodingites. Epidote-metarodingites released Ca, Mn, Pt and Pd into oxidizing fluids and partitioned Si, Sr, Pb, Ba ± Eu especially in epidote. Pyralspite-metarodingites formed at peak metamorphic conditions by, among other reactions, epidote breakdown that liberated Ca, Sr and Pb into fluids. Finally, all metarodingite types experienced variable degrees of retrograde amphibolitization induced by external metasediment-derived fluids, causing Ca depletion and enrichment in Mg, Ba and alkaline elements (Na, K, Cs and Rb).

These geochemical variations reflect the exchange of major and trace elements between different lithologies (serpentinites, metarodingites and metasediments) in a

subducting slab or slab-mantle interface. Metarodingites may influence the redox state and trace element signature of slab fluids, especially through iron oxidation, fractionation of Sr, Pb and Ba into epidote, and release of Ca, Re, Pt and Pd in the fluids. This flux of precious metals via metarodingites-derived fluids may produce arc magmas particularly suitable to generate economic ore deposits, and the Ca-rich nature of these fluids may induce metasomatism and refertilization in the sub-arc mantle. Deep recycling of residual metarodingites in the convective asthenosphere may produce Ca-rich reservoirs that resemble the sources of ocean island basalts.

Keywords: Cerro del Almirez, subduction, rodingite, serpentinite dehydration, fluid, oxygen fugacity, platinum-group elements.

Agradecimientos

Bueno, parece mentira que esté escribiendo al fin los agradecimientos, por fin se termina "la interminable". Después de estos cinco años, que se han hecho duros, al final, no tengo nada más que palabras de gratitud para la gente que me ha acompañado durante este viaje de cambio y aprendizaje. Aunque en principio la "petro metamórfica y la geoquímica" no eran mi campo, yo era más de "paleo y estructural", han llegado a fascinarme igual que aquellas. Se trata del gran puzle de la geología, te atrapa el hecho de querer completar una pequeña parte de su inmensidad.

En primer lugar, quiero dar las gracias a mis directores, ellos se han implicado muchísimo y eso se lo agradezco mucho. Gracias Vicente por estar ahí desde el principio, tú me abriste las puertas del "serpentinismo" y nos metimos de lleno a estudiar estas rocas tan raras y extrañas, pero la vez tan bonitas. Recuerdo las primeras veces que veíamos las láminas delgadas e íbamos hipotetizando y sacando conclusiones. Era emocionante cada vez que descubríamos algo nuevo y las piezas encajaban poco a poco. Recuerdo también las salidas de campo, que sin duda fueron lo mejor de la tesis. El Almirez es simplemente mágico. Muchas gracias Vicente por tu calidad humana, por tu espíritu crítico y tu gran bondad. Has actuado como padre científico, y en ciertas ocasiones, cuando yo me desviaba o no hacía las cosas bien me, recordabas mucho a mis padres, a lo que me decían de pequeño, o no tan pequeño. Creo que nos hemos complementado bien. En definitiva, gracias por estar ahí en los buenos y malos momentos, has sido un director genial.

En segundo lugar, dar las gracias a mi otro codirector, Claudio, tú has sido mi otro maestro en la otra parte del mundo que es esta tesis. El mundo de la geoquímica. De igual manera que Vicente, has estado siempre ahí, ayudándome en las tareas de relojero que son siempre los laboratorios, y que a mí se me dan regular dado mi pésimo pulso y mí nerviosismo. Tú también has disfrutado del campo, y hemos cargado a la espalda kilos y kilos de roca. Gracias por tu bondad, tu afabilidad, tu crítica y tu guía en este mundo. Has estado ahí en todos los momentos al igual que Vicente, cuando había que escribir trabajos interminables. Muchas gracias de verdad, me alegra que hayáis sido mis directores.

Quiero dar también las gracias a mi grupo de investigación. A María Teresa por ser una gran persona, por presentarme a Vicente y también apostar por mí. Eres una persona magnética, divertida y fuerte. Con una intuición excepcional, además de ser muy cálida. Gracias por estar ahí y por tu gran ayuda. Fuiste la primera que provocó en tus clases que me picara el *gusanillo de la "metamórfica" y el Nevado-*Filábride. *Quiero dar las gracias a también a Antonio, al cual quiero mucho, tú también me has apoyado mucho en este camino. Además de compañero científico con el que me encanta hablar del Nevado Filábride, eres un amigo. Quiero agradecer también al resto de miembros de mi grupo de investigación: a Carlos por ayudarnos, dejarnos utilizar sus equipos y brindar grandes aportaciones críticas; y a José Alberto, mi predecesor en El Almirez, que, aunque hayamos tratado poco por la distancia, lo he tenido muy presente y me ha brindado unas ideas geniales.*

Quiero agradecer también al resto de personas del IACT a Karoly y demás miembros del grupo de Carlos. Agradecer también a mis compañeros de las tesis hermanas de Nicole y de Manuel, que empezamos casi al tiempo y estamos acabando ya.

Gracias Alpiste por ayudarme tantísimo en los análisis y por los ratos y risas que echamos en el IACT, además de comprenderme. También dar las gracias a Chris W Dale por ayudarme e implicarse tanto en la ardua tarea que fue hacer los análisis del osmio y los platinoides.

Quiero agradecer también a la gente de estructural, Irene, Manuel, Juampe, Inma, Ángel, Cristina, Lourdes.

A mi antiguo director de tesis de máster Julio por iniciarme con él en el mundo de la investigación, por guiarme en aquella primera aventura científica con aquellos fósiles en mármoles. También quiero dar las gracias a Pilar, por aquella búsqueda de conodontos.

Después de los agradecimientos académicos, vienen los familiares, amigos y personas especiales que han estado siempre a mi lado.

En primer lugar, gracias a mi padre, Jacinto, a mi madre Victoria y a mi hermana María José. Habéis estado siempre ahí sois mi pilar fundamental, aunque estéis lejos. Gracias a toda mi familia, a mis abuelos Casto, Fina e Isabel, y a mi abuelo Vicente que en paz descanse, siempre me acordaré del campo del Molino y de Cope, pues fue donde comenzó mi amor por la geología.

Gracias a todos mis tíos y tías, y a mis primos (Rosa, Pedro, Tico, Miguel y Diego…). A toda mi familia de Águilas y Lorca.

Gracias a mis amigos de la carrera. En especial a mi amiga Sita, y a su familia. ¡Sita, a ti te queda nada también para acabar la tesis! Dentro de nada lo estaremos celebrando.

Quiero agradecer también a todo mi grupo de amigos de Murcia. A Borja, Peter, Paxy, Eider, Víctor, Clara, Mónica, Sandra, María, Marta, mi primo Juan, José Carlos, Antonio, Juanfra, Pepelu, ¡Qué ganas de verano!

Quiero dar las gracias también a los amigos de Granada, que me han tenido que aguantar en sus casas muchas veces. Gracias a Beni, Jorge, Jaime, Candela, Luisa, Rosa, Antonio, Anita, Reca, Raffa, Bob, Jesy, Sofi, María Teresa y a Carla.

Un recuerdo especial a mi amiga Io, que, aunque nos veamos una vez cada mil años la tengo muy presente. ¡Ya me tocaba acabar a mí también!

Dar las gracias también a mi amiga Maricarmen. También a Lucía a Gabriel y a sus "bebesas". Echo de menos los paseos por la tarde y las pizzas que hacíamos.

Quiero dar las gracias a una persona especial, a Carlos, que siempre me está acompañando, cuidando y que gracias a esta tesis lo conocí. ¡Pronto tú también serás libre "mi"!

Seguro que se me está olvidando gente, pero tengo que acabar ya. Gracias a toda esa gente que se me está olvidando, ellos lo entenderán.

Quiero agradecer también a mis compañeros linarenses, que me han acompañado a lo largo de este viaje. A Violeta, mi amiga y compañera que siempre me ha estado ayudando, ella hace maravillas con Matlab. Sobre todo, cuando le pedía que me dibujara una trayectoria. Gracias también a Antonio, por ayudarme, aunque le guste mucho el "bla bla bla" y a veces me dé por ladrarle. Lo siento por si alguna vez he ladrado. Gracias a Noe, Macarena, y demás gente de la escuela por todo el apoyo que habéis dado. Gracias también a Mª José por ayudarme con la preparación de algunas muestras aquí en Linares.

Por último, quiero agradecer y hacer una mención especial a los miembros del tribunal de mi tesis por aceptar evaluarla: José Ignacio Gil Ibarguchi, Juan Jiménez Millán, Gisella Rebay, Alberto Vitale Brovarone y Mario Sánchez-Gómez.

Así, también quiero agradecer a los miembros de la comisión académica del programa de doctorado TIERRAMAM por su excelente trato y gestión durante los años que he realizado esta tesis.

Casto

Índice

Part II

Part I

INTRODUCTION, AIMS AND THESIS STRUCTURE, AND METHODOLOGY

1 Introduction

1.1 General considerations

This Ph.D. Thesis deals with the significance of rodingites and their metamorphic and geochemical evolution during subduction to intermediate depths and subsequent exhumation. I present the results of an exhaustive field, petrological, and geochemical study of metarodingites from the Cerro del Almirez ultramafic massif (Betic Cordillera, southern Spain). This massif exceptionally preserves both the reactants and products of the most important fluid-releasing reaction that takes place in subduction zones at high-pressure conditions, i.e. the dehydration of antigorite serpentinite to chlorite harzburgite. Rodingite bodies are hosted in both these two ultramafic rock types. This location has permitted to investigate the interaction between metarodingites and enclosing rocks during their complete, subduction-linked metamorphic evolution, as well as to discuss the key role played by fluid-rock interaction in the origin of the mineral assemblages, textures, and compositions of metarodingites.

In this chapter, I present a brief introduction dealing with the main geological processes that take place in subduction settings

1.2 Plate tectonics and subduction zones

The Earth is a unique case among the active silicate planets of our Solar System. Mantle convection in the deep Earth generates a very unusual tectonic style, with a fragmented lithosphere that is constantly recycled (Fig. 1.1) (Schubert et al., 2001; Stern, 2018). Early in the Earth's history, the tectonic style was probably similar to that of Mars and Venus with a single lid tectonic regime (Stern, 2018). Then, cooling of the upper mantle, thickening of the lithosphere and deformation in weak zones (probably generated by meteoritic impacts or mantle plumes) favoured the birth of embryonic subduction zones and helped to change the tectonic regime into plate tectonics (e.g. Stern, 2018). The essential requirement for effective plate tectonics is that viscous stress exceeds the lithospheric stress. This condition not only depends on the applied stress and temperature but also on the rocks' water content (O'Neill et al., 2007). Numerical models reveal that subduction only starts if fluids are present (e.g. Dymkova and Gerya, 2013) as they notably reduce the friction coefficient of rocks (O'Neill et al., 2007). Moreover, small amounts of water have important effects on the melt productivity and mantle viscosity, favouring convection (e.g. Dymkova and Gerya, 2013, Inoue, 1994; Mei et al., 2002; van Keken et al., 2011). The great amount of hydrated materials generated on the ocean floors and carried down in subducting slabs accounts for the addition of water into the Earth's mantle.

In the tectonic plate regime, convective cells in the mantle generate new oceanic or transitional crust at mid-ocean ridges or continental rifts in divergent margins (Figs 1.1, 1.2). This crust mainly consists of igneous mafic and ultramafic rocks overlain by sediments of variable thickness. Trenches on the ocean floor mark the location of subduction zones at convergent plate margins (Stern, 2002; Turcotte and Schubert, 2014; van Keken et al., 2018). Subduction zones are the places in the Earth where oceanic crust is recycled as they drag an enormous portion of ocean floors back down into the mantle, together with volatiles (Fig. 1.3) (Furukawa, 1993; Hacker et al., 2003a, b; Peacock, 2001; Rüpke et al., 2004; Stern, 2002; Ulmer and Trommsdorff, 1995).

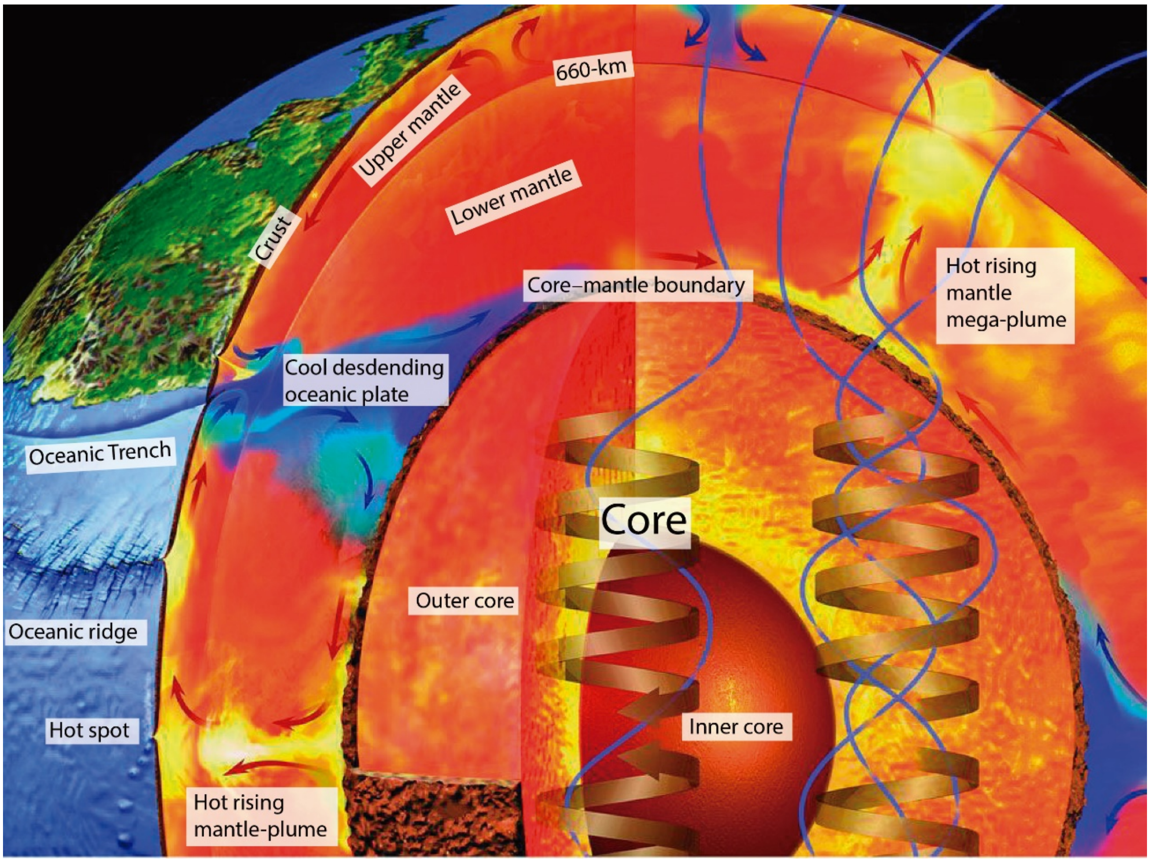

Figure 1.1. *General sketch of the Earth's mantle convection and plate tectonics regime. (Modified from: National Geographic Society, Illustration by Chuck Carter, 2019, Available at: https://www.nationalgeographic.org/encyclopedia/core/,).*

Slab pull is the main driving force that generates the plate motion. This force originates from the negative buoyancy of the subducting oceanic lithosphere, which provokes the slab gravitational sinking into the mantle and pulls the plate downward. (Davies and Richards, 1992; Forsyth and Uyeda, 1975; Hager and O'Connell, 1981; Royden, 1993; Spence, 1987; Wilson, 1993). Indirectly, the lithosphere subduction also causes mantle upwelling underneath mid-ocean ridges (Conrad and Lithgow-Bertelloni, 2002; Stern, 2018). The progressive consumption of oceanic lithosphere at trenches can lead to the closure of oceans and to subduction of continental lithosphere. The positive buoyancy force resulting from the subduction of continental lithosphere acts as an opposite force to oceanic lithosphere slab pull, leading to strain localization within the slab, necking, and ultimately to slab-breakoff (Davies and von Blanckenburg, 1995; Wong A Ton and Wortel, 1997).

Subduction zones are the loci of the most paroxistic phenomena on the Earth's surface, such as high-magnitude earthquakes, explosive volcanic eruptions and fast geomorphological evolution (Poli and Schmidt, 2002). In addition, they are the main

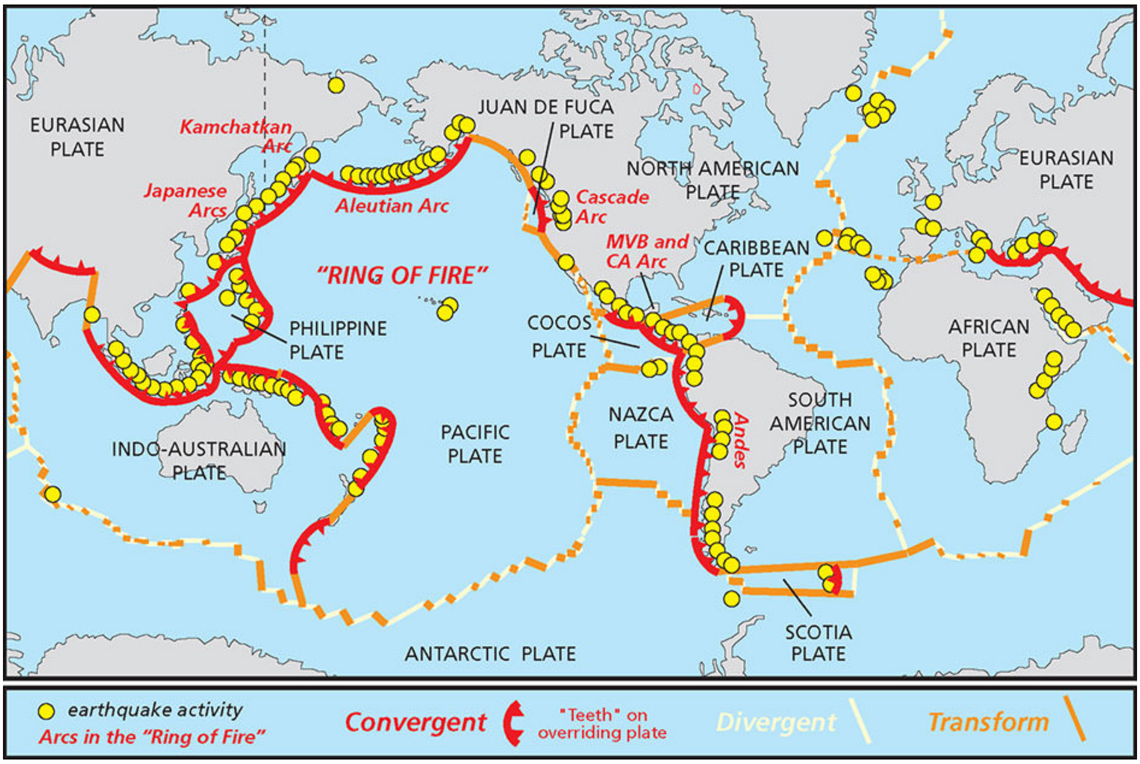

Figure 1.2. *Map illustrating the tectonic plates in the Earth. Convergent plate boundaries (red lines), volcanism and earthquakes (yellow dots), divergent boundaries (light yellow), main transform faults (orange lines) (https://www.nps.gov/subjects/geology/plate-tectonics.htm; Modified after Lillie, 2005).*

settings of continental crust generation during the Phanerozoic (e.g. Davidson and Arculus, 2006; Polat, 2012).

Subduction zones present four main interrelated parts: (1) the overriding or upper plate, (2) the downgoing plate or slab (subducting lithosphere), (3) the mantle wedge, and (4) the arc-trench complex or magmatic arc (Fig. 1.3; Stern, 2002). The machinery of subduction zones is described by the popular term "*Subduction Factory*" (e.g. Tasumi, 2005), where incoming materials are processed into arc magmas, ultimately generating continental crust. The term *Subduction Factory* has been used to describe accurately the flux of materials into and out of the subduction zones. Input materials — seafloor sediments, oceanic mafic crust and mantle lithosphere — penetrate in the Subduction Factory at the deep-sea trenches. In the subducting slab and mantle wedge above, incoming crustal materials mix with mantle rocks in heterogeneous mélanges. Then, output materials — melts, fluids, volatiles, gases, serpentinite diapirs, metasomatized materials, volcanic rocks, ore deposits, and continental and back-arc crust — are incorporated into the upper plate. Materials that sink into the mantle can eventually re-emerge in mantle plumes.

The mentioned evolution of subduction zones is inseparably linked to the petrological reactions that occur at different levels in this factory, and especially in the slab. These

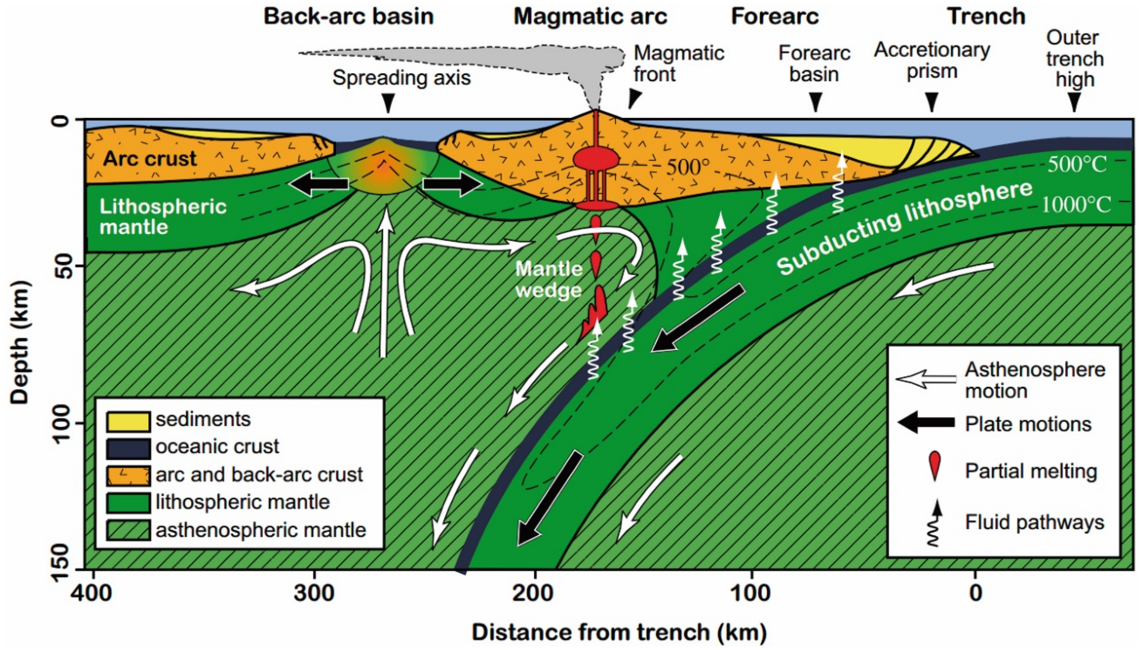

Figure 1.3. *Sketch of a typical subduction zone setting, with indication of the depths at which the main fluid release events take place (Modified by Padrón Navarta (2010) from Stern (2002)).*

reactions usually involve volatile components, which play a key role in the mineralogical and geochemical evolutions of subducted lithologies, such as serpentinites and associated rodingites, in the change of redox conditions and in the mobility and recycling of certain chemical elements.

1.3 Ocean floor serpentinization and metasomatism

The subduction zone water cycle, i.e. the hydration and dehydration of subducting oceanic lithosphere, is a key process in understanding arc magmatism and volatile recycling. At divergent margins or spreading rifts – ocean ridges and continental rifts –, upwelled mantle is incorporated into the newly-formed crust at shallow levels (e.g. Kelemen et al., 1995). Some of these ultramafic mantle rocks are exhumed on or close to the ocean-floor, thus allowing their complete or partial alteration by hydrothermal fluids generated by seawater circulation (e.g. Schaltegger et al., 2002). Alteration also occurs along sea floor faults at depth and, in a later stage, along bend faults outboard and within the subduction trench (Rüpke et al., 2004).

The mentioned metasomatic process affecting the ultramafic rocks is called **serpentinization** and mainly produces the transformation of olivine and other ferromagnesian minerals (orthopyroxene and clinopyroxene) into serpentine-group minerals (mostly chrysotile and lizardite) — generalized formula $Mg_3Si_2O_5(OH)_4$ — together with other minerals such as brucite, magnetite, tremolite and talc. During serpentinization, ultramafic rocks may capture an enormous amount of water — mainly chemically bound water in form of hydroxyl species like OH — (up to 15–16 wt% H_2O, average 13 wt%) and other volatile compounds (Deschamps et al., 2013; Faccenda, 2014; Ulmer and Trommsdorff, 1995; Wunder and Schreyer, 1997). Due to their high water and volatile contents, serpentine minerals have a predominant role in the water budget of subduction zones and lead to profound changes in the physical properties of ultramafic rocks (Faccenda, 2014). Serpentinization generally takes place at medium to low temperature (85-460ºC; Wenner and Taylor, 1971) and low-pressure conditions (e.g. Frost and Beard 2007).

Besides the formation of hydrated minerals, additional chemical changes occur during serpentinization. One of them is oxidation of Fe^{2+} — present in the ultramafic rock in ferromagnesian minerals — to Fe^{3+} (Andreani et al., 2013). This oxidation involves magnetite precipitation, generation of H_2, and release of fluids at extremely reducing conditions, congruent with low values of oxygen fugacity (fO_2) (ΔFMQ = -7 to -4) (e.g. Frost, 1985; Frost and Beard, 2007). Simultaneously, the formation of serpentine-brucite assemblages induces very low silica activity (Frost and Beard, 2007), which in turn leads to the incongruent dissolution of mantle clinopyroxene and the release of Ca, transported in the form of $CaOH^+$, in the fluids (Bach and Klein, 2009; Frost and Beard, 2007). These evolving serpentinization fluids are reputed some of the most alkaline fluids (pH >10) on Earth (Barnes et al., 1978), thus contributing to remobilization of light rare earth elements (LREE) and enrichment in fluid mobile elements in serpentinizing rocks (Kodolányi et al., 2012; e.g. Marchesi et al., 2013).

Similar to ultramafic rocks, mafic rocks — the other major constituents of the oceanic crust — may also experience seafloor hydrothermal alteration and metasomatism. The occurrence of mafic rocks in contact with or inside serpentinizing peridotites and the particular fluid chemistry mentioned above cause singular synergic metasomatic alteration in the mafic rock (**rodingitization**) that is described in section (1.5.2).

1.4 Subduction dehydration and recycling of volatiles

Devolatilization reactions are capital among the geodynamic and geochemical processes that occur in subduction zones. During the progressive down-going of oceanic lithosphere in subduction zones, a sequential set of metamorphic devolatilization reactions occurs in the subducted materials due to increasing pressure and temperature conditions over more than 150 km in the subducting slab (e.g. Rüpke et al., 2004). Fluids (mainly consisting of H_2O and CO_2) produced by these reactions control the buoyancy forces, drive slab pull, and account for volatiles transport and release (Poli and Schmidt, 2002). Additionally, the mass transfer to the mantle wedge generated by these fluids has crucial importance in the origin of arc magmas and continental crust (Dasgupta et al., 2004; Grove et al., 2012; Schmidt and Poli, 2014; Stern, 2002; Tumiati et al., 2013; Walowski et al., 2015). Fluids distilled from the subducted slabs can be partially re-emitted by volcanic arc magmatism.

In decreasing order, serpentinites, altered mafic rocks and metasediments are the most important water carriers in subduction zones. In these rocks, fluids are hosted in free-form in pores (e.g. metasediments), as fluid inclusions in minerals, or are chemically bound in the mineral structures (e.g. micas and amphiboles in mafic rocks or serpentine minerals in hydrated peridotites) (Hermann et al., 2006; Poli and Schmidt, 2002; Rüpke et al., 2004; Stern, 2002; Ulmer and Trommsdorff, 1999; van Keken et al., 2011). Serpentinites release the largest amount of water — 40 to 60 wt% of their initial water content — beyond arc depths (Rüpke et al., 2004; Schmidt and Poli, 1998), whereas hydrous mafic-rocks and sediments only release around 28 wt % and 5 wt%, respectively (Hacker, 2008). Hence, serpentine minerals play a fundamental role in subduction zones as the major water source from the subducting slab (Padrón-Navarta et al., 2011; Scambelluri et al., 2004).

Chrysotile/lizardite destabilization to produce antigorite is the first dehydration reaction undergone by ultramafic rocks during subduction (Fig. 1.4). This transition occurs progressively from LT- to MT-conditions (300-390 ºC) until lizardite is completely consumed (Evans, 2004; Schwartz et al., 2013). This reaction is followed by brucite destabilization to olivine (Trommsdorff and Evans, 1974) (Fig. 1.4) at 300-500 ºC, depending on pressure (Padrón-Navarta 2010; Plümper et al., 2017), which releases up to 5 vol% of water content (Padrón-Navarta 2010).

The most important metamorphic dehydration reaction in subducted serpentinites is the antigorite breakdown (Fig. 1.4; Ulmer and Trommsdorff, 1995), in which product minerals and the amount of released water depend on P-T conditions (Bromiley and Pawley, 2003; Ulmer and Trommsdorff, 1995; Wunder and Schreyer, 1997). At low pressure and high temperature conditions, like in contact metamorphism, water is mostly retained in talc, the main dehydration product of antigorite. On the contrary, at intermediate to hot subduction conditions (1-5 GPa and 620-650 ºC) most of the water content of antigorite (up to 12.3 wt% H_2O) can be released. High Al contents are common in antigorite at these conditions, so chlorite, together with olivine and enstatite, crystallizes as a typical product of antigorite dehydration, producing chlorite-harzburgite. In this case, the released water amount is about 9 wt%. This latter reaction is the cornerstone of the studies in the Cerro del Almirez ultramafic massif (the study area of this Thesis), and poses crucial implications for the present research. The specific features and implications of the antigorite breakdown reaction in this massif are described in section 1.6.3. Finally, at pressure conditions > 5 GPa, typical of cold subduction settings, antigorite-hosted water is mainly retained in phase A or 10 Å phase.

The main dehydration reaction in ultramafic rocks beyond antigorite breakdown is the breakdown of chlorite at 1-4.5 GPa and 700-800 ºC (Ulmer and Trommsdorff, 1995) (Fig. 1.4). By this reaction, total dehydration occurs at P > 2.5 GPa forming garnet-peridotite. Reactants and products of this reaction are well exposed in Cima di Gagnone, in the Central Alps (Evans and Trommsdorff, 1978). This massif is, thus, the ideal locality to compare with rocks from Cerro del Almirez in order to predict their possible metamorphic and geochemical evolution deeper in hot subduction settings.

Contrary to serpentinization, prograde serpentinite dehydration reactions induce Fe^{3+} reduction -hosted in magnetite and hydrated phases- to Fe^{2+}, which confers an oxidizing character to the dehydration fluids (Debret et al., 2014, 2015; Debret and Sverjensky, 2017; Merkulova et al., 2017). This character has great importance not only for the fluid capacity to transfer this oxidizing potential to the mantle wedge, but also for the interaction of such fluids with other subducted lithologies, including rodingites.

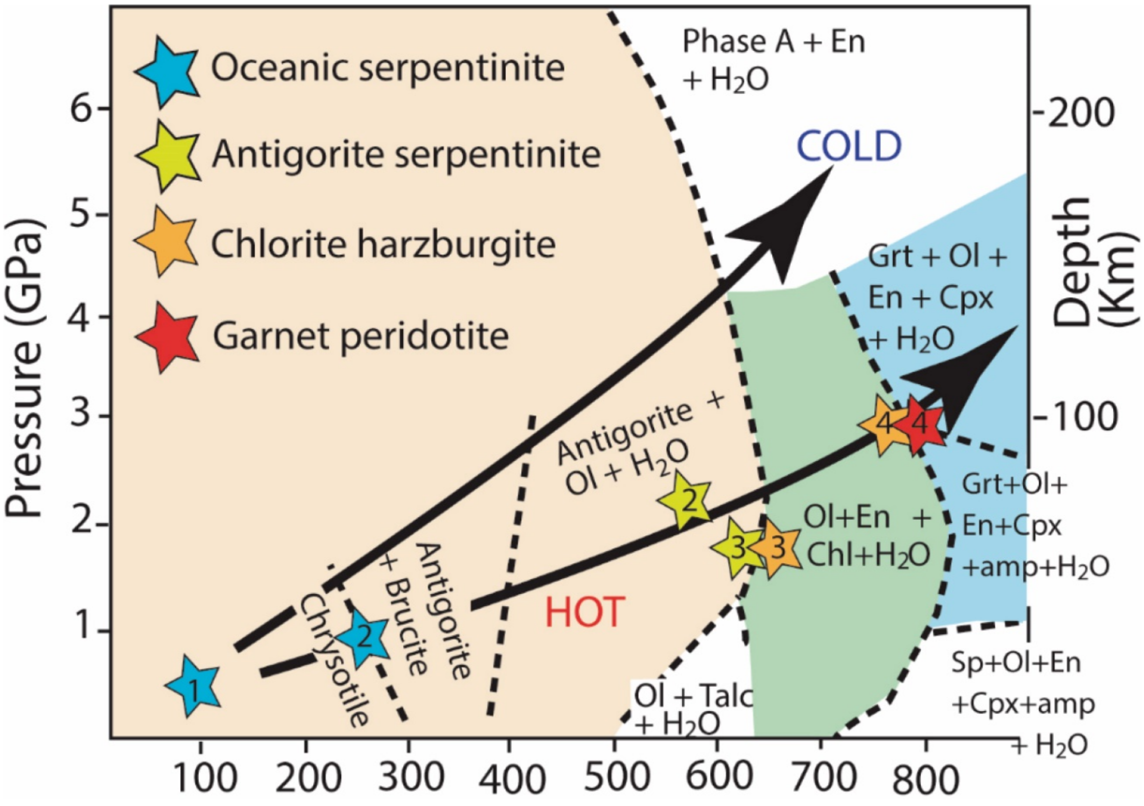

__Figure 1.4.__ Schematic P-T diagram representing the stability fields of the main mineral phases in serpentinites from ocean-floor conditions to subduction in hot and cold subduction zones. Stars indicate the deduced conditions for rocks in the following localities: (1) Monte Nero and IODP seafloor serpentinites; (2) Erro Tobbio; (3) Cerro del Almirez; and (4) Cima di Gagnone (Kendrick et al., 2018).

Dehydration reactions in subducted serpentinites also imply significant geochemical effects. Fluids released to the supra-subduction mantle wedge promote the recycling of water, LREE and large ion lithophile elements (LILE: Cs, Rb, Ba, Sr) that feed the sources of arc magmas (e.g. Spandler and Pirard, 2013). Moreover, Ca-silica-rich fluids also released from the slab may interact with the mantle wedge peridotite and cause metasomatic precipitation of secondary clinopyroxene and orthopyroxene (Grant et al., 2016; Ishimaru and Arai, 2011; Python et al., 2007). Therefore, slab dehydration not only may change the geochemical signature of the arc magma sources, but also refertilize the sub-arc mantle and increase its melt-productivity (e.g. Schiano et al., 2000).

1.5 Rodingites

1.5.1 Definition and origin of the term “rodingite”

Rodingites are common metasomatic rocks in the serpentinized oceanic lithosphere. They mostly form after a mafic rock precursor, generally basalts and gabbros, but uncommon protoliths are also intermediate and felsic igneous rocks, as well as sediments. These rocks underwent pervasive alteration by intense metasomatism, coeval with serpentinization of surrounding peridotites (Coleman, 1967; Frost, 1975; O'Hanley et al., 1992; Schandl et al., 1989).

First works on rodingites, in that time called "garnetites”, date from the 19th century and were focused mainly in case studies in the Western Italian Alps (references in Dal Piaz, 1967) and in the Paringu Massif in Rumania (Munteanu-Murgoci, 1900). Other names used to refer to rodingites are “Granat-Vesuvianfels” (Munteanu-Murgoci, 1900), “altered gabbro or eucrite” (Arsihnov and Merenkov 1930; Benson, 1926; Grange, 1927; Turner, 1933), “garnetized gabbros” (Miles, 1950), “ophispherites” (Jaffé, 1955), and “Kalksilikatfels” (Müller, 1963).

The term “*rodingite*” was employed for the first time by Marshall (in Bell et al., 1911) to describe altered (“garnetized”) gabbros from the Dun Mountain Ophiolite Belt (New Zealand). The name was taken from the Roding River that drains that area. Following this author, others used the same term to describe similar rocks hosted by serpentinites in different localities throughout the world: Australia (Benson, 1913, 1914, 1915, 1918), South Westland in New Zealand (Turner, 1933; Wells, 1949), southwestern Oregon (Cater and Wells, 1953), California (Chesterman, 1960), southwest British Columbia;

(Suzuki, 1953), Japan (Bloxam, 1954; Seki and Kuriyagawa, 1962), Scotland (Baker, 1959), Tasmania (Bilgrami and Howie, 1960), and northwest Syria (Schlocker, 1960). Since the 60ies, the term rodingite has been employed to name every mafic rock affected by Ca-metasomatism. After these first works, Coleman (1966, 1967) made and extensive revision of the knowledge about rodingites and reported a complete petrological and chemical description of both rodingites and their associated reaction rims (Fig. 1.5), proposing a model that explained their metasomatic formation.

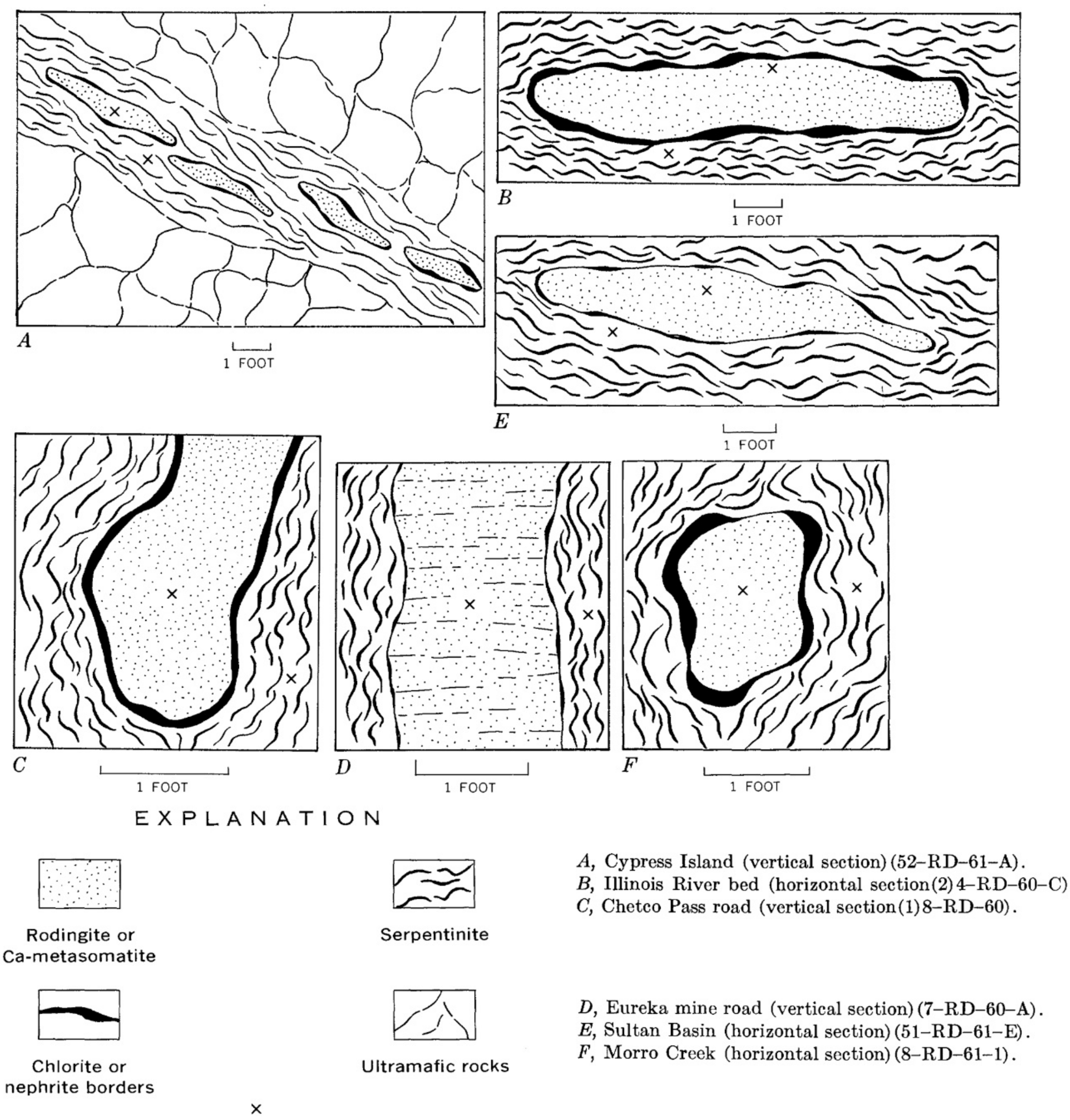

Figure 1.5. *Sketches of the field occurrence of rodingite bodies and their associated reaction rims studied in different localities by Coleman (1967). In every case, rodingites are embedded in serpentinites and chlorite-rich rims.*

Without exception, every known rodingite occurrence is associated with serpentinized ultramafic rocks. This fact has been documented in a wide range of tectonic settings including present-day ocean floors (Aumento and Loubat, 1971; Frost et al., 2008; Fruh-Green et al., 1996, 2017; Honnorez and Kirst, 1975; Kelemen et al., 2003), rifted continental margins and ocean-continent transition zones (Beard et al., 2002), Paleoproterozoic and Archaean mafic-ultramafic sequences from greenstone belts (Anhaeusser, 1979; Attoh et al, 2006; Schandl et al., 1989), and metamorphosed and un-metamorphosed ophiolitic complexes from Phanerozoic orogenic belts (Austrheim and Prestvik, 2008; Coleman, 1967; Dubinska, 1995; Dubińska and Wiewiora, 1999; Evans et al., 1979; Frost, 1975; Hatzipanagiotou et al., 2003, Hatzipanagiotou and Tsikouras, 2001; Li et al., 2004, 2007, 2008; Murzin and Shanina, 2007; Tsikouras et al., 2009; Zanoni et al., 2016).

The most common type of rodingite consists of a rock rich in granditic/hydrogranditic garnet (that is, a garnet rich in grossular, andradite and hydrogarnet end-members), with minor chlorite and tremolite or diopside (Bell et al., 1911; Coleman, 1967; Evans et al. 1979; Li et al., 2004, 2017; Miles, 1950; Mittwede and Schandl 1992; Suzuki, 1953; Schandal et al, 1989; Zanoni et al., 2016). In other, less common, rodingite-types – in some cases affected by subduction metamorphism – the main phase is prehnite (Bell et al., 1911; Grange, 1927; Katoh and Niida, 1983; Li et al., 2007, 2017; O'Hanley et al., 1992), epidote (Anhausen, 1979; Austrheim and Prestvik 2008; Dubińska, 1995; Evans et al. 1979; Fukuyama et al., 2014; Grange, 1927; Lan and Liu 1981; O'Hanley et al., 1992; Zanoni et al., 2016), vesuvianite (Coleman, 1967; Dubińska, 1995; Fukuyama et al., 2014; Zanoni et al., 2016), diopside (Damdinov, 2004; Schandal et al., 1989) or even pyralspitic-rich garnet (i.e. rich in pyrope, almandine, spessartine end-members) (Evans et al., 1979, Puga et al., 1999; 2011). This mineralogical variability depends on the preponderant physical conditions during their formation and subsequent metamorphic evolution (see section 1.5.2 below).

1.5.2 The rodingitization process

The first hypothesis about rodingitization was proposed by Weinschenk (1894), who considered that rodingites are the transformation products of calcite- or dolomite-bearing rocks due to contact metamorphism with an ultramafic intrusion. Marshall (in Bell et al., 1911) proposed a similar origin (digestion of limestone by peridotite). Contrastingly, the observed textural similarities between rodingites and saussurite-gabbros supported that rodingites are a form of altered gabbro (Benson, 1914; Munteanu-Murgoci, 1900). Later works, however, clearly linked the formation of rodingites to the interaction of Ca-rich hydrothermal fluids with mafic igneous rocks. These fluids mostly, but not always (Bloxam 1954; De, 1972; Hall and Ahmed, 1984), were related to serpentinization, in which Ca is released from clinopyroxene breakdown in the ultramafic rocks (Arsimov and Merenkov, 1930; Bilgrami and Howie, 1960; Grange, 1927; Miles, 1950; Thayer, 1966; Watson, 1953). After these studies, there was an almost general agreement on the concomitance between the rodingitization and serpentinization metasomatic processes (e.g. Honnorez and Kirst, 1975; O'Brien and Rodgers, 1973) and on the resulting Ca-enrichment and SiO_2- and alkalis (Na, K)-depletion in rodingites due to fluids circulation (Coleman, 1966; 1967; Leach and Rodgers 1978; Sarp and Deferne, 1978; Schandl et al., 1989). Coleman (1967) not only demonstrated that rodingitization involves a universal Ca gain and Si loss, but also suggested the reaction equation that explains the breakdown of plagioclase to hydrogrossular. This author also used for the first-time chemical activity diagrams to explain the different assemblages observed in rodingites and in their associated reaction rims. He was also the first to constrain pressure and temperature conditions of rodingitization. Based on the stability domains of hydrogrossular and serpentine, Coleman (1967) estimated that the formation of rodingites occurs at pressure ~ 4 kbar and temperatures between 290 °C and 450 °C.

In the last two decades, published works on rodingites have not been abundant compared to other rock types, and they have mostly focused on a better knowledge of the rodingitization process. Models of thermodynamic reaction paths by Bach and Klein (2009) provide insights into the formation of different rodingite types depending on temperature and composition of serpentinizing fluid. Typical grandite-rich rodingites (grossular + chlorite) form at very low pressure (500 bar) and temperatures below 300 ºC via fluids buffered by the equilibrium assemblage brucite-serpentine-diopside (Fig. 1.6

from Bach et al., 2013). At temperatures above 400 ºC, the equilibrium of the talc-tremolite-serpentine assemblage controls serpentinization fluids; if silica activity increases, clinozoisite is the main stable mineral in rodingites instead of granditic garnet. Bach and Klein (2009) conclude that rodingitization is most likely a result of diffusional metasomatism, driven by steep gradients in protons and silica activity (Fig. 1.6). In contrast, the activity gradient of Ca^{2+} is virtually zero and the diffusive mass transfer of

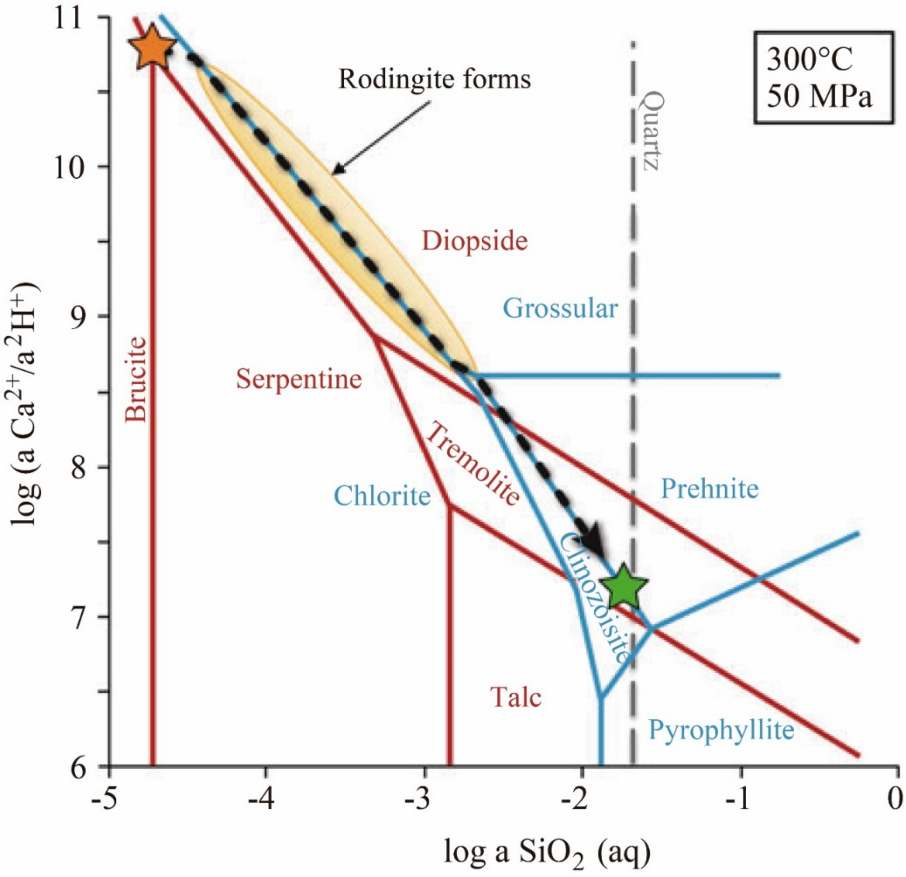

Figure 1.6. *log $a_{SiO2(aq)}$ versus log (a_{Ca2+}/a_{2H+}) diagram showing the phase relations in the system MgO-SiO_2-H_2O for a hydrated peridotite rock (i.e. serpentinite; in red) and in the system CaO-Al_2O_3-SiO_2-H_2O for a mafic rock (i.e. rodingite; in blue) at ocean-floor conditions (300 °C and 500 MPa). Fluid in equilibrium with the serpentine–brucite–diopside assemblage is predicted to induce rodingitization of an adjacent gabbro, giving place to the typical assemblage of grandite-rich rodingites (grossular-chlorite) along the black long-dashed line. At higher log a_{SiO2} conditions, the stable assemblage in serpentinite is serpentine-tremolite-talc and rodingite in equilibrium with the serpentinization fluid equilibrates in the prehnite or clinozoisite stability field (Bach et al., 2013, redrawn from Bach and Klein, 2009).*

Ca into rodingite is likely related to diffusion of hydroxo complexes (Bach and Klein, 2009). According to these conclusions, typical rodingitization is not caused by the Ca-rich nature of serpentinization fluids, but the stability of Ca-silicates (such as hydrogrossular) at low silica activity is imposed by host serpentinite (Frost and Beard, 2007; Frost et al., 2008). In this model, the prehnite-rich rodingite assemblages form due to the incomplete progression of rodingitization, below the maximum thermal stability limit of prehnite (350-400 ºC). Above this limit, epidote is present instead of prehnite (Bach and Klein 2009).

Vesuvianite-rich rodingites are also reported in ocean floor settings (e.g. Honnorez and Kirst, 1975). However, and opposite to the previous cases, the formation of these rocks has been usually ascribed to Ca enrichment in the serpentinization fluids (Fig. 1.7) (Li et al., 2004; 2008; 2010; 2017), and low X_{CO2} (Rice, 1983) and reducing (low fO_2) conditions (Ferrando et al., 2010; Zanoni et al., 2016).

Models also predict that, during rodingitization, pH conditions of fluids change from alkaline at low temperatures (~ 200 ºC) to neutral at ~ 300 ºC (Bach and Klein, 2009). Rodingitization also occurs at reducing conditions congruent with those of serpentinization (Dubińska, 2004b; Koutsovitis, 2008; Frost and Beard, 2007), by CO_2-free and moderately saline fluids (O`Hanley, 1992; Dubińska, 2004a). Low sulphur fugacity conditions during rodingitization are consistent with the presence of native metals, such as Au, Cu and Ag, in some rodingite outcrops (Frost and Beard, 2007; Leblanch and Lbouabi, 1988; Palyanova et al., 2018).

Besides ocean floor conditions, rodingitization has also been reported in metamorphic settings during the exhumation of eclogites (Li et al., 2007), or as superposed small-scale metasomatic events induced by metamorphic fluids (Li et al., 2004, 2017; Normand and Williams-Jones, 2007).

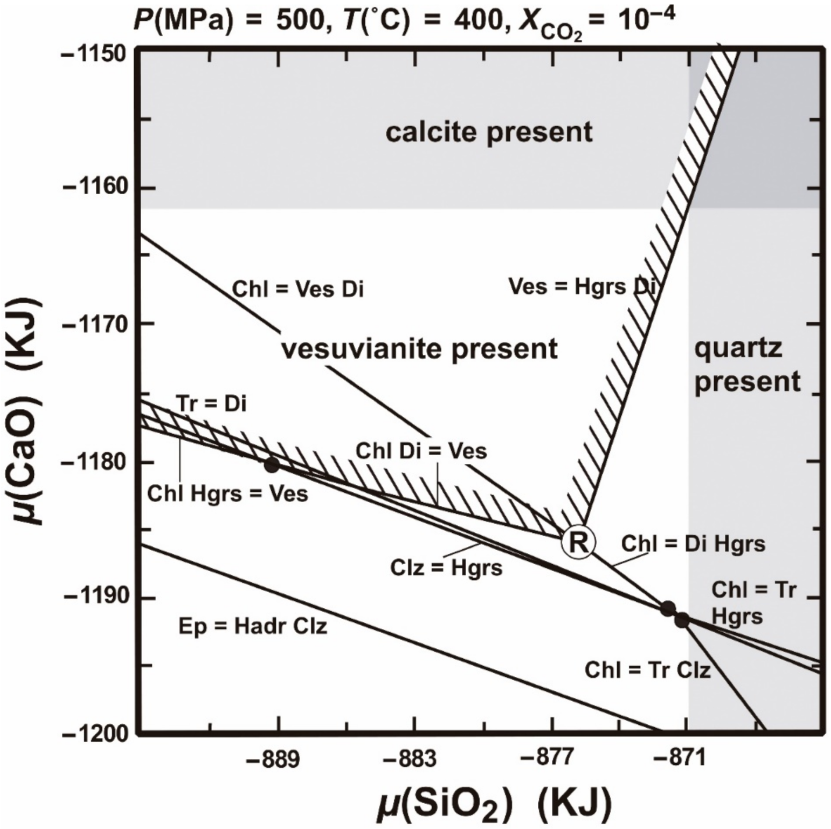

Figure 1.7. *a) μ(SiO_2)– μ(CaO) diagram showing rodingite equilibria at fixed X_{CO2} and P, T. Reaction equations are written such that the high μ(SiO_2) assemblage is on the right of the equation. Qtz- and Cal-present areas are highlighted with grey shadings, and vesuvianite by grey bars at Ves stable side. The conditions of vesuvianite-rodingites are close to the invariant point Ves-Hgrs-Di-Chl (R) (Li et al., 2008). This diagram shows that vesuvianite-bearing rodingites can only form at high μ(CaO) conditions.*

1.5.3 Geochemical implications of rodingitization

Apart from the mentioned enrichment in Ca and depletion in Si, alkalis (Na, K) are systematically lost from rodingites and incorporated into the serpentinization fluids (Evans et al., 1981; Frost et al., 2008; Koutsovitis et al., 2013; Li et al., 2007; O'Hanley, 1996;). Other elements, such as Al, Mg, Ti and Fe, can also be remobilised (Dubinska, 1997; Frost el al., 2008; Honnorez and Kirst, 1975; Koutsovitis et al., 2008; Li et al, 2004; Pomonis, 2008; Schandl et al., 1989). However, other studies considered the latter elements immobile, and considered their variations as artefacts of changing concentrations of other elements (Evans et al., 1981; Pusching, 2002; Li et al., 2007; Koutsovitis et al., 2013).

In terms of trace elements, rodingitization generally does not cause appreciable changes and preserves their magmatic signature (Dubińska, 1997; Evans et al., 1981; Fukuyama et al., 2014; Hatzipanagiotou and Tsikouras, 2001; Koutsovitis et al., 2018; Pomonis et al., 2008; Pusching, 2002;). High field strength elements (HFSE: Ti, Nb, Ta, Zr, Hf) normally remain immobile (Fukuyama et al., 2014), as well as Cr, Ni Sc, Y and REE. Occasional mobility of these elements has been related to particular conditions in specific geodynamic settings (Koutsovitis et al., 2008; 2013; Tsikouras et al., 2013). Exceptions are LILE (Cs, Rb, Ba, Sr), which may record contamination by seawater-derived fluids during rodingitization (Pusching, 2002).

1.5.4 Metasomatic reaction rims associated with rodingites

A common feature of rodingites is the occurrence of dark-coloured bimetasomatic zones (or reaction rims) in the contact with their hosting serpentinites, mainly consisting of chlorite and diopside or amphibole (Figs. 1.5 and 1.8). Suzuki (1953) first described these rocks. Coleman (1966, 1967) studied these rims in detail, and determined their clear metasomatic origin calling them "*blackwall*" (Chidester, 1962). Chlorite-rich metasomatic zones - usually named chlorite-blackwalls (e.g. Frost 1975) - are commonly in direct contact with rodingite, whereas diopside or tremolite richer zones occur toward the serpentinite (Fig. 1.8; Bøe, 1985; Dal Piaz, 1969; Fukuyama et al., 2014; Katoh and Niida, 1983, Larrabee, 1969; Nishiyama et al., 2017).

The main driving forces of formation of the reaction rims are the strong gradients in chemical potentials of some elements, mainly Ca and Mg, between Ca-rich rodingite and Mg-rich serpentinite (Coleman, 1966, 1967; Leach and Rodgers, 1978; Bøe, 1985; Li et al., 2004). The onset of the corresponding diffusion process occurs during rodingitization (Leach and Rodgers, 1978; Frost et al., 2008) and metasomatism may continue during subsequent subduction metamorphism (Li et al., 2004). Moreover, dehydration during subduction may release fluids from rodingites (by loss of H_2O from hydrogrossular) and promote brittle fractures and precipitation of tremolite veins in adjacent serpentinites (Nishiyama et al., 2017).

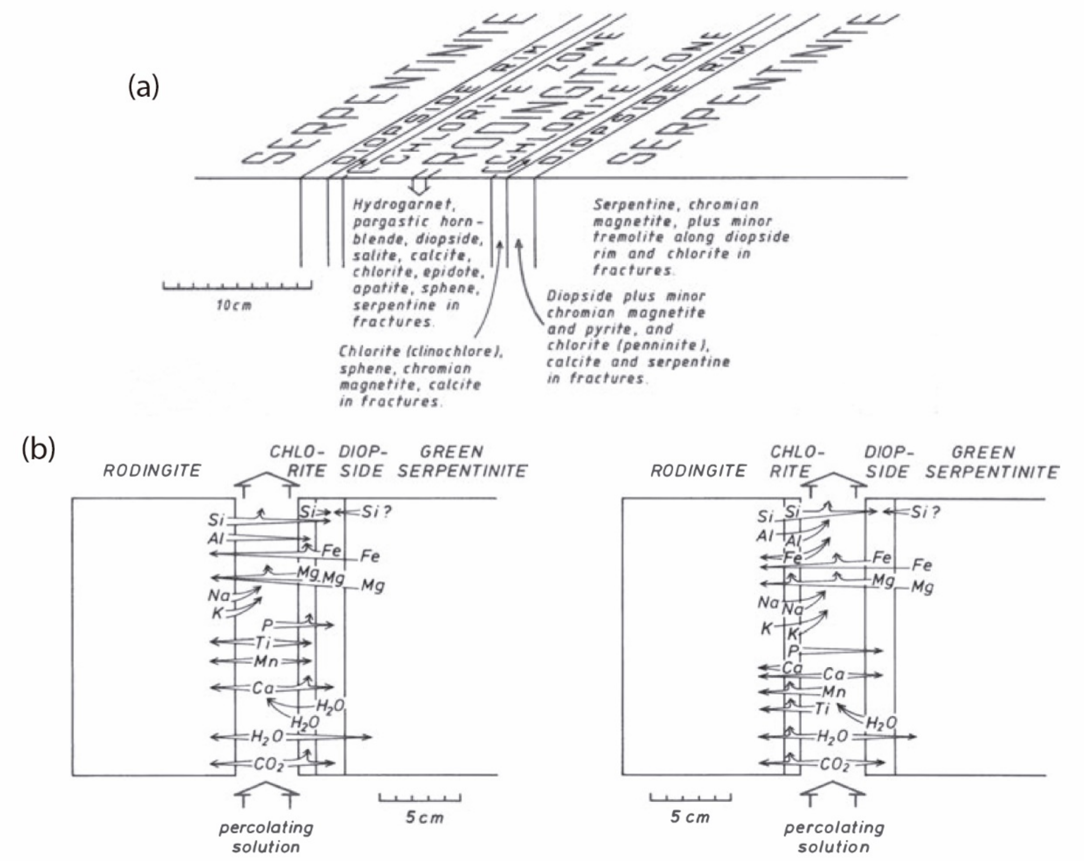

Figure 1.8. (a) *Sketch of rodingite, serpentinite and metasomatic reaction rims between them: chlorite zone (Chl-blackwall) and diopside zone (Di-reaction rims).* ***(b)*** *Proposed chemical exchanges during metasomatism between rodingite, reaction rims and serpentinite (from Bøe, 1985).*

1.5.5 Rodingite metamorphism: “metarodingites”

As already stated, (Cf. Section 1.3.1) rodingites associated with serpentinites are common rocks in metamorphic terranes of very different ages, geodynamic settings and grades of metamorphism. Frost (1975) firstly introduced the term “*metarodingite*” to identify rodingites in a contact metamorphism aureole generated by a granitic intrusion in ultramafic rocks. In the following years, several authors showed how orogenic metamorphism clearly induces mineralogical, compositional and textural changes in oceanic rodingites (Alberti et al., 1976; Anhaeusser, 1979; Honnorez and Kirst, 1975).

Detailed petrological and geochemical studies were conducted in metarodingites from Cima di Gagnone, in the Central Alps (Evans et al., 1979, 1981). These studies revealed the occurrence of different metarodingite types with different metamorphic mineral assemblages, textures, mineral chemistry and bulk compositions. These authors concluded that, together with progressive changes in P and T, variable extents of original rodingitization and significant mass transfer during metamorphism are key factors that control the evolution of rodingites during subduction.

Dubińska (2004b) emphasized the important effect of interaction with fluids with different oxygen fugacity for the metamorphic evolution of rodingites. In some rodingites from Lower Silesia, this author deduced low oxygen fugacity conditions for a grossular-rich garnet formed during rodingitization, and increasing oxygen fugacity for garnet with higher andraditic contents. This increase in oxygen fugacity was ascribed to interaction with fluids released from dehydration reactions in hosting serpentinites during subduction and prograde metamorphism.

Recent studies on rodingites under HT/HP and HT/UHP metamorphic conditions have shown that both chemical potential gradients and the redox state are essential variables to take into account for accurate thermodynamic modelling of phase relationships and mineral chemistry in metarodingites (Fig. 1.7) (Ferrando et al., 2010; Li et al., 2004; 2008; 2010, 2017; Zanoni et al., 2016).

1.6 Geological setting.

1.6.1 The Betic Cordillera

The Betic Cordillera is part of the Betic-Rif-Tell mountain belt, the westernmost segment of the circum-Mediterranean Alpine belt, and is located between the African and Eurasian plates (Fig. 1.9). This orogenic belt displays a tight arc-shape (the so-called Gibraltar Arc) that encircles the internal Alborán and South Balearic basins, and opens towards the Algero-Provençal Basin (Fig. 1.9). This configuration bears witness of a complex Alpine tectonic evolution, from subduction initiation to slab fragmentation and rollback, with associated intense crustal deformation (e.g. Hinsbergen et al., 2014 and references therein)

The Betic Cordillera has been divided into three main tectonic domains: External Zones, Flysch Trough Units and Internal Zones (Fig. 1.10) (e.g. Platt et al., 2013 and references therein). The External Zones represent the Mesozoic and Cenozoic sedimentary covers of the Iberian paleo-margin, detached, folded and thrusted toward the

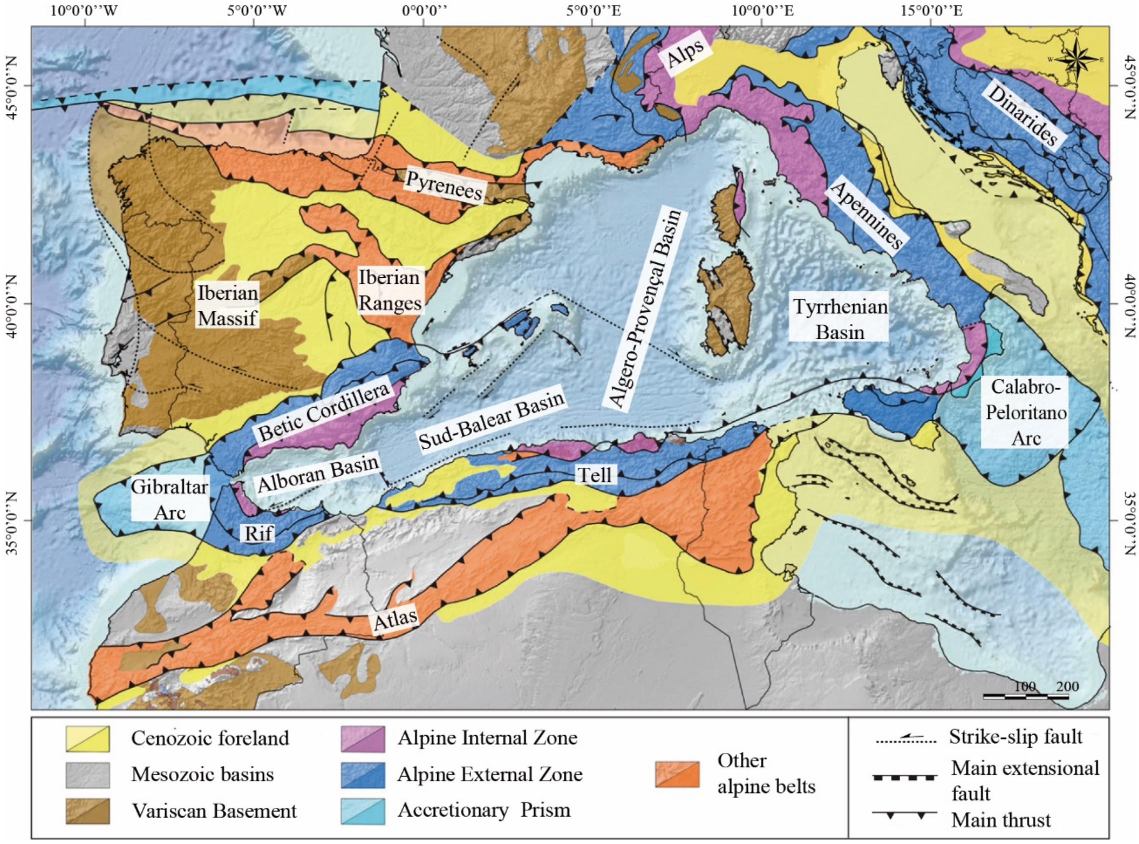

Figure 1.9. *Simplified geological map of the western Mediterranean Alpine belt showing the major Cenozoic structural features and the location of the Betic Cordillera. Modified from Etheve et al. (2016).*

foreland basins (Fig. 1.10). The Flysch Trough Units correspond to deep-water sediments with remains of ocean-like mafic rocks, indicating they were deposited in an oceanic basin (Fig. 1.10). The Flysch Trough represents the paleoceanic domain between the Iberian-paleomargin and the Alborán domain (see below). Finally, the Internal Zones include two different paleogeographic domains. The Alborán Domain comprises the Dorsal Units and the Maláguide and Alpujárride Complexes, representing a thinned allochthonous terrain that thrusted and folded onto the External Zones (Fig. 1.10). The second domain, i.e. the Nevado-Filábride Complex, represents part of the South-Iberian paleo-margin that subducted below the Alborán Domain and was later exhumed.

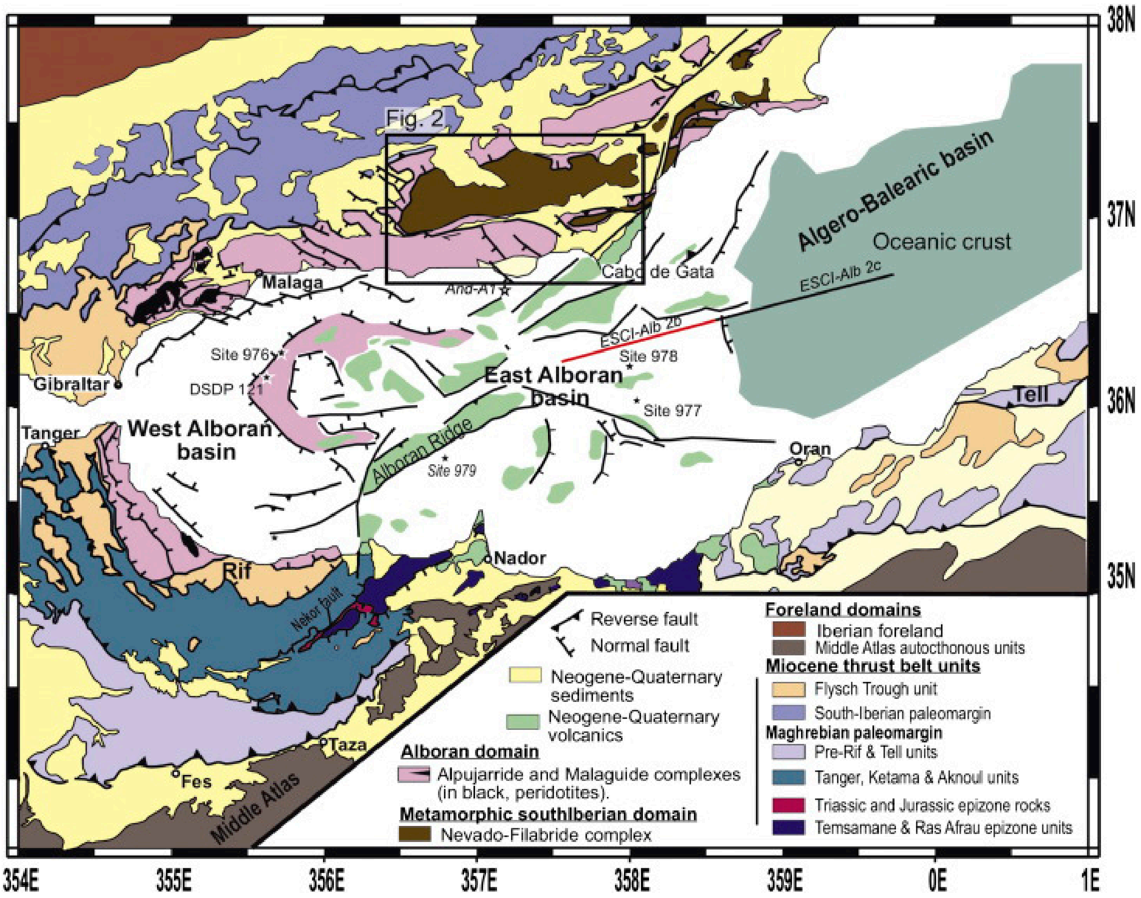

Figure 1.10. *Simplified geological map of the Betic-Rif-Tell mountain belt with location of the Nevado-Filábride Complex and Alborán domain (Booth-Rea et al., 2015).*

1.6.2 The Nevado-Filábride Complex

The Nevado-Filábride Complex (NFC) is the deepest metamorphic complex of the Internal Zones of the Betic Cordillera and crops out in the core of E-W elongated antiformal domes with core-complex-like structure (Fig. 1.11 and 1.12a). Despite lacking agreement about the specific number and names of the tectonic units within the NFC, this Complex can be essentially divided, from bottom to top, into the Veleta unit (equivalent to the Ragua unit) and Mulhacén unit (comprising the Calar Alto and Bedar-Macaél units defined by Martínez-Martínez et al., 2002).

The lithological sequence of the NFC consists of metapelites, marbles, and orthogneisses derived from the Palaeozoic (Variscan) basement (e.g., Gómez-Pugnaire et al., 2012; Laborda-López et al., 2015a and b, Rodríguez-Cañero et al., 2018 Santamaría-López and Sanz de Galdeano 2018) or the Permo-Triassic formations of the South-Iberian paleomargin (Booth-Rea et al., 2005; Jabaloy-Sánchez et al., 2018). Minor amounts of metaultramafic (mainly metaserpentinites) and Jurassic metamafic rocks (eclogites, amphibolites and rodingites) (Puga et al., 1999, 2011; Gómez-Pugnaire et al., 2000) occur in shear zones in the uppermost part of the sequence. In the following paragraphs, I present a summary of the tectono-metamorphic and geochronological evolution of the NFC and the different views about this topic (Booth-Rea et al., 2015; Gómez-Pugnaire et

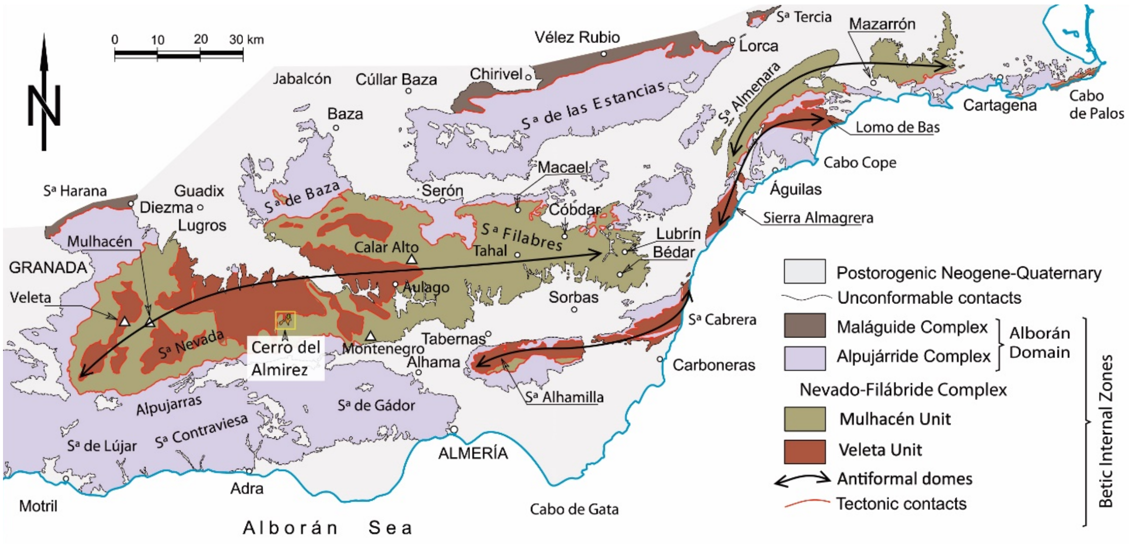

Figure 1.11. *Simplified geological sketch of the Nevado-Filábride Complex, divided into the Veleta and Mulhacén units. Modified from Rodríguez -Cañero et al. (2018).*

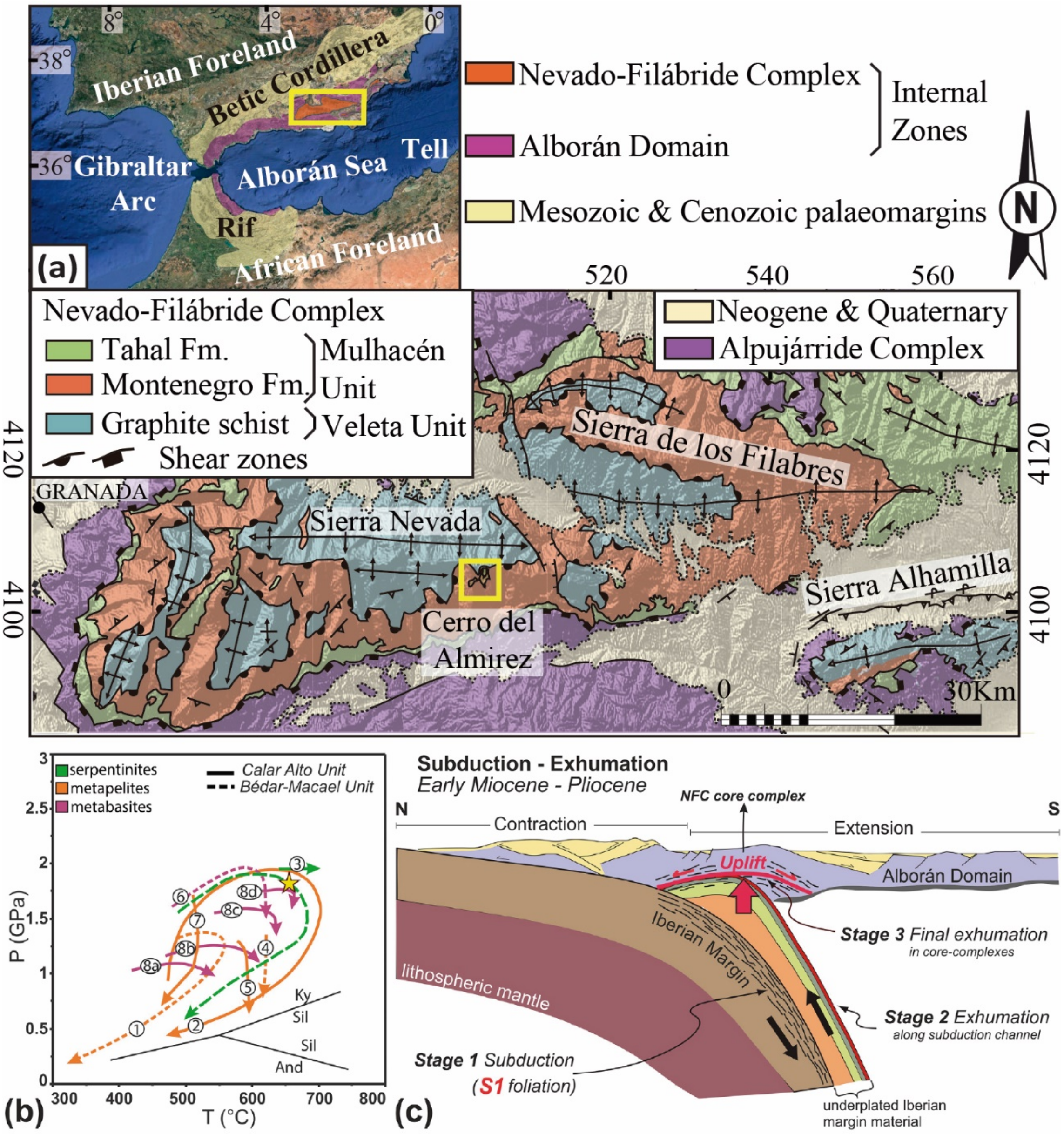

Figure 1.12. (a) *Geological map of E–W domes (Sierra Nevada, Sierra de los Filabres and Sierra Alhamilla) in the western part of the Nevado-Filábride complex (NFC) (modified after Jabaloy-Sánchez et al., 2015). The yellow inset shows the location of the Almirez massif. Upper left inset: main tectonic domains of the peri-Alborán orogenic system; the yellow inset indicates the location of the NFC map shown in Fig. 1a;* ***(b)*** *Compilation of representative P-T metamorphic paths of different lithologies in the NFC grouped by units (From Dilissen et al., 2018; modified from López Sánchez-Vizcaíno and Gómez-Pugnaire, in press): (1) Behr and Platt (2012, 2013); (2) Gómez-Pugnaire et al. (1994); (3) López Sánchez-Vizcaíno et al. (2009) and Padrón Navarta et al. (2010a); (4-6) Augier et al. 2005; (7) Jabaloy-Sánchez et al. (2015); (8 a–d) P-T-t paths of four eclogites from Platt et al. (2006). The P-T-t path of the Almirez massif (dashed green line) and the peak metamorphic conditions (yellow star) of the dehydration of Atg-serpentinite in this massif are also shown (after Jabaloy-Sánchez et al., 2015).* ***(c)*** *Tectonic model for the Alpine evolution of the NFC (from Dilissen et al., 2018, after Behr and Platt, 2012).*

al., 2012; Jabaloy-Sánchez et al., 2015, 2018; Kirchner et al., 2016; López Sánchez-Vizcaíno and Gómez-Pugnaire, in press; Platt et al., 2013; Puga et al., 2009, 2011). I put special emphasis on the metamorphic mafic and ultramafic rocks.

SHRIMP U–Pb ages of igneous zircons in metamafic rocks, including metarodingites, from the upper part of the Mulhacén unit yield crystallization ages of c. 185 ± 3 Ma (Puga et al., 1999; 2011). These ages, according to Puga et al. (2011), mark the Pangea break-up and the earliest opening of the western branch of the Alpine Tethys Ocean. However, the Iberian massif provenance of continental lithologies in the NFC and the E-MORB signature of metamafic rocks (Gómez-Pugnaire et al., 2000, 2004, 2012) support that the NFC sequence was part of the Jurassic, magma-poor, hyperextended continental margin of S–SE Iberia, with portions of exhumed mantle from an ocean-continent transition zone (Booth-Rea et al., 2015; Jabaloy-Sánchez et al., 2018). Toward the E and NE, an ocean basin existed between the S–SE Iberia continental margin and the terranes of the Alborán Domain (Booth-Rea et al., 2007; and references therein), beneath which it subducted during early to middle Miocene (see below).

The NFC experienced high-P metamorphic conditions linked to subduction below the Alborán Domain. The Mulhacén unit records peak P–T conditions in the range of 1.2-2.1 GPa and 550–650 °C (Fig. 1.12b) (Augier et al., 2005; Booth-Rea et al., 2005, 2015; Jabaloy-Sánchez et al., 2015; Puga et al., 1999). This peak metamorphism was followed by retrogression at amphibolite or greenschist facies conditions during exhumation. The NFC metaserpentinites and metamafic rocks mainly preserve the structures and mineral assemblages of the prograde subduction stage (Jabaloy et al., 2015). On the contrary, metasedimentary rocks were strongly overprinted during exhumation.

SHRIMP U-Pb ages of metamorphic zircon overgrowths, Lu-Hf in garnet, and Rb-Sr multi-grain isochron ages yield early to middle-Miocene ages, i.e. Burdigalian (15–18 Ma), for the NFC high-P metamorphic event (Gómez-Pugnaire et al., 2012; Kirchner et al., 2016; López Sánchez-Vizcaíno et al., 2001; Platt et al., 2006). These ages account for the subduction of the SE Iberian paleomargin beneath the extending Alborán domain, during the westward rollback of the subducting Alpine Tethys slab (Fig. 1.12c) (Behr and Platt, 2012, 2013; Booth-Rea et al., 2005, 2007, 2015; Gómez-Pugnaire et al., 2012). The petrological and geochemical evidence of oceanic seafloor alteration of Jurassic, hypabyssal mafic rocks to rodingites (Chapter 4), and their E-MORB geochemical signature (Gómez-Pugnaire et al., 2000, 2004; Chapter 5) unequivocally indicate the lower plate provenance of the NFC metaserpentinites and metamafic rocks from the subducted Iberian ocean-continent transition (Booth-Rea et al., 2015; Jabaloy-Sánchez et al., 2018).

Exhumation of the NFC occurred during the Miocene, from the Burdigalian to Messinian (Behr and Platt, 2013). The lower plate units of the NFC are at present exhumed along E-W dome core complexes separated by detachment faults from the upper plate Alpujárride Complex (Fig. 1.12a and c) (Booth- Rea 2005, 2015; Martínez-Martínez et al., 2002, 2006; Platt et al., 2013; and references therein). Data on zircon fission tracks indicate fast cooling and exhumation of the NFC. Behr and Platt (2013) proposed a two-stage exhumation process. The first stage corresponds to fast exhumation — along the subduction channel — from metamorphic peak conditions to mid-crustal levels. This was followed by shallower exhumation and cooling along low-angle detachment faults rooted at the brittle-ductile transition, forming the structures of the NFC core complex (Fig. 1.12c) (Behr and Platt, 2013; Platt et al., 2015).

1.6.3 The Cerro del Almirez massif

The Cerro del Almirez ultramafic massif (or Almirez massif) is the largest (2.3 km^2) of several bodies of metaserpentinites and metamafic rocks in the upper part of the NFC. The Cerro del Almirez outcrops are located on top of the metasedimentary sequence of the Mulhacén Unit, and are overthrusted both onto light micaschists (the so-called Tahal Formation) and dark, graphite-rich metapelites (the so-called Montenegro Formation), which in turn overly the Veleta Unit graphitic-schists (Fig. 1.13; Jabaloy et al., 2015).

The two mains ultramafic lithologies of the Cerro del Almirez massif are antigorite-serpentinite (hereafter Atg-serpentinite) and chlorite-harzburgite (Chl-harzburgite). Their respective outcropping areas are separated by ~ 1 to 8 m thick transitional lithologies (Padrón-Navarta et al., 2011). This contact shows no evidence of tectonic discontinuity (Trommsdorff et al., 1998) and represents the arrested dehydration front of Atg-serpentinite producing Chl-harzburgite, that is, the Atg-out isograd according to the reaction:

Antigorite → Olivine + Orthopyroxene + Chlorite + H_2O (Padrón-Navarta et al., 2011).

Strongly foliated Atg-serpentinite (Atg + Ol + Mag ± Di ± Tr ± Chl ± Ti-Chu; all mineral abbreviations after Whitney & Evans, 2010) crops out in the upper portion of the massif (~ 200 m thick) and records several prograde dehydration reactions: brucite breakdown (López-Sánchez-Vizcaíno et al., 2009; 2005), diopside transformation to tremolite (Jabaloy-Sánchez et al., 2015; Padrón-Navarta et al., 2012; Trommsdorff et al., 1998), titanian clinohumite breakdown (López-Sánchez-Vizcaíno et al., 2005, 2009), and antigorite reaction with talc forming orthopyroxene-, SiO_2-rich serpentinites (Padrón-Navarta et al., 2010b).

Atg-serpentinite became unstable at ~ 650°C and 16–19 kbar and dehydrated to prograde Chl-harzburgite (Ol+Opx+Chl+Mag±Tr±Ti-Chu), which experienced metamorphic peak at ~ 710 °C and similar pressure (López-Sánchez-Vizcaíno et al., 2009; Padrón-Navarta et al., 2010a). Chl-harzburgite crops out in the lower part of the ultramafic body (~ 200 m thick) with either granofelsic or spinifex-like texture (Padrón-

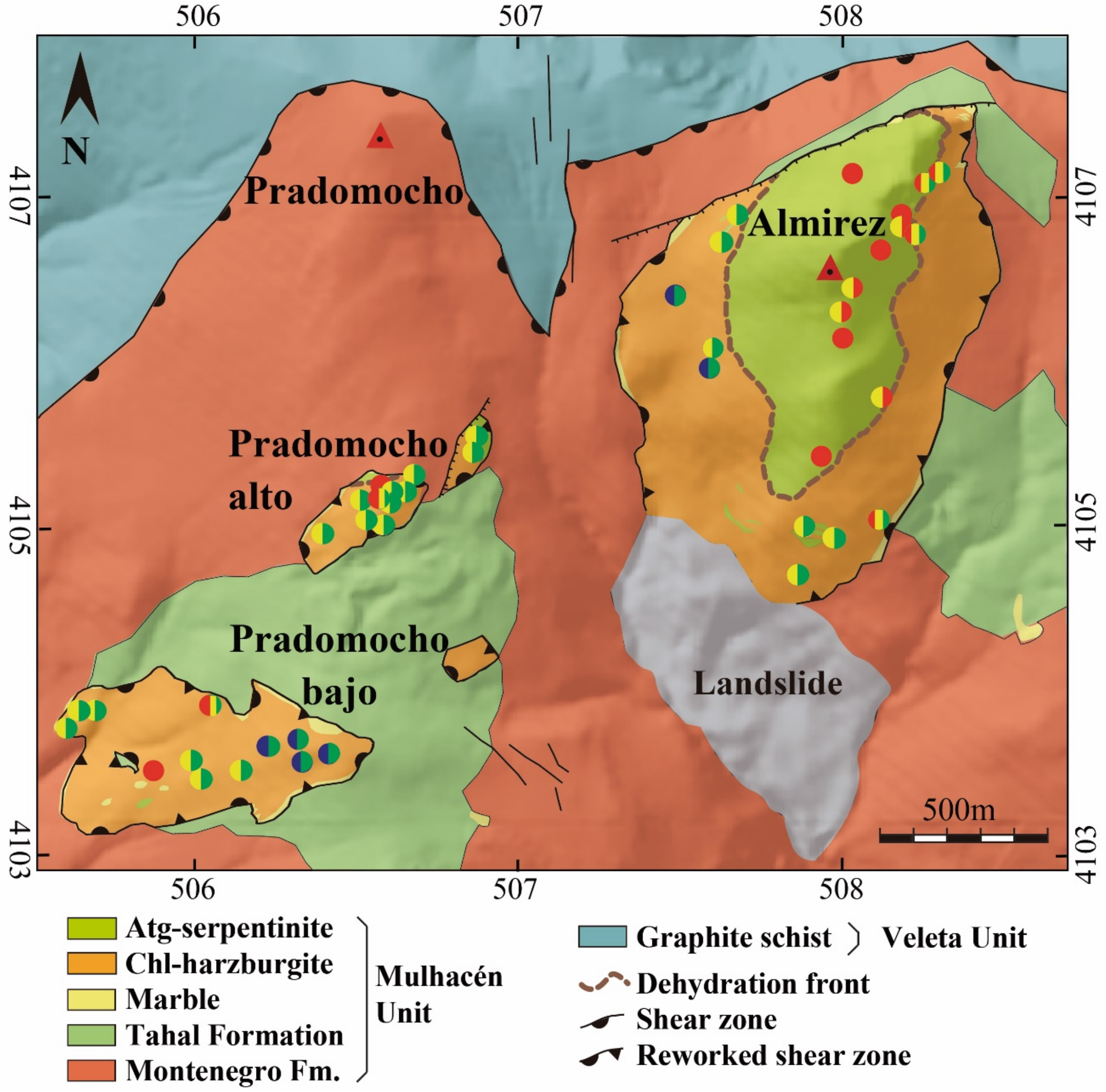

Figure 1.13. *Geological map of the Almirez ultramafic massif modified after Jabaloy-Sánchez et al. (2015). Locations of metarodingites are also shown (coloured circles)*

Navarta et al., 2010a; Padrón-Navarta et al., 2011; Dilissen et al., 2018). Metamorphic zircons from a metapyroxenite layer within Atg-serpentinite constrained the early middle-Miocene age (Langhian, 15 ± 0.6 Ma) of the high-P metamorphic event in these rocks (López Sánchez-Vizcaíno et al., 2001).

Isotopic and trace element studies (Alt et al., 2012; Marchesi et al., 2013) evidence that the former ultramafic protoliths of the Cerro del Almirez serpentinites were transformed to chrysotile and lizardite serpentinites at temperatures around ~ 200 °C in a seafloor setting. During subduction, the prograde transformation of seafloor serpentinite to Atg-serpentinite lowered the bulk ferric (Fe^{3+}) to ferrous (Fe^{2+}) iron ratio by magnetite dissolution into fluids (Debret et al., 2015). Further decrease in the amount of magnetite and bulk rock Fe^{3+}/Fe_{Total} occurred by the same mechanism during antigorite breakdown (Debret et al., 2015). Metarodingite bodies –which are the matter of this thesis– occur both in Atg-serpentinite and Chl-harzburgite with either granofelsic- or spinifex-like textures (Trommsdorff et al., 1998) and were first described by Puga et al., (1999). Further to the East, similar metarodingite bodies crop out in the Cerro Blanco and Montenegro ultramafic massifs (Puga et al., 1999).

2 Aims and Thesis structure

2.1 Motivation and statement of the problem

The Cerro del Almirez ultramafic massif has stimulated notable interest among geologists since its first description in the early thirties of the 20th century and the publication of some more detailed studies during the eighties. However, it was not until the very late years of the past century (Trommsdorff et al., 1998) that the unique feature of this outcrop was highlighted. Cerro del Almirez is the only known locality worldwide in which the antigorite-out isograd is preserved, thus attesting for the dehydration of serpentinites to peridotites at high-pressure metamorphic conditions during subduction.

This Ph.D. Thesis has been conducted within a research group that has investigated this isograd and its implications for the evolution of subduction zones during the last 25 years. Covered topics comprise the metamorphic conditions of the ultramafic rocks and the associated dehydration processes; the geochemical characterization and influence of dehydration on the composition of rocks and fluids; the mechanisms of dehydration and fluid flux; the thermodynamic modelling and petrophysical implications of dehydration; and finally, the tectonic evolution of the complex. These results have been published in 25 articles in high impact international journals. Research has been funded by five grants of the Spanish National Research Plan, two European Commission FP-7 Marie-Curie Initial Training Networks and one FP-7 Marie Curie European Reintegration Grant.

Rodingites (metarodingites in fact) are common rocks in Cerro del Almirez and they were already mentioned or partially studied in some previous works in this massif. However, this Ph.D. Thesis is the first comprehensive study of this rock type in this locality. Interest of this research is motivated by the occurrence of metarodingite bodies at both sides of the antigorite-out isograd. This provides a matchless opportunity for characterizing metarodingites and determining their metamorphic evolution as controlled by the simultaneous dehydration reactions in hosting serpentinites during the subduction event shared by these two lithologies.

2.2 Aims and approach

This Ph.D. Thesis aims to unravel the evolution of metarodingites enclosed in ultramafic rocks of the Cerro del Almirez massif, from their formation at ocean floor conditions to subduction and subsequent exhumation leading to partial retrogression. The results of this study are willing to contribute to the present body of knowledge on the complex metamorphic and geochemical processes linked to serpentinite dehydration in subducting slabs, and to the interaction of the released fluids with different rock types.

Accordingly, this research has focused on the following four main goals:

i. To establish the metamorphic evolution of the rodingites during subduction and their interaction with adjacent serpentinites and their dehydration products (i.e. chlorite-harzburgites).

ii. To determine the geochemical behaviour of lithophile major and trace elements during the metamorphic evolution of metarodingites and their mobility due to interaction with fluids from dehydrating subducted serpentinites.

iii. To establish the behaviour of highly siderophile elements (Re and platinum-group elements: Os, Ir, Ru, Pt and Pd) and the Re-Os isotopic system in metarodingites, associated metasomatic rims and embedding ultramafic rocks during oceanic rodingitization, subduction and serpentinite dehydration.

iv. To establish the general significance of metarodingites for geological processes occurring in subduction zones prior and beyond the antigorite dehydration reaction that takes place in subducting serpentinites.

To accomplish the aforementioned goals, I followed a combined field, petrological and geochemical approach.

i. To address the first goal, a detailed field study was made in order to map, locate and describe all the main metarodingite outcrops of the Cerro del Almirez massif and set their position with respect to the antigorite-out dehydration front. According to their macroscopic features, the main metarodingite types were differentiated and carefully sampled together with their hosting ultramafic rocks and transitional metasomatic rims. A representative number of selected samples was studied under the petrographic microscope, SEM microscopy and EPMA. Whole-rock analyses were obtained by XRF. Using these data, the complete sequence of stable mineral assemblages could be stablished for each metarodingite type as well as the compositional variations of major elements in whole-rocks and minerals. Thermodynamic modelling with Perple_X software package led to the calculation of the metarodingite prograde metamorphic evolution as a function of different intensive and extensive variables. The different types of metarodingites recognized in this study attest for successive stages in the prograde metamorphic evolution during subduction.

ii. To address the second and third goals, selected samples from each metarodingite type were prepared and analyses were performed for major elements (XRF), ferrous iron (potentiometric titration), lithophile trace elements in whole-rocks (ICP-MS) and minerals (LA-ICP-MS), highly siderophile elements (ICP-MS) and Os isotope ratios (N-TIMS). Data of highly siderophile elements and Os isotopes were obtained during a research stay at the Department of Earth Sciences of the Durham University, United Kingdom. This rather unique dataset was employed to determine the geochemical variations and partitioning processes of each group of elements during the previously stablished stages of their metamorphic evolution.

iii. The fourth final goal has been achieved by integrating and discussing all the previous results and comparing them with present models in the literature about the evolution of fluids and rocks in subduction zones, thus shedding new light on the influence of rodingites on these global processes.

2.3 Organization of the Thesis

The present Thesis is divided into three parts. **Part I** comprises: the introduction to the main topics dealt with in this research (**Chapter 1**); a short account of the motivation, aims and organization of the Thesis (**Chapter 2**); and a description of the methodology (**Chapter 3**), from field work to analytical techniques, employed for the results acquisition.

Part II corresponds to the core of the Thesis and reports its main results divided into two chapters. In **Chapter 4**, the first aim of the thesis is addressed. It shows a complete field and petrographic description of the studied metarodingites, followed by a detailed chemographical analysis of their mineral assemblages and the thermodynamic modelling of their metamorphic evolution during subduction. These results have been published in the JCR journal *Journal of Metamorphic Geology* [1] (SCI impact factor: 4.418, 2nd out of 49 journals in the Geology area, ISI JCR ® 2017). The second and third aims of the thesis are the main matter of **Chapter 5**, in which a detailed description is made of the main geochemical features and balances of the studied metarodingite types. In the discussion section of both chapters 4 and 5, the main petrological and geochemical implications of rodingites associated with ultramafic rocks in subduction zones are addressed, thus achieving the fourth main aim of this Ph.D. Thesis. In the final **Part III**, the main conclusions of the thesis are merged, the cited references are listed and all necessary appendixes are shown.

In addition to the paper cited above, the results of this thesis have been presented in several European Geoscience Union General Assemblies (2014–2018) (Vienna, Austria) and other international meetings, such as 4th International HSE Geochemistry Workshop (Durham, United Kingdom, 2016), 4th Serpentine days (Sète, France, 2016) and 12th International Eclogite Conference (Åre, Sweden, 2017).

---

[1] Laborda-López, C., López-Sánchez-Vizcaíno, V., Marchesi, C., Gómez-Pugnaire, M. T., Garrido, C. J., Jabaloy-Sánchez, A., Padrón-Navarta, J.A. & Hidas, K. (2018). High-P metamorphism of rodingites during serpentinite dehydration (Cerro del Almirez, Southern Spain): Implications for the redox state in subduction zones. *Journal of Metamorphic Geology*, *36*(9), 1141-1173.

3 Methodology

3.1. Field work and rock sampling

Field work and sampling were made mainly between spring and autumn of 2014, with sporadic campaigns in 2015 and 2016 to make punctual observations and take specific samples. The investigated outcrops include the Cerro del Almirez massif and the smaller nearby outcrops of Prado Mocho (Fig. 1.11). They are located in the eastern termination of the Sierra Nevada mountain-range, in the western part of the Almería province, in an area approximately bounded by latitudes 37º05’30’’ to 37º04’13’’ and longitudes 2º54’25’’ to 2º56’14’’, covering a surface of around 6.67 km^2. Elevations are comprised between 1963 m and ~ 2500 m with the highest altitudes corresponding to the so-called Cerro del Almirez twin peaks (2511 m and 2514 m).

In the mentioned ultramafic massifs, thirty-five metarodingite outcrops were totally localized (see Table 3.1 and 3.2, at the end of this chapter). In each of them, a detailed description of the macroscopic characteristics was made as well as a complete petrological and structural data compilation (Fig. 3.1). Homogeneous representative samples were collected from every outcrop. These include: the type or types of metarodingite; the sequence of metasomatic lithologies transitional to the host ultramafic rocks; one ultramafic rock sample (either Atg-serpentinite or Chl-harzburgite) in contact (less than 20 cm apart) with the most external metasomatic rim; and one ultramafic rock sampled several metres apart from the metarodingite (Fig. 3.1b, c and d). A total of 164 samples were collected.

Sixteen representative outcrops were selected for the detailed petrological and geochemical studies. Attending to their host ultramafic rock, they are distributed as following: five within Atg-serpentinite, nine within Chl-harzburgite, and two within the transitional lithologies at the antigorite dehydration front. In a total number of 80 selected samples, 27 samples correspond to metarodingites (i.e. 10 grandite-metarodingites, 11 epidote-metarodingites and 3 pyralspite-metarodingites; 3 mix samples cf. Chapter 4) with different degrees of amphibolitization; 23 samples correspond to metasomatic reaction rims (i.e. 14 Chl-blackwalls, 5 Chl-Di- and 4 Chl-Ol-Di-metasomatic rims; cf. Chapter 4); 30 samples correspond to host ultramafic rocks, either close or far from the metasomatic rims contact (i.e. 10 Atg-serpentinites, 12 Chl-harzburgites, 4 transitional rocks: 1 Chl-serpentinite and 3 Atg-Chl-Opx-Ol rocks) and 4 recrystallized Chl-harburgites.

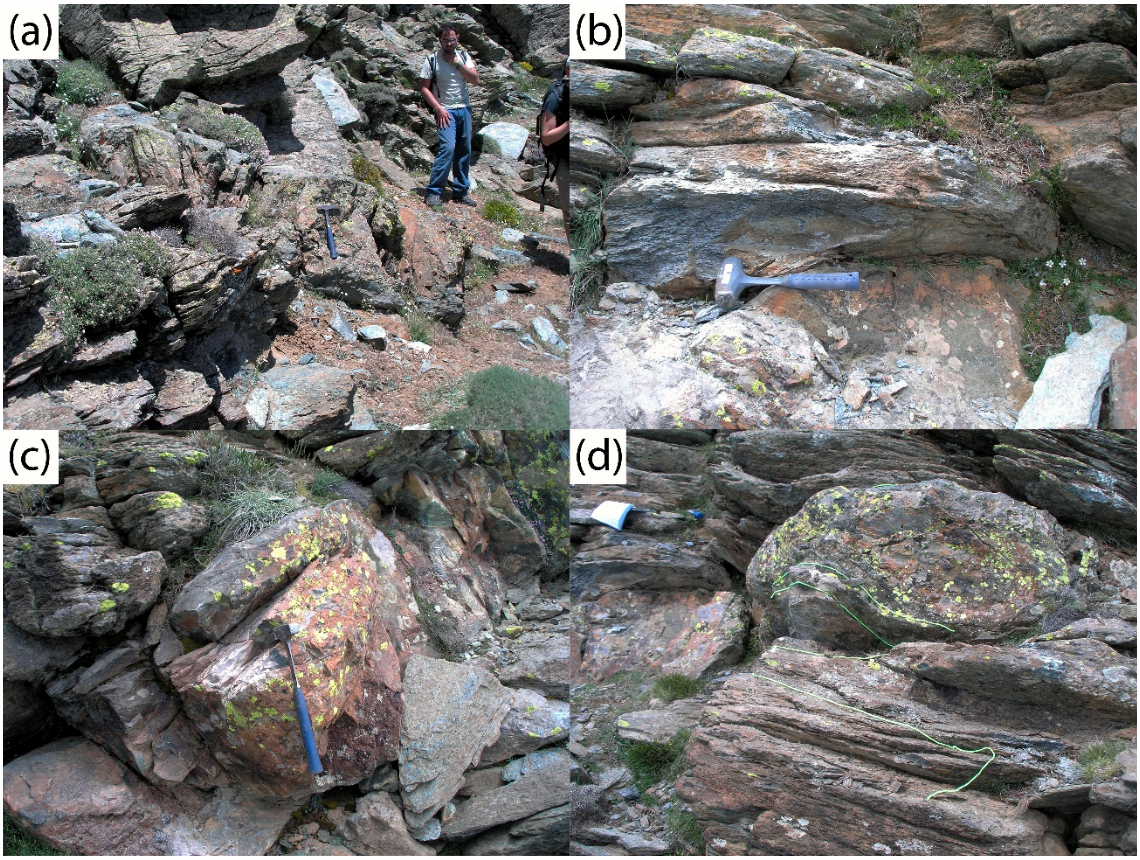

Figure 3.1. *Examples of sampled outcrops.* ***a)*** *metarodingite dike in serpentinites;* ***b)*** *metasomatic reaction rims (above hammer);* ***c)*** *metarodingite in antigorite serpentinite;* ***d)*** *sampling using strings to mark the size and limits of reaction rims and serpentinites around a metarodingite boudin.*

3.2 Sample preparation

Sample preparation for thin sections and chemical analyses was done in the scientific premises of the Instituto Andaluz de Ciencias de la Tierra (IACT; CSIC-University of Granada, Armilla, Granada, Spain). Each sample, of around 5-11 kg, was cut with a diamond saw (Fig. 3.2a) so that all altered external parts, veins and visible heterogeneities were removed, thus insuring the homogeneity of each sample. A representative slice of each sample was stored to prepare the thin sections. The remaining portion of each sample was cut forming small cubic pieces. These were ultrasonicated in distilled water during

30 minutes in order to remove all impurities such as dust, clays or metal particles. Samples were dried before crushing in a steel jaw crusher (Fig. 3.2b). The crushed samples were split by a riffle-splitter in order to obtain a representative aliquot. A part of the crushed samples was used to prepare the whole-rock powders and the rest was stored for future studies.

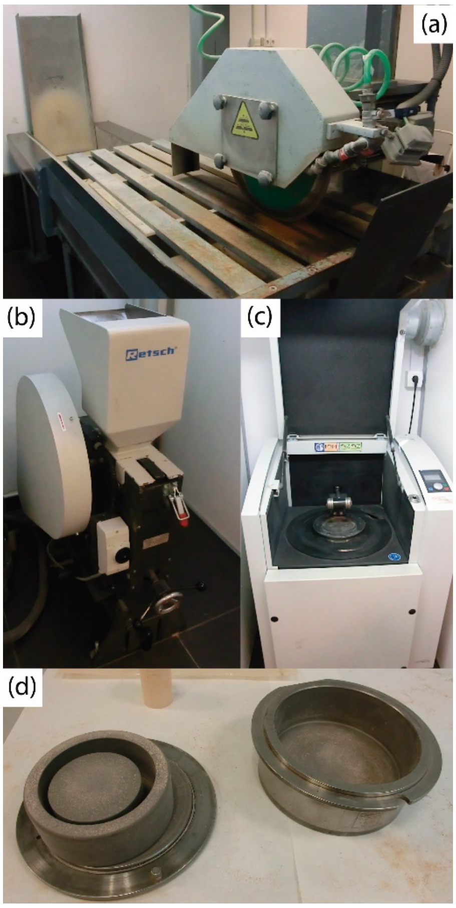

***Figure 3.2.** Equipment used for sample preparation at the IACT: **(a)** diamond saw;**(b)** steel jaw crusher; **(c)** Vibratory Disc Mill RS 200; and **(d)** agate grinding set.*

3.2.1 Preparation of thin sections

Thin sections were prepared at the Departamento de Mineralogía y Petrología of the University of Granada. The slices obtained from each sample were cut with a diamond saw into a thin sliver of rock (3 mm thick). These slivers were ground in one side to make a smooth flat surface by polishing with 3 µm diamond grit. The resulting samples, with a 30 µm standard thickness, were attached to a glass slice with epoxy resin.

3.2.2 Preparation of whole-rock powders

In order to obtain whole-rock powders (mesh size ≤ 25 µm), the crushed sample material was first milled by hand in an agate mill during one hour, and then in a second agate disc mill (Fig. 3c and d) during 40 minutes to 2 hours – depending on the nature of the sample- to obtain an extremely fine powder with talc texture. To avoid any kind of contamination, the jaw crusher, the agate mill and the agate disc mill were treated after the processing of each sample with quartz sand, and also were conscientiously washed in several cycles with an alcohol solution and distilled water. Finally, mills were dried with compressed air. The powders obtained were stored into PVC vials - previously cleaned with distilled water and alcohol and dried with compressed air – for whole-rock major and trace elements analyses.

3.3 Analytical methods

3.3.1 Electron microprobe analyses

Mineral analyses were obtained by a CAMECA SX100 electron microprobe (EPMA) at the Centro de Instrumentación Científica (CIC; University of Granada) or a JEOL JXA-8230 electron microprobe at the Scientific and Technological Centres of UB (University of Barcelona, Spain). Both instruments operated with 15–20 kV acceleration voltage, 10–15 nA beam current, and 5 μm beam diameter. Precision was about ± 1.5% for concentrations of 1 wt%. Natural minerals and synthetic glasses were used as standards. The peak measurement time was 10 s for Na, K, Mg, Ca, Al, Si, Mn, F and Cl, 20 s for Cr and Ti, and 30 s for Ni.

X-ray mapping was performed at 297 nA beam current and beam size spot (focused). The step (pixel) size was 2 μm and Dwell time 300 ms per pixel. X-ray maps were processed with the MATLAB©-based software XMapTools (Lanari et al., 2014).

3.3.2 Scanning electron microscopy

Qualitative chemical maps were acquired on carbon coated thin sections using a Carl Zeiss scanning electron microscopy (SEM) equipped with Oxford/Nordlys EBSD and EDS detectors at the IACT (Fig. 3.3a). Automated mapping and data processing were done using the Aztec software from Oxford Instruments. Additional maps were acquired by a Leo 1430VP SEM at the CIC, equipped with an Inca 350 v. 17 Oxford Instruments EDS system.

3.3.3 Whole-rock analyses of lithophile elements

Major elements and V, Cr, Co, Ni, Zn and Ga were analysed by X-ray Fluorescence (XRF) in a BRUKER S4-Pioneer instrument at the IACT (Fig. 3.3b), using standard sample preparation and analytical procedures. The accuracy of analyses was assessed by repeated analyses of international reference materials (JP-1 peridotite, UB-N serpentinite, UM-2 ultramafic rock, PM-S microgabbro, and BIR-1 basalt) handled as unknowns (Table A14 in the Appendices), which show good agreement with working values for these standards (Govindaraju, 1994; Imai et al., 1995; Jochum et al., 2016). Ferrous iron in whole-rocks was determined by potentiometric titration with a standardized permanganate solution at the Geoscience Laboratories (GeoLabs) of the Ontario Geological Service (Canada).

Whole-rock trace elements (Rb, Sr, Y, Zr, Nb, Cs, Ba, REE, Hf, Ta, Pb, Th and U) were analysed by an Agilent 8800 ICP-MS/MS (inductively coupled plasma mass spectrometer) at the IACT (Fig. 3.3c). To ensure the dissolution of potentially refractory minerals (e.g. titanite, zircon and oxides), digestion of metarodingites and metasomatic rims was carried out at high pressure in Parr PTFE-lined bombs adding 1 ml distilled HF and few drops of Milli-Q H_2O to 50 mg rock powder (Fig. 3.4d). This mixture was then heated to 190 °C for 48 hours in an oven (Fig. 3.4c). After cooling, the solution was transferred to a PFA Teflon vial along with 0.5 ml HF and Milli-Q H_2O used to carefully rinse the PTFE vessel of the bomb (Fig. 3.4a, b). After addition of 1 ml $HClO_4$, the solution was heated to 140 °C for 24 hours in the closed PFA vial on a hotplate (Fig. 3.4e). After evaporation, 0.5 ml $HClO_4$ was added to the residue, evaporated, and the samples were finally taken up in diluted HNO_3. Dissolution of host ultramafic rocks was performed following the HF–$HClO_4$ digestion procedure on hotplate described by Ionov et al. (1992). Element concentrations were determined by external calibration except for

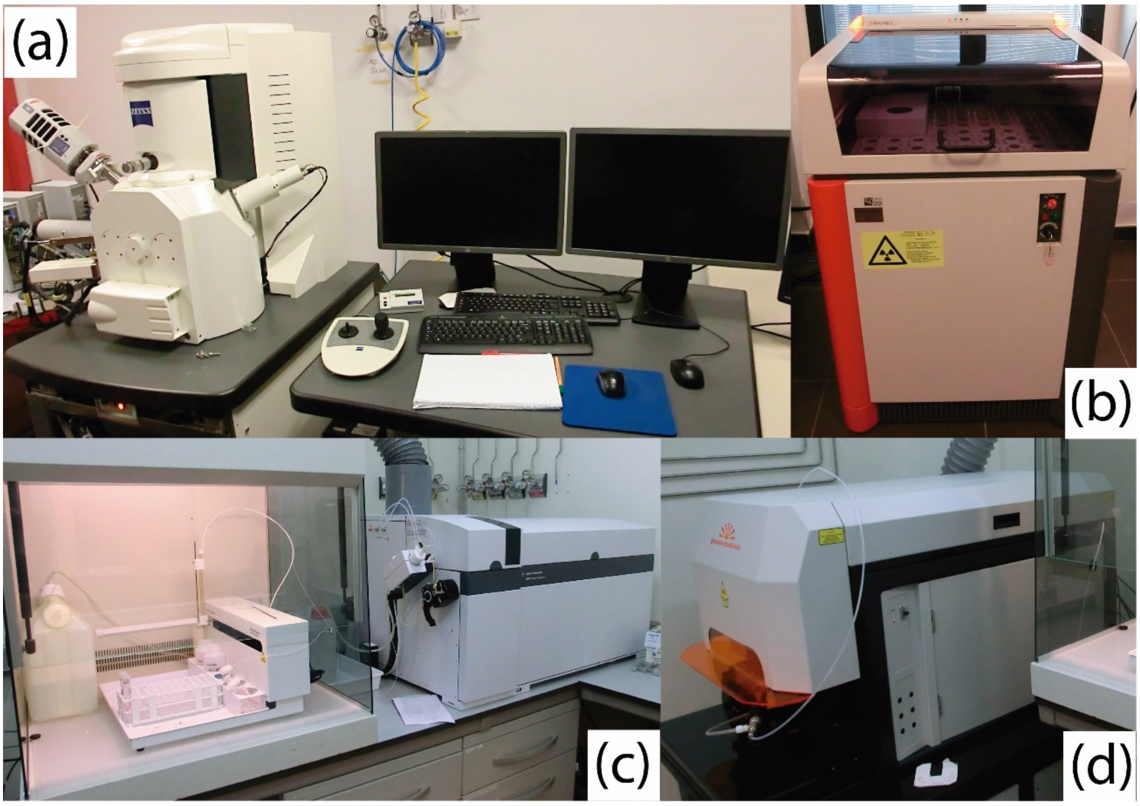

Figure 3.3. ***(a)*** *Carl Zeiss scanning electron microscopy (SEM) equipped with Oxford/Nordlys EBSD and EDS detectors at the IACT;* ***(b)*** *XRF BRUKER S4-Pioneer instrument at the IACT;* ***(c)*** *Agilent 8800 TripleQuad ICP-MS with auto-sampler at the IACT;* ***(d)*** *Photon Machine Analyte G2 excimer 193 nm laser coupled to the Agilent 8800 ICP-MS at the IACT.*

Nb and Ta that were calibrated by using Zr and Hf as internal standards, respectively. This technique was applied to avoid memory effects due to the intake of concentrated Nb–Ta solutions in the instrument and is an implementation to ICP-MS analysis of the method described by Jochum et al. (1990) for Nb measurement by spark-source mass spectrometry. The compositions of the reference samples JP-1, UB-N, PM-S and BIR-1, analysed as unknowns during the analytical runs, are in agreement with published values (Godard et al., 2009; Ionov et al., 2006; Jochum et al., 2016) and their reproducibility is better than 10% for most elements (Table A14).

3.3.4 Trace elements in minerals

Trace elements in minerals were analysed by LA (laser ablation)-ICP-MS using a Photon Machine Analyte G2 excimer 193 nm laser coupled to an Agilent 8800 ICP-MS/MS at the IACT (Fig. 3.3d). Analytical conditions were setup to get the maximum sensibility, minimize mass interferences and get accurate location of the spots, avoiding mixed areas, fractures and irregularities over the ablated area. The size of static spots was 65 to 110 microns, fluence was 10 J/cm^2 over a total laser energy of 7 mJ, repetition rate was 10 Hz for 40 s, and integration time was 100 milliseconds for each mass. Thin sections of the samples were located in a double volume ablation cell with He carrier flow of 1.2 l/min, and four unknown samples were ablated every one calibration standard

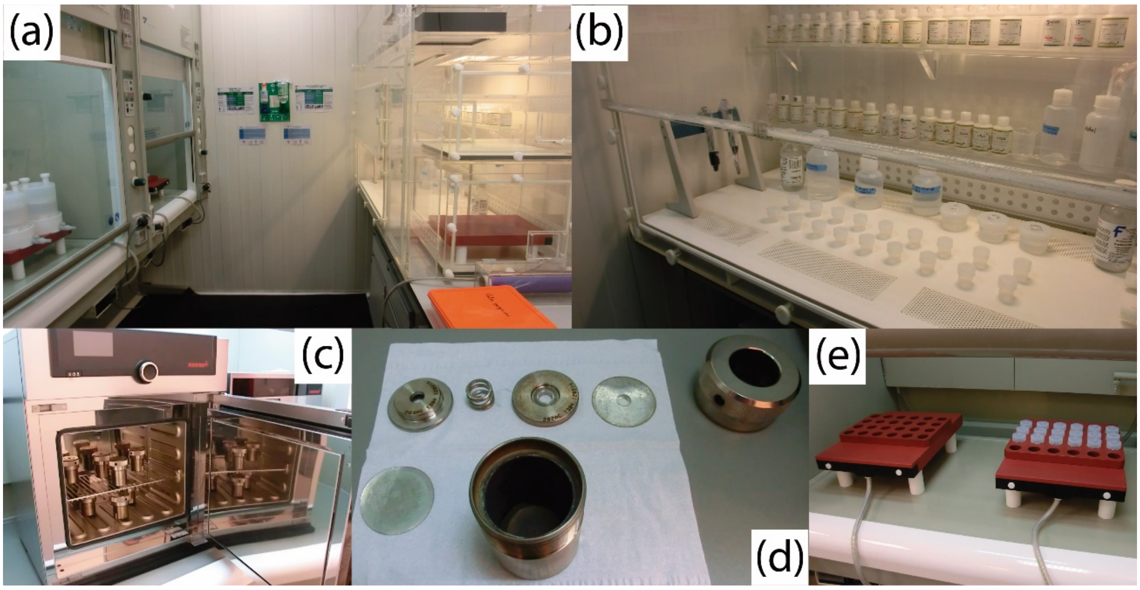

***Figure 3.4. (a)** Clean lab room at IACT; **(b)** extraction hood with the equipment (acids, beakers and pipettes) used to prepare samples for ICP-MS analyses of lithophile elements; **(c)** Hoven and Parr PTFE-lined bombs used for high-pressure digestion at the IACT; **(d)** view of the components of one high pressure Parr PTFE-lined bomb; **(e)** hot-plates used for acid attack and evaporation for ICP-MS analyses of lithophile elements at the IACT.*

(NIST 611 synthetic glass) and one validation standard (BHVO-2G basaltic glass, Table A15). After analysis, data reduction was done by Iolite software (Paton et al., 2011) and using ^{29}Si or ^{44}Ca from EPMA as internal standard. Representative trace element analyses of minerals are listed in Table A15 in the Supplementary material.

3.3.5 Concentrations of platinum-group elements (PGE) and Os isotopes in whole-rocks

Concentrations of PGE (Os, Ir, Ru, Pt, Pd) and Re and Os isotopes (Table A16) were measured at the Department of Earth Sciences, Durham University (UK), following the method of Dale et al. (2009) modified from Pearson and Woodland (2000). Whole-rock powders (~ 1.5 g) were digested and equilibrated with a mixed ^{190}Os-^{191}Ir-^{99}Ru-^{194}Pt-^{106}Pd-^{185}Re-enriched spike, using inverse aqua regia (2.5 ml 12M HCl and 5 ml 16M HNO_3) in quartz high-pressure asher (HPA) vessels. The vessels were placed in an Anton Paar HPA at 260-280 °C for 13-16 h. Osmium was extracted from the inverse aqua regia using CCl_4 (Cohen and Waters, 1996), back-extracted using 9M HBr, and then microdistilled (Birck et al., 1997). The inverse aqua regia was dried and re-dissolved in 1 ml 12M HCl and 5 ml 29M HF in order to achieve desilicification and ensure full extraction of Re (and possibly PGE) from silicates (Dale et al., 2009). The HCl-HF was then dried and 1 ml 20% H_2O_2 was added to the residue to reduce any Cr^{6+} formed during digestion, in order to avoid the partial elution of this form of Cr with PGE and isobaric interferences of polyatomic Cr compound with Ru during mass spectrometry. The H_2O_2 was then dried and the residue re-dissolved in 12 M HCl, dried, and taken up in 10 ml 0.5M HCl for purification of Re, Ir, Ru, Pt and Pd using AG1X-8 (100-200 mesh) anion-exchange resin.

Osmium was analysed on Pt filaments by N-TIMS (negative thermal ionization mass spectrometry) using the electron multiplier mode on a ThermoFinnigan Triton (see Dale et al. (2008) for details). Raw data were corrected offline for O isotope interference, mass fractionation (using $^{192}Os/^{188}Os = 3.08271$) and spike unmixing. Analyses of 10 and 100 pg aliquots of the DROsS standard solution gave $^{187}Os/^{188}Os$ values of 0.16136 and 0.16114, respectively, in agreement with values of Nowell et al. (2008). Rhenium, Ir, Ru, Pt and Pd were measured by ICP-MS on a ThermoFinnigan Element 2. Solutions were introduced using a MicroMist micro-concentric nebulizer and ESI stable sample introduction system (dual-cyclonic quartz spray chamber). Mixed solutions of natural PGE and solutions of Hf, Zr, Y and Mo (all at 1 ppb concentration) were used to quantify the degree of mass fractionation and the production rates of HfO^+, ZrO^+, YO^+ and MoO^+ (< 0.4%, < 1.1%, < 0.7%, < 0.2%, respectively) which have equivalent masses to isotopes of Ir^+, Pt^+ and Pd^+. These solutions were analysed before, during and at the end of each analytical session.

Total procedural blanks (n = 7) were: Os = 0.08-3.8 pg with $^{187}Os/^{188}Os$ between 0.137 and 0.275, Ir = 0.09-0.3 pg, Ru = 8-18 pg, Pt = 5-25 pg, Pd = 5-135 pg, Re = 1.4-11 pg. The percentage blank contribution to each analysis was always < 11% for Os (typically < 5%), < 21% for Ir (typically < 2%), < 22% for Pt, and < 25% for Ru, Pd and Re. Average analyses of international reference standards UB-N (serpentinite) and TDB-1 (diabase) are in good agreement with published values of these materials (Table A16) (Ishikawa et al., 2014; Puchtel et al., 2014). Replicate digestions of the same sample powders (one Atg-serpentinite (n = 2) and one Chl-harzburgite (n = 2), Table A16) indicate reproducibility (1 RSD) of 1-7% for Os, 14-19% for Ir, 1–2% for Ru, 3–20% for Pt, < 3% for Pd, 2-13% for Re, and < 0.4% for $^{187}Os/^{188}Os$.

Table 3.1. *Location of the sampled metarodingite outcrops studied in this thesis*

Outcrop number	Coordinates ED50 / UTM			Altitude (m)	Selected studied outcrops
	Zone	X	Y		
1	30S	508246	4105046	2444	x
2	30S	508208	4105007	2459	
3*	30S	508138	4104914	2480	x
4*	30S	508138	4104914	2480	
5	30S	508146	4104883	2470	
6	30S	508177	4104856	2448	x
7	30S	508075	4104374	2321	
8	30S	507993	4104703	2460	x
9	30S	507961	4104553	2404	
10	30S	507347	4104128	2300	x
11	30S	507583	4104362	2297	x
12	30S	507567	4104304	2286	x
13**	30S	507985	4103931	2223	x
14	30S	508089	4104030	2233	
15	30S	507961	4103785	2146	x
16	30S	506400	4103183	2180	
17	30S	506337	4103214	2159	x
18	30S	506356	4103162	2158	x
19	30S	506265	4103193	2122	
20	30S	506179	4103115	2099	
21	30S	506179	4103115	2099	
22	30S	506063	4103100	2091	
23	30S	506036	4103139	2054	
24	30S	505708	4103296	1866	
25	30S	505817	4103128	2009	x
26	30S	505979	4103334	2037	x
27	30S	506580	4104028	2274	
28	30S	506879	4104138	2251	x
29	30S	506684	4104048	2285	x
30	30s	506646	4103994	2288	
31	30s	506580	4104028	2269	
32	30S	506596	4104003	2277	
33	30S	506431	4103878	2198	
34	30S	506649	4103997	2288	
35	30S	507961	4103785	2146	

* Outcrops 3 and 4 are very close to each other and share coordinates

** Samples of two very close outcrops, same host rock samples.

Table 3.2. *List of rock samples studied in this thesis*

Sample	***Rock type / Amphibolitization***	***Outcrop***^{1}	***Thin-section***	***Powder***	***XRF***	***ICP-MS***
AL14-16	Grand-metarod.	1	X	X	X	X
AL14-16-2	Grand-metarod.	1	X			
AL14-16B	Grand-metarod.	1	X	X	X	
AL14-25	Grand-metarod.	1	X	X	X	X
AL14-17	Ep-metarod.	1	X	X	X	X
AL14-26E	Ep-metarod.	1	X	X	X	X
AL14-26E-2	Ep-metarod.	1	X			
AL14-26E-6	Ep-metarod.	1	X			
AL14-18	Ep-metarod. / Amphib.	1	X	X	X	X
AL14-26EA	Ep-metarod. / Amphib.	1	X	X	X	X
AL14-19	Chl-blackwall	1	X	X	X	X
AL14-20D-BW	Chl-Di-react. rim	1	X	X	X	X
AL14-24D-BW	Chl-Di-react. rim	1	X	X	X	X
AL14-24D-BW-B	Chl-Di-react. rim	1	X	X	X	
AL14-20L-V	Chl-Di-Ol-react. rim	1	X	X	X	X
AL14-24L-V	Chl-Di-Ol-react. rim	1	X	X	X	X
AL14-20	Chl-Di-(OL)-react. rim	1	X			
AL14-23	Chl-Di-Ol-react. rim	1	X	X	X	X
AL14-46	Atg-serp. (far)	1	X	X	X	X
AL14-30	Grand-metarod. / Amphib.	3	X	X	X	X
AL14-31	Chl-blackwall / Amphib.	3	X	X	X	X
AL14-32	Atg-serp. (close)	3	X	X	X	X
AL14-49	Atg-serp. (far)	3	X	X	X	X
AL14-40	Grand-Ep-metarod.	6	X	X	X	X
AL14-41	Chl-blackwall	6	X	X	X	X
AL14-51	Atg-serp. (close)	6	X	X	X	X
AL14-52	Atg-serp. (far)	6	X	X	X	X
AL14-53	Ep-metarod.	8	X	X	X	X
AL14-54	Chl-blackwall / Amphib.	8	X	X	X	X
AL14-55	Atg-serp. (close)	8	X	X	X	X
AL14-56	Atg-serp. (far)	8	X	X	X	X
AL14-63	Grand-metarod.	10	X	X	X	X
AL14-64	Grand-metarod.	10	X	X	X	X
AL14-04-B	Grand-metarod.	10	X			
AL14-04-C	Grand-metarod.	10	X			
AL14-04-5C	Grand-metarod.	10	X			
AL14-04-C2	Grand-metarod.	10	X			
AL95-36-C	Grand-metarod.	10	X			
AL2000-6	Grand-metarod.	10	X		X	
AL14-66	Chl-blackwall	10	X	X	X	X
AL14-67	Atg-serp. (close)	10	X	X	X	X
AL14-68	Atg-serp. (close)	10	X	X	X	X
AL14-69	Atg-Serp. (far)	10	X	X	X	X

1 Numbered outcrops correspond to the first column in Table 3.1

Table 3.2. *List of rock samples studied in this thesis*

Sample	***Rock type / Amphibolitization***	***Outcrop***[1]	***Thin-section***	***Powder***	***XRF***	***ICP-MS***
AL14-70	Ep-metarod. / Amphib.	11	X	X	X	X
AL14-71	Chl-blackwall	11	X	X	X	X
AL14-72	Chl-harzb.-spini. (close)	11	X	X	X	X
AL14-73	Chl-harzb.-spini. (far)	11	X	X	X	X
AL14-75	Chl-blackwall	12	X	X	X	X
AL14-76	Chl-harzb.-granof. (close)	12	X	X	X	X
AL14-77	Chl-harzb.-granof. (far)	12	X	X	X	X
AL14-78	Ep-metarod. / Amphib.	13	X	X	X	X
AL98-19B	Ep-metarod. / Amphib.	13	X			
AL14-79	Chl-blackwall	13	X	X	X	X
AL14-80	Chl-harzb.-spini. (close)	13	X	X	X	X
AL14-81	Chl-harzb.-granof. (far)	13	X	X	X	X
AL14-86	Ep-metarod.	15	X	X	X	X
AL14-87	Ep-metarod. / Amphib.	15	X	X	X	X
AL14-88	Chl-blackwall / Amphib.	15	X	X	X	X
AL14-89	Chl-harzb.-granof. (close)	15	X	X	X	X
AL14-90	Chl-harzb.-granof. (far)	15	X	X	X	X
AL14-95	Pyrals-metarod. / Amphib.	17	X	X	X	X
AL14-96	Chl-blackwall / Amphib.	17	X	X	X	X
AL14-97	Chl-harzb.-spini. (close)	17	X	X	X	X
AL14-98	Chl-harzb.-spini. (far)	17	X	X	X	X
AL14-99	Pyrals-metarod. / Amphib.	18	X	X		
AL14-99-1	Pyrals-metarod. / Amphib.	18	X			
AL14-99-2	Pyrals-metarod. / Amphib.	18	X			
AL96-24B	Pyrals-metarod. / Amphib.	18	X		X	
AL96-24A	Pyrals-metarod. / Amphib.	18	X			
AL14-01	Pyrals-metarod. / Amphib.	18	X			
AL14-101	Chl-harzb.-spini. (close)	18	X	X	X	X
AL14-102	Chl-harzb.-spini. (far)	18	X	X	X	X
AL14-127	Grand-metarod.	25	X	X	X	X
AL14-128	Chl-blackwall	25	X	X	X	X
AL14-129	Recryst. Chl-Harzb. (close)	25	X	X	X	X
AL14-130	Recryst. Chl-Harzb. (far)	25	X	X	X	X
AL14-133	Grand-Ep-metarod. / Amphib.	26	X	X	X	X
AL14-134	Chl-blackwall	26	X	X	X	X
AL14-134-D	Chl-Di-react. rim	26	X	X	X	X
AL14-134-L	Chl-Di-OL-react. rim	26	X	X		
AL14-135	Recryst. Chl-harzb. (close)	26	X	X	X	X

1 Numbered outcrops correspond to the first column in Table 3.1

Table 3.2. *List of rock samples studied in this thesis*

Sample	***Rock type / Amphibolitization***	***Outcrop***[1]	***Thin-section***	***Powder***	***XRF***	***ICP-MS***
AL14-136	Recryst. Chl-harzb. (far)	26	X	X	X	X
AL14-143	Ep-metarod. / Amphib.	28	X	X	X	X
AL14-144	Chl-blackwall / Amphib.	28	X	X	X	X
AL14-145	Chl-serp. (close)	28	X	X	X	X
AL14-146	Atg–Chl–Opx–Ol rock (far)	28	X	X	X	X
AL14-147	Chl-blackwall / Amphib.	29	X	X	X	X
AL14-148	Atg–Chl–Opx–Ol rock (close)	29	X	X	X	X
AL14-149	Atg–Chl–Opx–Ol rock (far)	29	X	X	X	X

1 Numbered outcrops correspond to the first column in Table 3.1

Part II

RESULTS

4 High-P metamorphism of rodingites during serpentinite dehydration (Cerro del Almirez, Southern Spain): Implications for the redox state in subduction zones[2]

4.1 Introduction

Rodingites are CaO-rich, SiO_2-, Na_2O-, and K_2O-poor rocks formed by metasomatic alteration (rodingitization) of mainly gabbros and basalts. They mostly consist of Ca-Al and Ca- Mg silicates and occur as dykes or boudins (<10 cm to several metres thick) included in serpentinized peridotites (e.g., Bach and Klein, 2009; Coleman, 1967; Frost, 1975). Since their first description in Bell et al. (1911), and Benson (1913, Part I), rodingites have been documented in a range of tectonic settings, including active seafloor spreading centres (Aumento and Loubat, 1971; Frost et al., 2008; Früh-Green et al., 2017; Honnorez and Kirst, 1975), rifted continental margins (Beard et al., 2002), greenstone belts (Anhaeusser, 1979; Attoh et al., 2006; Schandl et al., 1989), and Phanerozoic orogenic belts (Austrheim and Prestvik, 2008; Coleman, 1967; Dubińska, 1995; Evans et al., 1979; Frost, 1975; Hatzipanagiotou and Tsikouras, 2001; Li et al., 2004, 2007; Murzin and Shanina, 2007; Tsikouras et al., 2009; Zanoni et al., 2016)

Rodingitization of mafic igneous rocks and serpentinization of their host ultramafic rocks take place simultaneously on the seafloor (e.g., Arshinov and Merenkov, 1930; Coleman, 1967; Frost, 1975; O'Hanley et al., 1992; Schandl et al., 1990; Suzuki, 1953). Rarely, rodingites form during serpentinization of Archean komatiites (Mogessie and Rammlmair, 1994; Schandl et al., 1989), in the mantle wedge above a subducting slab (Koutsovitis et al., 2013), or through exhumation of slab eclogites (Li et al., 2007). During rodingitization, Ca-rich and Si-undersaturated fluids (Bach and Klein, 2009; Coleman, 1967; Frost and Beard, 2007; Li et al., 2004) react with igneous mafic rocks, sometimes in different stages (e.g., Normand and Williams-Jones, 2007; Schandl et al., 1989), leading to depletion of Na, K, and Si.Most petrological studies on metamorphosed rodingites (metarodingites) focus on their tectonometamorphic evolution based on their

---

[2] This chapter has been published: Laborda-López, C., López-Sánchez-Vizcaíno, V., Marchesi, C., Gómez-Pugnaire, M. T., Garrido, C. J., Jabaloy-Sánchez, A., Padrón-Navarta, J.A. & Hidas, K. (2018). High-P metamorphism of rodingites during serpentinite dehydration (Cerro del Almirez, Southern Spain): Implications for the redox state in subduction zones. *Journal of Metamorphic Geology*, 36(9), 1141-1173.

stable mineral assemblages and associated textures. In some of these investigations, mineralogical variations between different metarodingite types have been attributed to different degrees of oceanic metasomatism that were preserved during subsequent metamorphism (e.g., Ferrando et al., 2010; Li et al., 2004). However, only a few studies have precisely determined the metamorphic evolution of metarodingites by detailed thermodynamic modelling (e.g., Li et al., 2008, 2017; Zanoni et al., 2016).

The mineralogical and compositional changes produced in metarodingites by interaction with enclosing serpentinites have only seldom been dealt with (Li et al., 2004). Except for the Cima di Gagnone locality, where metarodingites are hosted by chlorite-harzburgite (Evans et al., 1979) formed after antigorite-serpentinite dehydration (Evans and Trommsdorff, 1978), all other metarodingite studies have examined rocks hosted by serpentinites, in which antigorite (e.g., Panseri et al., 2008; and references therein; Zanoni et al., 2016) but also chrysotile and lizardite (Coleman, 1967; Lan and Liou, 1981) were stable. That precluded the possibility to study the interaction between metarodingites and the fluids released during antigorite breakdown.

In this work, we describe the main structural, mineralogical, textural, and compositional features of metarodingites from Cerro del Almirez (Betic Cordillera, southern Spain) and present a detailed thermodynamic model of their meta- morphic evolution during subduction. The Cerro del Almirez ultramafic massif is a unique location where metarodingite bodies occur on both sides of the antigorite-out isograd mapped in their host ultramafic rocks (Trommsdorff et al., 1998). The breakdown of antigorite in serpentinite is the main dehydration reaction occurring at high pressure in subduction zones (Padrón-Navarta et al., 2010a; Ulmer and Trommsdorff, 1995). Owing to serpentinite dehydration, oxidizing fluids are released (Debret and Sverjensky, 2017; Debret et al., 2014, 2015; Merkulova et al., 2017) and may interact with subducted lithologies, including metarodingites, inducing mineralogical and/or compositional changes in rocks and fluids. Therefore, metarodingites from Cerro del Almirez are ideal for unravelling how fluids from dehydration reactions may trigger metamorphic/metasomatic reactions in subducted mafic rocks, and how these reactions affect the compositions of the slab recycled deep in the mantle and of fluids that migrate to inner regions of the mantle wedge where arc magmas are generated.

4.2 Results

4.2.1 Field occurrence and sample description

Metarodingites are heterogeneously distributed in the ultramafic domains of the Cerro del Almirez massif, that is, in Atg-serpentinite, Chl-harzburgite and close to the dehydration front defined by the Atg-out isograd (Fig. 4.1b). The current location of metarodingite bodies is controlled by the original distribution of their protoliths and by their progressive deformation and disruption during subduction. Their metamorphic evolution resulted in a large variety of mineralogies, sizes, shapes, and mesostructures (Fig. 4.1c; Table 4.1). According to them, three types of metarodingite can be defined: Type 1 Grandite-metarodingite, Type 2 Epidote-metarodingite, and Type 3 Pyralspite-

TABLE 4.1. *Summary of the Cerro del Almirez metarodingite types and associated metasomatic reaction rims.*

Host rock	Lithologies	Key macroscopic and textural features	Minerals and modal percentage (vol.%)	Mineral assemblages in equilibrium
Atg-Serp.	Grandite-metarodingite Type 1	Reddish brown, fine-grained rocks with relict igneous texture (porphyritic), with several vein generations.	(Grt-1 + Grt-2 + Grt-3) 66% + Chl 23% + Di 6.5% + Ttn 3% + Mag 2.7% +(Ap + Ilm + Aln +Zrn) <1%	Grt-1 + Chl + Di + Mag + Ilm Grt-2a + Chl + Di + Mag + Ilm Grt-2b + Chl + Ttn ± Di Grt-3 + Chl + Ttn
Atg-Serp. and Chl-Harzb.	Epidote-metarodingite Type 2	Yellowish, fine-grained rocks with granoblastic texture and relict garnet.	Ep 55% + Di 35% + Ttn 5% + (Grt-3 or Grt-4) 3.5% ± Chl + (Ap ± Mag ± Rt + Ilm + Zrn) 1%	Ep + Di + Ttn ± Grt-3 ± Chl Ep + Di + Ttn ± Grt-4 ± Chl
Chl-Harzb.	Pyralspite-metarodingite Type 3	Blackish green and greenish yellow rocks with granoblastic or nematoblastic texture.	Amp 50% + Ep/Zo 35% + Grt-5 10% ± Chl 0-4% ± Di 1% + Rt 2% +(Ap + Ilm + Aln +Zrn) <1%	Grt-5 + Ep/Zo + Amp-1 ± Chl ± Di + Ttn Grt-5 + Ep/Zo + Amp-1 ± Chl + Rt
Atg-Serp. and Chl-Harzb.	Chl-Blackwall	Silverish grey, strongly foliated rock.	Chl 70% + Di 22% ± Ttn 2% ± Mag 2.7 % ± Ilm 2.7-4% ± Rt 0-2% + Ap 0.6% ± Amp + Zrn	Ch + Di + Ttn + Mag Chl + Di + Ilm Chl + Amp-1 + Rt
Atg-Serp. and Chl-Harzb.	Chl-Di-metasomatic rim	Bluish white, foliated rock.	Di 60% + Chl 35% + Mag 4% + Ilm	Di + Chl + Mag + Ilm
Atg-Serp. and Chl-Harzb.	Chl-Di-Ol-metasomatic rim	Foliated rock with orangisch brown Ol porphyroblasts, and Ti-Chu.	Di 36% + Ol 36% + Chl 21% + Mag 5% ± Ti-Chu ± Atg	Ol + Di + Chl + Mag +Ti-Chu

metarodingite. Synmetamorphic interaction between metarodingites and host ultramafic rocks gave place to the progressive growth of chlorite-(Chl-) blackwalls and other metasomatic reaction rims (Fig. 4.1d) of variable thickness (~7-40 cm).

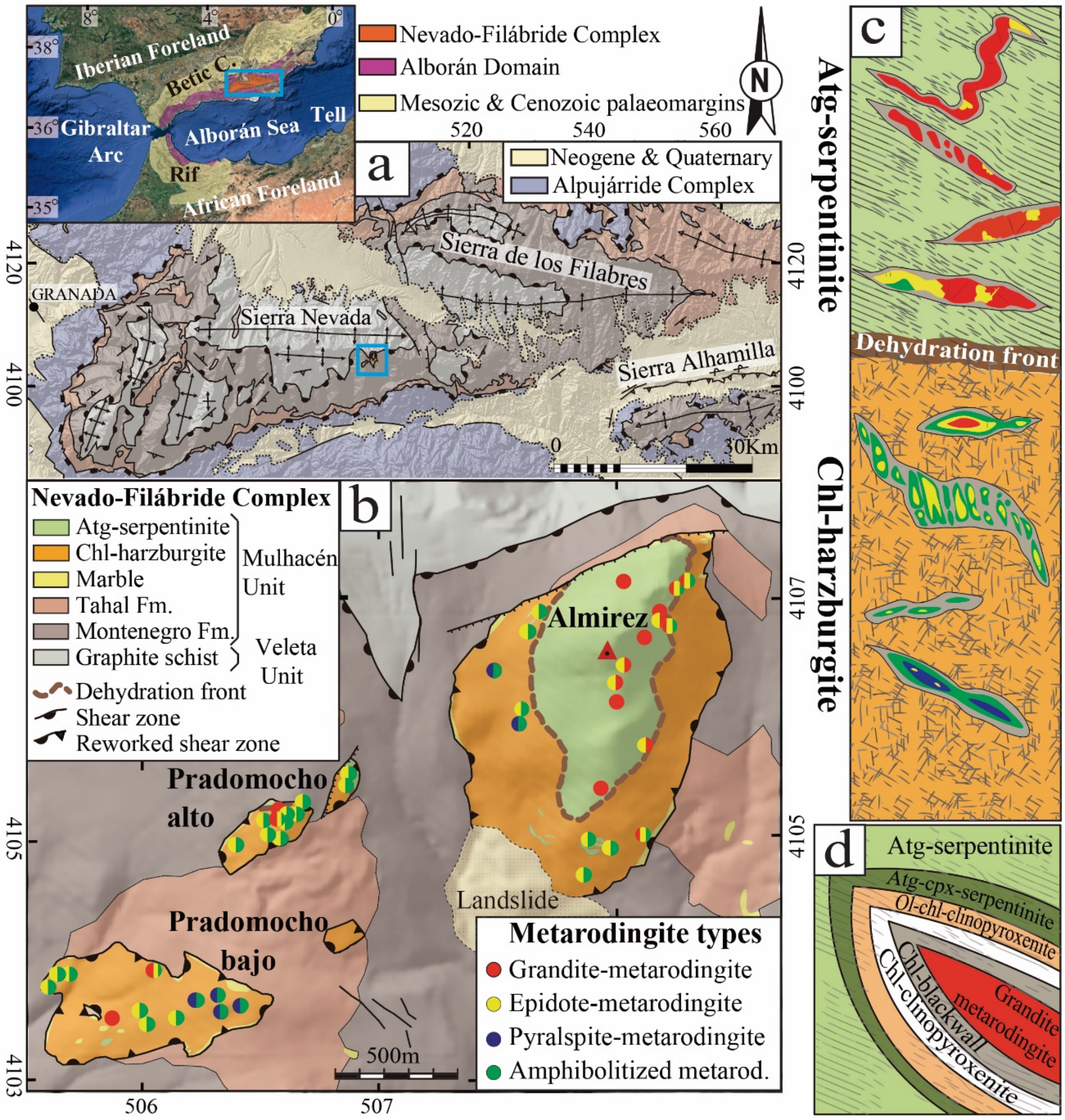

***Figure 4.1. (a)** Geological sketch map of the western part of the Nevado-Filábride Complex of the Betic Cordillera (modified from Jabaloy-Sánchez et al., 2015) with location of the Cerro del Almirez ultramafic massif (blue inset) shown in (b). **(b)** Geological map of the Cerro del Almirez area with the location of the sampled metarodingite bodies. Coloured circles correspond to the reported metarodingite types and amphibolitization degree. **(c)** Sketch column of the lithological sequence of the Cerro del Almirez ultramafic massif showing the different types and shapes of metarodingite bodies. Not to scale. Same colour key for metarodingite types as in (b). The grey rim represents the metasomatic reaction rims altogether. **(d)** Sketch diagram with the distribution pattern of metasomatic reaction rims around a Grandite-metarodingite boudin. Not to scale.*

4.2.1.1 Structural features of metarodingite bodies

Metarodingites enclosed in Atg-serpentinite occur as boudinaged and disrupted layers up to 42 m in length and 1.8 m in thickness. They present different structures depending on the angle between the contact surface of the body and the main foliation of host serpentinite. Bodies subparallel or at low angles with the serpentinite foliation (Fig. 4.2a, b) occur as boudin trains with different shapes depending on the intensity of shearing (Goscombe et al., 2004). Strike orientation of the boudins surfaces ranges from NE-SW to NW-SE and they dip between 20°-45° mainly to N-NW and rarely to W-SW. Only one body, 15 m long and 0.75 m thick, has E-W strike and subvertical dip, and is oblique to the serpentinite main foliation. In small shear zones in Atg-serpentinite (Jabaloy-Sánchez et al., 2015), asymmetric boudin trains of metarodingite are common (Fig. 4.2c). In these cases, the rodingite boudins are disrupted by small shear zones and rotated, forming decimetric ellipsoidal bodies embedded in Chl-blackwalls (Fig. 4.2c). Chl-blackwalls have a well-developed schistosity continuous with the penetrative S_1 foliation of Atg-serpentinite (Fig. 4.2a, b; Jabaloy-Sánchez et al., 2015). In the Atg-serpentinite-hosted metarodingites, two sets of conjugate fractures are found with low (< 60°) dihedral angles and few millimetres to two centimetres thickness, filled with garnet, chlorite or epidote (Fig. 4.2a, d).

Metarodingites enclosed in Chl-harzburgite mostly occur as small isolated boudins usually <1 m in length and 50 cm thick (Fig. 4.2e, f). Rare decametric boudin trains, some of them folded, are also visible. The contact surface orientation of these metarodingite bodies is variable and ranges between NE-SW strike with 30°-50° dip to NW or SE, and E-W strike with dip to the south ranging between 50° to subvertical. Millimetre thick conjugate hybrid joints are commonly filled by amphibole in these metarodingites (Fig. 4.2d, e). Chl-blackwalls show a well-developed S_2 schistosity with transposed hinges of the S_1 foliation of Atg-serpentinite (Fig. 4.3a). In some outcrops, especially in the Pradomocho Alto and Pradomocho Bajo ultramafic bodies (Fig. 4.1b), alternating layers of Chl-blackwall and amphibolitized metarodingite define a well-marked banding parallel to S_2 (Fig. 4.2f). In places, a late crenulation cleavage (S_3) affects the S_2 foliation (Fig. 4.2f and 4.3a). In contrast with the nondeformed Chl-harzburgite host (Jabaloy-Sánchez et al., 2015; Padrón-Navarta et al., 2010b), S-C structures in diopside-rich reaction rims

(Fig. 4.3b) indicate a top-to-the-west sense of shearing, similar to those of Atg-serpentinite and hosting metapelites (Jabaloy-Sánchez et al., 2015).

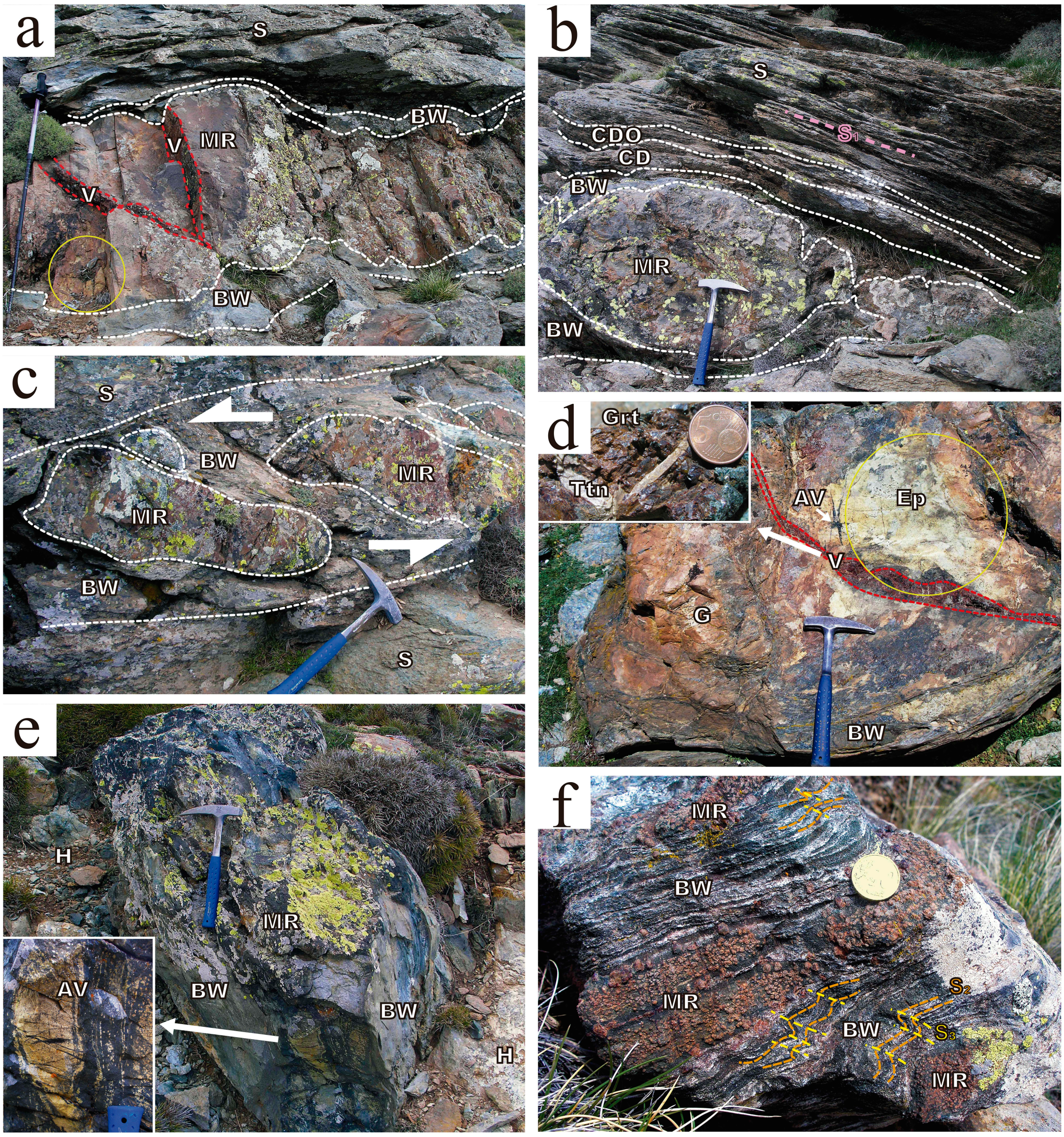

Figure 4.2. *Field occurrence of metarodingite bodies in the Cerro del Almirez ultramafic massif.* ***(a)*** *Type 1, Grand-metarodingite dyke hosted in Atg-serpentinite with incipient transformation into Epidote-metarodingite (yellow circle).* ***(b)*** *Barrel-shaped boudin of Grand-metarodingite hosted in Atg-serpentinite with well-developed S_1 foliation and metasomatic rims.* ***(c)*** *Asymmetric boundin trains of Grand-metarodingite hosted in Atg-serpentinite separated by small shear fractures in the Chl-blackwall. The sense of shear is indicated.* ***(d)*** *Atg-serpentinite-hosted, zoned boudin with well-defined Grand-(to the left; G) and Ep-metarodingite (to the right; Ep) zones cut by a thick Grt-3 vein (enlarged in the upper left inset showing coarse garnet and titanite crystals). Note also two amphibole veins (AV).* ***(e)*** *Partially amphibolitized Type-2, Ep-metarodingite boudin enclosed in Chl-harzburgites (H). Enlarged inset: epidote-rich core cut by amphibole veins (AV).* ***(f)*** *Partially amphibolitized, Type-3, Pyralspite-metarodingite boudin with folded S_2 foliation in Chlorite-blackwall and late development of S_3 crenulation cleavage. MR: metarodingite; V: garnet veins; S: Atg-serpentinite; BW: Chlorite-blackwall; (CD) Chorite-diopside metasomatic rim, (CDO) Chlorite–diopside–olivine–metasomatic rim.*

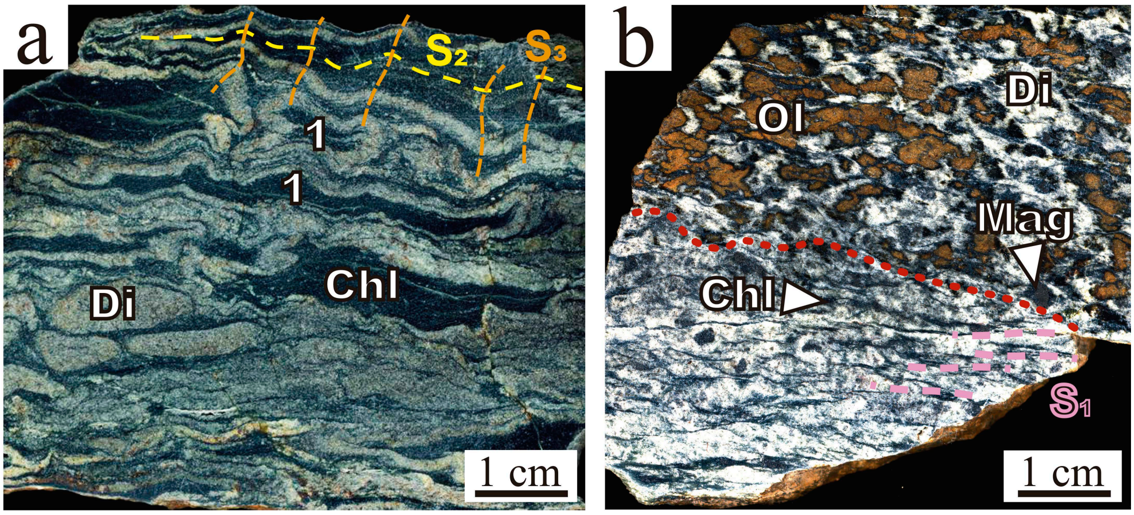

Figure 4.3. ***(a)*** *Polished surface of a Chl-blackwall hand sample with alternating layers of chlorite (Chl) and diopside (Di). It corresponds to an Ep-metarodingite hosted in Chl-harzburgite. Note the sheath folds (1) parallel to* S_2 *foliation, typical of shear zones and late* S_3 *crenulation cleavage.* ***(b)*** *Polished surface of a hand-sample with the chlorite–diopside- (lower part) and chlorite–diopside–olivine- (upper part) metasomatic rims of a Grand-metarodingite hosted in Atg-serpentinite.*

4.2.1.2 Metarodingite types and petrography

Metarodingites have different mineralogical and microstructural features at each side of the dehydration front (Fig. 4.1b, c). No systematic differences exist between metarodingite bodies hosted in Chl-harzburgite with spinifex-like or granofelsic texture.

Type 1 Grandite-metarodingite (in the following Grand-metarodingite) consists of Grs- and/or Adr-rich Grt + Chl + Di + Ttn + Mag + Ap + Ilm + Aln + Zrn (Table 4.1). This is the most abundant type of metarodingite enclosed in Atg-serpentinite (Fig. 4.1b, c and 4.2a-d). In Chl-harzburgite, it is preserved only as small relicts in the core of some Type 2 metarodingite boudins.

Macroscopically, Grand-metarodingite shows a reddish, garnet-rich groundmass. Porphyritic igneous textures typical of basaltic rocks are preserved in places (Fig. 4.4a). At the thin section scale, Grand-metarodingite shows a very fine-grained (5 to 50 µm) matrix consisting of allotriomorphic aggregates of anhedral pinkish or brownish garnet (Grt-1 hereafter), chlorite, titanite and less abundant diopside (Fig. 4.4a, b). The fine-grained Grt-1 aggregates replaced plagioclase in original igneous doleritic or fluidal textures, as well as plagioclase phenocrysts (1-3 cm) in porphyritic basalts (Fig. 4.4a, c). Pseudomorphs after igneous clinopyroxene are replaced by diopside with tiny magnetite, ilmenite and titanite exsolutions or, more rarely, by garnet-diopside symplectites. Rare olivine phenocrysts were transformed into dark pseudomorphs of chlorite-diopside-titanite-magnetite (0.5-2 cm). In the most deformed samples, igneous textures partially or completely recrystallized to homogeneous granoblastic or slightly oriented textures. The modal abundance of chlorite increases towards the contact with the Chl-blackwall.

Garnet veins of variable thickness (up to 2 cm) frequently cut the rock matrix (Fig. 4.2a, d). Two vein generations can be distinguished (Fig. 4.4b). The older veins are thin (< 1 cm), display irregular rims, and mainly consist of Grt-2 garnet (see section 4.2.2.1; Fig. 4.4b). Grt-2 has small grain size (< 50 µm) and occurs in massive aggregates with

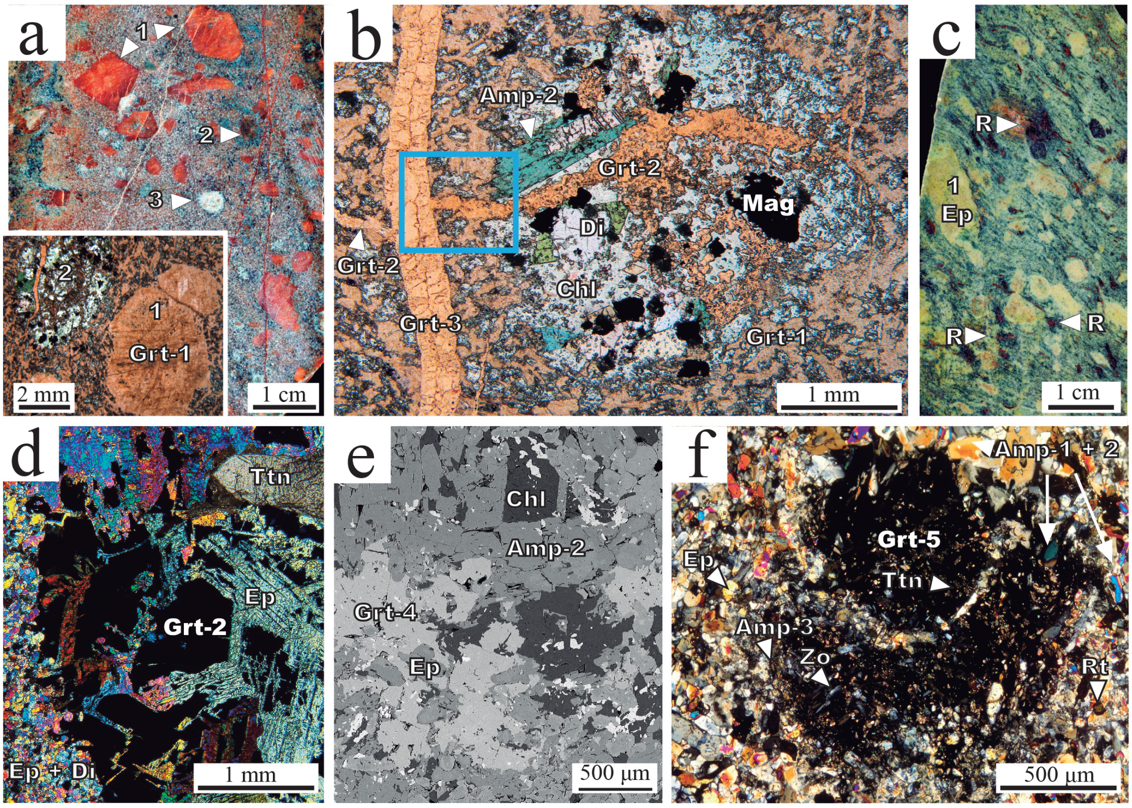

Figure 4.4. ***(a)*** *Polished surface of a Grand-metarodingite hand-sample with preserved porphyritic igneous texture. Lower left inset: same texture at thin section scale (parallel polars). (1) Garnet (Grt-1) pseudomorph after igneous plagioclase. (2) Igneous olivine replaced by chlorite, magnetite and diopside. (3) Igneous Ti-augite replaced by diopside, magnetite and ilmenite.* ***(b)*** *Texture of Grand-metarodingite at thin section with two vein generations mainly consisting of Grt-2 and Grt-3 respectively. Diopside was partially replaced by late green amphibole (Amp-2; parallel polars). The blue inset corresponds to the compositional maps area in Figure 4.7a, b.* ***(c)*** *Polished surface of an amphibolitized Ep-metarodingite hand-sample with preserved porphyritic igneous textures (1) and garnet relicts (R).* ***(d)*** *Ep-metarodingite at thin section with garnet relicts (Grt-2b) of a vein partially transformed into epidote (crossed polars).* ***(e)*** *SEM image of Ep-metarodingite hosted in Chl-harzburgite with recrystallized garnet relicts reequilibrated to Grt-4.* ***(f)*** *Pyrals-metarodingite at thin section with a Grt-5 porphyroblast crowded with titanite inclusions in the core and zoisite (Zo) and amphibole inclusions (Amp-1) in the rims. Matrix with amphibole (Amp-1 and Amp-2), epidote, zoisite and rutile (Rt). Amp-3 altered garnet rims. Crossed polars.*

titanite and minor chlorite. The second vein generation mostly consists of Grt-3 garnet (see section 4.2.2.1). These veins always cut those containing Grt-2 (Fig. 4.4b). They are decimetric in length and up to 2 cm thick (Fig. 4.2d). Grt-3 occurs as drusy, projecting aggregates of coarse (1-2 mm) idiomorphic grains, usually intergrown with chlorite flakes, rare diopside or epidote, apatite and large titanite crystals (up to 6 cm; inset in Fig. 4.2d). Both Grt-2 and Grt-3 may also occur in the rock matrix rimming Grt-1. These three garnet generations display slight anisotropy produced either by cell distortion due to the occurrence of OH groups (Andrut et al., 2002) or to strain caused by the intergrowth of different cubic phases (e.g., Antao et al., 2015). Exploratory infrared measurements confirm the occurrence of OH-groups in the Grand-metarodingite garnets as well as in diopside (Fig. 4.5).

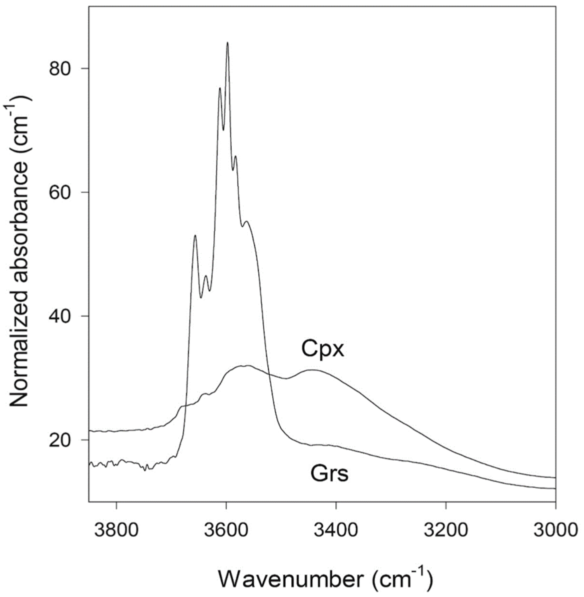

Figure 4.5. *Representative IR normalised spectra for garnet and diopside showing the occurrence of structurally bounded hydroxyl groups (sample AL14-04-5C).*

The occurrence of epidote in Type 1 metarodingite marks the transition to ***Type 2 Epidote-metarodingite*** (in the following Ep-metarodingite). This consists of Ep + Di ± Grt ± Chl + Ttn + Ap + Zrn ± Mag ± Rt ± Ilm (Table 4.1). Evidence of incipient transformation from Type 1 to Type 2 metarodingites is visible in almost each Grand-metarodingite outcrop (Fig. 4.2a, d). However, in the Atg-serpentinite domain well developed Ep-metarodingite assemblages are present only in some zoned boudins close to the dehydration front (Fig. 4.1c), in which they show irregular or patchy, sharp contacts with the garnet-rich zones (Fig. 4.2d). On the other hand, Type 2 is the most common metarodingite type within dehydrated Chl-harzburgite, where it is usually observed in the core of boudins that are partially transformed by late, retrograde amphibolitization (see below) (Fig. 4.2e and 4.4c).

The Ep-metarodingite is a fine-grained, granoblastic, yellowish rock. The matrix is made of polygonal (5-200 μm) epidote and diopside aggregates, formed after garnet, with disseminated chlorite flakes that are less abundant toward the core of the bodies.

Porphyroblasts consisting of fine-grained Grt-1 aggregates are here replaced by coarse epidote grains (Fig. 4.4c). Small metastable relicts of Grt-2 and Grt-3 are also visible (Fig. 4.4c, d). However, in some Atg-serpentinite-hosted bodies, some of these garnet grains (with a Grt-3 composition) are in equilibrium with the epidote-diopside-titanite assemblage. In a similar way, scarce grains of a different garnet (Grt-4, see section 4.2.2.1) are present in the Ep-metarodingite bodies hosted in Chl-harzburgite. Grt-4 appears as small xenomorphic grains locally overgrown by idioblastic recrystallized rims (Fig. 4.4e). Titanite is more abundant than in Type 1 metarodingite (Table 4.1) and forms aggregates (2-6 mm) disseminated in the matrix (which may include rutile) or thin (0.5 mm) irregular veins.

Type 3 Pyralspite-metarodingite (in the following Pyrals-metarodingite) crops out only in the Chl-harzburgite domain (Fig. 4.1b, c). In the field, it constitutes compact, decimetre long, ellipsoidal bodies embedded in a banded blackwall consisting of chlorite-rich light and amphibole-rich dark layers (Fig. 4.2f). The typical metarodingite assemblage consists of neoblasts of a new pyralspitic garnet generation Grt (Grt-5, see section 4.2.2.1) + Ep + Zo + Amp (Amp-1) ± Chl ± Di + Rt + Ap + Zrn ± Mag ± Ttn ± Ilm (Table 4.1). Grt-5 occurs as porphyroblasts of variable abundance and grain size. It is more abundant and smaller (1-3 mm) in the massive cores of the boudins, where it is rich in inclusions of colourless or slightly pleochroic amphibole (Amp-1), chlorite, epidote, zoisite, apatite, rare diopside, titanite in the core and rutile in the rim (Fig. 4.4f). Grt-5 porphyroblasts are hosted in a grano to nematoblastic matrix mainly consisting of epidote and zoned green-pleochroic amphibole (Amp-2) with colourless cores of Amp-1, chlorite, zoisite, rare diopside, and rutile and apatite as accessory phases.

Towards the Chl-blackwall, the modal abundances of epidote and diopside decrease until their complete disappearance, chlorite and zoned amphibole define a well-marked foliation (S_2), and Grt-5 porphyroblasts are less abundant but coarser (up to 6 mm). The rims of these garnet porphyroblasts are commonly corroded by late fine-grained chlorite. Amphibole, titanite and rutile inclusions in garnet are here arranged in rotated trails defining snowball orientations that are continuous with the matrix foliation. This rotation was due to the shearing responsible for the formation of banding and S_2 foliation (Jabaloy-Sánchez et al., 2015). This event was previous to the growth of the green pleochroic rims of amphibole (Amp-2). Late crenulation (Fig. 4.2f and 4.3a) defines a S_3 foliation and postdates the main metamorphic assemblage.

4.2.1.3 Amphibolitization of metarodingites

The growth of late amphibole (Amp-2) replacing previous mineral assemblages is common in all the metarodingite types. The intensity of amphibolitization is, however, very variable. In Grand-metarodingite within Atg-serpentinite, Amp-2 constitutes late, green, idiomorphic grains that overgrow diopside and corrode garnet (Fig. 4.4b). In boudins close to the dehydration front, centimetre thick, irregular bands or aggregates of dark amphibole are common. Conjugated sets of millimetre-thick amphibole veins are also very abundant (Fig. 4.2d), as well as reopened coarse-grained garnet (Grt-3) veins (Fig. 4.2d) refilled with aggregates of centimetre long, prismatic amphibole.

Within Chl-harzburgite, all Ep-metarodingite boudins are partially replaced by dark green aggregates of Amp-2 (Fig. 4.2e). Typically, the preserved epidote-rich cores are crosscut by conjugated sets of millimetre-thick amphibole veins (Fig. 4.2e).

In Pyrals-metarodingite and enclosing Chl-blackwall, amphibolitization can be also related with the growth of Amp-2. Grt-5 porphyroblasts are strongly corroded by a later, fine-grained amphibole corona (Amp-3) (Fig. 4.4f).

4.2.1.4 Metasomatic reaction rims

Interaction between metarodingites and host Atg-serpentinite produced three metasomatic rock-types that are, from the metarodingite body to the enclosing serpentinite, the following: chlorite- (Chl-) blackwall, chlorite-diopside- (Chl-Di-) rim and chlorite-diopside-olivine- (Chl-Di-Ol-) rim (Fig. 4.1d). In the Chl-harzburgite domain, only the first two lithologies are generally well developed.

The ***Chl-blackwall*** (5-20 cm thick) is a light silver, strongly foliated, Chl-Di schist (Fig. 4.2) with ± Ttn ± Ilm ± Rt ± Mag + Ap + Zrn. This rock essentially consists of alternating chlorite- and diopside-rich layers and veins parallel to the main foliation (Fig. 4.3a). Due to intense deformation, blackwalls in the Chl-harzburgite domain may constitute strongly thinned bands transposed from metarodingites. The contact between the Chl-blackwall and metarodingite is generally sharp (Fig. 4.2a, b). In some places, rare epidote, amphibole or garnet isolated grains or veins are visible within the blackwall.

At the thin section scale, Chl-blackwall has a clearly lepidoblastic texture marked by the preferred orientation of chlorite flakes. Diopside constitutes hypidiomorphic-isolated grains or granoblastic aggregates. In the Atg-serpentinite domain, oriented titanite (up to 1.5 cm) and magnetite grains are abundant, while ilmenite is less common. The Chl-blackwalls in the Chl-harzburgite domain lack magnetite but have large (up to 1 cm) idiomorphic pyrite crystals, abundant ilmenite and, around Pyrals-metarodingite, they also have rutile. Rare titanite appears only close to Ep-metarodingite bodies.

The ***Chl-Di-** and **Chl-Di-Ol- metasomatic rims*** have variable thickness (2-20 cm). The former is a whitish rock with nematoblastic texture, thin dark intercalations of chlorite between diopside and disseminated magnetite grains. The contact with the Chl-Di-Ol-rim is defined by the first occurrence of millimetre to centimetre long brownish aggregates of olivine, which confer a "leopard skin" appearance on the rock (Fig. 4.3b). Olivine aggregates have dark iddingsitic alteration rims and are in places intergrown with titanian-clinohumite. These aggregates are embedded in a granoblastic matrix of dusty diopside with clear rims. Chlorite flakes commonly have antigorite relicts in the core. Magnetite is disseminated in the rock. The contact with Atg-serpentinite is transitional and defined by the increasing amount of antigorite, the decrease of diopside and the absence of chlorite (Antigorite-Clinopyroxene serpentinite, Fig. 4.1d).

4.2.2 Mineral Chemistry

4.2.2.1 Garnet

According to their composition, the different types of garnet can be classified into two main groups: grandite- (Grt-1, Grt-2, and Grt-3) and pyralspite-garnets (Grt-5), with a third group (Grt-4) of intermediate composition (Tables 4.2 and A1).

The ***Grandite-garnet*** corresponds to the main rock-forming mineral of Grand-metarodingite and to relict grains in Ep-metarodingite hosted by Atg-serpentinite. These compositions plot along the Grossular-Andradite side in Fig. 4.6 and their pyralspite components (pyrope, almandine and spessartine end-members altogether) are below 25 mol.%. Several types of grandite garnet can be defined taking into account their textural and compositional features (Table 4.2a, b, Fig. 4.6). Grt-1 has the highest grossular values and lowest andradite and pyralspite contents (Grs_{64-84} Adr_{5-19} Prp_{0-1} Alm_{0-3} Sps_{0-1} $Ti\text{-}Grt_{2-11}$ Kat_{1-5}).

Two subtypes of Grt-2 have been differentiated. Grt-2a only occurs as very scarce grains within the first vein generation in Grand-metarodingite (Fig. 4.6a, b). It has a peculiar pyralspite-poor composition (Grs_{55-59} Adr_{20-24} $Prp_{0.7-0.9}$ $Alm_{0.7-0.9}$ $Sps_{0.2-0.6}$ $Ti\text{-}Grt_{13-16}$ $Kat_{1.9-3.4}$) when compared with the most abundant garnet type in these veins: Grt-2b (Grs_{42-61} Adr_{21-31} Prp_{3-7} Alm_{7-13} $Sps_{0.6-1}$ $Ti\text{-}Grt_{3-9}$ Kat_{2-3}), richer in andradite and pyralspite end-members than Grt-1 (Fig. 4.6). Grt-2b overgrows the Grt-2a grains in the first vein generation (Fig. 4.7a, b). Grt-2b relicts are found in Ep-metarodingite boudins from both the Atg-serpentinite and the Chl-harzburgite domains (blue triangles and blue squares in Fig. 4.6, respectively).

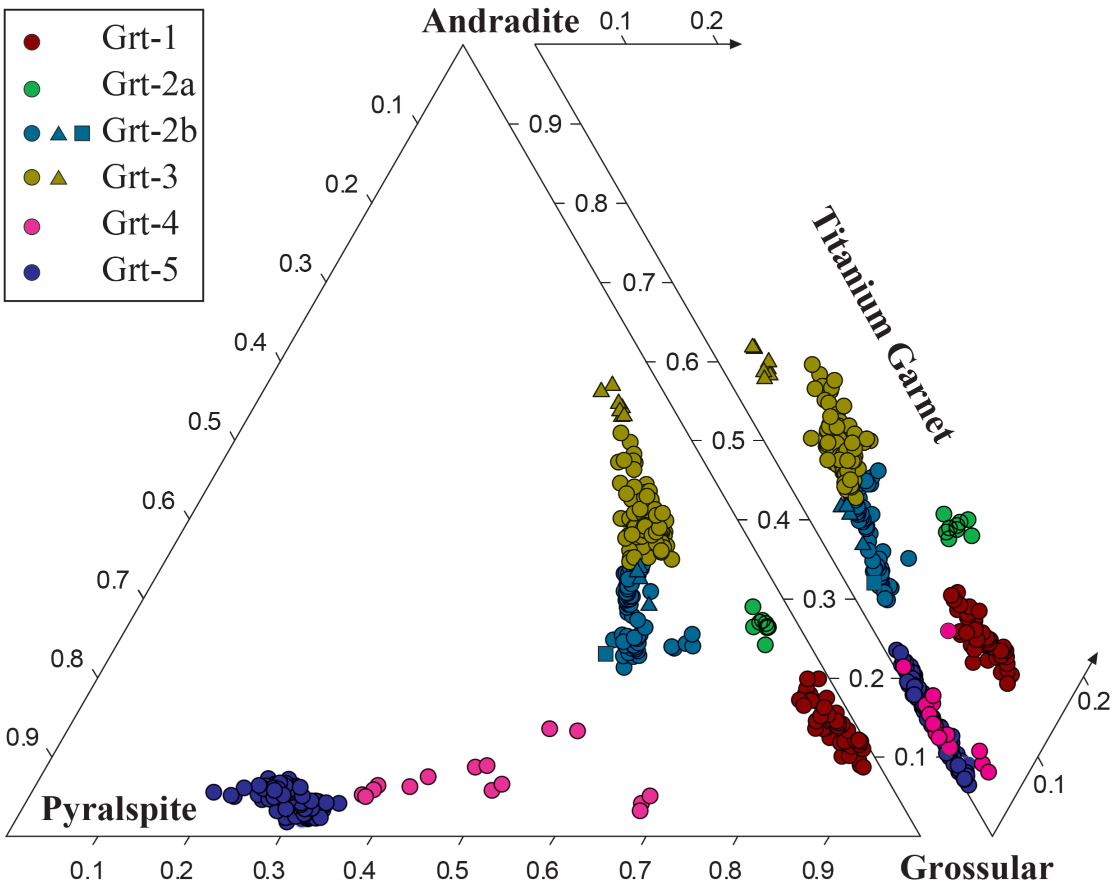

Figure 4.6. *Ternary plots with the composition of the different garnet generations found in the Almirez metarodingites. Pyralspite sums up the amounts of pyrope, almandine and spessartine components. Titanium garnet mainly corresponds to morimotoite component. Triangle symbols correspond to relicts of granditic garnet (Grt-2b and Grt-3) in Ep-metarodingite hosted in Atg-serpentinite. Squares represent relicts of granditic (Grt-2b) garnet in the cores of the Grt-4 grains in Ep-metarodingites hosted in Chl-harzburgites.*

Grt-3 is poorer in pyralspite and richer in andradite than Grt-2b (Grs_{38-56} Adr_{31-45} Prp_{1-4} Alm_{3-8} $Sps_{0.4-0.8}$ Ti-Grt_{5-10} Kat_{2-4}), especially the grains in Ep-metarodingites (Grs_{34-38} Adr_{49-53} Prp_{1-3} Alm_2 Sps_2 Ti-Grt_{4-5} Kat_{2-3}, dark yellow triangles in Fig. 4.6). Grt-3 grains from the second vein generation in Grand-metarodingite (Fig. 4.4b) display a drusy texture and oscillatory zoning in their andradite content (35-45 mol.%, Fig. 4.7a). This is typical of hydrothermal andraditic garnet precipitating in voids and cracks full of fluid (Jamtveit and Andersen, 1992). In these veins, Grt-3 is crosscut by irregular thin veinlets with Grt-2b composition (stars in Fig. 4.7a, b). Thin rims of Grt-3 also surround both Grt-1 and Grt-2 in Grand-metarodingite (Fig. 4.7a, b).

All the grandite-garnet is rich in OH (katoite end-member: $Ca_3Al_2OH_{12}$; Table 4.2a, b), especially Grt-1 (up to 5 mol.%), and in the Ti-bearing morimotoite end-member ($Ca_3[TiFe^{2+}]Si_3O_{12}$). The latter component is abundant in Grt-1 (up to 11 mol.%) and especially in Grt-2a (up to 16 mol.%) and poorer in Grt-2b (3-9

TABLE 4.2a *Garnet average compositions and standard deviation (σ) of microprobe analyses.*

GARNET						
Garnet type	Grt-1		Grt-2a		Grt-2b	
Metarod. type	Type 1		Type 1		Type 1	
n	33		11		72	
SiO_2	37.11	0.21	36.65	0.19	37.49	0.53
TiO_2	1.94	0.12	2.52	0.22	0.78	0.21
Al_2O_3	16.91	0.44	13.36	0.22	14.77	0.93
Cr_2O_3	0.01	0.01	0.02	0.01	0.07	0.18
FeO tot.	5.68	0.74	9.77	0.35	13.46	0.72
MnO	0.26	0.02	0.20	0.05	0.48	0.10
MgO	0.13	0.04	0.18	0.03	1.23	0.20
CaO	35.60	0.36	34.01	0.45	29.96	0.73
Na_2O	0.00	0.00	0.01	0.00	0.01	0.01
H_2O^{+}*	1.03	0.15	0.59	0.11	0.43	0.25
Total	98.69	0.27	97.31	0.85	98.67	0.54
final FeO	2.06	0.27	3.12	0.30	5.29	0.59
final Fe_2O_3	4.02	0.79	7.39	0.41	9.08	1.02
Total	99.09	0.29	98.05	0.86	99.58	0.53
Structural formula is calculated on the basis of 12 oxygen atoms and end-member fraction after Locock (2008).						
Si	2.87	0.02	2.92	0.01	2.94	0.03
Al	0.00	0.00	0.00	0.00	0.00	0.00
$4H^{+}$	0.13	0.02	0.08	0.01	0.06	0.03
Ti	0.11	0.01	0.15	0.01	0.05	0.01
Al	1.54	0.04	1.25	0.03	1.37	0.08
Cr	0.00	0.00	0.00	0.00	0.00	0.01
Fe^{2+}	0.11	0.01	0.15	0.01	0.05	0.01
Fe^{3+}	0.23	0.05	0.44	0.02	0.54	0.06
Fe^{2+}	0.02	0.02	0.06	0.02	0.30	0.05
Mn^{2+}	0.02	0.00	0.01	0.00	0.03	0.01
Mg	0.01	0.01	0.02	0.00	0.14	0.02
Ca	2.95	0.02	2.90	0.02	2.52	0.07
End-members (mol %)						
Grossular	70.79	2.31	57.01	1.46	50.56	3.06
Andradite	11.69	2.32	22.16	1.20	26.85	3.08
Almandine	0.72	0.61	1.95	0.51	10.07	1.55
Pyrope	0.45	0.21	0.73	0.11	4.79	0.77
Spessartine	0.57	0.05	0.46	0.11	1.07	0.23
Katoite	4.44	0.64	2.60	0.47	1.86	1.09
Morimotoite	11.14	0.58	14.98	1.25	4.52	1.25
Uvarovite	0.04	0.03	0.05	0.02	0.23	0.57
Hutcheonite	0.00	0.00	0.01	0.02	0.00	0.00
NaTi garnet	0.03	0.03	0.05	0.02	0.06	0.07
Morimotoite-Mg	0.10	0.25	0.00	0.00	0.00	0.00

*H_2O^{+} values are estimated to be equal to the amount compensating for the deficiency of silica.

mol.%) and Grt-3 (5-10 mol.%). Schorlomite ($Ca_3Ti_2[Fe_2^{3+}Si]O_{12}$) and NaTi-garnet ($[Na_2Ca]Ti_2Si_3O_{12}$) end-members only occur in scarce amounts.

The ***pyralspite-garnet*** (Grt-5) only occurs in Type 3 Pyrals-metarodingite. It has more than 60 mol.% of pyralspite components: Grs_{17-35} Adr_{2-7} Prp_{10-30} Alm_{35-50} Sps_{1-10} (Table 4.2b, Fig. 4.6). Grt-5 shows pyrope enrichment and almandine and spessartine depletion from the core (Grs_{28-35} Adr_{1-2} Prp_{10-17} Alm_{47-50} Sps_{2-4}) to the rims (Grs_{28-31} Adr_{1-2-3} Prp_{22-28} Alm_{35-41} Sps_{0-1}) (Fig. 4.6c). Towards the Chl-blackwall, the grossular component in Grt-

TABLE 4.2b *Garnet average compositions and standard deviation (σ) of microprobe analyses.*

GARNET										
Garnet type	Grt-3				Grt-4		Grt-5 core		Grt-5 rim	
Metarod. type	Type 1		Type 2		Type 2		Type 3		Type 3	
n	84		7		14		19		29	
SiO_2	36.53	0.28	36.45	0.10	38.53	0.31	37.69	0.36	38.89	0.43
TiO_2	1.23	0.28	0.79	0.07	0.32	0.28	0.17	0.13	0.09	0.04
Al_2O_3	12.05	0.78	9.42	0.34	19.93	1.33	21.02	0.17	21.56	0.30
Cr_2O_3	0.03	0.10	0.10	0.03	0.07	0.02	0.00	0.01	0.01	0.02
FeO tot.	14.34	0.76	16.63	0.33	13.63	1.57	23.63	0.30	18.99	0.85
MnO	0.28	0.06	0.89	0.09	2.50	1.07	1.17	0.07	0.54	0.29
MgO	0.70	0.14	0.35	0.15	3.70	1.97	3.26	0.32	7.04	0.37
CaO	32.12	0.55	32.95	0.12	20.65	4.66	12.53	0.37	12.55	0.89
Na_2O	0.01	0.01	0.02	0.01	0.01	0.02	0.00	0.00	0.00	0.00
H_2O^+*	0.71	0.17	0.55	0.11	0.05	0.09	0.00	0.00	0.00	0.00
Total	98.00	0.43	98.15	0.31	99.38	0.57	99.49	0.50	99.68	0.55
final FeO	3.49	0.43	1.58	0.11	10.82	1.98	22.16	0.41	17.41	0.68
final Fe_2O_3	12.06	0.87	16.72	0.40	3.12	1.42	1.63	0.46	1.76	0.76
Total	99.21	0.44	99.83	0.30	99.69	0.54	99.65	0.46	99.86	0.50
Structural formula is calculated on the basis of 12 oxygen atoms and end-member fraction after Locock (2008).										
Si	2.91	0.02	2.93	0.01	2.98	0.01	2.97	0.01	2.97	0.02
Al	0.00	0.00	0.00	0.00	0.02	0.02	0.03	0.01	0.03	0.02
$4H^+$	0.09	0.02	0.07	0.01	0.01	0.01	0.00	0.00	0.00	0.00
Ti	0.07	0.02	0.05	0.00	0.02	0.02	0.01	0.01	0.01	0.00
Al	1.13	0.07	0.89	0.03	1.80	0.11	1.92	0.02	1.91	0.03
Cr	0.00	0.01	0.01	0.00	0.00	0.00	0.00	0.00	0.00	0.00
Fe^{2+}	0.07	0.02	0.04	0.00	0.01	0.02	0.00	0.00	0.00	0.00
Fe^{3+}	0.72	0.05	1.01	0.03	0.18	0.08	0.10	0.03	0.10	0.04
Fe^{2+}	0.16	0.03	0.06	0.01	0.69	0.14	1.46	0.02	1.11	0.04
Mn^{2+}	0.02	0.00	0.06	0.01	0.16	0.07	0.08	0.00	0.04	0.02
Mg	0.08	0.02	0.04	0.02	0.43	0.23	0.38	0.04	0.80	0.04
Ca	2.74	0.05	2.83	0.01	1.71	0.39	1.06	0.03	1.03	0.07
End-members (mol %)										
Grossular	44.65	2.84	36.65	1.56	47.05	9.83	31.86	0.91	30.74	2.89
Andradite	36.09	2.71	50.50	1.31	8.02	4.54	2.84	0.45	3.20	1.01
Almandine	5.32	1.09	2.04	0.22	22.89	4.59	48.61	0.75	37.09	1.45
Pyrope	2.75	0.56	1.38	0.60	14.20	7.53	12.76	1.20	26.74	1.42
Spessartine	0.64	0.13	2.02	0.20	5.45	2.36	2.60	0.17	1.18	0.64
Katoite	3.12	0.74	2.47	0.46	0.23	0.38	0.00	0.00	0.00	0.00
Morimotoite	7.28	1.66	4.47	0.46	1.17	1.85	0.01	0.05	0.01	0.04
Uvarovite	0.10	0.33	0.32	0.09	0.21	0.07	0.01	0.03	0.04	0.08
Hutcheonite	0.00	0.00	0.00	0.00	0.30	0.36	0.49	0.35	0.26	0.11
NaTi garnet	0.04	0.05	0.14	0.05	0.04	0.07	0.00	0.00	0.00	0.00
Morimotoite-Mg	0.00	0.00	0.00	0.00	0.00	0.00	0.00	0.00	0.00	0.00

*H_2O^+ values are estimated to be equal to the amount compensating for the deficiency of silica.

5 is lower but it increases from the core (Grs$_{17}$ Adr$_{4\text{-}7}$ Prp$_{17}$ Alm$_{45}$ Sps$_{10}$) to the rims (Grs$_{27}$ Adr$_{4\text{-}7}$ Prp$_{30}$ Alm$_{35}$ Sps$_{4}$).

Finally, Grt-4 grains in Ep-metarodingite (Tables 4.2b, A1 and Fig. 4.4e) have intermediate compositions between those of grandite- and pyralspite-garnet groups (Grs$_{35\text{-}52}$ Adr$_{5\text{-}20}$ Prp$_{6\text{-}23}$ Alm$_{13\text{-}30}$ Sps$_{3\text{-}10}$ Ti-Grt$_{0\text{-}6}$ Kat$_{0\text{-}2}$; pink circles in Fig. 4.6). Individual Grt-4 grains display a well-defined core to rim increase of the pyralspitic components.

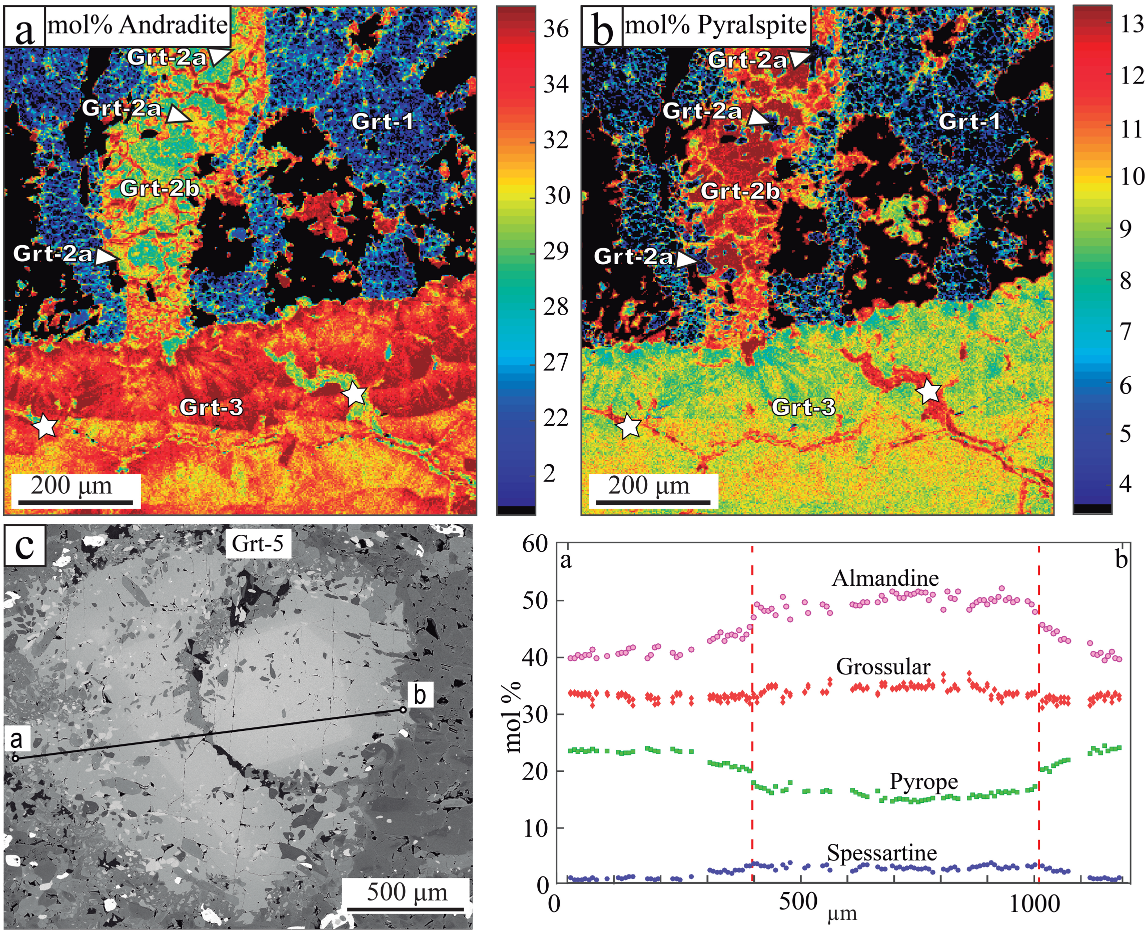

Figure 4.7. ***(a, b)*** *Compositional maps of garnet in Grand-metarodingite (blue inset from Figure 4.4b, for the andradite* ***(a)*** *and pyralspite (pyrope+almandine+spessartine);* ***(b)*** *end-members. Grt-2a corresponds to the earliest scarce, andradite-rich and pyralspite-poor garnet formed in the first vein generation. White stars mark late veinlets with composition very similar to Grt-2b crosscutting the Grt-3 veins. Data obtained using XMapTools© (module Chem2D and external function Gar-StructForm-Fe^{3+}; Lanari et al., 2014).* ***(c)*** *Compositional profile of Grt-5 in Pyrals-metarodingite.*

4.2.2.2 Chlorite

Chlorite has different compositional ranges in different rock types (Table A2). In metarodingites, irrespective of the rock type and textural position, this phase has sheridanite-clinochlore compositions (X_{Mg} = Mg/(Mg+Fe^{2+}) = 0.86-0.90, Al/Si = 0.80-0.90). Chlorite in Chl-blackwall has slightly higher X_{Mg} (0.89-0.95) and lower Al/Si (0.60-0.79) corresponding to the clinochlore and penninite end-members. In the Chl-Di- and Chl-Di-Ol- metasomatic rims, chlorite has similar and rather constant Mg-rich, Al-poor compositions (X_{Mg} = 0.93-0.96; Al/Si = 0.44-0.57), mostly corresponding to penninite. However, in the Chl-Di-Ol-rim it has high Cr_2O_3 contents (up to 2 wt.%) that are negatively correlated with Al_2O_3 ($CrAl_{-1}$ exchange vector), similar to chlorite in the transitional ultramafic lithologies between Atg-serpentinite and Chl-harzburgite (Padrón-Navarta et al., 2011). These high Cr contents suggest that metasomatic Chl-Di-and Chl-Di-Ol-metasomatic rims derives from precursor Atg-serpentinite.

4.2.2.3 Epidote

Representative epidote compositions are shown in Table A3. Epidote in equilibrium with chlorite and diopside in Grt-3 veins within Grand-metarodingite is iron-rich (X_{Ep} = $(Ca/[X])^2{*}Fe^{3+}(Si/3)^3$= 0.60-0.78). In the matrix of Type 2 Ep-metarodingite, epidote grains are zoned and have increasing values of pistacite component from the core (X_{Ep} = 0.11-0.50) to the rims (X_{ep} = 0.49-0.84). Coarse epidote that replaced Grt-1 aggregates in Ep-metarodingite and epidote in Pyrals-metarodingite have similar composition with X_{Ep} = 0.40-0.54. In contrast, zoisite coexisting with epidote in Pyrals-metarodingite is Fe^{3+}-poor (0.1 a.p.fu.; X_{Ep} = 0.1).

4.2.2.4 Diopside

Diopside occurs in all the studied lithologies (Table A4). X_{Mg} ranges between 0.90 and 0.96 in Grand- and Pyrals-metarodingites, and spans to lower values in Ep metarodingite (0.80-0.94) and the metasomatic reaction rims (0.85-0.99) (Table A4). Jadeite+Aegirine components are usually lower than 2 mol.%, except for grains in Pyrals-metarodingite which have up to 4 mol.% Jd+Aeg.

4.2.2.5 Amphibole

Amphiboles structural formulae were calculated after Locock (2014). Composition shows a continuous, well-defined trend between tremolite and pargasite end-members (Table A5 and Fig. 4.8). Amp-1 from Pyrals-metarodingite ranges between tremolite (X_{Mg} = 0.86-0.98) and Mg-Hornblende (X_{Mg} = 0.84-0.92) compositions. Extensive late amphibolitization produced Amp-2 that plots within the pargasite field (X_{Mg} = 0.72-0.85). Amp-3, which rims Grt-5 in Pyrals-metarodingite, has pargasite compositions with higher tschermakitic substitution (X_{Mg} = 0.60-0.83) (Fig. 4.8).

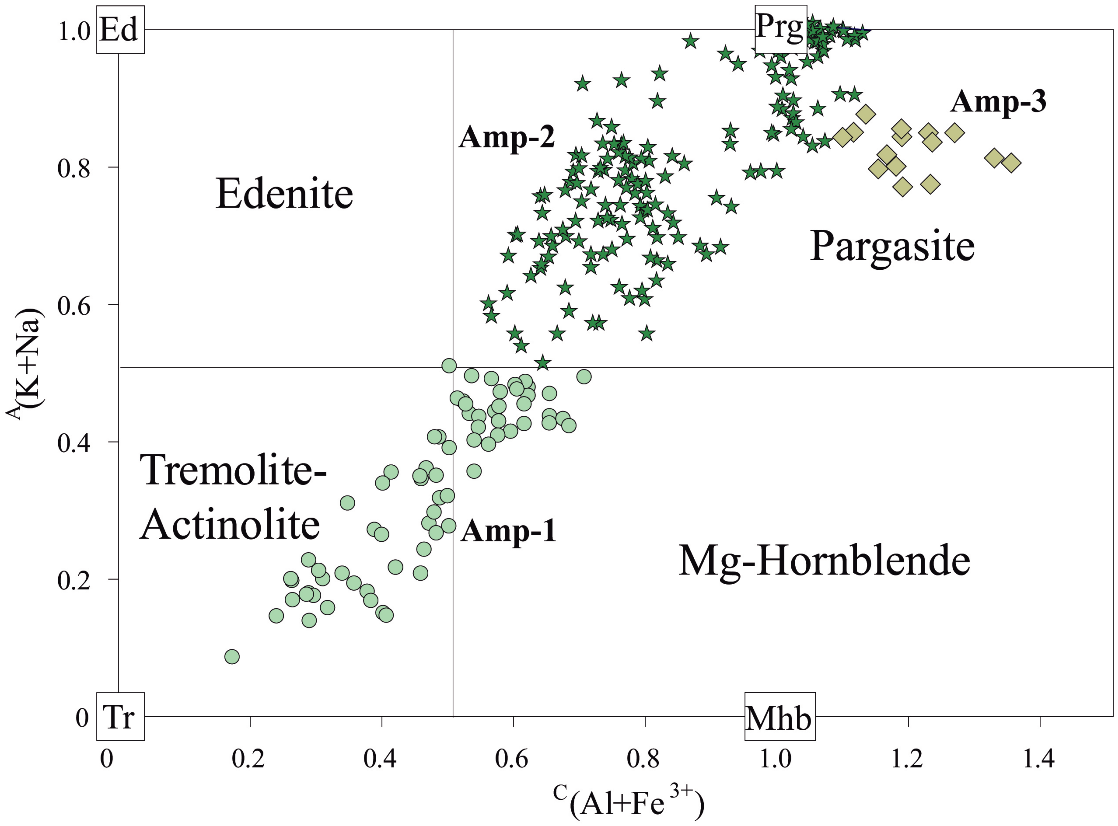

Figure 4.8. *Amphibole compositional variation in the A(K+Na) versus C(Al+Fe^{3+}) plot.*

4.2.2.6 Other minerals

Olivine in Chl-Di-Ol- metasomatic rim hosted by Atg-serpentinite presents X_{Mg} = 0.91-0.92, Ni = 0.005-0.007 a.p.f.u., and Mn = 0.004-0.005 a.p.f.u (Table A6). These values are similar to those reported for clinopyroxene-tremolite-rich serpentinite (Padrón-Navarta et al., 2011). In the only Chl-Di-Ol-rim found in the Chl-harzburgite domain, the X_{Mg} range of olivine (0.90-0.91) and its Mn content (0.002-0.003 a.p.f.u.) are similar to those of olivine in the wall Chl-harzburgite, but the Ni (0.012-0.015 a.p.f.u.) contents are much higher than those reported in any other rock type from the Cerro del Almirez massif. ***Antigorite*** in Chl-Di-Ol-rim has Si = 1.88-1.90 and Al = 0.17-0.21 a.p.f.u. (Table A7), similar to Si and Al abundances in antigorite from clinopyroxene-tremolite-rich serpentinite and from transitional Chl-serpentinite (Padrón-Navarta et al., 2011).

Magnetite is rich in Cr in Grand-metarodingite (up to 5.15 wt.% Cr_2O_3) and in all the metasomatic reaction rims (up to 8.5 wt.% Cr_2O_3) (Table A9). In contrast, magnetite in Ep-metarodingite is Cr-free. Irrespective of the rock type, ***titanite*** has stoichiometric composition with low Al (0.12-0.41 a.p.f.u.) and F contents (below detection limit) (Table A8).

4.2.3 Bulk-rock compositions and oxidation state

Bulk-rock analyses (Table 4.3) and ternary diagrams in the ACFS system (Fig. 4.9a) reveal significant compositional differences between metarodingite types, their associated metasomatic rims, and hosting ultramafic rocks. Type 1 Grand-metarodingite

TABLE 4.3 *Bulk-rock analyses of representative samples from different metarodingite types.*

Metarodingite type	Grandite-metarodingite Type 1	Epidote-metarodingite Type 2		Amphibolitized Epidote-metarodingite Type 2		Pyralspite-metarodingite Type 3
Host rock	Atg-Serp.	Atg-Serp.	Chl-Harz.	Atg-Serp.	Chl-Harzb.	Chl-Harzb.
Sample wt%	Al14-64	AL14-17	AL14-86	**AL14-26EA**	AL14-143	AL 96-24B
SiO_2	35.24	44.13	44.01	40.90	42.13	42.55
Al_2O_3	16.49	14.57	15.44	17.10	15.42	17.70
TiO_2	2.53	1.77	1.51	2.10	1.94	1.98
Fe_2O_3 tot.	10.01	7.38	7.25	10.65	9.48	8.96
MnO	0.17	0.07	0.09	0.11	0.12	0.14
MgO	6.97	6.37	6.45	7.25	9.17	9.31
CaO	25.72	24.92	24.52	19.5	19.25	17.36
Na_2O	0.09	0.20	0.18	1.26	1.21	0.97
K_2O	0.020	0.00	0.02	0.59	0.33	0.44
P_2O_5	0.40	0.2	0.19	0.20	0.24	0.20
LOI	2.31	0.39	0.33	0.34	0.69	0.40
Total	99.95	100	99.99	100	99.98	100.01
CaO*	24.40	24.27	23.87	18.84	18.46	16.71
FeOtot	9.00	6.64	6.52	9.58	8.53	8.06
FeO**	3.68	1.63	1.92	3.34	4.02	4.97
Fe_2O_3	5.92	5.56	5.11	6.94	5.02	3.44
Total	99.54	99.81	99.78	99.63	99.53	99.46
A	0.24	0.21	0.21	0.24	0.20	0.21
C	0.26	0.25	0.25	0.20	0.20	0.18
F	0.12	0.08	0.09	0.12	0.14	0.15
S	0.38	0.46	0.46	0.44	0.45	0.46

CaO* = CaO - (3.33 P_2O_5) apatite Ca correction for pseudosections. FeO** analysed.

is the CaO richest (25.7-30.3 wt.%) and SiO_2 poorest (34.9-42.2 wt.%) metarodingite type. Compared to Type 1, Type 2 Ep-metarodingite is CaO depleted (22.79-24.9 wt.%) and SiO_2 enriched (43.2-44.1 wt.%) and has similar MgO contents (6.3-6.7 wt.% for both lithologies) (Fig. 4.9a). A stronger CaO depletion (~ 19 wt.%), coupled to MgO enrichment (~ 9-12 wt.%), characterizes Pyrals-metarodingite (Fig. 4.9a). Strong amphibolitization explains the high Na_2O contents (up to 1.8 wt.%; Table 4.3) of Pyrals-metarodingite and some Ep-metarodingite samples. All the metasomatic reaction rims plot at intermediate compositions between those of metarodingites and host ultramafic rocks. No clear compositional differences in terms of major elements exist between Chl-blackwalls hosted in the Atg-serpentinite and Chl-harzburgite domains. (Fig. 4.9a).

Systematic differences in terms of bulk Fe^{3+}/Fe_{Total} ratios exist between the studied lithologies (Fig. 4.9b, Table 4.3). The highest values correspond to Grand-metarodingite (Fe^{3+}/Fe_{Total} = 0.66-0.83) and especially Ep-metarodingite (Fe^{3+}/Fe_{Total} = 0.76-0.89) from the Atg-serpentinite domain. Non amphibolitized Ep-metarodingite in Chl-harzburgite displays values within this range (Fe^{3+}/Fe_{Total} = 0.78). However, Pyrals-metarodingite has much lower Fe^{3+}/Fe_{Total} (0.38-0.48). Amphibolitization of Ep-metarodingites was coupled with a decrease in Fe^{3+}/Fe_{Total} independently of the host (Fig. 4.9b).

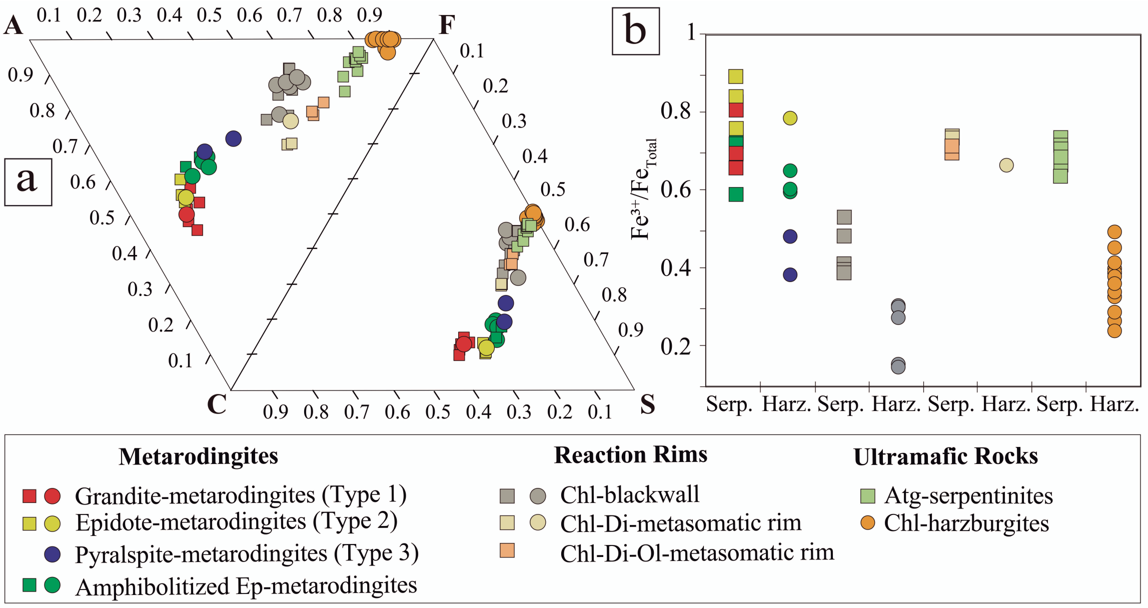

Figure 4.9. ***(a)*** *ACFS diagram (Winkler, 1979) showing the bulk-rock compositional variation of metarodingites, metasomatic reaction rims and hosting ultramafic rocks. Squares and circles indicate lithologies in the Atg-serpentinite and Chl-harzburgite domains respectively. A=Al_2O_3+Fe_2O_3-(Na_2O+K_2O); C=CaO-(3.33*P_2O_5); F=FeO+MgO+MnO; S=SiO_2.* ***(b)*** *Plot of bulk Fe^{3+}/Fe_{Total} ratios for all the studied lithologies distinguished according to their ultramafic host domain.*

Chl-blackwalls have lower Fe^{3+}/Fe_{Total} than the associated metarodingites, and Fe^{3+}/Fe_{Total} is higher in Chl-blackwalls from the Atg-serpentinite than from the Chl-harzburgite domains (Fig. 4.9b). In contrast, Chl-Di- and Chl-Di-Ol- metasomatic rims have Fe^{3+}/Fe_{Total} much higher than Chl-blackwalls, similar to values of Atg-serpentinites. The latter have Fe^{3+}/Fe_{Total} notably higher than Chl-harzburgites (Fig. 4.9b), in agreement with the results of Debret et al. (2015).

4.2.4 Chemographic relationships and metamorphic reactions in metarodingites

The chemographic analysis of metarodingites (Fig. 4.10) allows the extent of thermodynamic equilibrium achieved during their metamorphic evolution to be assessed, and deduction of the reactions that explain the main compositional changes in minerals and bulk-rocks.

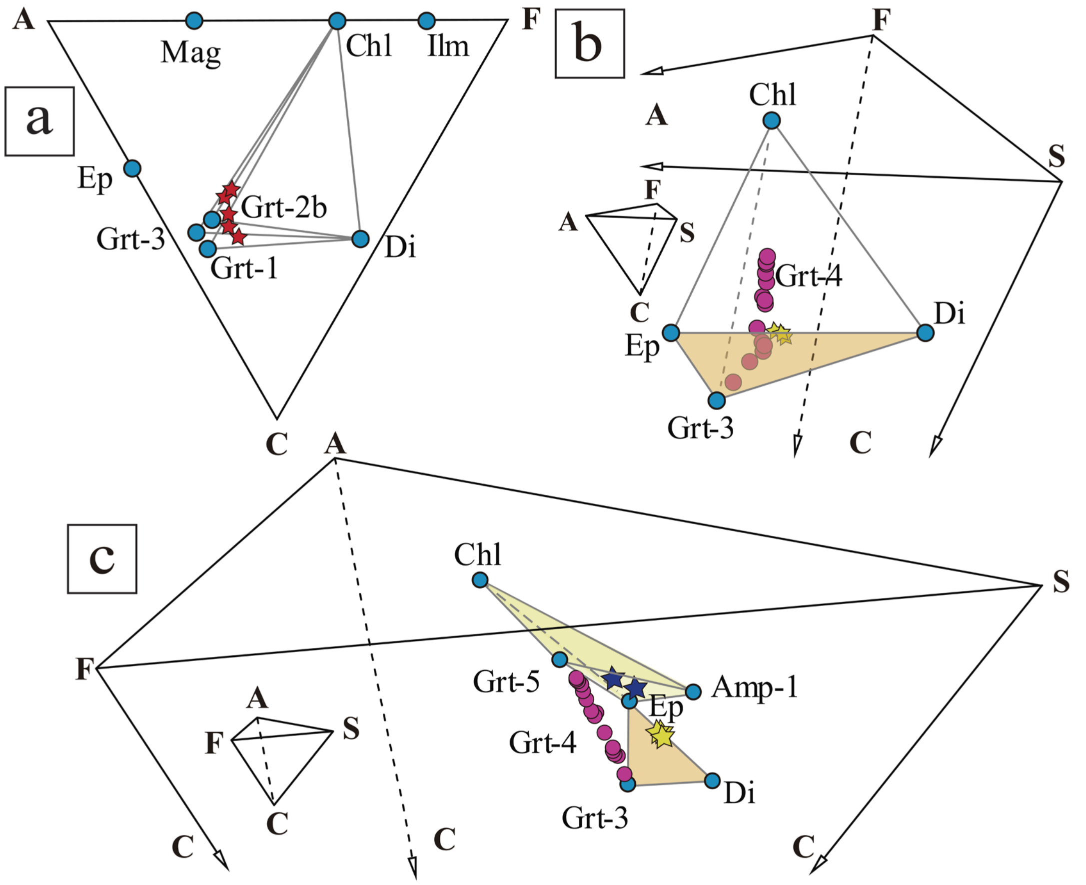

Figure 4.10. *Chemographic relationships for the different metarodingite types in the ACFS system. Bulk-rock compositions are indicated by stars and mineral compositions by dots.* ***(a)*** *Grandite-metarodingite.* ***(b)*** *Epidote-metarodingite. Purple dots represent the composition of Grt-4 grains in equilibrium in Ep-metarodingite from the Chl-harzburgite domain.* ***(c)*** *Transition between Epidote- and Pyralspite-metarodingites (green tetrahedron) viewed in a different orientation compared to* ***(b)****.*

4.2.4.1 Grandite-metarodingite

In the ACFS system, the bulk-rock compositions of Grand-metarodingites plot inside the space defined by Chl-Di and Grt-1, or Grt-2b, or Grt-3 (Fig. 4.10a). This indicates that the mineral assemblages of Grand-metarodingites are in equilibrium. The chemographic relationships between the mineral and bulk-rock compositions of these rocks (Fig. 4.10a) reflect: (i) the dominant modal abundance of garnet compared to chlorite and diopside (Table 4.1); (ii) the different garnet compositions of Grt-1, Grt-2b and Grt-3 (Fig. 4.6); and (iii) the decrease of the diopside/chlorite modal ratio accompanied by the change from Grt-1 to -2b and -3. The most primitive bulk composition of Grand-metarodingite plots close to the Grt-1 - Di tie line and evolved towards the Grt-2b (or Grt-3) - Chl tie line with increasing metamorphic grade (Fig. 4.10a). This change may have occurred through the reaction:

(Grt-1) $Ca_3Al_2(SiO_4)_{3\,(grossular)} + 5\ Ca[X]Si_2O_{6(diopside)} + 4\ H_2O_{(fluid)} \rightarrow$
$([X]_5Al)(AlSi_3)O_{10}(OH)_{8(chlorite)} + 10\ SiO_{2(aq)} + 8\ CaO_{(aq)}$ ***(1)***,

where $Grt\text{-}1_{Grs}$ represents the grossular component in Grt-1 and [X] represents the $FeMg_{-1}$ substitution in diopside and chlorite. This reaction, and the following ones, was balanced after the ideal stoichiometric composition of minerals. At least part of the fluid consumed in reaction (1) might have come from the breakdown of the katoite component in the primitive hydrogranditic garnet (Grt-1) according to the simultaneous reaction:

(Grt-1) $Ca_3[Y]_2(SiO_4)_{3-x}(OH)_{4x\,(hydrograndite)} + xSiO_{2(aq)} \rightarrow$ ***(Grt-1)*** $Ca_3[Y]_2(SiO_4)_{3(grandite)}$
$+\ 2x\ H_2O_{(fluid)}$ ***(2)***,

where x, with a maximum possible range of 0-3, represents the SiH_{-4} substitution in Grt-1 (ranging between 0.06 and 0.18 in these rocks) and [Y] sums up the octahedral cations.

During the transformation of Grt-1 into Grt-2b or Grt-3 (Fig. 4.7a, b), the observed decrease in the grossular and increase in the almandine and andradite contents can be explained by the breakdown of magnetite according to reaction:

(Grt-1) $Ca_3Al_2(SiO_4)_{3(grossular)} + 3\ Fe^{2+}Fe^{3+}{}_2O_{4(magnetite)} + 6\ CaO_{(aq)} + 9\ SiO_{2(aq)} \rightarrow$
(Grt-2b-3) $(1-x)\ Fe^{2+}{}_3Al_2(SiO_4)_{3(almandine)}$ + ***(Grt-2b-3)*** $(3+x)\ Ca_3Fe^{3+}{}_2(SiO_4)_{3(andradite)}$
$+\ 3x\ e^-{}_{(electrons)}$ ***(3),***

where x ranges from 0 to 1. In the case of Grt-2b x = 0, thus the amount of almandine is the highest possible one and the almandine/andradite ratio (1/3) is similar to that observed in Grt-2b (Alm_{7-13} Adr_{21-31} mol.%). In the case of Grt-3, an oxidizing agent is required to induce the partial oxidation of Fe^{2+} from magnetite and x is > 0, (almandine/andradite ratio < 1/3, Alm_{2-8} Adr_{31-53} mol.%). Therefore, contrary to the transformation of Gr-1 into Grt-2, the growth of Grt-3 implies an increase in the bulk-rock Fe^{3+}/Fe_{Total} ratio.

The increase in the pyrope component of Grt-2b and Grt-3 (up to 7 mol.%) compared to Grt-1 is consistent with the diopside-consuming reaction:

(Grt-1) $Ca_3Al_2(SiO_4)_{3\,(grossular)} + 3\ CaMgSi_2O_{6(diopside)} \rightarrow Mg_3Al_2(SiO_4)_{3(pyrope)}$
$+ 6\ CaO_{(aq)} + 6\ SiO_{2(aq)}$ **(4)**.

The growth of titanite, which coexists with Grt-2b and Grt-3, can be explained by Ti release from Grt-1 through the breakdown of the garnet morimotoite component:

(Grt-1) $Ca_3TiFe^{2+}Si_3O_{12\,(morimotoite)}$ + **(Grt-1)** $Ca_3Al_2(SiO_4)_{3(grossular)}$
$+ 4\ CaMgSi_2O_{6(diopside)} + 4\ H_2O_{\ (fluid)} \rightarrow (Mg_4Fe^{2+}Al)(AlSi_3)O_{10}(OH)_{8(clinochlore\ 80)}$
$+ CaSiTiO_{5(titanite)} + 10\ SiO_{2(aq)} + 9\ CaO_{(aq)}$ **(5)**,

This reaction contributes to the decrease in the bulk diopside/chlorite ratio (Fig. 4.10a).

4.2.4.2 Epidote-metarodingite

The bulk-rock compositions of Ep-metarodingites from both the Atg-serpentinite and Chl-harzburgite domains plot very close to the tie line epidote-diopside (Fig. 4.10b), which are the main minerals in these rocks (Table 4.1). In agreement with petrographic observations, these compositions are also in equilibrium with low amounts of Grt-3 and chlorite (Fig. 4.10b). The transformation of Grand- into Ep-metarodingites likely occurred by several independent reactions. The breakdown of grandite garnet (Grt-1, Grt-2b, Grt-3), which represents around 70 vol.% of Grand-metarodingite, may have occurred by the hydration reaction:

(Grt-1-2b-3) $3\ Ca_3[Y]_2(SiO_4)_{3(grandite)} + H_2O_{(fluid)} \rightarrow$
$2\ Ca_2Al_2[Y](Si_2O_7)(SiO_4)O(OH)_{(epidote)} + 5\ CaO_{(aq)} + 3\ SiO_{2(aq)}$ **(6)**,

where [Y] represents the $Fe^{3+}Al_{-1}$ substitution in the garnet granditic components and in epidote. The possible maximum range of [Y] consistent with stoichiometry spans from $[Al_1]$ to $[Fe^{3+}_{0.33}\ Al_{0.67}]$.

A concomitant reaction should have oxidized Fe^{2+} in the almandine component of Grt-2b and Grt-3 at water-saturated conditions:

$$\begin{aligned}&\textbf{(Grt-2b-3)}\ 3\ Fe_3Al_2(SiO_4)_{3(almandine)} + 4\ Ca_2Al_3(Si_2O_7)(SiO_4)O(OH)_{(clinozoisite)} + 10\ CaO_{(aq)}\\ &+ 6\ SiO_{2(aq)} + 9\ OH^-_{(aq)} \rightarrow 9\ Ca_2Fe^{3+}Al_2(Si_2O_7)(SiO_4)O(OH)_{(epidote)} + 2\ H_2O_{(fluid)}\\ &+ 3\ e^-_{(electrons)} \qquad \textbf{(7)}.\end{aligned}$$

The observed breakdown of chlorite and growth of new diopside may have occurred through reaction:

$$\begin{aligned}&3\ ([X]_5Al)(AlSi3)O_{10}(OH)_{8(chlorite)} + 27\ SiO_{2(aq)} + 19\ CaO_{(aq)} \rightarrow 15\ Ca[X]Si_2O_{6(diopside)}\\ &+ 2\ Ca_2Al_3(Si_2O_7)(SiO_4)O(OH)_{(clinozoisite)} + 11\ H_2O_{(fluid)} \qquad \textbf{(8)},\end{aligned}$$

where [X] represents the $FeMg_{-1}$ substitution in chlorite and diopside.

The relative importance of reactions (6), (7) and (8) was controlled by the different chlorite/garnet ratios in precursor Grand-metarodingite, which is richer in Chl towards the Chl-blackwall. However, an external source of water and an oxidizing agent (reaction 7) must be invoked. Additionally, Ti in grandite-garnet was fully incorporated into titanite by reaction (5). This may explain the higher amounts of titanite in Type 2 Ep-metarodingites compared to Type 1. Newly formed magnetite, texturally related to titanite, may have grown by reaction:

$$\begin{aligned}&\textbf{(Grt-1-2b-3)}\ Ca_3TiFe^{2+}(SiO_4)_{3(morimotoite)} + \textbf{(Grt-1-2b-3)}\ 4\ Ca_3(Fe^{3+}Al)\ (SiO_4)_{3(grandite)}\\ &+ 4\ OH^-_{(aq)} \rightarrow 2\ Ca_2Fe^{3+}Al_2(Si_2O_7)(SiO_4)O(OH)_{(epidote)} + CaTiO_{5(titanite)}\\ &+ Fe^{2+}Fe^{3+}{}_2O_{4(magnetite)} + 10\ CaO_{(aq)} + 9\ SiO_{2(aq)} + H_2O_{(fluid)} \qquad \textbf{(9)},\end{aligned}$$

Ep-metarodingites from the Chl-harzburgite domain have small recrystallized grains of Grt-4 (Fig. 4.4e) with a particular compositional trend (Fig. 4.6). In Fig. 4.10c, these garnet compositions span the range between grandite garnet (Grt-3) and newly formed pyralspite garnet (Grt-5) of Type 3 metarodingite. Each of these compositions would set a different position of the Grt-apex of the Grt-Ep-Di-Chl tetrahedron that defines the mineral assemblage of Ep-metarodingite (Fig. 4.10b). Irrespective of the location of the

Grt-apex, the bulk-rock compositions of Ep-metarodingite plot within this tetrahedron and, hence, Grt-4 is in equilibrium with the main mineral assemblage.

4.2.4.3 Pyralspite-metarodingite

Transformation of Ep-metarodingite into Pyrals-metarodingite is marked by the crystallization of both pyralspitic Grt-5 and amphibole (Amp-1; green tetrahedron in Fig. 4.10d). This metarodingite type is usually very poor in Chl and bulk composition analyses plot within the Chl-Ep-Grt-5-Amp-1 tetrahedron (Fig. 4.10c).

The growth of Grt-5 can be explained by the following simultaneous reactions:

$$\begin{aligned}&15\ CaMgSi_2O_{6(diopside)} + 12\ Ca_2Al_3(Si_2O_7)(SiO_4)O(OH)_{(clinozoisite)} \rightarrow\\ &\mathbf{(Grt\text{-}5)}\ Mg_3Al_2(SiO_4)_{3\ (pyrope)} + \mathbf{(Grt\text{-}5)}\ 13\ Ca_3Al_2(SiO_4)_{3\ (grossular)} + 6\ H_2O_{(fluid)}\\ &+ 12\ SiO_{2(aq)} \qquad \mathbf{(10)},\end{aligned}$$

and

$$\begin{aligned}&9\ Ca_2Fe^{3+}Al_2(Si_2O_7)(SiO_4)O(OH)_{(epidote)} + 2\ H_2O_{(fluid)} + 3\ e^-_{(electrons)} \rightarrow\\ &\mathbf{(Grt\text{-}5)}\ 3\ Fe_3Al_2(SiO_4)_{3(almandine)} + 4\ Ca_2Al_3(Si_2O_7)(SiO_4)O(OH)_{(zoisite/clinozoisite)}\\ &+ 10\ CaO_{(aq)} + 6\ SiO_{2(aq)} + 9\ OH^-_{(aq)} \qquad \mathbf{(11)}.\end{aligned}$$

These reactions released fluid, CaO and SiO_2. Reaction (11) is the reverse of reaction (7) and produces the reduction of Fe^{3+} in epidote to Fe^{2+} in almandine. This process may hence account for the strong drop in Fe^{3+}/Fe_{Total} between Ep-metarodingite and Pyrals-metarodingite (Fig. 4.9b).

Amphibole possibly formed by the diopside-consuming reaction:

$$4\ CaMgSi_2O_{6(diopside)} + MgO_{(aq)} + H_2O_{(fluid)} \rightarrow 2\ CaO_{(aq)} + Ca_2Mg_5Si_8O_{24}H_{2(tremolite)}\ \mathbf{(12)},$$

which requires the addition of MgO and the loss of CaO in the metarodingite bulk chemical system. This compositional change between Ep- and Pyrals-metarodingites (Fig. 4.9a and 4.10c) was probably enhanced by chemical potential gradients between metarodingites and host Chl-harzburgite.

4.2.5 Thermodynamic modelling

Pseudosections for each metarodingite type have been calculated using Perple_X 6.7.6 (Connolly, 2009) in the system NCFMASHTO (Fig. 4.11). According to chemographic analysis (Fig. 4.10), thermodynamic equilibrium was reached in every metarodingite type. The reactive bulk composition considered in the calculations was obtained: (i) by substracting from the bulk rock composition the amount of CaO in apatite (= 3.33*P_2O_5 wt.%), not relevant for the rock´s phase relationships; and (ii) by excluding bulk Na_2O contents as Na_2O concentrates only in amphibole (Amp-2 and Amp-3) formed during retrograde metasomatic amphibolitization and was not involved in the prograde metamorphic path of the rocks. We used the internally consistent thermodynamic database of Holland and Powell (1998, revised version of 2002) and the following solid solution models: Orthopyroxene, Clinopyroxene (Holland and Powell, 1996); Olivine, Spinel, Saphirine, Staurolite, Chloritoid (Holland and Powell, 1998); Chlorite (Holland et al., 1998); Epidote (Holland and Powell, 2011); Antigorite (Padrón-Navarta et al., 2013); Amphibole (Dale et al., 2000); Garnet (White et al., 2007); Magnetite Ulvospinel (Andersen and Lindsley, 1988); Plagioclase (Newton and Haselton, 1981); Pumpellite (Massonne and Willner, 2008). Ideal solution models were adopted for Talc, Brucite, Anthophillite, Wustite, Ilmenite, Clinohumite, Carpholite and Sudoite. Zoisite was considered as a pure phase. We used the CORK equation of state for H_2O-CO_2 fluids (Holland and Powell, 1998), although fluids have been considered pure H_2O.

The lack of suitable solid solution models may explain some inconsistencies between the observed and predicted phase compositions. This is especially the case of garnet, whose solution model does not consider H_2O- and Ti-rich end-members ($Ca_3Al_2OH_{12}$ and $Ca_3[TiFe^{2+}]Si_3O_{12}$, respectively). Thus, excess Ti in the form of low amounts (< 4 vol.%) of ilmenite -not always observed in the rocks- is commonly predicted by the calculations (e.g., Ilm in the blue-labelled fields in Fig. 4.11a). Moreover, the exclusion from calculations of the CaO contents of these end-members results in an overestimation (< 10 mol.%) of the calculated amounts of the grossular component.

4.2.5.1 Grandite-metarodingite

The P-T pseudosection for a representative Type 1 Grand-metarodingite (Al14-64 without Na_2O component; Table 4.3) is shown in Fig. 4.11a. The mineral assemblage observed in this rock (Grt + Chl + Ttn, labelled in blue) is stable at temperatures and pressures of 560-675 °C and 9-20 kbar, respectively. These conditions are constrained by the stability of epidote at low P and T, rutile at high P, and clinopyroxene at low P and high T, which are not present in this rock. The calculated composition of garnet (Grs_{62-64} Adr_{22-33} $Pyrals_{13-16}$) matches that of Grt-2b (Table 4.2a, Fig. 4.6), and the modal amounts of minerals (70-74 vol.% Grt; 23 vol.% Chl; 4 vol.% Ttn) are also consistent with those of the rock (Table 4.1).

Grossular-rich and pyralspite-poor garnet, similar to Grt-1, is stable at < 7 kbar and 200-400 °C and coexists with clinopyroxene, chlorite, magnetite and titanite (Fig. 4.11a, green label), coinciding with the observed mineral assemblage in equilibrium with Grt-1. Epidote, however, is also predicted in this field (7-8 vol.%), but this mineral did not crystallize in Type 1 metarodingite. Moreover, no garnet composition equivalent to Grt-3 is predicted to be stable in the whole P-T field of this pseudosection.

Besides P and T, oxygen fugacity should also have changed during the metamorphic evolution of Grand-metarodingite, as evidenced by the variation in the bulk-rock Fe^{3+}/Fe_{Total} ratio produced by the crystallization of Grt-3 (reaction 3). Isobaric T vs log fO_2 pseudosections for the same Grand-metarodingite sample calculated at different pressures (Fig. 4.11b, c) show that the original rodingitic assemblage (Grt + Chl + Cpx + Mag + Ilm) and the observed composition of Grt-1 (Grs_{64-84} Adr_{5-19} $Pyrals_{0-3}$) are stable at 2 kbar, 150-325 °C and log fO_2 ranging from -55 to -35, equivalent to the fayalite-magnetite-quartz redox buffer (FMQ) ranging from -2 to +3 (Fig. 4.11 b). These fO_2 conditions are well constrained by the calculated Grt-1 composition and the lack of epidote, olivine and vesuvianite in the observed mineral assemblage.

Grt-2b is stable at minimum pressure = 10 kbar. At this pressure, the typical assemblage (Grt + Chl ± Cpx + Ttn (+ Ilm)) coexisting with Grt-2b is stable at 350-650 °C and log fO_2 = -25 to -15, equivalent to FMQ ranging from -1 to + 3 (Fig. 4.11c). At these conditions, the model predicts several petrographic and compositional features of Type-1 Grand-metarodingite, such as the stability of titanite, the lack of magnetite, the progressive decrease of diopside abundance, and the composition of garnet (Grs_{65-70} Adr_{20-30} $Pyrals_{12}$), which is very similar to that of Grt-2b (Grs_{42-61} Adr_{21-31} $Pyrals_{10-13}$). At

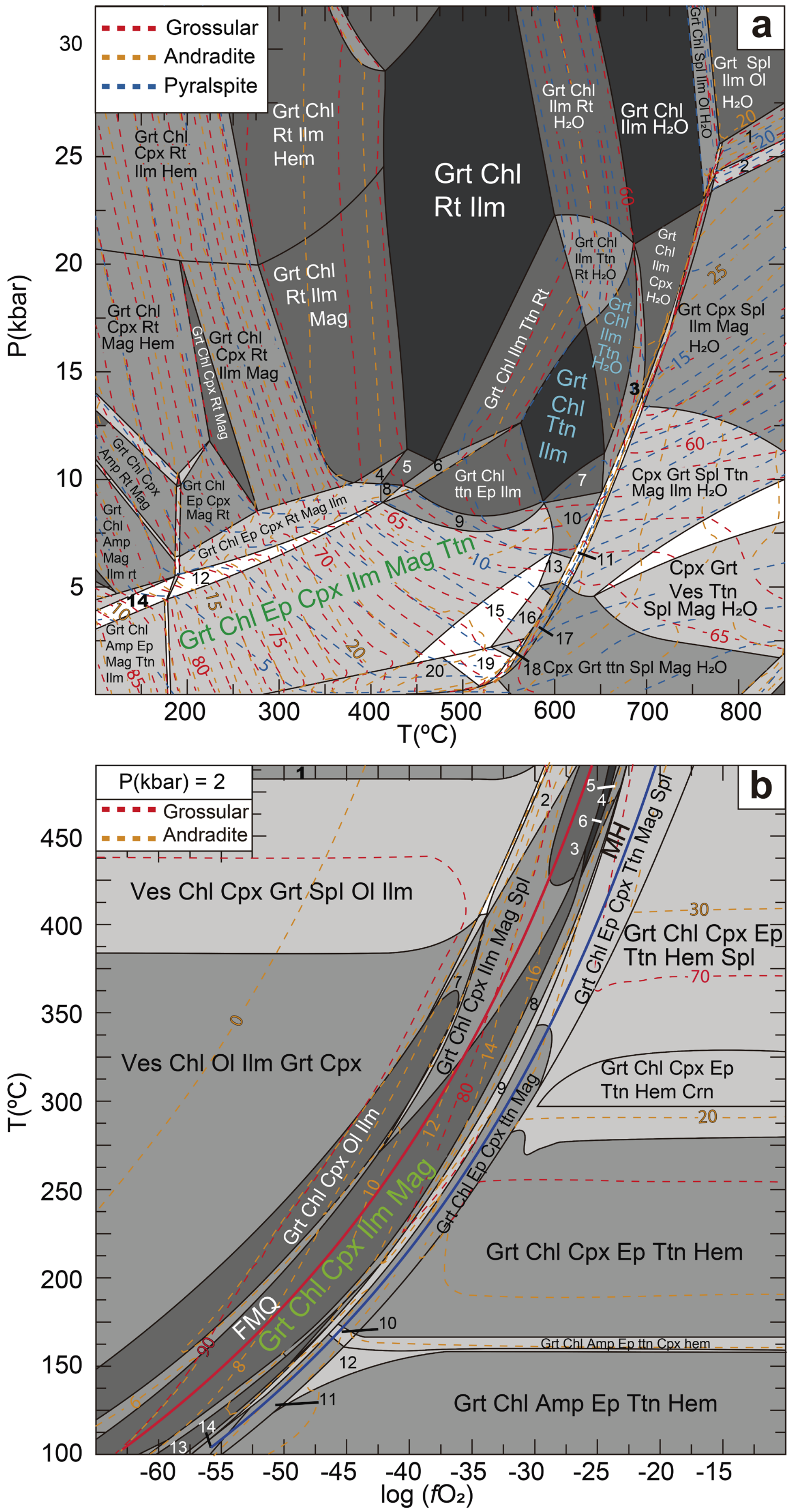
a
Grossular
Andradite
Pyralspite
P(kbar)
T(ºC)
30
25
20
15
10
5
200
300
400
500
600
700
800
Grt Chl Cpx Rt Ilm Hem
Grt Chl Rt Ilm Hem
Grt Chl Rt Ilm
Grt Chl Ilm Rt H₂O
Grt Chl Ilm H₂O
Grt Chl Spl Ilm Ol H₂O
Grt Spl Ilm Ol H₂O
Grt Chl Rt Ilm Mag
Grt Chl Cpx Rt Mag Hem
Grt Chl Cpx Rt Ilm Mag
Grt Chl Cpx Rt Mag
Grt Chl Ilm Ttn Rt H₂O
Grt Chl Ilm Cpx H₂O
Grt Cpx Spl Ilm Mag H₂O
Grt Chl Ilm Ttn Rt
Grt Chl Ilm Ttn H₂O
Grt Chl Ttn Ilm
Grt Chl Cpx Amp Rt Mag
Grt Chl Amp Mag Ilm rt
Grt Chl Ep Cpx Mag Rt
Grt Chl Ep Cpx Rt Mag Ilm
Grt Chl ttn Ep Ilm
Cpx Grt Spl Ttn Mag Ilm H₂O
Grt Chl Ep Cpx Ilm Mag Ttn
Cpx Grt Ves Ttn Spl Mag H₂O
Cpx Grt ttn Spl Mag H₂O
Grt Chl Amp Ep Mag Ttn Ilm
1
2
3
4
5
6
7
8
9
10
11
12
13
14
15
16
17
18
19
20
60
65
70
75
80
85
60
65
10
15
20
25
5
10
15
20
b
P(kbar) = 2
Grossular
Andradite
T(ºC)
log (fO₂)
450
400
350
300
250
200
150
100
-60
-55
-50
-45
-40
-35
-30
-25
-20
-15
Ves Chl Cpx Grt Spl Ol Ilm
Ves Chl Ol Ilm Grt Cpx
Grt Chl Cpx Ilm Mag Spl
Grt Chl Cpx Ol Ilm
FMQ
Grt Chl Cpx Ilm Mag
MH
Grt Chl Ep Cpx Ttn Mag Spl
Grt Chl Ep Cpx ttn Mag
Grt Chl Cpx Ep Ttn Hem Spl
Grt Chl Cpx Ep Ttn Hem Crn
Grt Chl Cpx Ep Ttn Hem
Grt Chl Amp Ep ttn Cpx hem
Grt Chl Amp Ep Ttn Hem
1
2
3
4
5
6
7
8
9
10
11
12
13
14
30
70
20
0
16
14
12
10
8
6
80
90

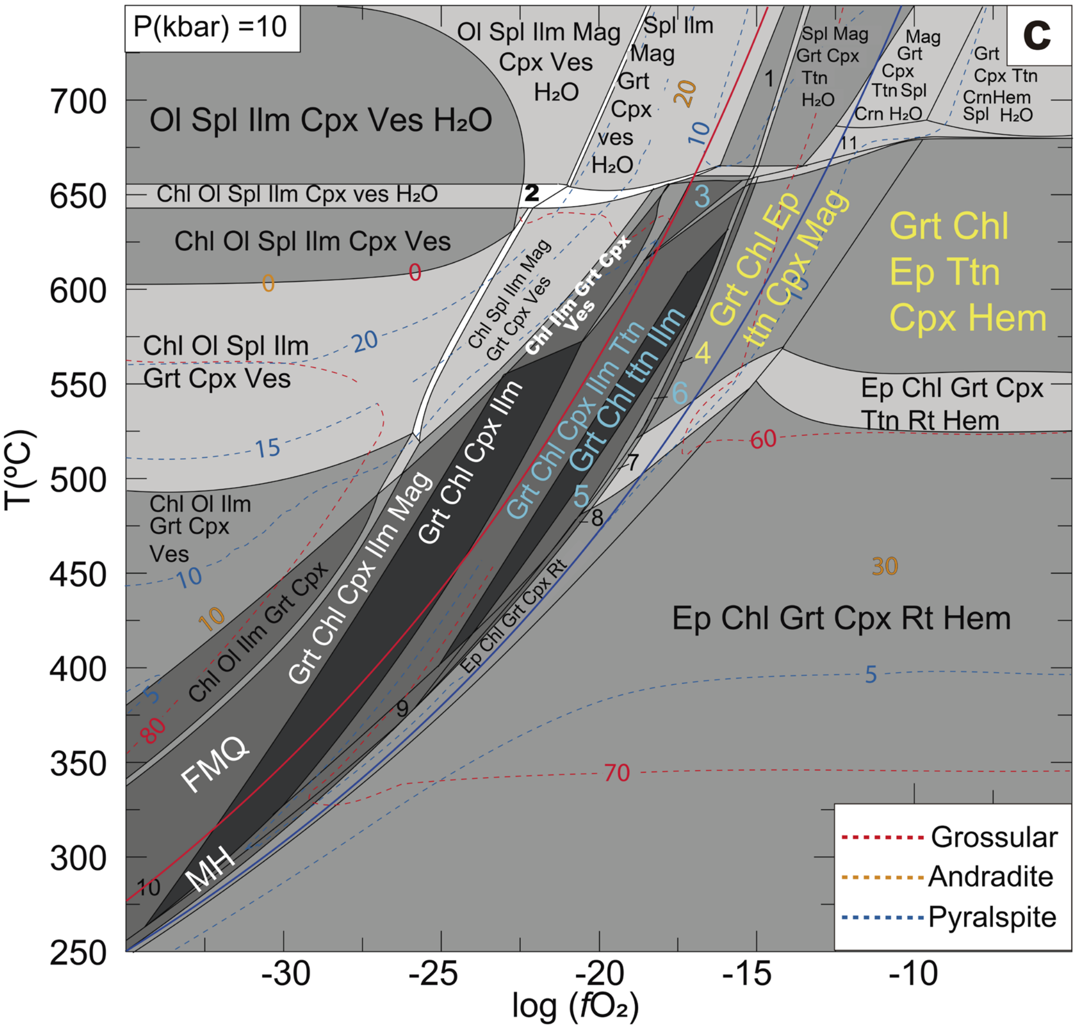

Figure 4.11. *P–T-log fO_2 constraints from thermodynamic modelling using Perple_X for Type 1 Grand-metarodingite (sample Al14-64 bulk-rock composition; Table 4.3).* ***(a)*** *P–T pseudosection. The blue-labelled assemblages are those observed in the rock. At these conditions, the Grt-2b composition is stable, as indicated by isopleths (dashed lines) for the grossular, andradite and pyralspite (pyrope + almandine + spessartine) garnet end-members. Grt-1 composition is stable at lower P–T conditions (green-labelled assemblage), where it coexists with epidote (absent in the rock).* ***(b)*** *T-log fO_2 pseudosection at 2 kbar. Grt-1 composition and the observed coexisting mineral assemblage are stable in the green-labelled field up to ~325°C. Stability of this assemblage is limited by that of olivine and vesuvianite at low log fO_2 conditions and by stability of epidote at high log fO_2.* ***(c)*** *T-log fO2 pseudosection at 10 kbar. Grt-2b composition (pyralspite >10 mol.%) and the observed coexisting mineral assemblage are stable in the blue-labelled fields at >400°C and log fO_2 >−25. Grt-3 composition (andradite >30 mol.%) and the observed coexisting mineral assemblage (including up to 16 vol.% epidote) are stable in the yellow-labelled fields at >550°C and log fO_2 > −15. Thick red and purple lines show the conditions of FMQ and MH buffers of oxygen fugacity respectively. Stable assemblages in the numbered fields are shown in Table A12.*

P = 10 kbar, epidote-bearing assemblages with garnet compositions ($Grs_{<60}$ $Adr_{>30}$ $Pyrals_{<10}$) equivalent to those of Grt-3 are stable at log fO_2 > -19, over and above the magnetite-hematite redox buffer (MH), and T between 525 °C (below which rutile is stable) and 675 °C (above which spinel is stable) (Fig. 4.11c). The maximum pressure at which grandite-garnet bearing assemblages are stable cannot be constrained by isobaric T vs log fO_2 phase diagrams.

4.2.5.2 Epidote-metarodingite

The thermodynamic model shown in Fig. 4.11c predicts the stability of the mineral assemblages of Ep-metarodingite (yellow-labelled fields) but the calculated modal proportions (4-16 vol.% epidote and 2-4 vol.% clinopyroxene) strongly differ from the real ones (~50-55 vol.% epidote and ~35-40 vol.% clinopyroxene). Thus, increasing oxygen fugacity alone (log fO_2 = -20 to -5) cannot explain the complete transformation of Grand-metarodingite into Ep-metarodingite. Bulk compositional differences between these metarodingite types (Fig. 4.9a) and reactions (6) and (8) instead support that the chemical potentials of SiO_2 (μSiO2) and CaO (μCaO) acted, together with P, T and fO_2, as independent thermodynamic variables during this transformation (Fig. 4.12a).To investigate this hypothesis, we calculated a μSiO_2-μCaO pseudosection for the same Grand-metarodingite bulk composition (Al14-64; Table 4.3) at H_2O saturated conditions,

---

Figure 4.12 *Thermodynamic modelling using Perple_X for constraining the transition from Type 1 to Type 2 metarodingites and for the stability conditions of Type 2, Ep-metarodingite.* ***(a)*** *μSiO_2-μCaO pseudosection for the bulk-rock composition of a Grand-metarodingite sample (Al14-64; Table 4.3) at constant 16 kbar and 625°C and H_2O saturation conditions. It reproduces the transition from Grand-metarodingite to Ep-metarodingite (white-dashed arrow). The red star, red-labelled assemblages and the corresponding garnet composition defined by isopleths (dashed lines) are those of Grand-metarodingite with Grt-2b. Transition to the typical mineralogy of Ep-metarodingite (yellow-labelled fields) and stable Grt-3 composition (yellow star) is enhanced by μCaO decrease and μSiO_2 increase. The predicted bulk-rock composition at the yellow star conditions (SiO_2 = 44.10; TiO_2 = 2.13; Al_2O_3 = 13.93; Fe_2O_3 = 5; FeO = 3.11; MnO = 0.14; MgO = 5.89; CaO = 24.79; H_2O = 0.90 wt%) compares well with the analysed composition of an Ep-metarodingite from the Atg-serpentinite domain (sample Al14-17; Table 4.3).* ***(b)*** *T-log fO_2 pseudosection calculated at constant 16 kbar and H2O saturation conditions for the bulk-rock composition obtained by Perple_X at the yellow star conditions in (a). The Ep-metarodingite assemblage (yellow label) is stable over a wide temperature range and at log fO_2 higher than Grand-metarodingite. Garnet isopleths indicate that, at the conditions marked by the yellow star, stable Grt-4 has the lowest almandine-pyrope and the highest grossular-andradite contents. Thick red and purple lines show the conditions of FMQ and MH buffers of oxygen fugacity respectively. Stable assemblages in the numbered fields are shown in Table A12.*

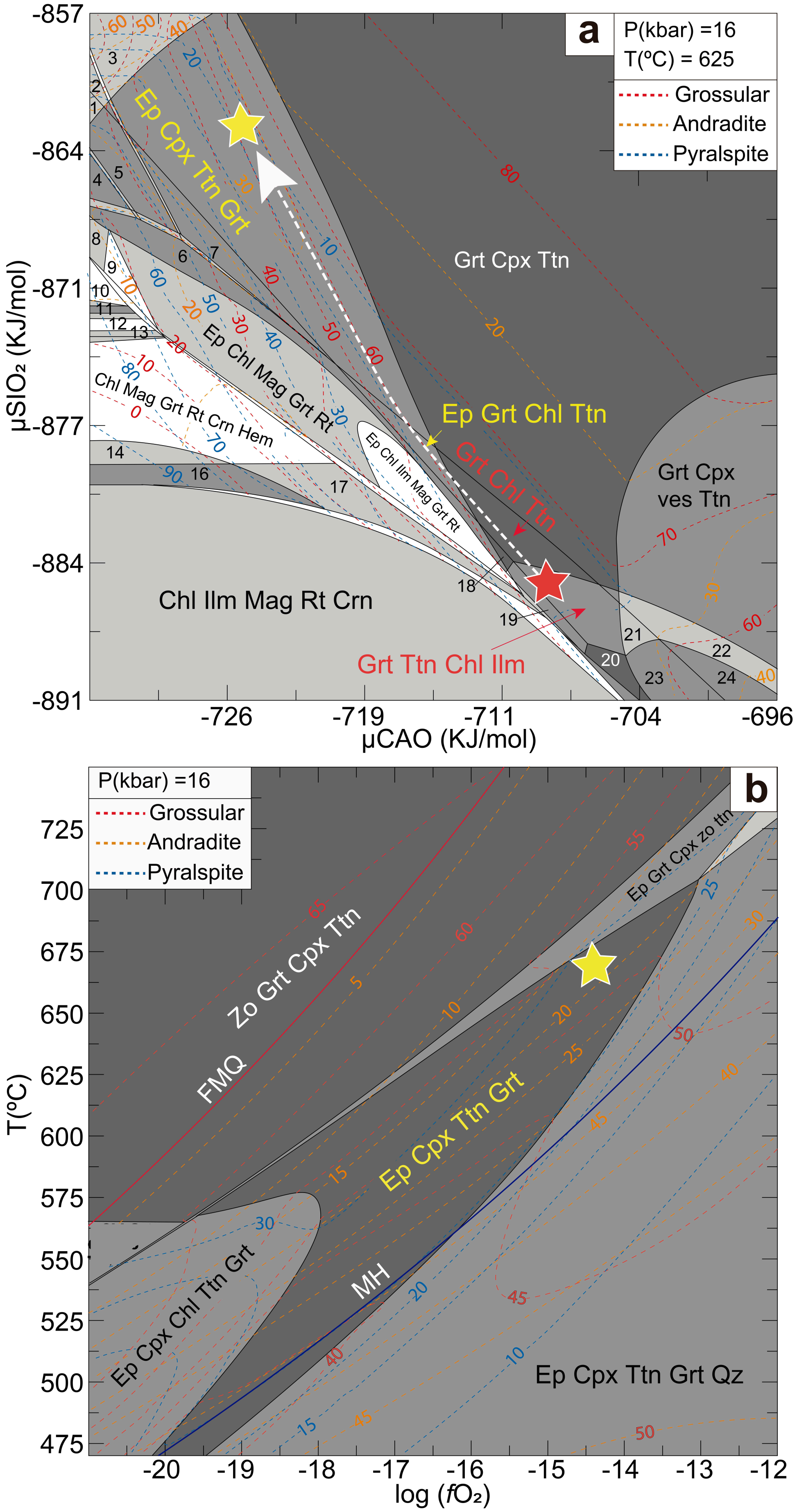
a
P(kbar) =16
T(ºC) = 625
Grossular
Andradite
Pyralspite
Ep Cpx Ttn Grt
Grt Cpx Ttn
Ep Chl Mag Grt Rt
Chl Mag Grt Rt Crn Hem
Ep Chl Ilm Mag Grt Rt
Ep Grt Chl Ttn
Grt Chl Ttn
Grt Cpx ves Ttn
Chl Ilm Mag Rt Crn
Grt Ttn Chl Ilm
µSIO₂ (KJ/mol)
µCAO (KJ/mol)
-857
-864
-871
-877
-884
-891
-726
-719
-711
-704
-696
b
P(kbar) =16
Grossular
Andradite
Pyralspite
Zo Grt Cpx Ttn
FMQ
Ep Grt Cpx zo ttn
Ep Cpx Ttn Grt
Ep Cpx Chl Ttn Grt
MH
Ep Cpx Ttn Grt Qz
T(ºC)
log (fO₂)
725
700
675
650
625
600
575
550
525
500
475
-20
-19
-18
-17
-16
-15
-14
-13
-12

for 16 kbar and 625 °C (Fig. 4.12a). These P-T values are consistent with the stability conditions of Grt-2b in Grand-metarodingites (blue-labelled fields in Fig. 4.11a), which form boudins partially transformed into Ep-metarodingite in the Atg-serpentinite domain (Fig. 4.2d). Fields labelled in red and yellow in Fig. 4.12a match very well the assemblages of Grand- (Grt-2b-Chl-Ttn) and Ep- (Ep-Cpx-Ttn-Grt-3) metarodingites, respectively. The predicted garnet compositions, indicated by isopleths (Grs_{65} Adr_{25} $Pyrals_{10}$ for Grt-2b, and Grs_{50-60} Adr_{33} $Pyrals_{10-20}$ for Grt-3), are also consistent with those of the rocks (Fig. 4.6). Transformation from Grand- to Ep-metarodingites was thus enhanced by decreasing μCaO (-708 to -725 kJ/mol) and increasing μSiO_2 (-884 to -860 kJ/mol) values. Moreover, the bulk-rock composition predicted for Ep-metarodingite at the stability conditions marked by the yellow star in Fig. 4.12a (i.e., those corresponding to the observed composition of Grt-3) compares very well with the composition of a real Ep-metarodingite (sample Al14-17; Table 4.3) from the Atg-serpentinite domain.

The possible influence of fO_2 in the stability of Ep-metarodingite assemblages is represented in an isobaric T vs fO_2 pseudosection (Fig. 4.12b) for the bulk composition of sample Al14-17 (Table 4.3). Because Ep-metarodingite bodies with identical mineral assemblages occur both in Atg-serpentinite and Chl-harzburgite domains, the pressure for modelling (16 kbar) was chosen in agreement with the minimum pressure at which the assemblages of both Atg-serpentinite and Chl-harzburgite equilibrated (Padrón-Navarta et al., 2012). In Ep-metarodingite, the stability conditions of the assemblage Ep + Cpx + Ttn + Grt (in yellow; Fig. 4.12b) spans from 475 to 700 °C for a wide range of $\log fO_2$ between -20 and -13.2, equivalent to MH ranging from -2 to -1. Within this field, isopleths indicate that Grt-4 (Fig. 4.6) with composition Grs_{50-55} Adr_{15-20} $Pyrals_{25-30}$ is stable at > 650 °C and $\log fO_2 = -15$ to -13 (yellow star in Fig. 4.12b). Modal proportions within this field (32-42 vol.% epidote, 47-53 vol.% clinopyroxene, 2 vol.% garnet, 4 vol.% titanite) also match those of Type 2 Ep-metarodingite. These results demonstrate that Grt-4-bearing assemblages in Ep-metarodingite formed at temperatures within the Chl-harzburgite stability field and beyond Atg breakdown in serpentinite.

4.2.5.3 Pyralspite-metarodingite

Phase relations show that neither Grt-5 nor tremolite-rich amphibole, both typical of Pyrals-metarodingite, are stable at conditions modelled in the pseudosection of Fig. 4.12b. The compositional differences between Type 2 and Type 3 metarodingites (Fig. 4.9a) and metamorphic reactions (10), (11), and (12) support that the chemical potentials of MgO (μMgO) and CaO (μCaO) were independent thermodynamic variables, jointly with P, T and fO_2, during the transformation of Ep-metarodingite into Pyrals-metarodingite. Another important observation is that a significant chemical transfer between the metarodingites and the ultramafic host is indeed observed in the complex sequence of the metasomatic reaction rims that equally attest for spatial (and temporal) variations in μMgO and μCaO. This variation in chemical potentials along cm- to m-scale reflects the time-dependent (diffusional) process of reequilibration between the two contrasting bulk chemical compositions (mafic and ultramafic in origin) induced by fluid-mediated dissolution-precipitation processes. This process allows the relaxation of the initial stepped chemical potential gradients by effective chemical diffusion (by advection in the aqueous fluid) thus justifying the use of μMgO and μCaO as independent thermodynamic variables.

We thus calculated a μMgO-μCaO pseudosection (Fig. 4.13a) for the Ep-metarodingite bulk composition corresponding to the yellow star in Fig. 4.12b, i.e., at 16 kbar and 660 °C, (i.e., well within the stability field of Chl-harzburgite), log $fO_2 = -14.5$ and H_2O saturation conditions. Fields labelled in yellow and blue colours match very well the assemblages of Ep- (Ep + Cpx + Ttn + Grt) (hosted in Chl-harzburgite) and Pyrals- (Ep + Chl + Amp + Grt + Cpx + Rt) metarodingites, respectively (Fig. 4.13a). μCaO and μMgO values corresponding to the yellow star are those established by Perple_X for the stability conditions of Grt-4 (yellow star in Fig. 4.12b). The predicted garnet compositions (indicated by isopleths) in each field are also consistent with those of the corresponding rock type, and in particular with the decrease in the andradite and grossular end-members and increase of pyralspitic contents from Grt-4 (Grs_{35-52} Adr_{5-20} Prp_{6-23} Alm_{13-30} Sps_{3-10}) in Ep-metarodingite to Grt-5 (Grs_{17-35} Adr_{2-7} Prp_{10-30} Alm_{35-50} Sps_{1-10}) in Pyrals-metarodingite. Therefore, as indicated by the white arrow in Fig. 4.13a, the transformation from Type 2 into Type 3 metarodingites was enhanced by decreasing μCaO (-726 to -735 kJ/mol) and increasing μMgO (-630 to -626 kJ/mol). Additionally,

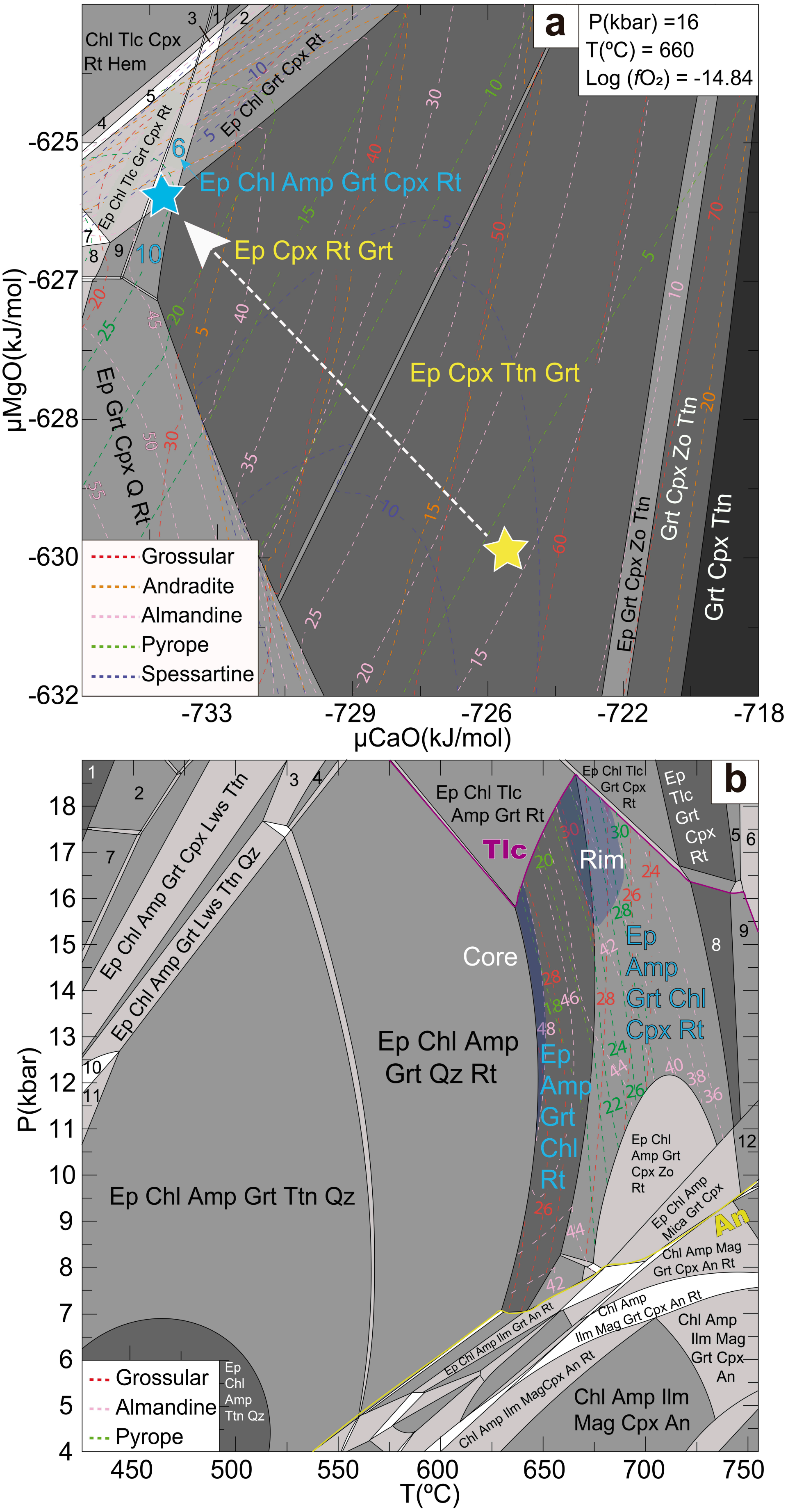
a
P(kbar) =16
T(ºC) = 660
Log (fO₂) = -14.84
Chl Tlc Cpx Rt Hem
Ep Chl Grt Cpx Rt
Ep Chl Tlc Grt Cpx Rt
Ep Chl Amp Grt Cpx Rt
Ep Cpx Rt Grt
Ep Cpx Ttn Grt
Ep Grt Cpx Q Rt
Ep Grt Cpx Zo Ttn
Grt Cpx Zo Ttn
Grt Cpx Ttn
Grossular
Andradite
Almandine
Pyrope
Spessartine
μMgO(kJ/mol)
μCaO(kJ/mol)
-625
-627
-628
-630
-632
-733
-729
-726
-722
-718
b
Ep Chl Amp Grt Cpx Lws Ttn
Ep Chl Amp Grt Lws Ttn Qz
Ep Chl Tlc Amp Grt Rt
Ep Chl Tlc Grt Cpx Rt
Ep Tlc Grt Cpx Rt
Tlc
Rim
Core
Ep Amp Grt Chl Cpx Rt
Ep Chl Amp Grt Qz Rt
Ep Amp Grt Chl Rt
Ep Chl Amp Grt Cpx Zo Rt
Ep Chl Amp Mica Grt Cpx
An
Chl Amp Mag Grt Cpx An Rt
Chl Amp Mag Grt Cpx An Rt
Chl Amp Ilm Mag Grt Cpx An
Ep Chl Amp Ilm Grt An Rt
Chl Amp Ilm Mag Grt Cpx An Rt
Chl Amp Ilm MagCpx An Rt
Chl Amp Ilm Mag Cpx An
Ep Chl Amp Grt Ttn Qz
Ep Chl Amp Ttn Qz
Grossular
Almandine
Pyrope
P(kbar)
T(ºC)
450
500
550
600
650
700
750

the predicted bulk-rock composition of Pyrals-metarodingite at the conditions marked by the blue star in Fig. 4.13a compares well with that of the Pyrals-metarodingite sample AL96-24B (Table 4.3). The only minor discrepancies in Al_2O_3 and MgO may be due to the incomplete removal of Chl-rich zones during the preparation of this sample.

Fig. 4.13b shows a P-T pseudosection for a representative Type 3 Pyrals-metarodingite (Al96-24B; Table 4.3). The mineral assemblages of Pyrals-metarodingite are stable at 635-740 °C and 7-18.5 kbar (blue labels in Fig. 4.13b). The main difference between the observed (Ep + Amp + Grt + Rt + Chl) and predicted (Ep + Amp + Grt + Rt + Chl + Cpx) mineral assemblages consists in the expected stability of Cpx (< 5 vol.%) at > 660 °C. Although not present in all Pyrals-metarodingites, relicts of diopside have been detected in some of these samples. On the other hand, zoisite is observed in the studied rocks but the model predicts that this phase is stable at lower pressures than those corresponding to the actual garnet compositions (Fig. 4.13b). However, the relative stability of epidote and zoisite is highly conditioned by slight shifts of oxygen fugacity, and we cannot exclude that the analysed Fe^{3+}/Fe_{Total} ratio used in calculations was affected by late amphibolitization.

Garnet isopleths constrain the conditions of formation of Grt-5 almandine-rich cores (Alm_{48-49} Prp_{17-18} Grs_{26-28}) in Type 3 Pyrals-metarodingites at 640-650 °C and 11-16 kbar

Figure 4.13. *Thermodynamic modelling using Perple_X for constraining the transition from Type 2 to Type 3 metarodingites and the stability conditions of Type 3 Pyrals-metarodingite.* ***(a)*** *μMgO-μCaO pseudosection at constant 16 kbar, 660°C and H_2O saturation conditions for the Ep-metarodingite bulk-rock composition and log fO_2 value estimated by Perple_X for the yellow star in Figure 4.12b (SiO_2 = 44.52; TiO_2 = 1.79; Al_2O_3 = 14.70; O_2 = 0.36; FeO = 6.70; MnO = 0.07 wt%). This model reproduces the transition from Ep-metarodingite (yellow-labelled assemblages) to Pyrals-metarodingite (blue-labelled assemblages). μCaO and μMgO values marked by the yellow star correspond to those of the yellow star in Figure 4.12b. At these conditions, the calculated garnet composition matches that of Grt-4 grains from Ep-metarodingites hosted in Chl-harzburgites with the lowest almandine, pyrope and the highest grossular contents. Change in garnet composition along the white arrow matches the observed compositional range of Grt-4 (Figure 4.6). Transition to the typical mineralogy of Pyrals-metarodingite (blue-labelled fields) and the stable Grt-5 composition (blue star) is enhanced by μCaO decrease and μMgO increase. The predicted bulk-rock composition at the blue star conditions (SiO_2 = 43.6; TiO_2 = 1.75; Al_2O_3 = 14.4; O_2 = 0.35; FeO = 6.56; MnO = 0.07; CaO = 17.80; MgO = 12.37; H_2O = 2.89 wt%) compares well with the analysed composition of a Pyrals-metarodingite from the Chl-harzburgite domain (sample AL96-24B; Table 4.3).* ***(b)*** *P–T pseudosection for Type 3 Pyralspite-metarodingite at H_2O saturation conditions (sample Al96-24B bulk-rock composition excluding Na_2O; Table 4.3). The blue-labelled assemblages are those observed in the rock. Garnet isopleths (dashed lines) constrain the stability conditions for the Grt-5 cores and rims (blue shaded areas). Peak P–T conditions were reached by rims at 660–684°C and 15.5–18.5 kbar. Stable assemblages in the numbered fields are shown in Table A12.*

(Fig. 4.13b), whereas pyrope-richer rims (Alm_{37-42} Prp_{22-30} Grs_{27-30}) formed at 660-684 °C and 15.5-18.5 kbar. The latter conditions set the peak pressure and temperature for the prograde evolution of metarodingites at Cerro del Almirez.

Precise oxygen fugacity conditions for Pyrals-metarodingite could not be independently determined. However, a log fO_2 value of -14.84 was assumed for the pseudoseccion of Fig. 4.13a after the stability conditions deduced for Ep-metarodingite in Chl-harzburgite (yellow star in Fig. 4.12b). At this log fO_2 value the stability conditions of the Pyrals-metarodingite assemblages can also be deduced (blue fields in Fig. 4.13a) and thus assume these oxygen fugacity conditions as valid for these rocks.

4.3 Discussion

The Cerro del Almirez metarodingites underwent a complex tectono-metamorphic evolution including peak metamorphism at eclogite-facies conditions. The deduced P-T path has been summarized in Fig. 4.14, in which the different transformation stages of metarodingites were superposed on a representative pseudosection for the enclosing serpentinites. Variation in the amount of H_2O coexisting with the serpentinite and Chl-harzburgite stable assemblages and their possible correlation with metamorphic changes in the hosted metarodingites are also shown (see discussion below).

4.3.1 Seafloor origin of rodingites

Rodingitic metastable assemblages are preserved in the less deformed Grand-metarodingites (Fig. 4.2a). Despite the lack of relicts of igneous rocks, an igneous mafic protolith of metarodingites is indicated by: i) preserved igneous porphyritic textures (Fig. 4.4a, c); ii) garnet pseudomorphs after plagioclase (Fig. 4.4a) (similar to those reported by Frost et al., 2008), of diopside (with exsolved inclusions of magnetite and ilmenite) after clinopyroxene (see also Ferrando et al., 2010), and of Chl + Di + Mag + Ilm after olivine (e.g., Früh-Green et al., 2003); and iii) the presence of Cr-rich magnetite, coexisting with Grt-1, possibly derived from igneous Cr-spinel.

Metarodingites in Cerro del Almirez are associated to Atg-serpentinites or their dehydration products, i.e., Chl-harzburgites (Fig. 4.1b). Rodingitization of igneous mafic rocks is always simultaneous with serpentinization of host peridotites (Coleman, 1963; O’Hanley, 1996). Rodingites are typically considered to form by Ca-metasomatism at low SiO_2 activities at the seafloor (Coleman, 1967; Frost, 1975; Schandl et al., 1990;

O'Hanley et al., 1992; Bach and Klein, 2009). The Cerro del Almirez ultramafic rocks were originally serpentinized at ~200 °C at the seafloor (Alt et al., 2012; Marchesi et al., 2013). Simultaneous rodingitization of mafic rocks is indicated by the low temperature (150-325 °C) and low pressure (2 kbar) calculated for the stability of the most primitive assemblage preserved in Grand-metarodingite (Grt-1 + Chl + Cpx + Mag + Ilm, Fig. 4.10b). Indeed, the assemblage Hgr + Clc + Di is typical of current seafloor rodingites (Früh-Green et al., 1996, Frost et al., 2008). Moreover, these P-T conditions are similar to those estimated by O'Hanley et al. (1992) (~ 300 °C, < 800 bar) and Frost et al. (2008) (~350 °C, 0.4-1 kbar) for modern rodingitization at the seafloor, and with those calculated by Bach and Klein (2009) (200-300 °C at 500 bar) for gabbro rodingitization by fluids related to serpentinization of host peridotites. Furthermore, the amounts of garnet (63-65 wt.%), chlorite (18-23 wt.%) and clinopyroxene (6-18 wt.%) calculated for rodingites formed at 300 °C (Bach and Klein, 2009; their Fig. 10) match our results at 100-325 °C (Fig. 4.11b, green-labelled field): 64-70 wt.% garnet, 18-19 wt.% chlorite, and 6-8 wt.% diopside. Moreover, when the latter data are expressed as volume % (61-65 vol.% garnet, 20-24 vol.% chlorite, 6-9.5 vol.% diopside) they also match very well the observed modal amounts in Grand-metarodingite (Table 4.1): 66 vol.% garnet, 23 vol.% chlorite, 6.5 vol.% diopside.

The low log fO_2 calculated for the primitive rodingite assemblage (log fO_2 =-55 to -35, above FMQ ranging from -2 to +3, Fig. 4.11b) support that rodingitization occurred simultaneously with serpentinization at very reducing conditions (Charlou et al., 2002; Frost and Beard, 2007; Frost et al., 2008, Frost et al., 2013).The composition of Grt-1 (Grs_{64-84} Adr_{5-19} Prp_{0-1} Alm_{0-3} Sps_{0-1} Ti-Grt_{2-11} Kat_{1-5}) is similar to that of hydrogrossular garnet in seafloor rodingites, but with lower katoite amounts (13-16 mol.%) (Rossman and Aines, 1991; Frost et al., 2008). This depletion in water probably reflects the progressive dehydration of Grt-1 by reaction (2), and constitutes the first subduction-related compositional change in garnet after seafloor rodingitization.

Garnet similar to Grt-1 occurs in metarodingites equilibrated at sub-greenschist to greenschist facies (Schandl et al., 1989; O'Hanley et al., 1992; Mittwede and Schandl, 1992; Boev et al., 1999; Pomonis et al., 2008; Perraki et al., 2010; Tsikouras et al., 2013;

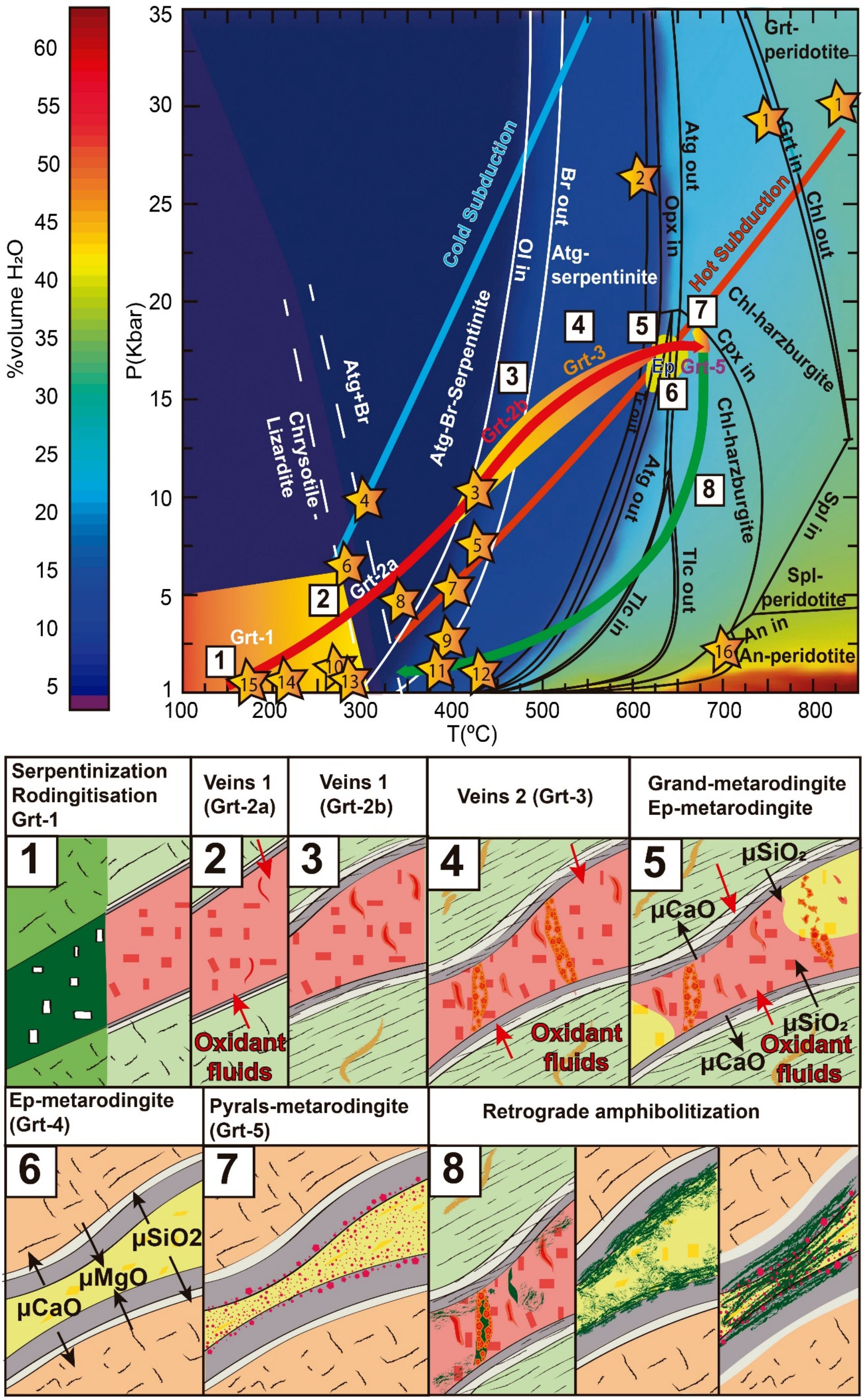
%volume H₂O
60
55
50
45
40
35
30
25
20
15
10
5
P(Kbar)
35
30
25
20
15
10
5
1
100
200
300
400
500
600
700
800
T(ºC)
Grt-peridotite
Grt in
Chl out
Hot Subduction
Cold Subduction
Br out
Ol in
Atg-serpentinite
Atg out
Opx in
Chl-harzburgite
Cpx in
Atg+Br
Chrysotile - Lizardite
Atg-Br-Serpentinite
Grt-3
Grt-2b
Grt-2a
Grt-1
Ep
Grt-5
Atg out
Tlc out
Tlc in
Spl in
Spl-peridotite
An in
An-peridotite
1
2
3
4
5
6
7
8
9
10
11
12
13
14
15
16
Serpentinization Rodingitisation Grt-1
Veins 1 (Grt-2a)
Veins 1 (Grt-2b)
Veins 2 (Grt-3)
Grand-metarodingite Ep-metarodingite
Oxidant fluids
μSiO₂
μCaO
Ep-metarodingite (Grt-4)
Pyrals-metarodingite (Grt-5)
Retrograde amphibolitization
μSiO2
μMgO
μCaO

Koutsovitis et al., 2013). It is also preserved in metarodingites that reached eclogite-facies conditions (Li et al., 2008; Ferrando et al., 2010; Crossley et al., 2017).

For the Cerro del Almirez metarodingites, complete rodingitization at the seafloor is supported by: i) the lack of relict igneous protoliths or intermediate assemblages in the inner parts of the bodies; and ii) the widespread occurrence of the rodingitic assemblage (Grt-1 + Chl + Cpx + Mag + Ilm) in Grand-metarodingite bodies.

4.3.2 Subduction evolution of metarodingites before the antigorite breakdown in host serpentinites

4.3.2.1 Type 1 Grandite-metarodingite

After rodingitization at the seafloor, mineralogical changes in metarodingites were mainly driven by subduction-related, prograde metamorphic reactions and by interaction with fluids derived from dehydration and redox reactions in the host Atg-serpentinite (Fig. 4.14; stages 2 to 4). From ~150 to 325 °C, depending on pressure, the early assemblage Grt-1 + Chl + Cpx + Mag + Ilm was stable at log fO_2 conditions corresponding to the FMQ-buffer, and andradite contents progressively increased in garnet (Fig. 4.11b). The maximum pressure of stability of Grt-1 cannot be precisely constrained but must be lower than 10 kbar, as supported by the higher amounts of

---

Figure 4.14. *Summary of the proposed P–T path for the Cerro del Almirez metarodingites superposed on a P–T pseudosection calculated for a representative Atg-serpentinite. Background colours (see chart) show increasing H_2O amounts released with temperature due to prograde dehydration reactions. The stability limits of chrysotile and lizardite are taken from Evans (2004). Numbers in the white squares mark the approximate formation conditions for the different garnet generations and metarodingite types shown in the sketch diagrams below:* ***1****: Rodingitization;* ***2****: Probable Grt-2a formation conditions during chrysotile-lizardite breakdown;* ***3****: Grt-2b formation;* ***4****: Grt-3 formation during brucite breakdown;* ***5****: Growth of Ep-metarodingite due to progressive Atg breakdown;* ***6****: Complete Ep-metarodingite transformation; 7: Growth of Grt-5 rim;* ***8****: Retrograde amphibolitization. Orange stars represent the estimated stability conditions of different rodingites and metarodingites in literature that are shown for comparison. 1: Cima di Gagnone (Cannaò et al., 2015; Evans and Trommsdorff, 1978; Evans et al., 1979), 2: Zermat Saas (Barnicoat and Fry, 1986; Ferrando et al., 2010; Li et al., 2004; Zanoni et al., 2016), 3: Meliatic Bôrka Nappe (Li et al., 2014), 4: Kamuikotan Tectonic Belt (Banno, 1986; Katoh and Niida, 1983), 5: Tianshan (Li et al., 2007), 6: Cape San Martín (Franciscan Complex; Coleman, 1967; Ernst, 2011; Terabayashi and Maruyama, 1998), 7: Val Malenco (Berger and Bousquet, 2008; Puschnig, 2002), 8 and 11: JM Asbestos mine (Normand and Williams-Jones, 2007), 9: Abitibi belt (Schandl et al., 1989), 10: Bou Azzer (Leblanc and Lbouabi, 1988), 12: Appalachian Piedmont (Mittwede and Schandl, 1992), 13: Cassiar (O'Hanley et al.,1992), 14 and 15: Mid Atlantic ridge (Frost et al., 2008; Honnorez and Kirst, 1975), 16: Paddy-Go-Easy Pass (Frost, 1975).*

pyralspite components calculated at this pressure (5-10 mol.%, blue isopleths in Fig. 4.11c) compared to those in Grt-1 (< 3 mol.% pyralspite).

In the first set of veins that cut Grand-metarodingites, scarce garnet grains occur (Grt-2a; Fig. 4.7a, b) with high andradite (24-20 mol.%) and low pyralspite (3-4 mol.%) contents (green dots in Fig. 4.6). Thermodynamic model predicts that similar andradite-rich compositions are stable at T > 300 °C and log fO_2 = -30 to -23, in between that of FMQ and MH (Fig. 4.11b), and coexist with phases (epidote and spinel) that are not observed in Grand-metarodingite. We thus suggest that Grt-2a crystallized during an episodic flux of oxidizing fluids that were not buffered by the metarodingite mineral assemblage. Therefore, Grt-2a was not in equilibrium with the bulk-rock composition and cannot be reproduced by thermodynamic models. Such oxidizing fluids may have been released by the transformation of lizardite to antigorite, concomitant with a decrease in the magnetite modal amount, at 300-325 °C (Debret et al., 2015) in host serpentinites. This process has been reported in several alpine serpentinite localities (Debret et al., 2014) and might be the reason for the ubiquitous formation of garnet similar to Grt-2a in low to medium grade metarodingite outcrops (Dubińska, 1995; Hatzipanagiotou and Tsikouras, 2001; Koutsovitis et al., 2013; Mittwede and Schandl, 1992).

Grt-2b is the main component of the first vein generation (Fig. 4.7a, b), and also occurs in chlorite-rich and diopside-poor domains of the matrix or as thin rims surrounding Grt-1. Grt-2b is calculated to be stable with chlorite and titanite at significantly higher temperature (560-675 °C) and pressure conditions (9-20 kbar) than Grt-1 (Fig. 4.11a). However, at oxygen fugacity above FMQ buffer, this assemblage can be stable at temperatures as low as 350 °C (Fig. 4.11c).

The change from the assemblage Grt-1 + Chl + Cpx + Mag + Ilm to the assemblage Grt-2b + Chl + Ttn reflects the simultaneous development of a set of prograde metamorphic reactions in Grand-metarodingites: Grt-1 partially broke down and dehydrated (reaction 2), reacted with magnetite (that almost disappeared) producing the almandine and andradite components of Grt-2b (reaction 3), and released Ti from the morimotoite component producing significant amounts of titanite (reaction 5). Reactions (1) and (5) consumed diopside and may thus explain its lack in the Grt-2b bearing domains of Grand-metarodingites.

The Grt-2b + Chl + Ttn were stable at higher log fO_2 conditions (between the FMQ and MH buffers) compared to Grt-1 bearing assemblages, probably owing to the release of water by reaction (2) (Fig. 4.11c). In this diagram vesuvianite is expected to be stable at buffered FMQ conditions and temperatures above 550 °C. This might explain the presence of this phase in other metarodingites equilibrated at high temperature and pressure (e.g., Li et al., 2004, 2008; Zanoni et al., 2016). In the case of metarodingites from Cerro del Almirez, log fO_2 remained buffered at higher values by the rock mineral assemblage, as evidenced by the parallel orientation of the assemblage stability fields to the oxygen buffers (Fig. 4.11c).

Granditic garnet with significant pyralspite contents, as is the case of Grt-2b (up to 16 mol.%), has been reported in other high-pressure metarodingites (Evans et al., 1979; Ferrando et al., 2010, their Type II and Type IV veins; Crossley et al., 2017). Isopleths from Fig. 4.11a demonstrate that the amount of the garnet pyralspite component in the metarodingite system increases with pressure and temperature, allowing the stability conditions of the Grt-2b-bearing assemblage to be constrained.

Grt-3 is the main component of the second vein generation and also rims previous garnets (Fig. 4.7a, b). Grt-3 composition cannot be reproduced in the P-T pseudosection from Fig. 4.10a suggesting that it was not buffered by the mineral assemblage but from external fluids that induced changes in oxygen fugacity. However, T-log fO_2 calculations are not precise enough in constraining the conditions of Grt-3 formation (Fig. 4.11c). As textural relationships indicate that Grt-3 formed after Grt-2b, the minimum pressure of its stabilization can be fixed at 10 kbar. Considering the garnet isopleths and the limiting stability of rutile, the temperature of Grt-3 crystallization was > 525 °C at log $fO_2 > -19$, over and above that of MH (Fig. 4.11c, yellow labelled fields). At these conditions, the thermodynamic model predicts the presence of small amounts of coexisting epidote that are also observed in some veins.

High fO_2 conditions during the formation of Grt-3 were possibly induced by the release of oxidizing fluids due to magnetite destabilization during brucite breakdown in host serpentinite or even during the progressive decrease in the antigorite amount in serpentinites between 550 and 650 °C, at 20 kbar, as observed in experimental determinations (Merkulova et al., 2016; 2017). In the Cerro del Almirez Atg-serpentinites, brucite breakdown occurred at 10 kbar and ~475 °C (López-Sánchez-Vizcaíno et al., 2005, 2009; Padrón-Navarta et al., 2012). Accordingly, Grt-3 veins might have formed in a wide temperature range between ~475 and 625 °C in Grand-metarodingite (Fig. 4.14; stage 4). Discrepancy with the mineral assemblages in Fig. 4.11c can be explained by the lack of complete thermodynamic equilibrium between the metarodingite mineral assemblages and the external oxidizing fluids that fluxed through them.

Andradite-rich garnet similar to Grt-3 is reported by Li et al. (2004, 2008) and Ferrando et al. (2010; their veins V). In the former case, a distinct and continuous change in fO_2 is invoked that progressed from ocean-floor metamorphism to initial burial and then subduction (Li et al., 2004).

Thin veinlets with Grt-2b composition cut Grt-3 veins (white stars in Fig. 4.7a, b) and they may record the stop in the percolation of oxidizing fluids and the restoration of fO_2 conditions buffered by the rock mineral assemblage. Alternation of andradite-rich (equivalent to our Grt-3) and andradite-poor (equivalent to our Grt-2b) garnet generations is also described by Ferrando et al (2010) but they did not explore the potential reasons for it.

Grt-3 with the highest andradite contents (up to 53 mol.%) is also in equilibrium within Ep-metarodingites close to the Atg-serpentinite dehydration front. This indicates that oxidizing conditions finally stabilized at $\log fO_2 > -20$, over and above that of MH (Fig. 4.12b) at P-T conditions close to those of Atg breakdown (~650 °C and 16-19 kbar, Padrón-Navarta et al., 2012).

4.3.2.2 Grandite- to Epidote-metarodingite transformation

The formation of Ep-metarodingite after Grand-metarodingite at Cerro del Almirez was the result of the growth of epidote after the hydration (reaction 6) and oxidation (reaction 7) of grandite garnet, and of the growth of diopside after chlorite breakdown (reaction 8). This partial or total transformation was driven by the increase of μSiO_2 and the drop of μCaO at H_2O-saturated and high fO_2 conditions (Fig. 4.12a). The gradients of chemical potentials during metamorphism were controlled by the strong compositional differences between the CaO-rich Grand-metarodingites and their MgO- and SiO_2-richer host rocks, including the diopside-bearing metasomatic rims. The extent of transformation of Grand-metarodingite bodies within the Atg-serpentinite domain is very variable. In most cases transformation was only incipient (Fig. 4.2a). At the thin section scale, millimetre to centimetre square-sized domains can be found that display the complete transition between the garnet-bearing assemblages and those consisting of epidote-diopside-titanite and minor amounts of Grt-3 (Fig. 4.15), as reproduced by the path (white arrow) in the calculated pseudosection from Fig. 4.12a.

Transformation to homogeneous Ep-metarodingite is well developed only in some boudins close to the dehydration front (Fig. 4.2d), thus indicating that in this region the physicochemical conditions were more favourable to the change. In this case, mineral modes indicate that reactions (6), (7) and (8) completely consumed garnet and chlorite. During garnet destabilization, mobile components CaO and SiO_2 were released by reaction (6) and consumed by reaction (7). However, grandite components (involved in reaction 6) in Grt-1, -2b and -3 were much more abundant than almandine (involved in reaction 7) and, thus, the global balance of garnet breakdown resulted in the release of CaO and SiO_2. Due to the higher abundance of garnet compared to chlorite in Grand-metarodingite (66 and 23 vol.%, respectively) the amount of these two mobile components contributed to the simultaneous chlorite destabilization through the CaO- (19 moles per 3 moles of consumed chlorite) and, especially, SiO_2-consuming (27 moles per

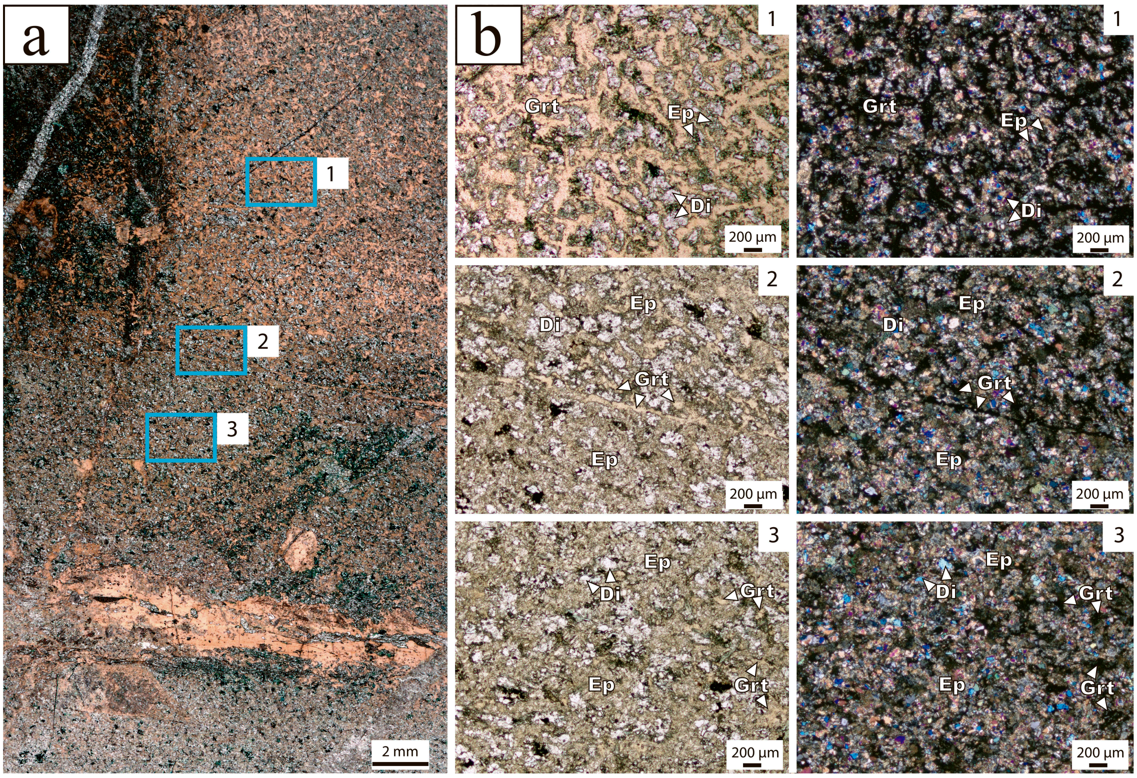

Figure 4.15. *Transition at the thin section scale between Grand– and Ep-metarodingite.* ***(a)*** *Scanned image of a complete thin section showing the "patchy" distribution of this transformation and the preservation of a relict garnet vein in the lower part. Dark green areas are rich in late amphibole. The location of micrographs from b are outlined in blue colour.* ***(b)*** *Micrographs of selected areas (with parallel and crossed polars: left and right images, respectively) showing the complete transition from garnet-rich zones, with only incipient transformation into green microaggregates of epidote* ***(1)****, to zones progressively richer in epidote and diopside* ***(2)*** *and the final transformation* ***(3)*** *to the typical assemblage of Ep-metarodingite with only rare garnet relicts. Chlorite is lacking in every zone.*

3 moles of chlorite) reaction (8). The net balance of Grand- to Ep-metarodingite transformation was CaO liberation and SiO_2 absorption (Fig. 4.9a and 4.12a). Released CaO most probably diffused towards the borders of the metarodingite bodies, and contributed to the growth of Chl-Di- and Chl-Di-Ol-metasomatic rims. These reaction rims are clearly thicker in the boudins with well-developed Ep-metarodingite zones (Fig. 4.2b) than around poorly transformed Grand-metarodingites (Fig. 4.2a). On the contrary, silica consumed during the formation of Ep-metarodingite likely diffused from the SiO_2-rich wall rocks to the metarodingite bodies.

Element diffusion and chemical potential gradients are clearly enhanced by the presence of a free fluid in the rocks (e.g., Gasc et al., 2016). However, water amounts released by chlorite breakdown through reaction (8) were not sufficient for inducing fluid saturation required by thermodynamic model (Fig. 4.12), as evidenced by the preservation of grandite garnet in rock domains in which chlorite has been already transformed to diopside (Fig. 4.15). Thus, an additional external fluid released from host Atg-serpentinite must be invoked to favor element diffusion in metarodingites. The higher abundance of Ep-metarodingite close to the dehydration front is in agreement with a higher concentration of fluids in these areas.

Two possible mechanisms of fluid production in serpentinites that did not reach the conditions of antigorite breakdown (~16-19 kbar, 650 °C) are the OH-titanian clinohumite breakdown reaction (López-Sánchez-Vizcaíno et al., 2005, 2009, and references therein) and the antigorite consuming dioposide-out, tremolite-in reaction (Trommsdorff and Evans, 1974). Considering the very low abundance of Ti-Chu compared to antigorite and diopside, the latter reaction was much more relevant in the Cerro del Almirez serpentinite (Jabaloy-Sánchez et al., 2015; López-Sánchez-Vizcaíno et al., 2009). Both reactions, nevertheless, were almost simultaneous at well-known pressure and temperature ranges (16-19 kbar and 620-630 °C; López-Sánchez-Vizcaíno et al., 2009; Padrón-Navarta et al., 2012), thus constraining the onset of transformation of Grand-metarodingite into Ep-metarodingite at these conditions (Fig. 4.14; stage 5). Experimental determinations by Merkulova et al. (2017) also agree with a progressive decrease in the antigorite amount in serpentinites between 550 and 650 °C at 20 kbar accompanied by a progressive loose of H_2O.

The irregular distribution of Ep-metarodingites in the Atg-serpentinite domain and their higher abundance close to the dehydration front attest to a very irregular flux pattern of fluids within metarodingites. Even in the case of the most transformed boudins, the distribution of Ep-metarodingite lacks a well-defined development pattern (e.g., from rims to core) suggesting that the transformation into Ep-metarodingite progressed only in the boudin volume that attained fluid saturation.

The calculated prevailing oxidized conditions for the formation of Ep-metarodingites (Fig. 4.12b) and their generally higher Fe^{3+}/Fe_{Total} compared to Grand-metarodingites (Fig. 4.9b) might be due to the combined effects of oxidizing reaction (7) and oxidizing external fluids that fluxed through metarodingites. Calculations of Debret and Sverjensky (2017) point to high oxygen fugacity and high amounts of dissolved sulfates in fluids released from dehydrating serpentinites at the onset of tremolite formation and magnetite consumption (> 630 °C, 20 kbar). Oxygen release during progressive, and simultaneous, breakdown of antigorite and magnetite at similar P-T conditions was also reported in experiments (Merkulova et al., 2017). Formation of Ep-metarodingites from the Atg-serpentinite domain at oxidizing conditions also accounts for the composition of Grt-3 in these rocks, which has the highest andradite contents of any garnet type in the Cerro del Almirez metarodingites (dark yellow triangles in Fig. 4.6).

4.3.3 Evolution of metarodingites during and after serpentinite dehydration

4.3.3.1 Type 2 Epidote-metarodingite

Beyond the dehydration front, that is, within the Chl-harzburgite domain, all the metarodingite bodies are transformed into Ep-metarodingite, and Grand-metarodingite only occurs as scarce relicts in the core of some boudins. This supports the hypothesis that flux of high amounts (~9 wt.% H_2O; Padrón-Navarta et al., 2010b) of oxidizing fluids (Debret and Sverjensky, 2017; Debret et al., 2015; Merkulova et al., 2017) released during Atg-breakdown in serpentinite favored the transformation of Grand-metarodingite into Ep-metarodingite (Fig. 4.14, stage 6).

However, Ep-metarodingites in the Atg-serpentinite and Chl-harzburgite domains show significant mineralogical and compositional differences, in particular the presence in the latter of (i) a new generation of progressively pyralspite-richer garnet (Grt-4) (Fig. 4.6) in equilibrium with epidote-diopside-titanite and (ii) a generally lower bulk Fe^{3+}/Fe_{Total} ratio (Fig. 4.9b). Grt-4 formed by re-equilibrium of relict Grt-2b and Grt-3 grains, as evidenced by their higher pyralspite contents, which increase towards the borders, and the common precipitation of idiomorphic rims. H_2O saturation conditions and increasing temperatures facilitated this re-equilibrium (Ague and Carlson, 2013), as well as the large reactive surface of the grains owing to their small size and irregular shape. Equilibrium conditions of Grt-4 have been calculated at 16 kbar, 670 °C, log fO_2 = -14.5 and H_2O-saturated conditions (yellow star in Fig. 4.12b), well within the stability field of Chl-harzburgite. This log fO_2 value matches the estimations of Debret et al. (2015) for the host Chl-harzburgite.

Due to the strong compositional differences between metarodingites and their host ultramafic rocks, chemical potential gradients of CaO and MgO were the driving forces of the change of Grt-4 composition towards pyralspite-rich contents (as indicated by the values of garnet isopleths along the white arrow in Fig. 4.13a). Direction of μMgO gradient was opposite to that of μCaO (Fig. 4.14, stage 6) and was probably responsible for the observed stabilization of chlorite-richer zones around metarodingite boudins (Li et al., 2004), but this effect was not evident in their cores. This only happened when the boudins were small enough, as is the case of the Ep-metarodingites hosted by Chl-harzburgite.

4.3.3.2 Epidote- to Pyralspite-metarodingite transformation

With increasing temperature, keeping of the μCaO and μMgO gradients at H_2O saturation conditions favored the transformation of Ep-metarodingite into Type 3 Pyrasl-metarodingite (blue fields in Fig. 4.13a) in some small boudins of the Chl-harzburgite domain (Fig. 4.2f).

This transformation occurred through epidote-consuming reactions (10) and (11), which respectively account for the pyrope and almandine components in the crystallization of Grt-5. However, (11) is a reducing reaction. The driving force of this reduction might have been the strong gradient in the oxygen quantity (nO_2; Evans, 2006; Tumiati et al., 2015) between Ep-metarodingite and host Chl-harzburgites, as revealed by the sharp difference in their Fe^{3+}/Fe_{Total} ratios: ~0.8 and 0.25-0.5, respectively (Fig. 4.9b). These low values in Chl-harzburgite can be explained by the strong drop in Fe^{3+}/Fe_{Total} ratio produced during the transformation of Atg-serpentinite (0.63-0.74) into Chl-harzburgite owing to the very significant reduction of Fe^{3+} hosted in both magnetite and antigorite during dehydration (Debret et al., 2015). The subsequent transformation of Ep-metarondigite into Pyrals-metarodingite caused the progressive change of the Fe^{3+}/Fe_{Total} ratio in metarodingites, which finally re-equilibrated at values (0.38-0.35) within the range of Chl-harzburgites (Fig. 4.9b). On the other hand, increasing μMgO and decreasing μCaO (Fig. 4.13a) also triggered the crystallization of tremolitic amphibole (Amp-1) in Pyrals-metarodingite by diopside-consuming reaction (12).

Despite significant changes in μMgO, μCaO and Fe^{3+}/Fe_{Total}, thermodynamic equilibrium was reached in Pyrals-metarodingite as evidenced by the good agreement between the modelled stable assemblages, modal amounts and mineral chemistry (Fig. 4.13b) and those observed in rocks. The estimated P-T conditions calculated for the almandine-rich cores of Grt-5 (11-16 kbar, 640-650 °C), and especially their pyrope-rich rims (15.5-18.5 kbar, 660-684 °C) (Fig. 4.13b), mark the peak metamorphic conditions of metarodingites. The latter compare very well with independent P-T determinations for host Chl-harzburgites (16-19 kbar, < 710 °C, López-Sánchez-Vizcaíno et al., 2005, 2009; Padrón-Navarta et al., 2010a) and for some ophicarbonate lenses hosted within these same rocks (18 kbar, 650-670 °C; Menzel et al., 2019).

Metarodingites from Cima di Gagnone in Central Alps are also hosted in Chl-harzburgite formed after serpentinite dehydration (Evans and Trommsdorff, 1978). Similar to the Cerro del Almirez Pyrals-metarodingites, they are rich in epidote (up to 25 vol.%), in garnet with composition close to that of Grt-5, and have very similar bulk compositions except for lower Al_2O_3 contents (Evans et al, 1981). All these features support a comparable, subduction-related metamorphic evolution for these two metarodingite suites.

The only previous study of the Cerro del Almirez metarodingites (Puga et al., 1999) used a completely different terminology that is not sustained by our study. According to these authors, only the here-called Grand-metarodingites can be considered as pure metarodingites and all other types are referred to as “eclorodingites”, that is, rocks with “transitional parageneses from rodingites to eclogites”, attributed to metamorphism of protoliths, which underwent different degrees of oceanic metasomatism and Na_2O loss. As discussed, all our results support a very different interpretation: (i) complete seafloor rodingitization affected the mafic protoliths of the Cerro del Almirez metarodingites (section 4.3.1); (ii) all their mineralogical and bulk compositional changes took place during subduction metamorphism; and (iii) all Na_2O present in some rocks was clearly gained during retrograde amphibolitization (see below).

4.3.3.3 Retrograde amphibolitization

The mineral assemblages of all metarodingite types from Cerro del Almirez were partially replaced by late Na-bearing Ca-amphiboles corresponding to the above-defined Amp-2 (Fig. 4.2e, f and 4.8). Textural relationships and low bulk Na_2O contents of Grand-metarodingites (Table 4.3) indicate that amphibolitization was caused by percolation of external alkalis-rich fluids. The very low abundances of Na_2O and K_2O in both Atg-serpentinite and Chl-harzburgite (Garrido et al., 2005) support that these fluids were probably released from metasediments that host the Cerro del Almirez ultramafic complex (Fig. 4.1a). According to Jabaloy-Sánchez et al. (2015) the Cerro del Almirez ultramafic massif and their host metasediments were coupled after the peak of metamorphism and underwent a common tectonometamorphic evolution during exhumation. The retrograde origin of amphibolitization is also in agreement with textural relationships in Pyrals-metarodingites, in which Amp-2 crystallization occurred after that of Amp-1, which in turn marks the peak metamorphic conditions in equilibrium with Grt-5.

4.3.4 The role of metarodingites in the redox state of subduction zones

Serpentinites and metarodingites are coupled in exhumed metamorphic terrains owing to their simultaneous formation and paired evolution during subduction. Nevertheless, the significance of metarodingites for the petrological and geochemical processes that take place in subduction zones has been usually disregarded. Increasing attention has been recently devoted to the presence of relatively oxidized materials in subduction zones and their role on deep element cycling (e.g., Evans and Powell, 2015; Malaspina et al., 2017; Tumiati et al., 2015). Oxidizing agents may be transported into the sub-arc mantle by metamorphic fluids produced by devolatilization of the subducting slab (Evans, 2012). The oxidizing capacity of these fluids relative to a reference state (the redox budget; Evans, 2006) is of great importance for the composition of arc magmatism and arc-related ore deposits (Evans and Powell, 2015 and references therein). The role of dehydration reactions in serpentinite for the redox state of subduction zones has been well studied (Debret and Sverjensky, 2017; Debret et al., 2014, 2015; Merkulova et al., 2017). These studies emphasize the importance of fluids released from serpentinites as oxidizing agents of adjacent slab lithologies (mostly anhydrous mantle peridotites) at the meter scale.

However, metarodingites have been rarely considered in the studies of fluid-rock interactions in subduction zones (Crossley et al., 2017).

The metarodingites from the Cerro del Almirez ultramafic complex are an illustrative and unique case study of the subduction evolution of igneous mafic rocks originally rodingitized at the seafloor. Their mineralogical, textural and compositional features, generally reproduced by the thermodynamic models presented in this work (Fig. 4.11, 4.12 and 4.13), reveal that metarodingites were affected by the main dehydration and redox reactions that occurred in their host serpentinite.

Higher Fe^{3+}/Fe_{Total} ratios in Ep- than in Grand-metarodingites (Fig. 4.9b) indicate that metarodingites oxidized during dehydration of host serpentinites up to Atg-breakdown. Thus, metarodingite bodies enclosed in Atg-serpentinites, and in their reaction product Chl-harzburgites, acted as sinks of oxidizing fluids travelling from dehydrating serpentinites to the inner mantle wedge. Subsequent transformation into Pyrals-metarodingite strongly decreased Fe^{3+}/Fe_{Total}, which reached values in equilibrium with the host Chl-harzburgite (Fig. 4.9b). Therefore, the transformation of Ep-metarodingite into Pyrals-metarodingite further released oxidizing fluids at temperatures ~40 °C higher than those corresponding to Atg-breakdown (Fig. 4.14; stage 7).

However, field observations in Cerro del Almirez show that Type-3 Pyrals-metarodingites are scarce, and so significant volumes of Fe^{3+}-rich metarodingite boudins (Type-1 and Type-2) were metastably preserved within the Chl-harzburgite domain far beyond the antigorite dehydration front (Fig. 4.1b). The kinetic limitation for reequilibration can be explained by the strong rheology (dominated by garnet, e.g., Karato et al., 1995) and the intrinsically low permeability (e.g., Katayama et al., 2012) of metarodingites. Similar preservation of metastable metarodingite bodies is reported also at Cima di Gagnone (Evans et al., 1979). This suggests that Fe^{3+}-rich, metastable metarodingites can be transported to the deep mantle through subduction, and their recycling into the asthenosphere may affect the oxidation state of the deep Earth

5 Geochemical evolution of rodingites from seafloor formation to subduction dehydration of enclosing serpentinites

5.1 Introduction

Rodingites are the product of hydrothermal alteration of mafic to felsic rocks, usually gabbroic and basaltic rocks, induced by reactive fluids from enclosing peridotites being serpentinized (Coleman, 1967). Rodingites are thus commonly in close association with serpentinites formed at slow mid-ocean ridges (e.g., Frost et al., 2008; Früh-Green et al., 2017), continental passive margins (Beard et al., 2002), or in subduction zones (Koutsovitis et al., 2013; Li et al., 2004, 2007). Serpentinites and rodingites are less common at fast spreading centres, where hydrothermal alteration mostly affects thick oceanic crust (Bosch et al., 2004) that hinders the penetration of seawater-derived fluids to deeper mantle peridotites. During rodingitization, the primary mineral assemblage of mafic intrusions is mainly replaced by Ca-Al silicates (grossular/hydrogrossular, prehnite, zoisite, vesuvianite), Ca-Mg silicates (diopside, tremolite) and chlorite through metasomatic reactions promoted by highly reducing fluids (e.g., Bach and Klein, 2009; Frost and Beard, 2007). In subduction zones, dehydration of differently altered oceanic lithosphere, which may include serpentinites and rodingites, releases a significant amount of fluids to the supra-subduction mantle wedge, triggering partial melting and generation of arc magmas (e.g., Hacker et al., 2003; Rüpke et al., 2004; van Keken et al., 2011). Slab fluids commonly transfer the geochemical imprint of subducted lithologies to the sub-arc mantle, causing for instance the enrichment of large-ion lithophile elements (LILE: K, Cs, Rb, Ba, Sr) and Pb in subduction-related lavas compared to mid-ocean ridge basalts (MORB) (e.g., Kelemen et al., 2014), and Mg-Ca-Si metasomatism in the mantle wedge (Ishimaru and Arai, 2011).

The study of the geochemistry of high-pressure metamorphic rocks (metasediments, metamafic and metaultramafic rocks, and hybrid lithologies in mélanges) can contribute to constrain the slab component added to arc magma sources, as chemical processing during subduction influences the element budget and isotopic composition of slab fluids and melts (e.g., Bebout, 2014). Petrological and geochemical studies of element mobility in subducted mafic rocks usually consider starting MORB-like compositions with variable H_2O-CO_2 contents that evolve to blueschist and eclogite mineral assemblages (e.g., Marschall et al., 2006; Schmidt and Poli, 2014; Spandler and Pirard, 2013; Zack et al., 2002). Conversely, the compositional and mineralogical changes undergone by subducting oceanic rodingites, which are notably richer in Ca and poorer in Si, Na, and K than MORB (e.g., Bach and Klein, 2009; Frost and Beard, 2007), are often disregarded in global geochemical balances despite their possible contribution to mass exchanges in subduction zones and to the geochemical signature of arc magmas. Moreover, metasomatic reactions between metarodingite layers and enclosing ultramafic rocks may contribute to the lithological and compositional heterogeneity of subduction mélanges, which may produce fluids with many of the geochemical features of subduction-related lavas (e.g., Bebout and Barton, 2002).

In this work, we examine the geochemical imprints that seafloor rodingitization, subduction metamorphism and exhumation imposed to the compositions of metarodingites from the Cerro del Almirez ultramafic massif (Betic Cordillera, southern Spain) in terms of major, lithophile and strongly chalcophile trace elements (Re and platinum-group elements, PGE: Os, Ir, Ru, Pt and Pd). This massif preserves an exceptional record of antigorite (Atg) breakdown in subducted serpentinites (Padrón-Navarta et al., 2011; Trommsdorff et al., 1998), which is the most important devolatilization reaction that occurs at intermediate depths in subduction zones (Ulmer and Trommsdorff, 1995). The Almirez metarodingites are enclosed in both Atg-serpentinites and partially dehydrated chlorite (Chl)-harzburgites, and have mineral assemblages that record oceanic rodingitization, prograde metamorphism and interaction with fluids during exhumation (cf. Chapter 4). Therefore, these rocks represent a unique opportunity to constrain the impact of metarodingites on the geochemical signature of fluids derived from subducted serpentinites, including the fluid budget of chalcophile metals that may favour the generation of economic ore deposits (McInnes et al., 1999). We present whole-rock and mineral compositional data of metarodingites, their enclosing ultramafic rocks, and the transitional metasomatic rims located between these two rock-types. Based on these data, we obtain new insights into compositional changes during rodingitization, subduction and exhumation of rodingites, and into element transfer at different scales in the dehydrating subducted lithosphere, at the slab-mantle interface and to the deep Earth.

5.2 Sampling

For this study, we selected 69 samples of 16 metarodingite outcrops that represent the lithological variability of the Cerro del Almirez metarodingite-ultramafic rock suites. In each outcrop, we sampled one metarodingite, its metasomatic reaction rims, one ultramafic rock in contact or close to (< 20 cm apart) the metasomatic rims and one ultramafic rock 2-3 m apart from them. Chapter 4 presents a detailed description of the field occurrence, mineral assemblages, microstructures and mineral chemistry of the different types of metarodingites and metasomatic reaction rims from Cerro del Almirez. Full details on the mineralogical and petrographic features and major element compositions of minerals of the host ultramafic rocks can be found in Padrón-Navarta et al. (2011) (cf. Chapter 1).

Twenty samples selected for analyses of lithophile elements are metarodingites (8 Grandite (Grand)-metarodingites, 10 Epidote (Ep)-metarodingites and 2 Pyralspite (Pyrals)-metarodingites) with different degrees of amphibolitization, and 20 are metasomatic reaction rims (14 Chl-blackwalls, 3 Chl-Di- and 3 Chl-Ol-Di-metasomatic rims). Samples of host ultramafic rocks (close or far from the metasomatic rims) are 10 Atg-serpentinites, 4 transitional rocks from the Atg dehydration front (1 Chl-serpentinite and 3 Atg-Chl-Opx-Ol rocks) and 15 Chl-harzburgites. Whole-rock analyses of PGE-Re abundances and Os isotopes were performed in a representative subset of samples (2 Grand-metarodingites, 4 Ep-metarodingites, 1 Pyrals-metarodingite, 5 Chl-blackwalls, 1 Chl-Di- and 2 Chl-Ol-Di-metasomatic rims, 3 Atg-serpentinites, and 6 Chl-harzburgites).

5.3 Results

5.3.1 Whole-rock major elements

5.3.1.1 Metarodingites

There are significant differences between the major element compositions of the metarodingite types from Cerro del Almirez, especially in terms of CaO and SiO_2. Type 1 Grand-metarodingites have the highest CaO and commonly the lowest SiO_2 contents (Fig. 5.1a, Table A13). These compositions are similar to those of rodingites rich in

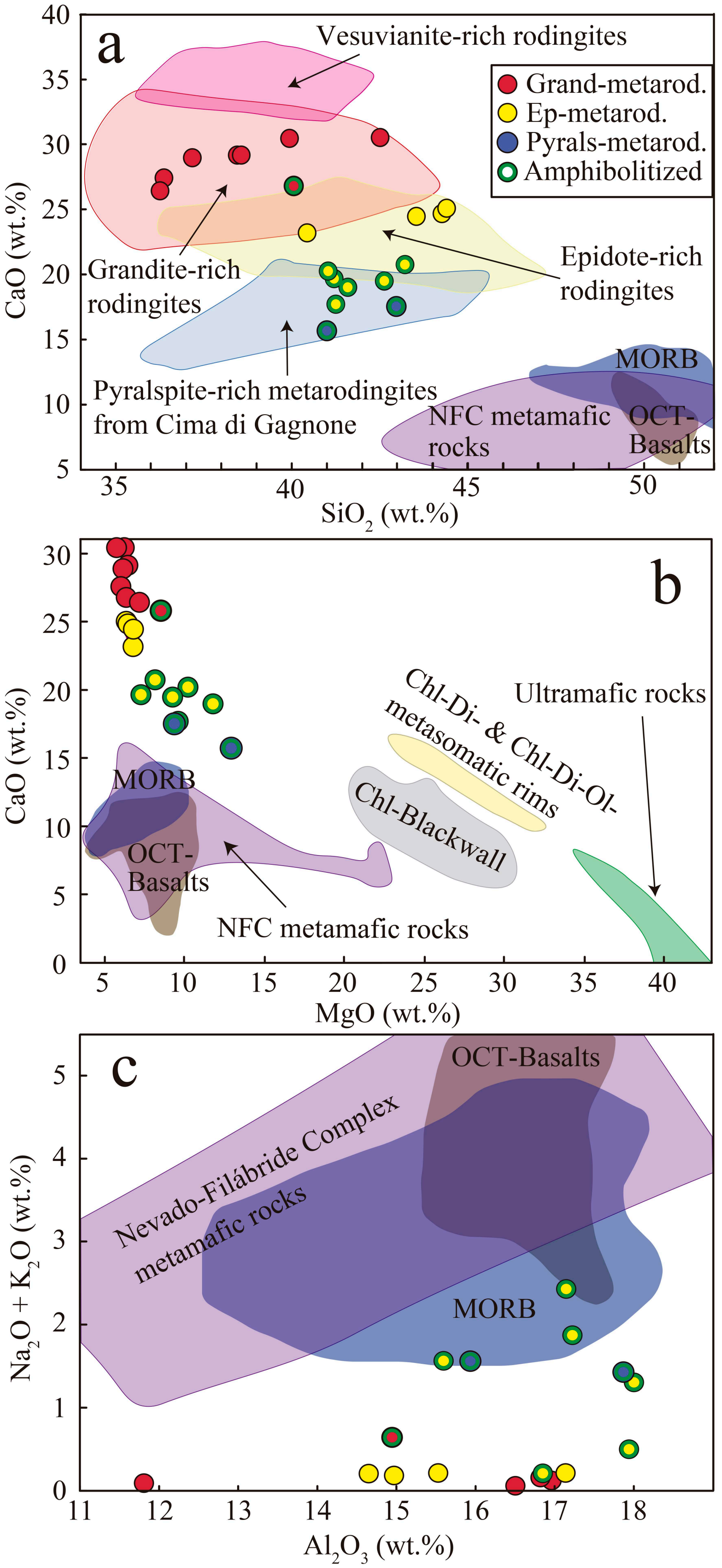
a
Vesuvianite-rich rodingites
Grand-metarod.
Ep-metarod.
Pyrals-metarod.
Amphibolitized
Grandite-rich rodingites
Epidote-rich rodingites
Pyralspite-rich metarodingites from Cima di Gagnone
MORB
NFC metamafic rocks
OCT-Basalts
CaO (wt.%)
SiO_2 (wt.%)
40
35
30
25
20
15
10
5
35
40
45
50
b
Chl-Di- & Chl-Di-Ol-metasomatic rims
Ultramafic rocks
Chl-Blackwall
MORB
OCT-Basalts
NFC metamafic rocks
CaO (wt.%)
MgO (wt.%)
30
25
20
15
10
5
0
5
10
15
20
25
30
35
40
c
OCT-Basalts
Nevado-Filábride Complex metamafic rocks
MORB
$Na_2O + K_2O$ (wt.%)
Al_2O_3 (wt.%)
5
4
3
2
1
0
11
12
13
14
15
16
17
18

granditic garnet from the seafloor (Früh-Green et al., 2017) and subduction-related terranes (Koutsovitis et al., 2013; Li et al., 2004, 2017), and point to complete seafloor rodingitization at lower temperatures (< 325 ºC) (Chapter 4, Fig. 4.13) than those producing epidote-rich rodingites (Bach and Klein, 2009). MgO (Fig. 5.1b) and Al_2O_3 (Fig. 5.1c) in Type 1 have concentrations similar to MORB, basalts from ocean-continent transition zones (OCT) and Mesozoic (non-rodingitized) metamafic rocks from the Nevado-Filábride Complex (NFC), but CaO is notably more abundant and SiO_2 (Fig. 5.1a), Na_2O and K_2O more depleted (Fig. 5.1c). FeO and Fe_2O_3 contents in Type 1 metarodingites vary according to the degree of sample re-equilibration during prograde metamorphism. Indeed, the most re-equilibrated samples, with abundant andradite-rich Grt-2 and Grt-3 (Chapter 4), have high Fe_2O_3 concentrations up to ~ 7 wt.% (Fig. 5.2a). Loss on ignition (LOI) values range from ~ 0.5 wt.% in diopside-rich to 3.7 wt.% in the chlorite-richest sample.

Type 2 Ep-metarodingites are depleted in CaO and enriched in SiO_2 compared to Grand-metarodingites (Fig. 5.1a). These concentrations overlap those of epidote-rich rodingites from other localities (Attoh et al., 2006; Fukuyama et al., 2014; Li et al., 2017). Contents of MgO (Fig. 5.1b), Al_2O_3 (Fig. 5.1c), FeO and Fe_2O_3 (Fig. 5.2a) are similar to those of Grand-metarodingites. Loss on ignition values range from 0.33 to 1.57 wt.% and are higher in chlorite-rich samples.

Type 3 Pyrals-metarodingites are partially amphibolitized. They are generally depleted in CaO (Fig. 5.1a) and enriched in MgO (Fig. 5.1b), Na_2O and K_2O (Fig. 5.1c) compared to the other metarodingite types, and resemble amphibolitized Ep-metarodingites. In terms of CaO-SiO_2 variations, these rocks overlap the compositions of pyralspite-rich

---

Figure 5.1. *Whole-rock abundances of SiO_2 versus CaO* ***(a)****, MgO versus CaO* ***(b)*** *and Al_2O_3 versus Na_2O + K_2O* ***(c)*** *of the Cerro del Almirez metarodingites. All data on anhydrous basis in wt.%. Red circles = Grandite (Grand)-metarodingites; yellow circles = Epidote (Ep)-metarodingites; blue circles = Pyralspite (Pyrals)-metarodingites; green ring = amphibolitized samples. Compositional fields of metarodingites from other locations are plotted in (a) for comparison: pink area =vesuvianite-rich rodingites; red area = grandite-rich rodingites; yellow area = epidote-rich rodingites (all data from Panseri et al., 2008, and references therein); light blue area = pyralspite-rich metarodingites from Cima di Gagnone (Evans et al., 1979, 1981). The dark blue field represents the composition of MORB (Jenner and O´Neill, 2012), the brown area the composition of ocean-continent transition (OCT) basalts (Desmurs et al., 2002), the purple area the composition of metamafic (non-rodingitized) rocks from the Nevado-Filábride Complex (NFC) (Gómez-Pugnaire et al., 2000, and references therein; Puga et al., 2017, and references therein). The compositional variations of chlorite (Chl)-blackwalls (grey area), chlorite-diopside (Di)- and chlorite-olivine (Ol)-diopside-metasomatic rims (yellow area), and host ultramafic rocks (green area) are also shown in (b).*

metarodingites from the Cima di Gagnone massif (Fig. 5.1a) (Evans et al., 1979, 1981). Amphibolitized Type 3 Pyrals-metarodingites have the highest FeO and lowest Fe_2O_3 contents among the Almirez metarodingites (Fig. 5.2a).

Amphibolitized samples (mostly derived from Type 2 Ep-metarodingites) are depleted in CaO (Fig. 5.1a) and enriched in MgO (Fig. 5.1b), Na_2O, K_2O (Fig. 5.1c) and FeO (Fig. 5.2a) compared to the corresponding non-amphibolitized metarodingite type.

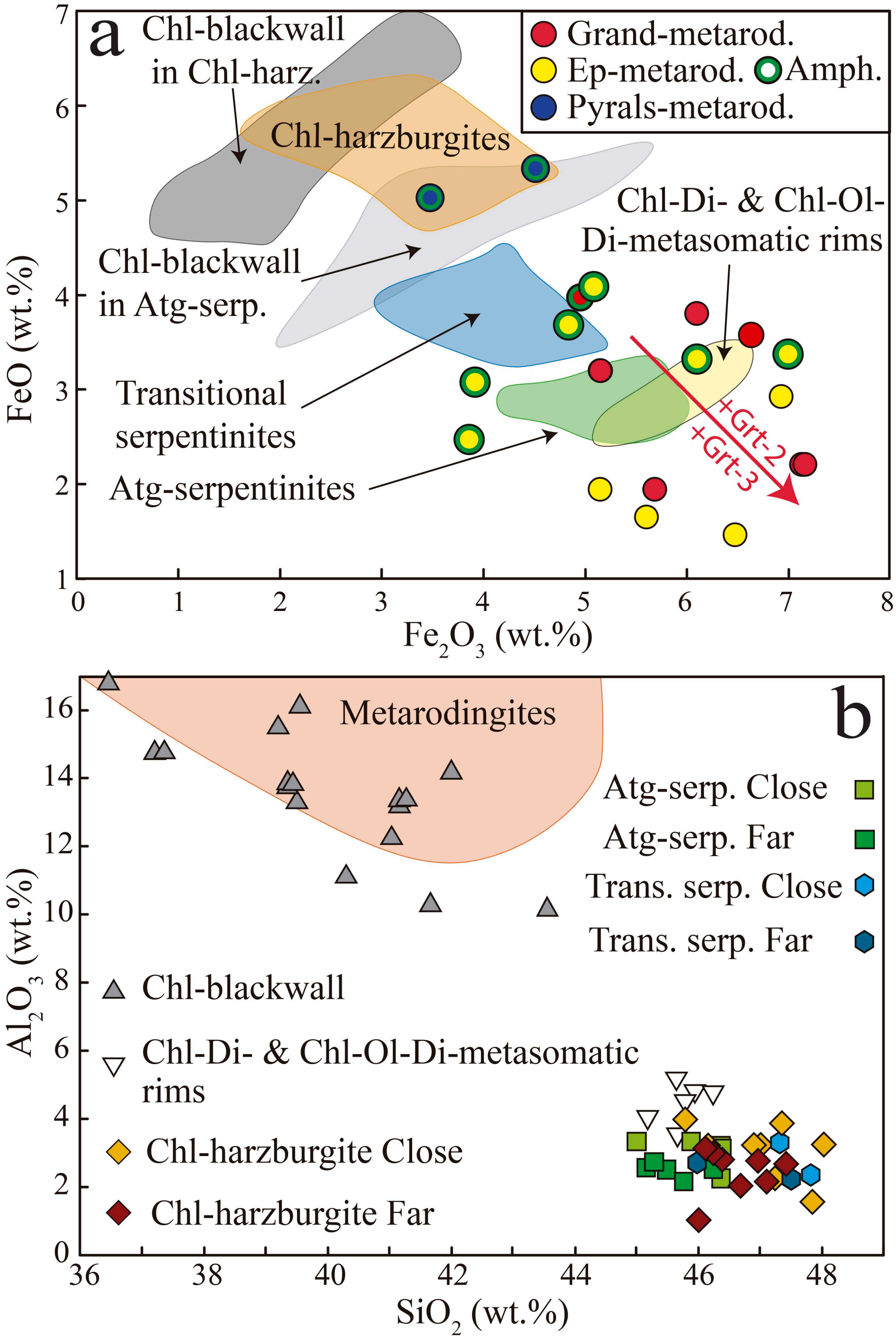

5.3.1.2 Metasomatic reaction rims and ultramafic rocks

Compared to metarodingites, Chl-blackwalls are enriched in MgO, depleted in CaO (Fig. 5.1b, Table A13) and have similar SiO_2 and Al_2O_3 contents (Fig. 5.2b). Chl-blackwalls hosted in Atg-serpentinites have higher Fe_2O_3 and lower FeO than Chl-blackwalls in Chl-harzburgites (Fig. 5.2a), in agreement with their higher abundances of magnetite (Chapter 4).

Chl-Di-metasomatic rims are richer in CaO (Fig. 5.1b) and SiO_2 (Fig. 5.2b) and poorer in Al_2O_3 (Fig. 5.2b), MnO and TiO_2 than Chl-blackwalls. Chl-Ol-Di-metasomatic rims are poorer in CaO and richer in MgO than Chl-Di-metasomatic rims. Both these rock-types have relatively low FeO and high Fe_2O_3 contents, which overlap with the values of host Atg-serpentinites (Fig. 5.2a).

Atg-serpentinites in contact or close to metasomatic reaction rims are generally richer in CaO, Al_2O_3 and SiO_2 (Fig. 5.2b), and poorer in MgO and MnO than Atg-serpentinites farther from metarodingites. On the contrary, FeO and Fe_2O_3 do not vary according to the distance from metarodingites and overlap with concentrations in metasomatic rims (Fig. 5.2a). Transitional Chl-serpentinite and Atg-Chl-Opx-Ol rocks at the serpentinite dehydration front mostly have lower Fe_2O_3 and higher FeO (Fig. 5.2a) and SiO_2 than Atg-serpentinites (Fig. 5.2b). Chl-harzburgites are depleted in CaO and Fe_2O_3 (Fig. 5.2a) and normally enriched in SiO_2 (Fig. 5.2b), FeO and MgO compared to Atg-serpentinites.

Figure 5.2. *Whole-rock abundances of Fe_2O_3 versus FeO* ***(a)*** *and SiO_2 versus Al_2O_3* ***(b)*** *in metarodingites, metasomatic reaction rims and host ultramafic rocks from Cerro del Almirez. All data on anhydrous basis in wt.%. Metarodingite symbols in (a) as in Fig. 2. Panel (a) also shows the compositional fields of Chl-blackwalls around metarodingites in the Atg-serpentinite (light grey area) and Chl-harzburgite domains (dark grey area), Chl-Di- and Chl-Ol-Di-metasomatic rims (yellow area), Atg-serpentinites (green area), transitional Chl-serpentinites and Atg-Chl-Opx-Ol rocks at the dehydration front (blue area), and Chl-harzburgites (light brown area). The red arrow in (a) represents the trend due to increasing abundances of andradite (Fe^{3+})-rich garnets (Grt-2 and Grt-3) in Grand-metarodingites. In (b), grey triangles represent Chl-blackwalls, white inverse triangles represent Chl-Di- and Chl-Ol-Di metasomatic rims, squares represent Atg-serpentinites close to (light green) and far from (dark green) metarodingites, hexagons represent transitional Chl-serpentinites and Atg-Chl-Opx-Ol rocks close to (light blue) and far from (dark blue) metarodingites, and diamonds represent Chl-harzburgites close to (light brown) and far from (dark brown) metarodingites. Metarodingite compositional field (red area) is also plotted for comparison in (b).*

5.3.2 Whole-rock lithophile trace elements

5.3.2.1 Metarodingites

The three types of metarodingite present very similar chondrite-normalized REE patterns (La_N/Sm_N = 1.14-1.78, Sm_N/Yb_N = 1.37-3.04), akin to those of E-MORB and basalts from OCT (Fig. 5.3a, Table A13). Metarodingites have variable Eu anomalies (Eu_N/Eu^* = 0.87-1.98), which are especially positive in Ep-metarodingites (Eu_N/Eu^* = 1.07-1.64). Amphibolitized samples have REE signatures similar to the corresponding non-amphibolitized metarodingites (Fig. 5.3a).

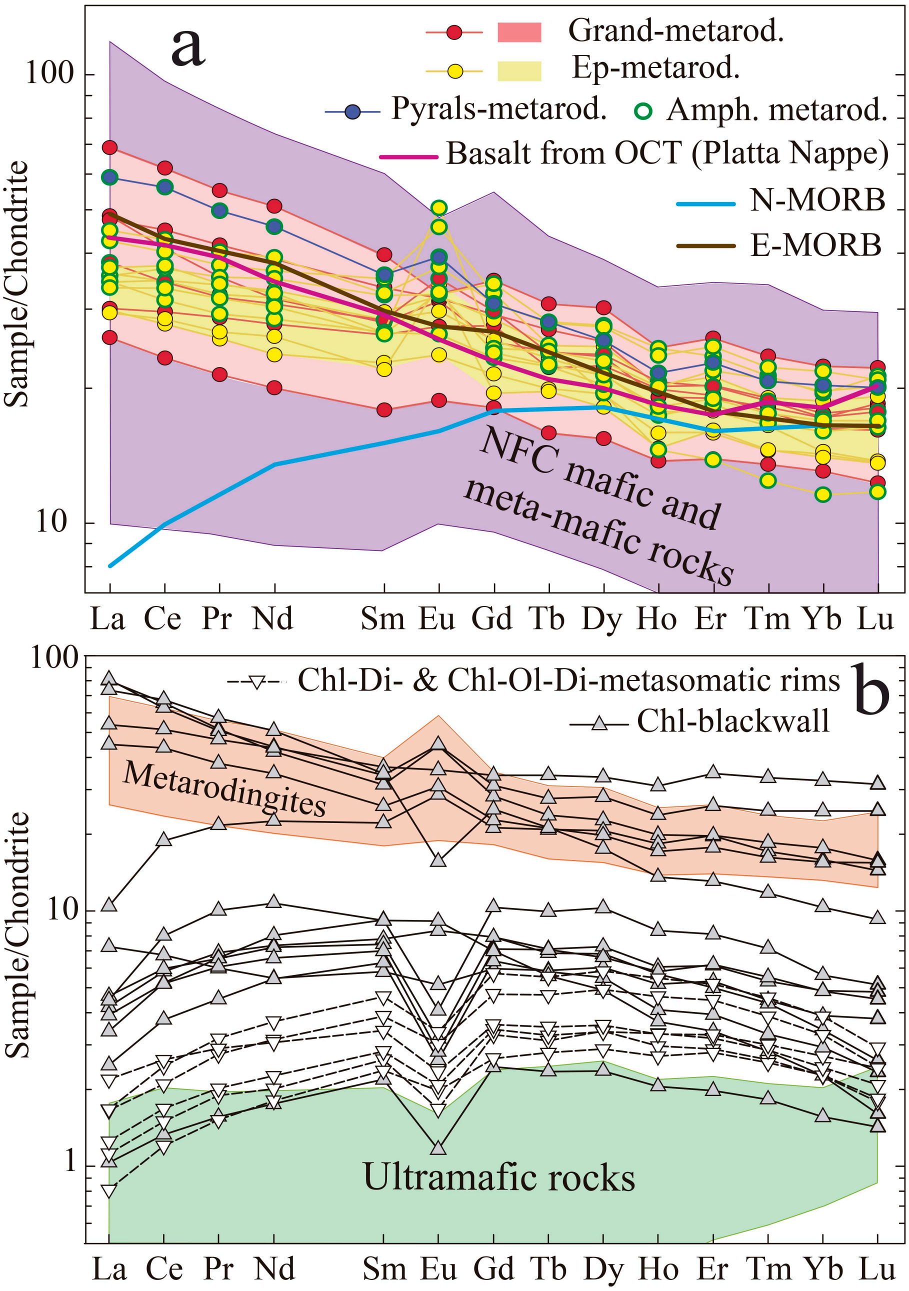

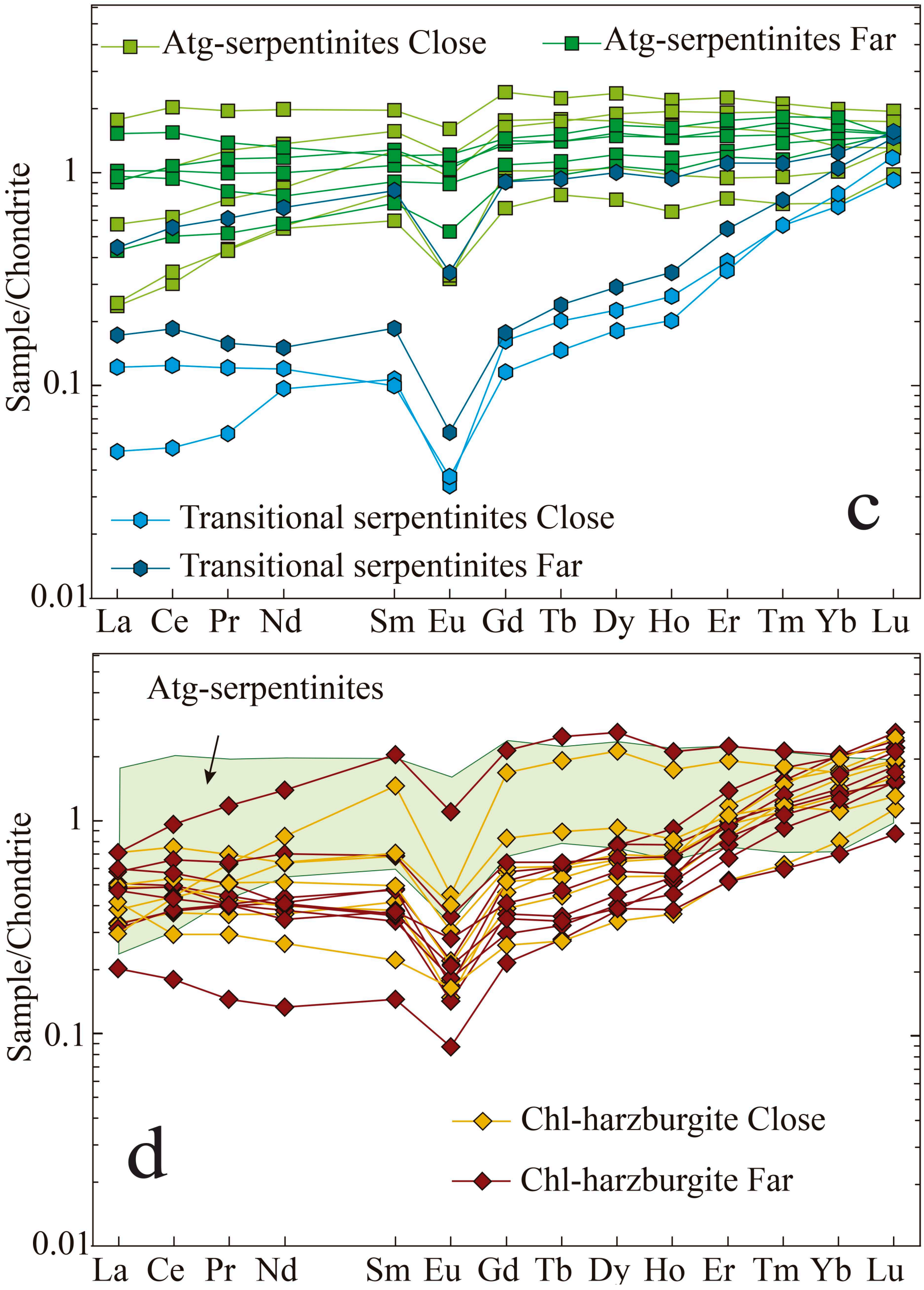

Figure 5.3. *Chondrite-normalized REE patterns of metarodingites* ***(a)****, metasomatic reaction rims* ***(b)****, Atg-serpentinites and transitional Chl-serpentinites and Atg-Chl-Opx-Ol rocks* ***(c)****, and Chl-harzburgites* ***(d)*** *from Cerro del Almirez. Normalizing values from Anders and Grevesse (1989). Symbols as in Figs. 2 and 3. E-MORB (black line) and N-MORB (blue line) compositions are from Klein (2003). Representative composition of ocean-continent transition (OCT) basalt (pink line) from the Platta Nappe is from Desmurs et al. (2002). The purple area represents the REE variations of the Nevado-Filábride Complex (NFC) (not rodingitized) (meta-)mafic rocks. In (b), the compositions of metarodingites (red area) and host ultramafic rocks (green area) are plotted for comparison, as well the compositions of Atg-serpentinites (light green area) in (d).*

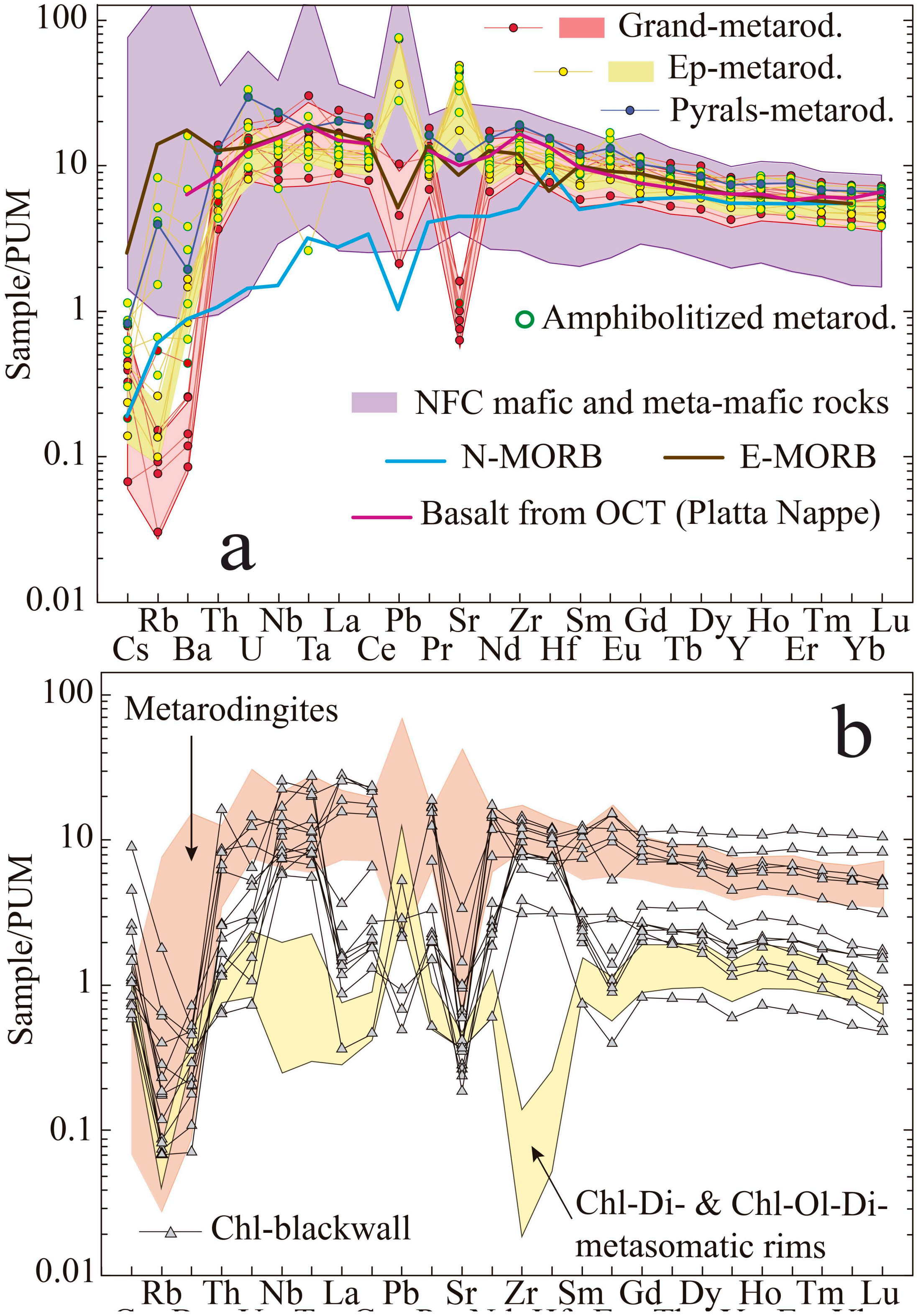
a
Sample/PUM
100
10
1
0.1
0.01
Grand-metarod.
Ep-metarod.
Pyrals-metarod.
Amphibolitized metarod.
NFC mafic and meta-mafic rocks
N-MORB
E-MORB
Basalt from OCT (Platta Nappe)
Rb Th Nb La Pb Sr Zr Sm Gd Dy Ho Tm Lu
Cs Ba U Ta Ce Pr Nd Hf Eu Tb Y Er Yb
b
Metarodingites
Chl-blackwall
Chl-Di- & Chl-Ol-Di-
metasomatic rims
Rb Th Nb La Pb Sr Zr Sm Gd Dy Ho Tm Lu

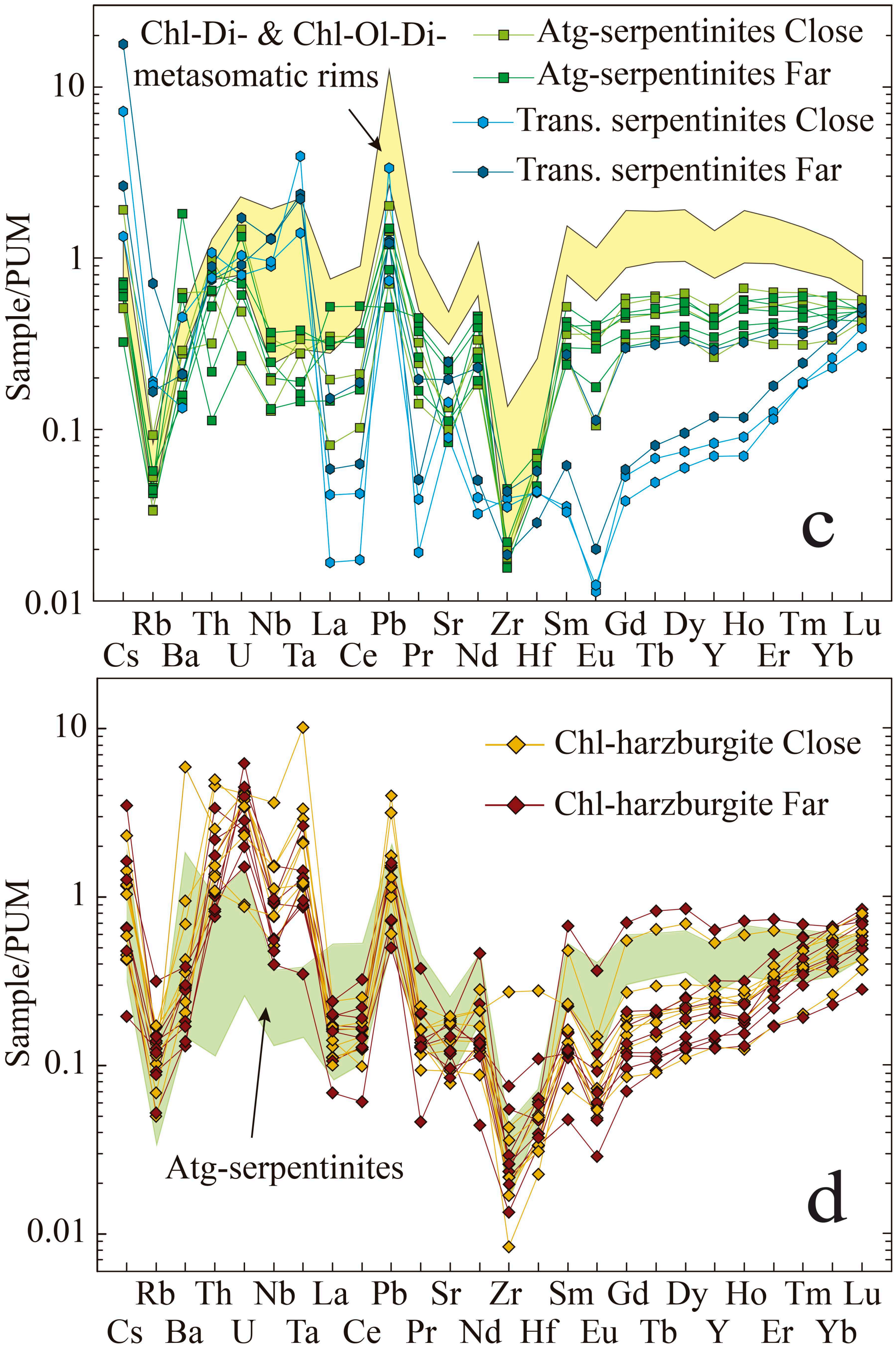

Figure 5.4. *Primitive upper mantle (PUM)-normalized trace element patterns of metarodingites* ***(a)****, metasomatic reaction rims* ***(b)****, Atg-serpentinites and transitional Chl-serpentinites and Atg-Chl-Opx-Ol rocks* ***(c)****, and Chl-harzburgites* ***(d)*** *from Cerro del Almirez. Normalizing values from Sun and McDonough (1989). Symbols and sources of reference compositions as in Figs. 2, 3 and 4. The yellow areas in (b) and (c) represent the compositions of Chl-Di- and Chl-Ol-Di-metasomatic rims.*

Type 1 Grand-metarodingites are depleted in Cs, Rb and Ba compared to E-MORB, OCT basalts and NFC metamafic rocks, and their normalized patterns present evident negative anomalies of Pb and Sr (Fig. 5.4a). Type 2 Ep-metarodingites are richer in Ba than Grand-metarodingites and, opposite to them, show strong positive Pb and Sr spikes (Fig. 5.4a). Amphibolitized metarodingites have higher concentrations of Cs, Rb and Ba than the corresponding non-amphibolitized samples (Fig. 5.4a). Amphibolitized Type 3 Pyrals-metarodingites have lower Sr abundances than amphibolitized Ep-metarodingites (Fig. 5.4a).

5.3.2.2 Metasomatic reaction rims

Chl-blackwalls present a large variability in terms of REE concentrations. Some of their chondrite-normalized REE patterns resemble those of metarodingites but have more variable LREE/MREE and MREE/HREE fractionations ($La_N/Sm_N = 0.47\text{-}2.56$, $Sm_N/Yb_N = 1.13\text{-}3.52$) (Fig. 5.3b, Table A13). The rest of Chl-blackwalls have notably lower REE abundances and are relatively depleted in LREE ($La_N/Sm_N = 0.37\text{-}0.63$, except one sample with $La_N/Sm_N = 1.25$) and HREE ($Sm_N/Yb_N = 1.40\text{-}4.05$) (Fig. 5.3b). The Eu anomaly of these patterns is variable ($Eu_N/Eu^* = 0.40\text{-}1.50$) but is usually negative in REE-depleted samples (Fig. 5.3b).

Chl-Di- and Ch-Ol-Di-metasomatic rims have normalized REE patterns similar to Chl-blackwalls depleted in REE ($La_N/Sm_N = 0.31\text{-}0.64$), but in general have lower REE concentrations and are less MREE/HREE fractionated ($Sm_N/Yb_N = 1.04\text{-}1.26$) (Fig. 5.3b). Their compositions are transitional to those of Atg-serpentinites, and similar to the latter they present negative Eu anomalies (Fig. 5.3b).

Chl-blackwalls and Chl-(± Ol)-Di-metasomatic rims have Cs, Rb and Ba concentrations similar to metarodingites (Fig. 5.4a, b), but Chl-(± Ol)-Di-metasomatic rims normally have lower Cs and Rb concentrations than Chl-blackwalls (Fig. 5.4b). Abundances of Th and U in the latter are coupled to those of REE, i.e. they are higher in REE-enriched than in REE-depleted Chl-blackwalls. On the other hand, high field strength elements (HFSE: Nb, Ta, Zr and Hf) are systematically more abundant in Chl-blackwalls than in Chl-Di- and Chl-Ol-Di-metasomatic rims, irrespective of their REE contents, and have concentrations similar to metarodingites (Fig. 5.4b). Lead in the normalized patterns of Chl-blackwalls shows positive or negative spike relative to LREE, whereas it is systematically enriched in Chl-Di- and Chl-Ol-Di-metasomatic rims (Fig.

5.4b). On the contrary, Sr is relatively depleted in both Chl-blackwalls and Chl-(± Ol)-Di-metasomatic rims (Fig. 5.4b).

5.3.2.3 Host ultramafic rocks

Atg-serpentinites close to metasomatic rims are normally enriched in MREE (La_N/Sm_N = 0.30-0.90, Sm_N/Yb_N = 0.72-1.18) relative to Atg-serpentinites far from the rims (La_N/Sm_N = 0.60-1.27, Sm_N/Yb_N = 0.63-0.80) (Fig. 5.3c, Table A13). All patterns of Atg-serpentinites show negative Eu anomalies (Fig. 5.3c). Transitional Chl-serpentinite and Atg-Chl-Opx-Ol rocks and Chl-harzburgites are normally depleted in LREE and MREE and more MREE/HREE fractionated (Sm_N/Yb_N = 0.10-0.66) than Atg-serpentinites (Fig. 5.3c, d) (see also Garrido et al., 2005 and Marchesi et al., 2013), except two Chl-harzburgites with abundant tremolite (Fig. 5.3d). Chl-harzburgites are generally richer in LREE and MREE than transitional Chl-serpentinite and Atg-Chl-Opx-Ol rocks (Fig. 5.3d). Similar to Atg-serpentinites, these rocks present negative Eu anomalies (Fig. 5.3c, d).

Atg-serpentinites usually have lower Cs, Rb, Th, U, Nb and Ta concentrations than transitional Chl serpentinite and Atg-Chl-Opx-Ol rocks (Fig. 5.4c). Lead shows positive anomaly in the patterns of these lithotypes, whereas Sr is enriched relative to LREE in transitional rocks and depleted in Atg-serpentinites (Fig. 5.4c). As noted by Garrido et al. (2005) and Marchesi et al. (2013), Chl-harzburgites are enriched in Th, U, Nb and Ta compared to Atg-serpentinites (Fig. 5.4d). Similar to serpentinites, Chl-harzburgites have patterns with positive spike of Pb, while Sr is more variable. No systematic differences exist between the trace element abundances of Chl-harzburgites close or far from the metasomatic rims (Fig. 5.4d).

5.3.3 Lithophile trace elements in minerals

5.3.3.1 Garnet

Granditic garnets of Type 1 metarodingites (Grt-1, Grt-2 and Grt-3) are all enriched in MREE and HREE relative to LREE (La_N/Sm_N = 0.005-0.014, La_N/Yb_N = 0.24-0.92), but their REE patterns have some differences (Fig. 5.5a, Table A15). Grt-1 has higher HREE concentrations and generally negative Eu anomaly (Eu_N/Eu^* = 0.75–1.02). Grt-2 is normally more enriched in MREE than Grt-1, has opposite MREE/HREE

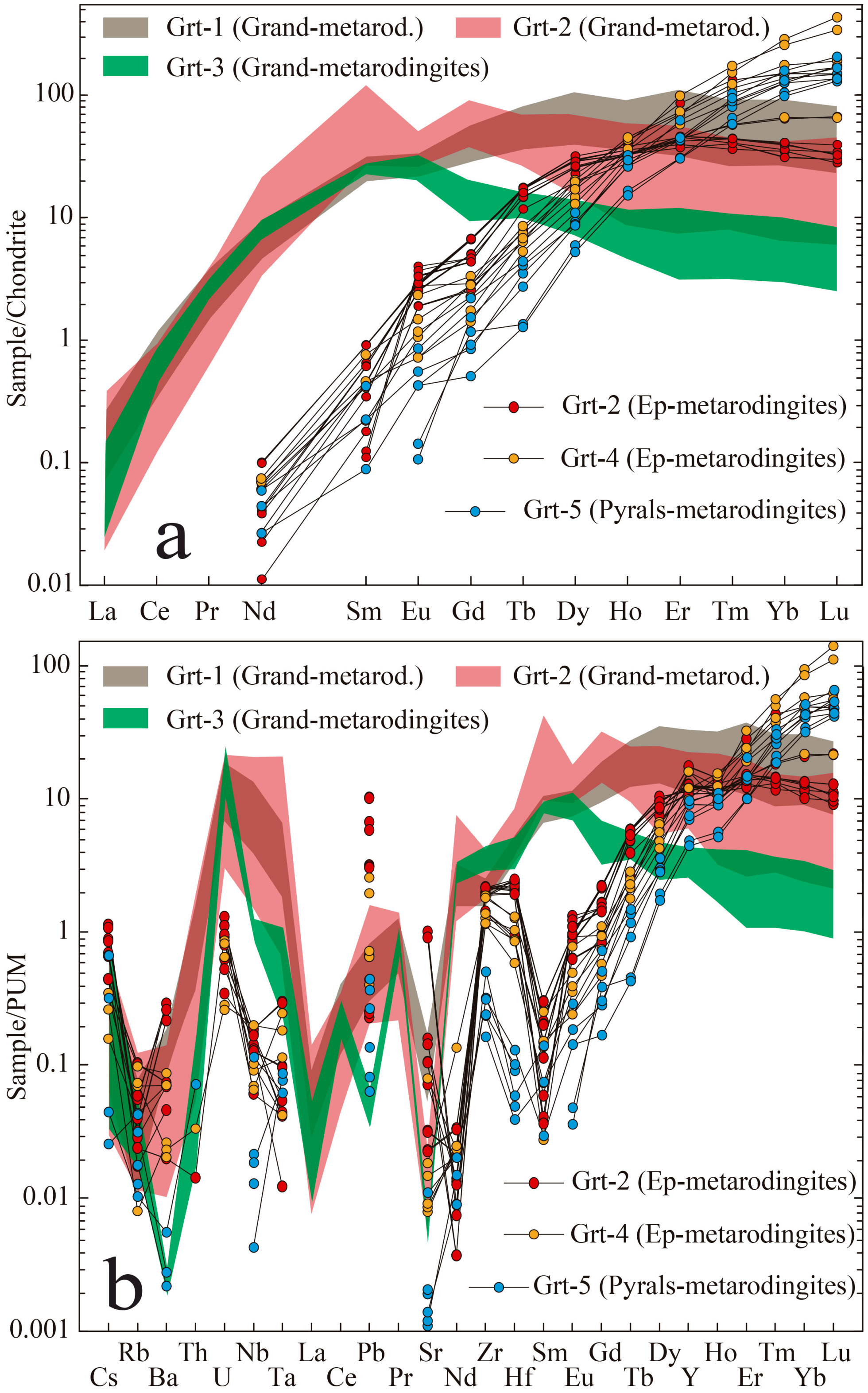

Figure 5.5. *Chondrite-normalized REE patterns **(a)** and primitive upper mantle (PUM)-normalized trace element patterns **(b)** of the different types of garnet in the Almirez metarodingites. Normalizing values from Anders and Grevesse (1989) and Sun and McDonough (1989). Brown, pink and green areas mark the compositional variations of Grt-1, Grt-2 and Grt-3 in Grand-metarodingites, respectively. Red and orange circles indicate the compositions of relic Grt-2 and new Grt-4 in Ep-metarodingites, respectively. Blue circles indicate the compositions of Grt-5 in Pyrals-metarodingites.*

fractionation (Sm_N/Yb_N = 0.84-11.05), and has more pronounced negative Eu anomaly (Eu_N/Eu^* = 0.48–0.95). Grt-3 has concentrations of LREE similar to Grt-1 and Grt-2, but is notably more depleted in MREE and HREE and has slightly positive Eu anomaly (Eu_N/Eu^* = 1.15–1.56). All these garnet types are enriched in Th, U, Nb, Ta, Zr and Hf compared to adjacent elements in the normalized patterns (Fig. 5.5b). Strontium in Grt-1 and, especially, Grt-2 displays a pronounced negative anomaly. Grt-3 has lower Ba, Th, Nb and Ta abundances than Grt-1 and Grt-2, and evident negative anomalies of Pb and Sr (Fig. 5.5b). Progressive depletion in Sr and Ba from Grt-1 to Grt-3 (Fig. 5.5b) correlates with slightly decreasing Ca abundances in successive garnet generations (Chapter 4).

Relic Grt-2 in Type 2 Ep-metarodingites is notably more depleted in LREE, MREE (Sm_N/Yb_N = 0.001-0.03) (Fig. 5.5a), Th, U, Nb, Ta and Hf than Grt-2 in Grand-metarodingites, and is also normally enriched in Pb and Sr compared to the latter (Fig. 5.5b). More pyralspitic Grt-4 and Grt-5 in Type 2 and Type 3 metarodingites, respectively, have LREE-MREE compositions similar to Grt-2 in Type 2 but higher HREE abundances (Fig. 5.5a). These types of garnet also have Cs, Rb, Ba, Th, U, Nb and Ta concentrations similar to Grt-2 in Type 2 metarodingites but lower Pb, Sr, Zr and Hf abundances (Fig. 5.5b).

5.3.3.2 Allanite and epidote

Allanite in Type 1 Grand-metarodingites is extremely rich in LREE and MREE (La_N/Sm_N = 8.01–19.32, Sm_N/Yb_N ~ 1000-10000) and presents negative Eu anomaly (Eu_N/Eu^* = 0.49–0.77) (Fig. 5.6a, Table A15). Normalized patterns of this mineral show prominent positive spikes of Th and U and negative peaks of Nb, Ta, Pb, Sr, Zr and Hf (Fig. 5.6b).

Epidote has similar compositions in Type 2 Ep- and Type 3 Pyrals-metarodingites. This phase is generally enriched in LREE and MREE compared to HREE (La_N/Yb_N = 1.33–66.55, Sm_N/Yb_N = 1.15-47.9), except rare epidote in veins (La_N/Yb_N = 0.47–1.58, Sm_N/Yb_N = 0.42-0.92), and commonly shows positive Eu anomaly (Eu_N/Eu^* = 0.92-2.56) (Fig. 5.6a). Epidote is depleted in Th, U, LREE and MREE and enriched in Ba, Pb, Sr and HREE compared to allanite (Fig. 5.6).

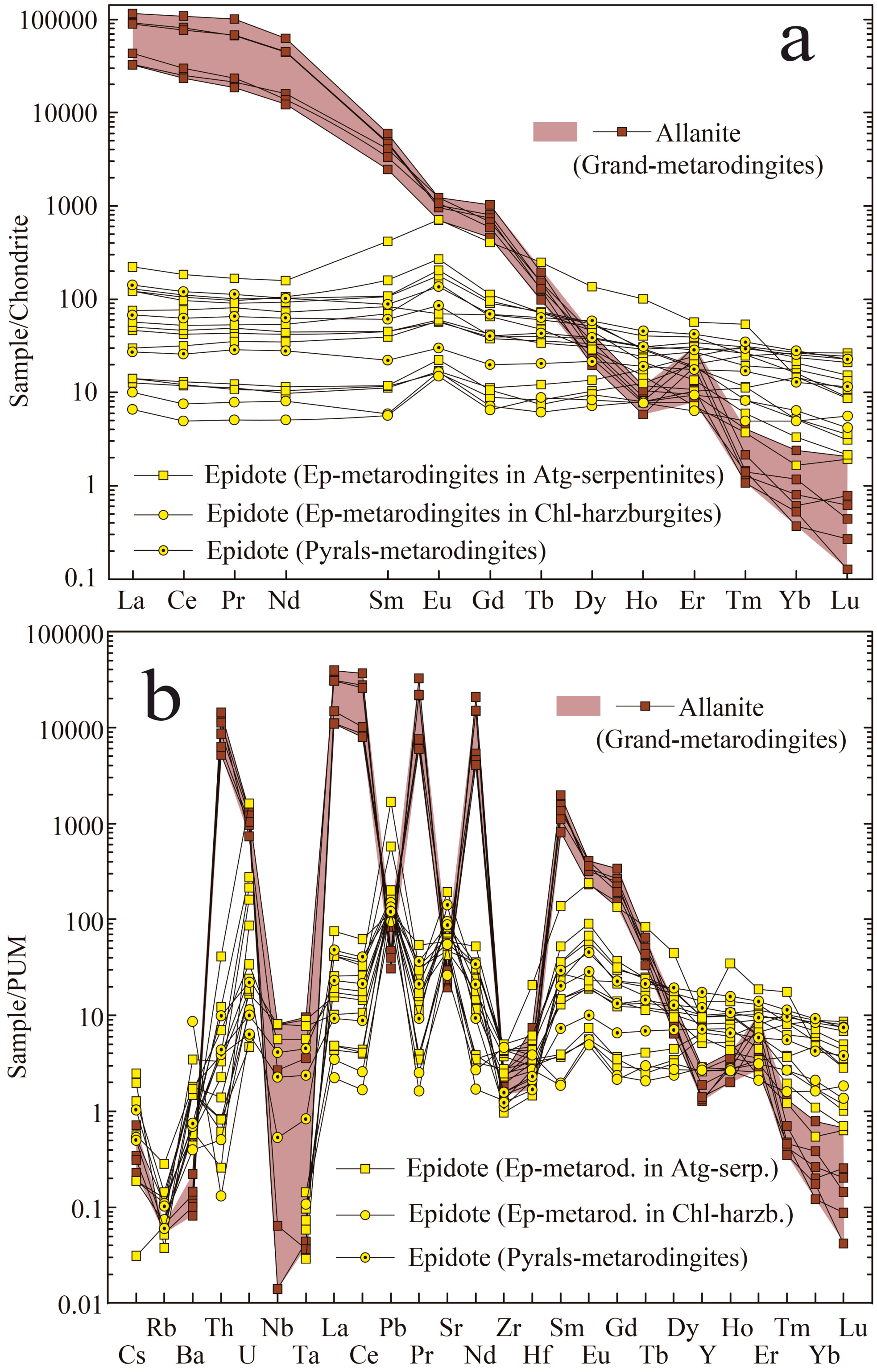

Figure 5.6. *Chondrite-normalized REE patterns* ***(a)*** *and primitive upper mantle (PUM)-normalized trace element patterns* ***(b)*** *of allanite and epidote in the Almirez metarodingites. Normalizing values from Anders and Grevesse (1989) and Sun and McDonough (1989). Red squares and area indicate the composition of allanite in Grand-metarodingites. Yellow squares and circles mark the compositions of epidote in Ep-metarodingites from the Atg-serpentinite and Chl-harzburgite domains, respectively. Dotted yellow circles mark the compositions of epidote in Pyrals-metarodingites.*

5.3.3.3 Diopside and amphibole

Diopside in Grand-metarodingites has lower REE concentrations than chondrite (Fig. 5.7a, Table A15). This phase is enriched in MREE compared to LREE and HREE (La_N/Sm_N = 0.06-0.16, Sm_N/Yb_N = 23.4-50.0) (Fig. 5.7a), and in Pb and Sr relative to adjacent elements in the normalized patterns (Fig. 5.7b). Late amphibole (Amp-2) in Type-1 metarodingites is enriched in REE (especially HREE) (Fig. 5.7a), Rb, Ba, U and Sr compared to diopside in the same rocks (Fig. 5.7b).

Diopside in Ep-metarodingites is depleted in LREE and MREE and enriched in HREE relative to diopside in Grand-metarodingites, and displays variable MREE/HREE fractionation (Sm_N/Yb_N = 0.27-2.12) (Fig. 5.7a) and normally positive Eu anomaly (Eu_N/Eu^* = 0.96-2.28). Similar to diopside in Type 1 Grand-metarodingites, this phase is relatively enriched in Pb and Sr (Fig. 5.7b).

Diopside in Type 3 Pyrals-metarodingites is enriched in MREE and HREE and has similar LREE concentrations compared to diopside in Grand-metarodingites, and presents evident Eu negative anomaly (Eu_N/Eu^* = 0.45-0.60). MREE/HREE fractionation is variable (Sm_N/Yb_N = 0.84-2.57) (Fig. 5.7a). Rubidium, Ba, U, Pb and Sr are enriched relatively to adjacent elements (Fig. 5.7b). Amp-2 in Type 3 Pyrals-metarodingites has lower LREE and MREE concentrations than diopside in the same rocks and presents variable Eu anomaly (Eu_N/Eu^* = 0.67-1.19) (Fig. 5.7a). On the other hand, Rb, Ba, Nb, Ta, Zr and Hf are enriched compared to concentrations in diopside (Fig. 5.7b).

5.3.4 PGE-Re abundances and Os isotopes in whole-rocks

All metarodingite types from Cerro del Almirez have similar PGE-Re concentrations (between 10^{-6} and 10^{-2} the chondrite values) that are analogous to those of MORB, except for rather lower contents of Re (Fig. 5.8a, Table A16). Their normalized PGE-Re patterns are depleted in Os Ir, Ru (I-PGE) compared to Pt, Pd (P-PGE) and Re (e.g., Pt_N/Os_N = 1.1-9.8) except in one atypical Os-rich Grand-metarodingite (AL14-16 with Pt_N/Os_N = 0.2). Type 2 Ep-metarodingites have slightly lower P-PGE concentrations than the other metarodingite-types (Fig. 5.8a).

Independently on their REE contents, Chl-blackwalls have PGE-Re abundances very similar to metarodingites (Fig. 5.8b). These rocks are depleted in Ir compared to Os and have P-PGE concentrations similar to or lower than Ep-metarodingites (Fig. 5.8b). Chl-(± Ol)-Di-metasomatic rims have PGE concentrations two to four orders of magnitude

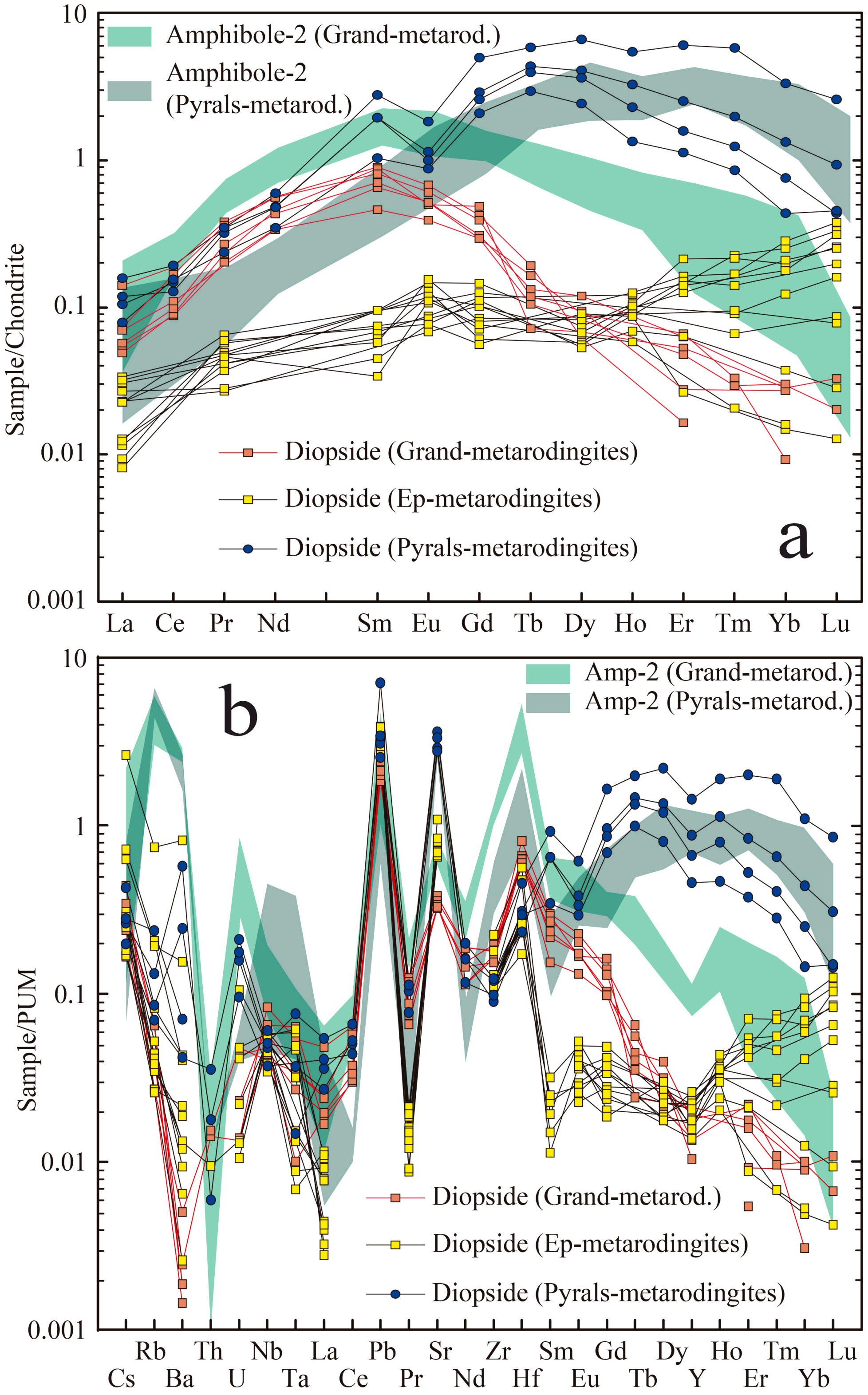

Figure 5.7. *Chondrite-normalized REE patterns **(a)** and primitive upper mantle (PUM)-normalized trace element patterns **(b)** of diopside and pargasitic amphibole (Amp-2) in the Almirez metarodingites. Normalizing values from Anders and Grevesse (1989) and Sun and McDonough (1989). Orange and yellow squares indicate the compositions of diopside in Grand- and Ep-metarodingites, respectively. Blue circles indicate the compositions of diopside in Pyrals-metarodingites. Green and grey areas mark the compositional variations of Amp-2 in Grand-and Pyrals-metarodingites, respectively.*

higher than metarodingites and Chl-blackwalls, and their normalized patterns are commonly flat (Pt_N/Os_N = 1.0-1.1) except for one sample with lower I-PGE contents (AL14-23 with Pt_N/Os_N = 4.4) (Fig. 5.8b). Rhenium in Chl-(± Ol-)Di-metasomatic rims is significantly depleted relative to Pd.

Atg-serpentinites have PGE-Re concentrations that resemble those of Chl-(± Ol)-Di-metasomatic rims (Fig. 5.8c). No clear relationships exist between the distance of Atg-serpentinites from metarodingites and their PGE-Re concentrations, which coincide with those of depleted MORB mantle (DMM) (Fig. 5.8c). Chl-harzburgites have PGE-Re compositions also similar to DMM but they are more heterogeneous compared to Atg-serpentinites. Chl-harzburgites close to metarodingites commonly have lower P-PGE and higher Re concentrations than harzburgites far from the mafic layers (Fig. 5.8d).

The present-day $^{187}Os/^{188}Os$ ratios of metarodingites, which are controlled by the time-integrated decay of ^{187}Re to ^{187}Os, are very variable (0.1993-1.0721) and notably higher than the chondritic (0.1270, Shirey and Walker, 1998) and DMM values (0.1281, Walker

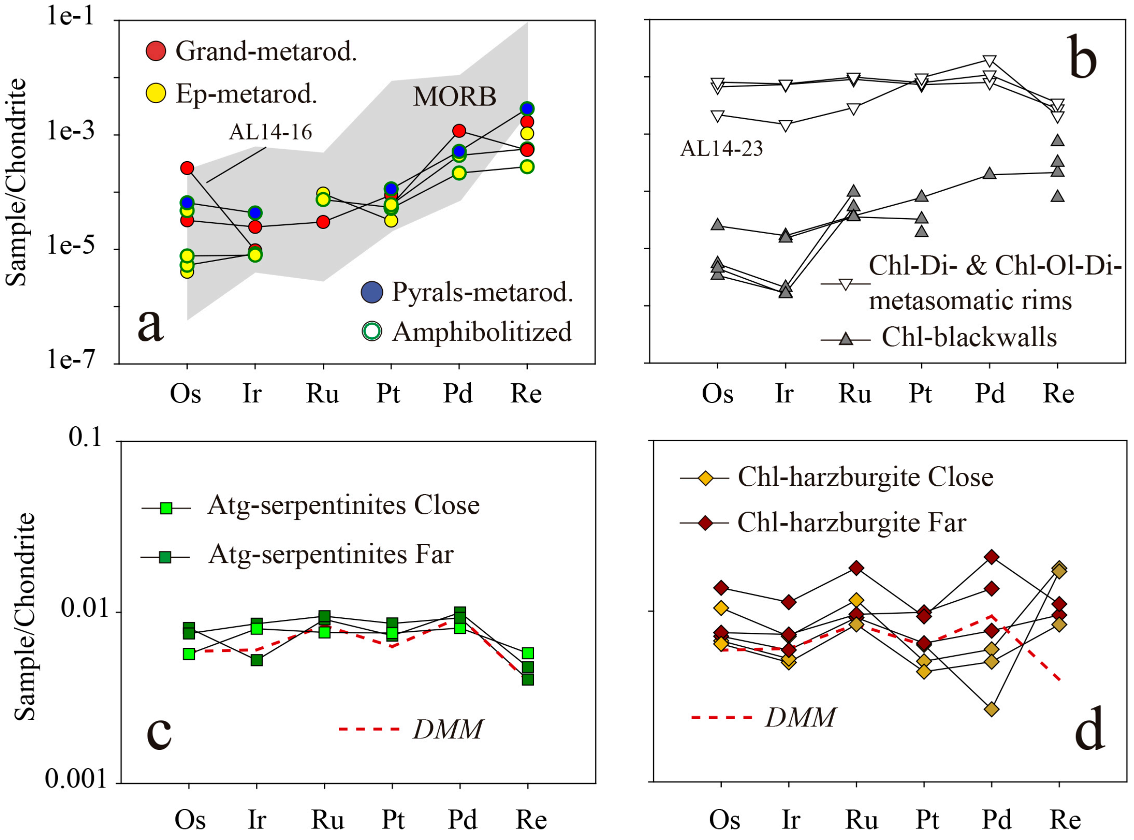

Figure 5.8. *CI chondrite-normalized PGE-Re patterns of metarodingites **(a)**, Chl-blackwalls and Chl-(±Ol)-Di-metasomatic rims **(b)**, host Atg-serpentinites **(c)** and Chl-harzburgites **(d)** from Cerro del Almirez. Normalizing values from Palme and Jones (2003). Symbols as in Figs. 5.1 and 5.2. PGE-Re compositions of MORB (grey field) in (a) is from Gannoun et al. (2016), and references therein. DMM composition in (c) and (d) (red dashed line) is from Salters and Stracke (2004).*

et al., 2002) (Fig. 5.9). These Os isotopic compositions are unrelated to the metarodingite type and coincide with those of Chl-blackwalls (Fig. 5.9). Higher Os concentrations in Chl-(± Ol)-Di-metasomatic rims are coupled to significantly lower $^{187}Os/^{188}Os$ (0.1248-0.1341) (Fig. 5.9). Atg-serpentinites have subchondritic Os isotopic compositions lower than DMM ($^{187}Os/^{188}Os = 0.1219\text{-}0.1257$) and similar to Chl-(± Ol)-Di-metasomatic rims (Fig. 5.9). In particular, $^{187}Os/^{188}Os$ is lower in serpentinites close to metarodingites than in serpentinites far from the mafic layers. A similar trend also characterizes Chl-harzburgites, which are less radiogenic close to metarodingites ($^{187}Os/^{188}Os = 0.1189\text{-}0.1229$) than far from them ($^{187}Os/^{188}Os = 0.1219\text{-}0.1258$).

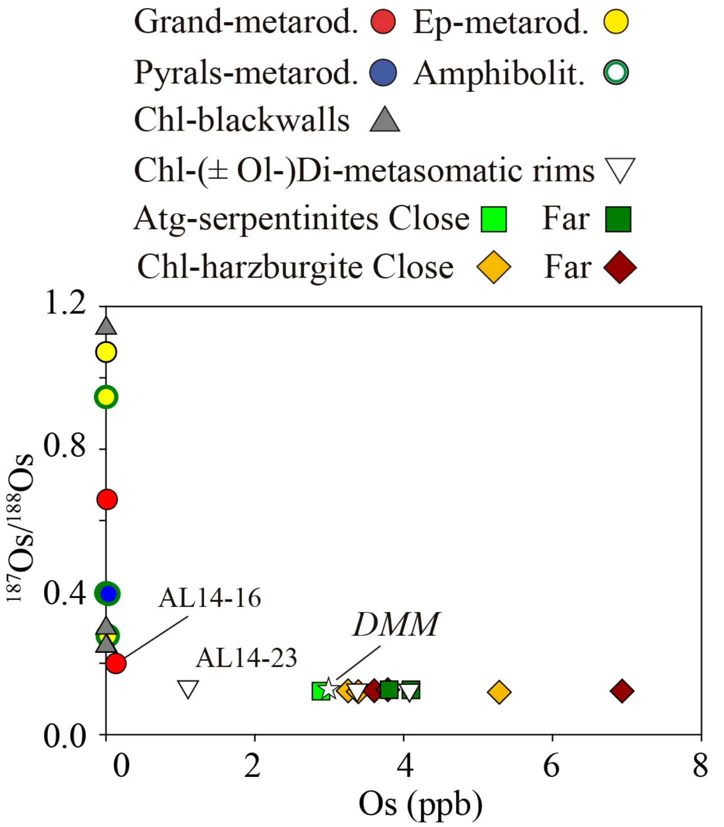

Figure 5.9. *Os concentrations (ppb) versus present-day $^{187}Os/^{188}Os$ in metarodingites, Chl-blackwalls, Chl-(± Ol)-Di-metasomatic rims, and host Atg-serpentinites and Chl-harzburgites from Cerro del Almirez. Symbols as in Fig. 5.8. DMM composition is from Salters and Stracke (2004) and Walker et al. (2002).*

5.4 Discussion

Metarodingites, spatially related metasomatic rims and host ultramafic rocks from Cerro del Almirez underwent a complex petrological evolution from seafloor hydrothermal alteration to subduction metamorphism in the eclogite facies, and exhumation (cf. Chapter 4; Padrón-Navarta et al., 2011). During this evolution, metasomatic and metamorphic reactions involving fluids with different oxidizing capacity occurred in the metarodingite-ultramafic suites. The geochemical data presented in this work permit to infer how the main stages of this evolution, including the exceptionally well documented dehydration of Atg-serpentinites, affected the bulk and mineral compositions of these rocks (Figs. 5.10 and 5.11). The discussion of these results aims to constrain for the first time the role of subducted metarodingites in the geochemical signature of slab fluids, including their redox state, and element recycling at different depths in subduction zones.

5.4.1 Seafloor rodingitization

5.4.1.1 Lithophile elements

The igneous protoliths of the Almirez metarodingites were mafic rocks with different proportions of plagioclase, clinopyroxene and olivine arranged in doleritic or porphyritic textures (Chapter 4, Fig. 4.4). Rodingitization of these mafic intrusions was concomitant with seafloor serpentinization of enclosing ultramafic rocks (Alt et al., 2012) due to mantle exhumation by continental rifting (Gómez-Pugnaire et al., 2000) or ultra-slow oceanic spreading (Puga et al., 2011). This extensional event produced mafic intrusions of Jurassic age (~ 185 Ma) with E- or T-MORB geochemical signatures (Puga et al., 2011) likely emplaced in an ocean-continent transition zone (Fig. 5.10a) or at a tectonically similar (Manatschal and Müntener, 2009) ultra-slow spreading centre. To assess the chemical variations induced by seafloor rodingitization, we compare the compositions of Grand-metarodingites with those of representative MORB, OCT basalts and Mesozoic (non-rodingitized) metamafic rocks from the NFC. This comparison supports that, among major elements, seafloor rodingitization by reducing fluids (Frost and Beard, 2007) caused prominent Si, Na and K loss and Ca incorporation in metarodingites (Fig. 5.1a, c) by element transfer with serpentinized peridotites (Fig. 5.10b, c) (Bach and Klein, 2009; Evans et al., 1981; Tang et al., 2018).

Whole-rock REE concentrations in Grand-metarodingites match those of E-MORB, OCT basalts and NFC metamafic rocks (Fig. 5.3a), supporting that REE remained

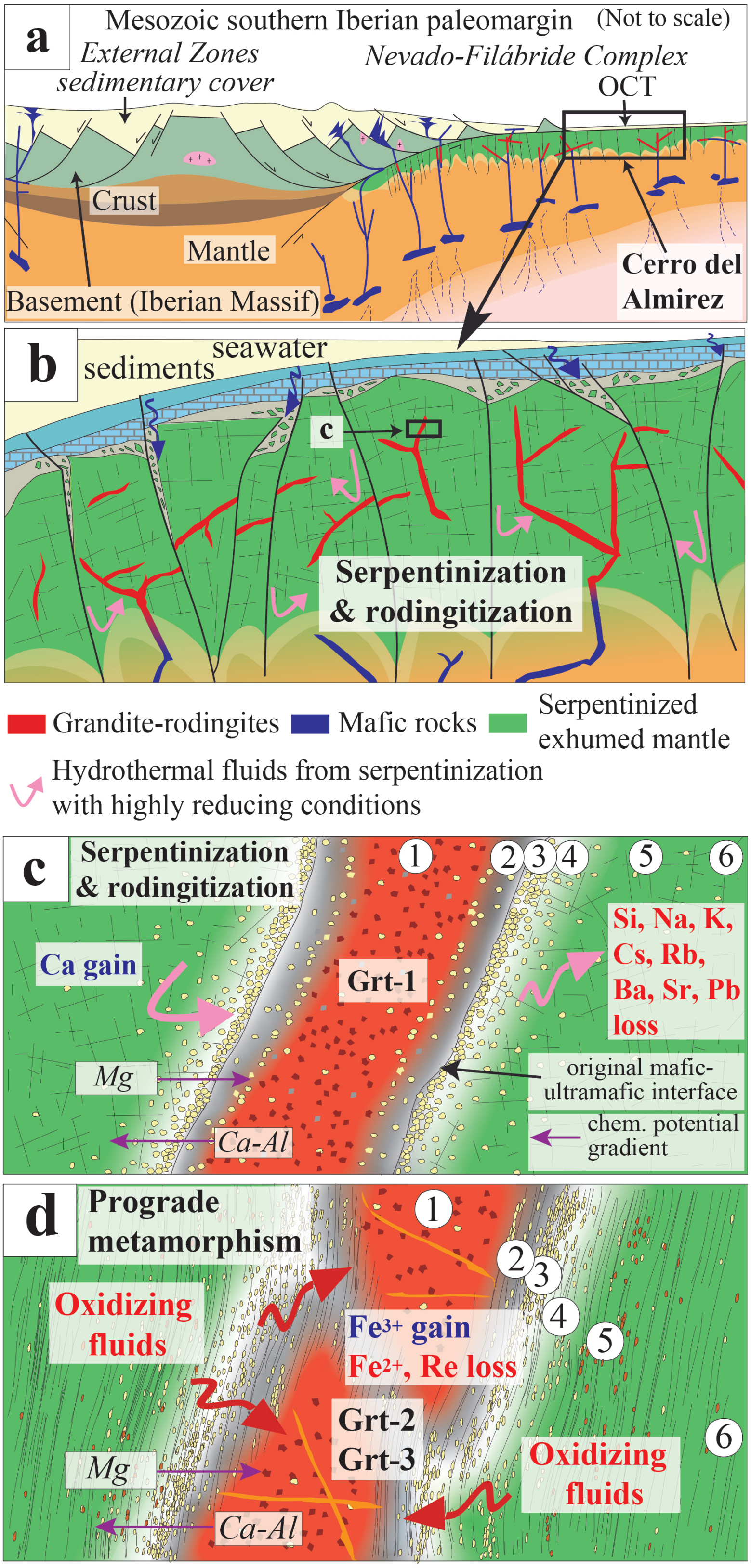

immobile during rodingitization of the core portion of the mafic intrusions (e.g., Dubińska, 1997; Evans et al., 1981; Fukuyama et al., 2014; Hatzipanagiotou and Tsikouras, 2001; Koutsovitis et al., 2018; Pomonis et al., 2008; Pusching, 2002). Moreover, LREE and HREE in Grand-metarodingites correlate with similarly incompatible elements such as Nb-Ta and Al-V, respectively (not shown). The latter elements are commonly not mobilized in aqueous fluids at low pressure (Niu, 2004); supporting that REE patterns in the core of Grand-metarodingite layers mostly preserve the imprint of crystal fractionation in their igneous protoliths. However, rodingitization caused the REE redistribution at the sample scale between different minerals. Taking into account the uncertainties on modal proportions (Chapter 4, Table 4.1) and the variabilities of trace element compositions of minerals (Figs. 5.5, 5.6 and 5.7), mass balance calculations (Table A17) show that Grt-1 in Type 1 metarodingites concentrates ~ 70% of whole-rock HREE. These high concentrations of HREE are typical of Al-rich hydrothermal garnets similar to Grt-1 (with up to 70-73 mol.% grossular component, Chapter 4, Table 4.2), and indicate prolonged fluid-rock interaction in a system buffered by the rock composition (Gaspar et al., 2008). Relative high contents of HFSE in Grt-1 (Fig. 5.5b) characterize granditic garnets with high amounts of Ti-rich components (up to 11 mol.% in Grt-1, Chapter 4, Table 4.2) (Marks et al., 2008) but the whole-rock budget of these elements is most likely controlled by accessory titanite and zircon (Chapter 4, Table 4.1). Diopside in Type 1 Grand-metarodingites is depleted in REE, especially HREE (Fig. 5.7a), as consequence of concomitant crystallization with abundant Grt-1 and subsequent metamorphic re-equilibration with Grt-1 and other phases during subduction (mainly Grt-2, Grt-3 and allanite, see section 5.4.3.). Clinopyroxene in metamafic rocks subducted to high-pressure is typically depleted in REE (e.g., Hermann, 2002; Spandler

---

Figure 5.10. (a) *Geological sketch of the Mesozoic ocean-continent transition zone (OCT) in which serpentinites and rodingites from Cerro del Almirez may have formed on the seafloor.* ***(b)*** *Detailed representation of oceanic serpentinization of exhumed mantle peridotites and rodingitization of mafic dykes by percolation of reducing fluids (pink arrows).* ***(c)*** *Cartoon illustrating the generation of Grand-rodingites and metasomatic reaction rims on the seafloor (rodingitization). Light yellow spots symbolize diopside grains. Pink arrows represent the fluid-mediated element exchanges between ultramafic and mafic rocks during rodingitization, and purple arrows the subsequent diffusion of Mg, Ca and Al between rodingite and serpentinite forming the metasomatic rims.* ***(d)*** *Sketch of structural (deformation) and chemical processes (Fe oxidation) triggered by prograde metamorphism in Grand-metarodingites prior to Atg-breakdown in host serpentinites. Red arrows: oxidant fluids.*

et al., 2003; Tribuzio et al., 1996) but diopside was likely a more important repository of LREE and MREE in oceanic rodingites before subduction.

Similar to Na and K (Fig. 5.1c), Cs, Rb, Ba and Sr are notably depleted in Grand-metarodingites compared to E-MORB, OCT basalts and NFC metamafic rocks (Fig. 5.4a), supporting that LILE were remobilized during rodingitization (Fig. 5.10c) (e.g., Evans et al., 1981; Pusching, 2002) and incorporated into enclosing serpentinites (Marchesi et al., 2013). We ascribe this behaviour to the breakdowns of primary igneous minerals, mainly clinopyroxene and plagioclase, to diopside and granditic garnet during rodingitization. Through these reactions, alkaline metals, LILE and Pb were mobilized into the fluid phase (Fig. 5.10c) as they are incompatible in Grt-1 (Fig. 5.5b) and only in part incorporated into less abundant diopside (especially Sr and Pb) (Fig. 5.7b).

5.4.1.2 PGE-Re abundances and Os isotopes

Concerning strongly chalcophile elements, hydrothermal alteration at reducing conditions, like those that characterize oceanic rodingitization, normally does not change the PGE abundances of mafic igneous rocks (Peucker-Ehrenbrinck et al., 2003), but may cause important uptake of Re from seawater (Reisberg et al., 2008). Metarodingites from Cerro del Almirez have PGE patterns that overlap the compositions of MORB (Fig. 5.8a), pointing to minor or insignificant mobility of PGE during rodingitization and subduction. However, opposite to the trend caused by reducing hydrothermal alteration, Re is generally more depleted in these rocks than in MORB (Fig. 5.8a) suggesting that Re was lost after igneous crystallization. Using the measured Re/Os ratio of metarodingites to calculate $^{187}Os/^{188}Os$ back to the age of intrusion (185 Ma) results in $^{187}Os/^{188}Os_{(185\ Ma)}$ = 0.1969-0.8864, which are notably higher than values expected for mantle-derived magmas (Fig. 5.9). These high initial $^{187}Os/^{188}Os$ can be either due to incorporation of radiogenic Os from Jurassic seawater, or lowering of the Re/Os ratios long after the magmatic emplacement, possibly during Alpine subduction. Osmium uptake from seawater occurs by precipitation of Fe-Mn oxyhydroxides at oxidative conditions (Ravizza et al., 2001) that are very different from the low fO_2-conditions of oceanic rodingitization (Frost and Beard, 2007). We thus conclude that seafloor rodingitization did not significantly influence the primary igneous budget of Re and PGE, but metarodingites likely experienced Re loss during subduction by mobilization in oxidizing fluids (see section 5.4.3.) (Reisberg et al., 2008).

5.4.2 Element mobility at the rodingite-serpentinite interface

Metasomatic reaction rims are present at the contact between metarodingites and enclosing ultramafic rocks (Fig. 5.10c). Metasomatic exchanges between mafic and chemically distinct rocks at the seafloor and during subduction are driven by strong gradients of chemical potentials of major elements and are favoured by infiltration of aqueous fluids (e.g., Bebout and Barton, 2002; Penniston-Dorland et al., 2014; Sorensen and Barton, 1987; Spandler et al., 2008). During seafloor rodingitization, replacement of primary minerals by Ca-Al-rich phases further promotes metasomatic alteration at the contact between serpentinite and rodingitized igneous intrusions (Boschi et al., 2006).

Along with usually fluid-immobile HFSE, strongly chalcophile elements can reveal the nature of the protoliths of metasomatic rims as they commonly preserve the imprint of their source material (Penniston-Dorland et al., 2012, 2014). Irrespective of their variable REE contents (Fig. 5.3b), Chl-blackwalls from Cerro del Almirez have abundances of HFSE (Fig. 5.4b), PGE-Re (Fig. 5.8b), and Os isotopes (Fig. 5.9) that match those of metarodingites. This coincidence indicates that Chl-blackwalls formed by massive precipitation of chlorite in the external portion of the mafic bodies, mainly triggered by chemical potential gradient of Mg toward the rodingite at the seafloor and during subduction (Fig. 5.10c, d). The variable modal abundances of chlorite and diopside in Chl-blackwalls at the sample scale (5-20 cm) (Chapter 4, Fig. 4.3) point to heterogeneous degrees of chloritization in different portions of the mafic layers. Stronger chemical potential gradients and higher-integrated fluid/rock ratios at the original rodingite-serpentinite interface likely led to greater precipitation of hydrous chlorite than inward the rodingite bodies (Fig. 5.10c). Rare earth elements (plus Th and U, Fig. 5.4b) of rodingite rims in contact with serpentinite were thus remobilized in fluids, possibly as chloride complexes (Haas et al., 1995), as they could not be incorporated into the new mineral assemblage dominated by chlorite. On the other hand, Chl-blackwalls richer in diopside from inner portions of low permeable rodingites mostly retained the original trace element abundances of their protoliths (Fig. 5.4b). Higher fluid/rock ratios (and consequently higher Cl^- concentrations) during initial formation of REE-poor Chl-blackwalls at the seafloor are also supported by their negative Eu anomaly opposed to general positive Eu anomaly in REE-rich Chl-blackwalls (Fig. 5.3b). These negative anomalies suggest Eu incorporation into hydrothermal fluids in the soluble Eu^{2+} state that forms strong aqueous complexes with dissolved Cl at reducing conditions (Allen and

Seyfried, 2005), in agreement with the low *f*O_2 conditions of rodingitization of Grand-metarodingites (Chapter 4).

Normalized patterns of strongly chalcophile elements and Os isotopes of Chl (± Ol)-Di-metasomatic rims are very similar to those of Atg-serpentinites (Figs. 5.8b, c and 5.9). These rocks thus most likely formed by massive precipitation of diopside, tremolite and chlorite in previous serpentinites triggered by strong gradients of Ca and Al chemical potentials toward the ultramafic rock at the seafloor and during subduction (Fig. 5.10c, d). Diopside in these rocks likely captured most of the trace elements (especially REE) liberated by rodingites transformed to Chl-blackwalls, increasing their bulk concentrations compared to precursor serpentinites (Fig. 5.4c).

During subduction, metasomatic reaction rims and metarodingites likely experienced local mechanical mixing possibly assisted by fluids. This interaction is suggested by higher Os concentrations and lower $^{187}Os/^{188}Os$ in one Grand-metarodingite (AL14-16) (Figs. 5.8a and 5.9), and lower Os-Ir-Ru abundances and higher Os isotopic ratios in one Chl-Ol-Di-metasomatic rim (AL14-23) (Figs. 5.8b and 5.9) compared to other samples of the same lithologies. The Os signature of AL14-16 is reproduced by simple mixing of typical metarodingite with ~ 3% Os from Chl-Di-metasomatic rim, and the I-PGE composition of AL14-23 supports contamination of a typical Chl-Ol-Di-metasomatic rim with ~ 80% of Chl-blackwall component. Physical mixing between these lithologies likely occurred by deformation and shearing during subduction (Fig. 5.10d) and was favoured by the abundance of weak layers rich in chlorite that caused juxtaposition of close lithologies at the sample scale (Bebout and Barton, 2002; Penniston-Dorland et al., 2012).

5.4.3 Geochemical evolution of Grand-metarodingites during subduction

After seafloor rodingitization, Grand-metarodingites underwent subduction metamorphism at increasing P-T up to ~1.6-1.9 GPa and 620-630 ºC (Chapter 4, Fig. 4.14). The most significant compositional changes that occurred in Grand-metarodingites during subduction were the increase of Fe_2O_3 and decrease of FeO contents due to interaction with oxidizing fluids released by the prograde transformation of lizardite to antigorite and subsequent brucite breakdown in host serpentinites (Fig. 5.10d) (Chapter 4). Higher andradite and lower grossular components in Grt-2 and Grt-3 than in Grt-1 reflect the relative high *f*O_2 composition of fluids that precipitated these new garnet-types in veins (Chapter 4, Fig. 4.4b). This change in major element composition explains the high MREE/HREE ratios of Grt-2 and Grt-3 (Fig. 5.5a), as thermodynamic data support that HREE are less compatible in Fe^{3+}-rich garnet generated at relatively high fluid/rock ratios (Gaspar et al., 2008). Despite this restriction, mass balance shows that Grt-2 and Grt-3 still host ~ 25% and 5% of whole-rock HREE, respectively. Middle rare earth elements captured in veins of Grt-2 and Grt-3 were likely remobilized in fluids at the sample scale by concomitant breakdown of diopside (Chapter 4, reactions 4 and 5).

The mineral assemblage of Grand-metarodingites also includes accessory allanite apparently in textural equilibrium with Grt-1 generated during seafloor rodingitization. However, allanite in subducted mafic rocks is normally stable from blueschist to eclogite facies conditions up to ~ 4.5 GPa and 1000 ºC (Hermann, 2002; Spandler et al., 2003; Tribuzio et al., 1996), suggesting that this phase might have crystallized during subduction of Grand-metarodingites. Mass balance calculations show that allanite, despite its very low modal amount (~ 0.1%), hosts ~ 85-95% of bulk LREE and Th in Grand-metarodingites. The presence of this accessory phase thus supports that metarodingites did not liberate significant amounts of LREE and Th into fluids during subduction up to ~ 2 GPa. This behaviour is similar to that envisaged for eclogites and metapelites (Hermann, 2002; Spandler et al., 2003; Tribuzio et al., 1996) and is consistent with the relatively low contents of LREE and Th in arc lavas generated from mantle sources contaminated by slab fluids (e.g., Elliott et al., 1997; Pearce and Peate, 1995).

As noted in section 5.4.1, the Almirez metarodingites are relatively depleted in Re compared to MORB (Fig. 5.8a). These low Re abundances are not due to subaerial volcanic degassing as the igneous protoliths of the Almirez metarodingites were doleritic dykes intruded in peridotites close to the seafloor (Fig. 5.10b) (Puga et al., 2011). Therefore, rhenium in metarodingites was most likely lost during subduction (Fig. 5.10d). Subducted metabasalts equilibrated at blueschist, eclogite or granulite facies conditions lost 40-90% of their original Re budget (Becker, 2000; Dale et al., 2007), especially in samples derived from basalts strongly affected by hydrothermal alteration (Dale et al., 2009). Subducted metarodingites from Cerro del Almirez, whose protoliths were pervasively altered close to the seafloor, thus likely experienced similar depletion in Re. As consequence of Re loss long after igneous crystallization, the Almirez metarodingites have Re/Os ratios that are too low to explain their radiogenic Os isotope compositions (Fig. 5.9). In particular, metarodingites lost on average ~ 80% of Re necessary to obtain initial $^{187}Os/^{188}Os_{(185\ Ma)}$ around the values expected for Jurassic MORB (~ 0.130)

(Gannoun et al., 2016). Partial replacement of Grt-1 induced by flux of external oxidizing fluids may have caused this important loss of Re (Fig.5.10d), as Re is mobile at oxidizing conditions (Reisberg et al., 2008) and Al-garnet is a primary repository of Re in subducted mafic rocks (Dale et al., 2009; Righter and Hauri, 1998). Flux of Re from subducting metarodingites to the mantle wedge may contribute to Re metasomatism in arc peridotites and to generation of Re-rich magmas (Sun et al., 2003).

5.4.4 Metarodingite evolution during dehydration of enclosing antigorite serpentinites

The circulation of fluids released during dehydration of Atg-serpentinites and their transformation to Chl-harzburgites produced significant changes in the whole-rock and mineral compositions of enclosed metarodingites. These changes were driven by the increase of SiO_2 and decrease of CaO chemical potentials at H_2O-satured and high fO_2 conditions favoured by the flux of abundant fluids from dehydrating serpentinites (Chapter 4). The interaction of metarodingites with these oxidizing fluids produced the replacement of granditic garnets (Grt-1, Grt-2 and Grt-3) by epidote/clinozoisite and of chlorite by diopside, leading to the oxidation of ferrous iron (Chapter 4, reaction 6 and 7). These processes finally resulted in the formation of Type 2 Ep-metarodingites from precursor Type 1 Grand-metarodingites at ~ 1.6-1.9 GPa and 630-650 °C (Chapter 4, Fig. 4.14). The extent of this transformation is related to the abundance of fluids in the system, and is thus commonly incipient in many metarodingite layers enclosed in Atg-serpentinites and well developed in boudins close to the serpentinite dehydration front (Chapter 4, Fig. 4.2d).

In terms of major elements, the transition of Grand- to Ep-metarodingites mainly caused Ca-Mn depletion, related to the replacement of granditic garnets, and enrichment in Si (Fig. 5.1a) leading to crystallization of new diopside (Fig. 5.11a) (Chapter 4, reaction 8). Except for Eu concentrations (see below), no appreciable differences exist between Grand- and Ep-metarodingites in terms of whole-rock REE abundances (Fig. 5.3a), supporting that REE in metarodingites were mostly not mobilized by interaction with serpentinite-derived fluids. This behaviour is different from that of enclosing serpentinites, which lost MREE during dehydration (Fig. 5.3d) owing to the absence of a suitable repository for MREE in Chl-harzburgites (Garrido et al., 2005; Marchesi et al., 2013). However, REE in Ep-metarodingites were redistributed in the new mineral assemblage, especially into epidote (Fig. 5.6a), garnet (Grt-2, Grt-3 and Grt-4) (Fig. 5.5a) and likely titanite (Spandler et al., 2003). Mass balance shows that epidote hosts almost all LREE, ~ 80-95% of MREE and 45-70% of HREE, and garnet and titanite accommodate the rest of the whole-rock REE budget. Epidote in Type 2 metarodingites is slightly enriched in Eu (Fig. 5.6a) similar to epidote in hydrothermal veins (Frei et al., 2004). This Eu enrichment, evident also in some whole-rock Ep-metarodingites (Fig. 5.3a), possibly reflects early crystallization of titanite (Chapter 4, reaction 9) that generates a positive Eu anomaly in the residual fluid and in minerals crystallizing with or after titanite (Loader et al., 2017). Epidote also hosts almost all Sr and Pb and ~ 90% of Ba in Ep-metarodingites, which are notably enriched in these elements compared to Grand-metarodingites at the whole-rock scale (Fig. 5.4a). Type 2 metarodingites thus likely partitioned Sr, Pb and Ba from serpentinite-derived fluids (Fig. 5.11a) by simple homovalent substitution for Ca^{2+} in epidote (Frei et al., 2004). The mobility of Si, Sr, Pb and Ba in serpentinite-derived fluids is confirmed by their abundance in fluid inclusions from high-pressure Chl-harzburgites generated by antigorite breakdown (Scambelluri et al., 2001, 2004, 2015). These inclusions also bear Cl-apatite (Scambelluri et al., 2001), supporting that Ca was mobile in the dehydrating system and fluids were rich in Cl that promoted the mobility of trace elements (Kendrick al., 2011).

Epidote-metarodingites also have slightly lower Pt and Pd concentrations than Grand-metarodingites (Fig. 5.8a) suggesting that fluids extracted P-PGE from metarodingites. Platinum and Pd loss in metabasalts equilibrated at eclogite facies conditions has been ascribed to addition of a sulphur-rich oxidizing fluid that promoted the replacement of igneous sulphides by pyrite (Dale et al., 2009). Oxidizing fluids produced by Atg-breakdown have a significant budget of sulphur (Alt et al., 2012, 2013; Schwarzenbach et al., 2018) and may be able to slightly remobilize Pt and Pd as bisulfide complexes (Pan and Wood, 1994) especially in metamafic rocks derived from highly deformed and altered protoliths (Dale et al., 2009). Strong flux of fluids produced by Atg-breakdown thus possibly promoted the alteration of the primary sulphide assemblage of metarodingites and the partial release of Pt and Pd (Fig 5.11a). Chl-harzburgites close to Ep-metarodingites also have lower Pt and Pd abundances, lower $^{187}Os/^{188}Os$, and usually higher Re contents than Chl-harzburgites far from the mafic layers (Fig. 5.8d and Table A16). These variations suggest that serpentinite-derived fluids removed interstitial magmatic sulphides, with relatively radiogenic Os and high Pt-Pd concentrations (Alard et al., 2005; Luguet et al., 2003), from the ultramafic rocks proximal to metarodingites and precipitated Re-rich pyrite (Reisberg et al., 2008). Fluids possibly transferred radiogenic Os and P-PGE to Chl-harzburgites far from the mafic layers (Fig. 5.8d) or to the mantle wedge. Contamination by fluids issued from subducting eclogites, metarodingites and host ultramafic rocks may thus explain the relatively high $^{187}Os/^{188}Os$ of some arc mantle xenoliths (Brandon et al., 1996) and the high Pt-Pd abundances in the mantle beneath giant porphyry ore deposits of chalcophile elements (McInnes et al., 1999).

5.4.5 Formation of Pyralspite-metarodingites and open-system late amphibolitization

Rare bodies of Pyrals- metarodingites occur exclusively within the Chl-harzburgite domain (Chapter 4, Fig. 4.1). This metarodingite type derives from Ep-metarodingite by partial epidote breakdown to new pyralspitic garnet (Grt-5) and diopside transformation to tremolitic amphibole (Amp-1) at peak metamorphic conditions (~ 1.6-1.9 GPa, 660-685 °C) (Chapter 4, Fig. 4.14). The gradient of chemical potentials of major elements (mainly Mg and Ca) between metarodingites and host Chl-harzburgites controlled the formation of Pyrals-metarodingites (Chapter 4, Fig. 4.13a). This gradient induced the loss of Ca (Fig. 5.1a), the incorporation of Mg (Fig. 5.1b) and the reduction of Fe^{3+} in metarodingites (Fig. 5.2a) at fluid saturation conditions. The other differences in terms of major elements between Ep- and Pyrals-metarodingites are due to late amphibolitization (see below).

Whole-rock concentrations of REE in Pyrals-metarodingites are similar to those of the other metarodingite-types (Fig. 5.3a), pointing to no remobilization of REE at peak metamorphic conditions. In these rocks, REE were partitioned mainly between epidote (~ 95-100% of LREE and MREE, and 65-90% of HREE) (Fig. 5.6a), Grt-5 (~ 5-30% of HREE) (Fig. 5.5a) and Amp-1/diopside (~ 1-5% of MREE and HREE) (Fig. 5.7a). Contrary to REE, whole-rock Sr concentrations are lower in Pyrals-metarodingite than in Ep-metarodingite (Fig. 5.4a), due to lower epidote amounts partially replaced by Grt-5 that is notably poor in Sr (Fig. 5.5b). Therefore, the formation of Pyrals-metarodingites from precursor Ep-metarodingites induced the release in fluids of elements manly hosted in epidote, such as Ca, Sr and most probably Pb, and the incorporation of Mg likely from enclosing Chl-blackwalls (Fig. 5.11b).

After the formation of the main mineral assemblages, pargasitic amphibole (Amp-2) crystallized in each metarodingite type at retrograde conditions (Chapter 4). These variably amphibolitized samples have compositional differences compared to non-amphibolitized corresponding metarodingites. In terms of major elements, amphibolitization mainly caused enrichment in Mg (Fig. 5.1b), Na, K (Fig. 5.1c), Fe^{2+} (Fig. 5.2a), and depletion of Ca (Figs. 5.1a and 5.11c). On the other hand, REE remained immobile (Fig. 5.3a). Amphibolitization also caused whole-rock enrichment in Cs, Rb and Ba (Fig. 5.4a, 5.11c) that are notably partitioned in Amp-2 (Fig. 5.7b). These compositional changes are due to fluxing of external metasediment-derived fluids (from metapelites and metaevaporites) into the ultramafic-metarodingite system, which led to crystallization of Amp-2 (Chapter 4) possibly initiating at P-T conditions close to antigorite breakdown in serpentinites (Marchesi et al., 2013) and formation of spinifex-like Chl-harzburgites (Dilissen et al., 2019). This scenario is similar to that envisioned for the Cima di Gagnone Chl-harzburgites, which have relatively radiogenic Sr and Pb isotopic signatures due to prograde interaction with fluids from host metapelites (Cannaò et al., 2015). Interaction of metarodingites from Cerro del Almirez with fluids from metasediments continued during exhumation (Chapter 4), when the Almirez ultramafic section was tectonically joined to subducted micaschists (Jabaloy-Sánchez et al., 2015).

5.4.6 The role of metarodingites in the fluid-mediated element recycling in subduction zones

During subduction, mantle and crustal rocks in the slab and slab-mantle interface experiment successive metamorphic reactions that release fluids to the supra-subduction mantle wedge and promote recycling of mobile elements (e.g., B, Li, As, Sb and LILE) in the sources of arc magmas (Fig. 5.11d) (e.g., Scambelluri and Tonarini, 2012; Schmidt and Poli, 2014; Spandler and Pirard, 2013). Subducted serpentinites and subduction mélanges with serpentinite matrix contain metarodingites (e.g., Cannaò et al., 2015; Hu et al., 2017; Koutsovitis et al., 2013; Li et al., 2007; Scambelluri and Rampone, 1999; Zanoni et al., 2016) but the role of these rocks in the geochemical processes occurring in subduction zones has generally been neglected. This scarce attention is possibly due to the lower abundance of rodingites in the oceanic crust compared to serpentinites and mafic rocks less affected by hydrothermal alteration. For instance, metarodingites constitute only ~ 0.03% of the outcropping surface in the Almirez ultramafic massif. However, field observations show that metarodingites may locally be abundant in subduction mélanges (Cannaò et al., 2015) and subduction-related ophiolites (~ 5% in volume) (Dai et al., 2016). Rodingites may also be relatively common in lithologically heterogeneous oceanic core complexes exhumed by detachment faulting at slow

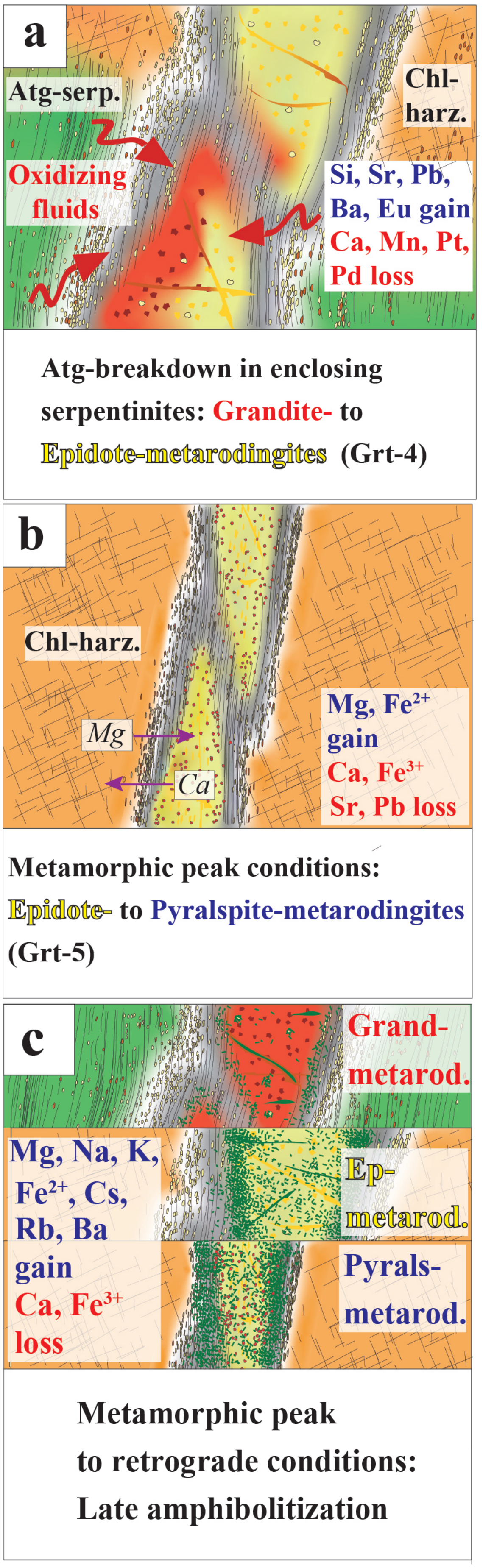

spreading centres (Boschi et al., 2006). At the present day, material produced at slow and ultra-slow spreading ridges is a minor portion of the oceanic lithosphere subducted globally (Alt et al., 2013), implying that minimal amount of rodingites is currently subducted. However, these lithologies may have had greater impact in the Cretaceous and Cenozoic when the Jurassic Tethys oceanic lithosphere generated at slow and ultra-slow ridges subducted (e.g., Handy et al., 2010).

Thermodynamic modelling of the subduction evolution of metarodingites from Cerro del Almirez (Chapter 4) shows that these rocks underwent a P-T path similar to that of sub-arc domains in relatively hot and flat subduction zones (Syracuse et al., 2010). The geochemical evolution of the Almirez metarodingites summarized in Figs. 5.10 and 5.11 can therefore assess the impact of these lithologies on the composition of fluids released in subduction zones and of crustal material recycled in the deep mantle.

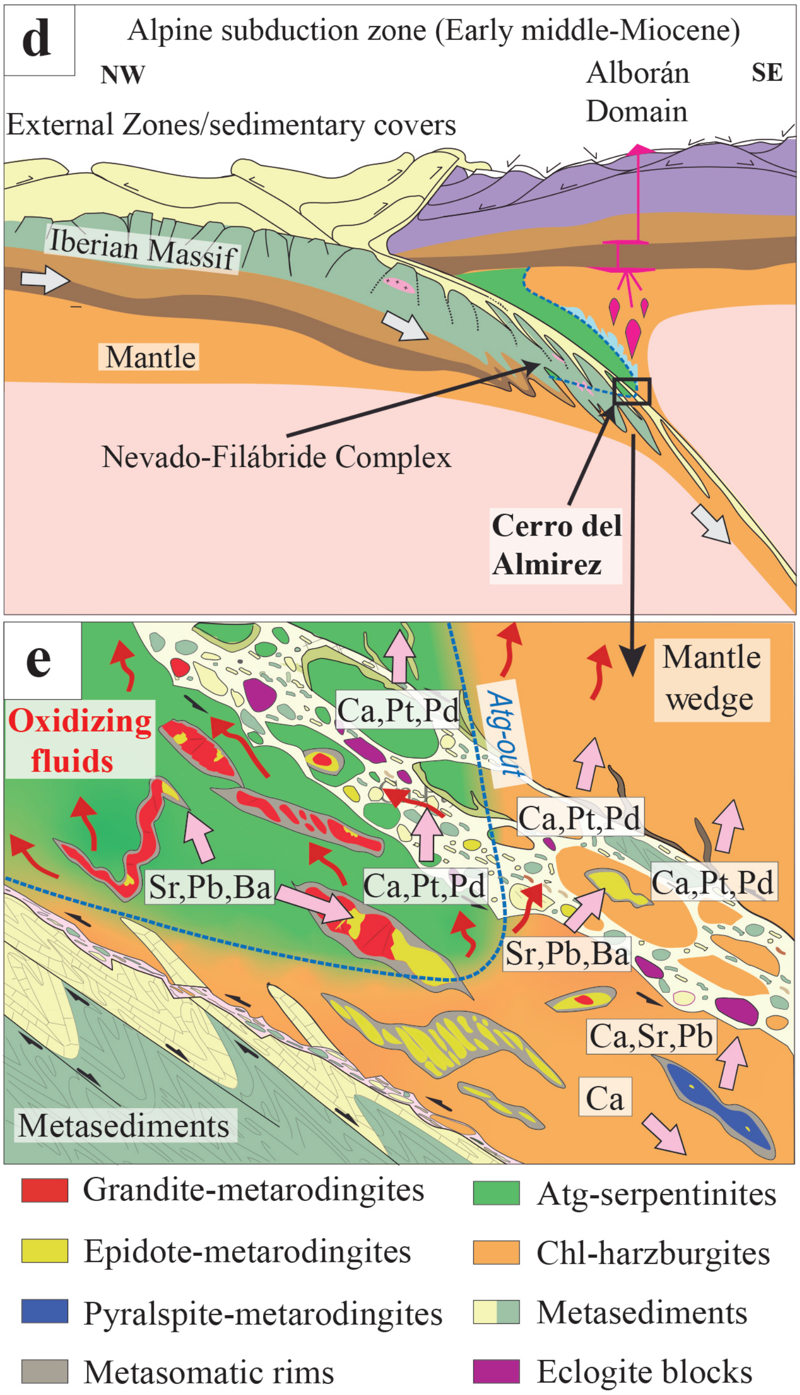

Figure 5.11. ***(a)*** *Sketch showing the mineralogical and compositional changes associated with transformation of Grand- to Ep-metarodingites triggered by fluids liberated through dehydration of Atg-serpentinites to Chl-harzburgites. Red arrows: oxidant serpentinite-derived fluids.* ***(b)*** *Cartoon resuming the compositional changes related to transformation of Ep- to Pyrals-metarodingites at peak metamorphic conditions in the Chl-harzburgite stability field.* ***(c)*** *Sketch of the mineralogical and geochemical modifications due to late amphibolitization of metarodingites.* ***(d)*** *Geological sketch representing the proposed setting of the Cerro del Almirez ultramafic massif (black box) during the Miocene subduction of the Nevado-Filábride Complex.* ***(e)*** *Schematicrepresentation of the main geochemical exchanges (pink arrows) at the slab-mantleinterface caused by the presence of metarodingites fluxed by fluids from dehydratingserpentinites (red arrows).*

5.4.6.1 Significance of metarodingites for the redox state of subduction zones

During progressive subduction before antigorite breakdown, dehydration reactions in serpentinites discharge fluids that oxidize iron in metarodingites (Fig. 5.10d). Fluids produced by incipient antigorite breakdown induce a similar effect (Chapter 4). Subducted metarodingites thus react with oxidizing fluids generated by dehydration reactions in serpentinites over a large range of pressure, and possibly limit the capacity of fluids to oxidize mantle wedge peridotites far from the slab (Debret and Sverjensky, 2017; Debret et al., 2014, 2015; Merkulova et al., 2017). Conversely, the formation of Pyrals-metarodingites and Chl-blackwalls in Chl-harzburgites occurs via reducing reactions (Fig. 5.11b) and may thus contribute to the redox budget of the deep sub-arc mantle (Evans, 2012) close to and beyond the P-T conditions of Atg breakdown. Moreover, metastable oxidized Grand- and Ep-metarodingites are preserved in the Chl-harzburgite domain as their complete transformation to Pyrals-metarodingites is kinetically inhibited (Chapter 4). Oxidized metastable metarodingites may thus subduct to the deep mantle and mix with the asthenosphere influencing its oxidation state.

5.4.6.2 Trace element partitioning into slab fluids

The mineral assemblages of metarodingites contain epidote minerals (allanite and epidote) during most of their subduction evolution up to ~ 2 GPa (Chapter 4). These phases are the main repositories of LREE in metarodingites and preferentially partition these elements against fluids (Frei et al., 2004). Therefore, the presence of metarodingites in the subducting slab hinders the transfer of significant amounts of LREE to the mantle wedge. The stability of epidote in Type 2 metarodingites also causes the incorporation of Sr, Pb and Ba (± Eu) from serpentinite-derived fluids (Fig. 5.11a). This effect is reverted at higher metamorphic grade when Type 2 Ep-metarodingites convert to Type 3 Pyrals-metarodingites (Fig. 5.11b) by, among other reactions, partial epidote breakdown to new pyralspitic Grt-5. Ep-metarodingites may thus hamper the transfer of the Sr-Pb isotopic signatures of subducted lithologies to the source of arc magmas (Fig. 5.11e) and incorporate Sr-Pb from dehydrating metasediments more efficiently than ultramafic rocks (Cannaò et al., 2015). Moreover, the partitioning of Ba into epidote of metarodingites generates slab fluids with low Ba/Th and Ba/Nb ratios that mimic the geochemical imprint of a sediment melt component (Elliott et al., 1997). Therefore, the application of trace element ratios in arc lavas to identify the subduction components in their sources (e.g., Pearce et al., 2005) should take into account the misleading effect of element fractionation by minerals in the slab.

5.4.6.3 Lithological heterogeneity at the slab-mantle interface

Similar to metasediments and other metamafic rocks, subducted metarodingites and spatially related reaction rims may experience tectonic and metasomatic mixing at the slab-mantle interface (Fig. 5.11e) (e.g., Bebout and Barton, 2002; Bebout and Penniston-Dorland, 2016; Schwarzenbach et al., 2018). Indeed, PGE abundances and Os isotopes indicate local mixing between metarodingites and metasomatic rims likely favoured by the weak rheology of the latter (see section 5.4.2). Fluid-mediated mass transfer and metasomatic alteration caused by juxtaposition of disparate lithologies in subduction mélanges may generate hybrid domains with the trace element and isotopic signatures of arc magmas (e.g., Bebout and Barton, 2002; Spandler et al., 2008). These domains may then rise in buoyant diapirs toward the inner and hotter region of the mantle wedge and produce magmas with subduction-related affinity (Marschall and Schumacher, 2012).

Chl-blackwalls formed by metasomatic reactions at the metarodingite-serpentinite interface (Fig. 5.10c, d) illustrate an example of the potential impact of metarodingites on the transfer of trace elements at the slab-mantle interface. These lithologies are dominated by chlorite and are so similar to chlorite schists present in high-pressure subduction mélanges (Spandler et al., 2008). Owing to the high stability of chlorite in this type of rocks (Bebout, 1991), Chl-blackwalls around metarodingite bodies may be important carriers of volatiles in the deep mantle, especially beyond the stability field of serpentinites, and may liberate fluids able to strip high contents of trace elements from metasediments and mafic rocks. Therefore, metarodingites and associated metasomatic rims, which can metastably persist beyond their stability field in the slab (Chapter 4), are additional lithologies that should be considered in models of trace element mobility in subduction mélanges (Fig. 5.11e).

5.4.6.4 Behaviour of strongly chalcophile elements

Metarodingites from Cerro del Almirez underwent significant loss of Re, Pt and Pd during subduction (Figs. 5.10d and 5.11a). The mobility of these chalcophile elements may have been favoured by the oxidizing nature of fluids produced by serpentinite dehydration, as solubility of S, Re and P-PGE is promoted at relative high fO_2 (Pan and Wood, 1994; Reisberg et al., 2008). The redox signature of fluids from serpentinites is linked to the extent of serpentinization of their mantle precursors (Evans et al., 2017). Extensive serpentinization at the seafloor of hyperextended continental margins (Fig. 5.10a) or ultra-slow spreading centres induces the release of oxidizing fluids by serpentinite dehydration at high pressure (Evans et al., 2017). The oxidant character of these fluids enhances the mobility of S and therefore the concentration of sulphide complexes, thus favouring the transport of chalcophile metals to the mantle wedge. Therefore, subduction of metarodingites from magma-poor tectonic settings may promote metal endowment in the supra-subduction mantle as these rocks may release P-PGE and Re in serpentinite-derived fluids (Fig. 5.11e). Enrichment of supra-subduction peridotites in P-PGE and Re from metarodingites may generate arc magmas relative rich in these metals, and explain the relatively radiogenic $^{187\text{-}186}$Os/^{188}Os signature of some arc lavas and arc mantle xenoliths, which implies relatively high time-integrated Re/Os and Pt/Os ratios (Gannoun et al., 2016).

5.4.6.5 Ca recycling in subduction zones

An important influence of metarodingites on the composition of fluids liberated by subducting slabs is to enhance their Ca concentrations. Metarodingites incorporate Ca mainly from abyssal serpentinites on the seafloor, and they are notably richer in Ca than other high-pressure metamafic rocks (i.e., blueschists and eclogites). However, around half of the whole-rock Ca budget of metarodingites (Fig. 5.1a) is released in fluids upon subduction at the P-T conditions of Grand-Ep (Fig. 5.11a) and Ep-Pyrsals metarodingite transitions (Fig. 5.11b). The interaction of Ca-silica-rich fluids with mantle peridotites in different tectonic settings, including subduction zones (Fig. 5.11e), causes precipitation of secondary clinopyroxene and orthopyroxene (Grant et al., 2016; Ishimaru and Arai, 2011; Python et al., 2007). This process may generate replacive lithologies in the sub-arc mantle, such as pyroxenites and refertilized lherzolites, and hence change not only the geochemical signature of the arc magma sources but also increase their melt-productivity (e.g., Schiano et al., 2000). Subduction of metarodingites may thus promote the lithological and geochemical heterogeneity of the supra-subduction mantle and the generation of arc magmas from Ca-bearing refractory mantle peridotites, such as the clinopyroxene-poor lherzolite sources of high-Ca boninites (Cooper et al., 2010).

Despite their important Ca loss during subduction, metarodingites subducted to ~ 2 GPa are still richer in calcium than metamafic rocks with MORB-like compositions (Fig. 5.1a). Moreover, metastable Ca-rich Grand- and Ep-metarodingites may subduct to higher depths than those corresponding to their transformation to Ca-poorer Pyrals-metarodingites, as this reaction is hampered by the strong rheology and low permeability of metarodingites (Chapter 4). Crystallization of Ca-rich minerals in polyphase inclusions in diamond from 300-360 km depths has been ascribed to subduction and recycling of crustal Ca-rich lithologies in the convective upper mantle (Brenker et al., 2005). Metarodingites, ophicarbonates, and calcareous-siliceous oozes are plausible sources of this calcium-silicate reservoir in the deep mantle (Brenker et al., 2005). Subduction and recycling of Ca-rich metarodingites in the asthenosphere (Fig. 5.11e) may therefore generate a deep Ca-rich reservoir with some of the geochemical characteristics of ocean island basalts (OIB) (Brenker et al., 2005).

Part III

CONCLUSIONES, CONCLUSIONS, REFERENCES AND APPENDICES

6 Conclusiones

Esta tesis aporta nuevos conocimientos sobre la evolución petrológica y geoquímica de las metarrodingitas encajadas en las rocas ultramáficas del Cerro del Almirez (Cordillera Bética, sur de España), desde su formación en el fondo oceánico hasta la subducción a profundidades "sub-arco". Las observaciones de campo de estas rocas y su estudio petrológico y geoquímico han arrojado nueva luz sobre: (i) la evolución metamórfica de las metarrodingitas durante la subducción; (ii) el comportamiento geoquímico de los elementos litófilos mayores y trazas, y de los elementos altamente sideróflos; (iii) la interacción de las metarrodingitas con fluidos liberados por reacciones de deshidratación en las serpentinitas que las alojan; y (iv) la importancia general de las metarrodingitas en el marco de los procesos de subducción.

Las relaciones de campo, las texturas, las composiciones de la roca total y de los minerales, además del análisis quimográfico y los modelos termodinámicos, definen la evolución metamórfica de las metarrodingitas del Cerro del Almirez durante la subducción. Los protolitos máficos ígneos, después de haber sufrido una completa rodingitización en condiciones altamente reductoras en el fondo oceánico (<2 kbar, ~150–325 °C, ~FMQ), se transformaron en rodingitas con grandita (ricas en granate grandítico (Grt-1), diópsido, clorita y magnetita) que recristalizaron durante el inicio de la subducción a metarrodingitas con grandita. Durante la evolución metamórfica progrado, dos generaciones de granate se formaron en las metarrodingitas con grandita a alta presión y temperatura (> 10 kbar, ~350–650 °C). El Grt-2b, más rico en los componentes andradita y piralspita que el Grt-1, cristalizó en condiciones tamponadas por la composición de la propia metarrodingita (fO_2 ~FMQ). El Grt-3, notablemente más rico en andradita, se formó debido a la entrada de fluidos oxidantes que probablemente se liberaron a partir de la desestabilización de brucita y antigorita en las serpentinitas encajantes (fO_2 ~HM).

La transformación de las metarrodingitas con grandita en metarrodingitas con epidota (epidota, diópsido, granate y titanita) fue impulsada por el efecto simultáneo de gradientes de potencial químico, que produjeron el aumento de μSiO_2 y la disminución de μCaO, y el flujo de grandes cantidades de fluidos de carácter oxidante liberados por la completa deshidratación de la antigorita en las serpentinitas encajantes. Dentro de las harzburgitas con clorita, producto de la deshidratación de serpentinitas, algunos cuerpos de metarrodingitas con epidota se transformaron en metarrodingitas con piralspita (Grt-5, Amp-1 tremolítico, epidota, zoisita, clorita y rutilo) en condiciones del pico metamórfico (16–19 kbar, 660–684 °C). Esta transformación fue impulsada por la disminución de μCaO, el aumento de μMgO, y la fuerte disminución en la proporción Fe^{3+} / Fe_{Total} de la roca. El contraste entre las proporciones de Fe^{3+}/Fe_{Total} entre las serpentinitas con antigorita y las harzburgitas con clorita, y entre los tres tipos de metarrodingitas encajadas en estas rocas ultramáficas, atestigua un grado de oxidación altamente heterogéneo de la losa de subducción, e indica que las metarrodingitas juegan un papel importante en la transferencia de materiales oxidados al manto profundo.

Las metarrodingitas del Cerro del Almirez derivan de basaltos y doleritas que experimentaron una pérdida de Si, Na, K y un enriquecimiento en Ca durante la rodingitización en el fondo oceánico, coetánea a la serpentinización de las peridotitas encajantes. Durante la rodingitización, las tierras raras (REE) permanecieron inmóviles a escala de la roca total, pero se redistribuyeron entre las nuevas fases metamórficas de las rodingitas con grandita. En particular, las tierras raras pesadas (HREE) se concentraron principalmente en el Grt-1. Por el contrario, los elementos litófilos de alto radio iónico (LILE: Cs, Rb, Ba y Sr) y el Pb se removilizaron en los fluidos reductores como resultado de la ruptura de los minerales ígneos primarios durante la rodingitización. En el fondo oceánico y durante la subducción posterior, los fuertes gradientes de potenciales químicos de Mg, Ca y Al en el contacto rodingita-serpentinita causaron la cloritización heterogénea de los bordes de las rodingitas, transformándolos en *blackwalls* de clorita, e impulsaron la precipitación masiva de diópsido en las serpentinitas adyacentes, transformándolas en bordes de reacción ricos en clorita y diópsido, o clorita, diópsido y olivino, enriquecidos en REE.

Durante la subducción, las metarrodingitas y los bordes de reacción metasomáticos se mezclaron localmente por mecanismos de cizallamiento favorecidos por la abundancia de clorita en el contacto entre estas rocas. Durante la subducción de las metarrodingitas con grandita, el hierro se oxidó y el Re se removilizó en los fluidos relacionados con el reemplazamiento del Grt-1 por Grt-2 y Grt-3 con una mayor proporción de componente andradítico. Por otro lado, la presencia de allanita accesoria en las metarrodingitas con grandita inmovilizó las LREE y el Th durante la subducción.

Debido al intenso flujo de fluidos oxidantes producidos por la ruptura final de la antigorita en las serpentinitas encajantes, las metarrodingitas con grandita se transformaron en metarrodingitas con epidota, las cuales atraparon, principalmente en la epidota, Si, Sr, Pb, Ba y Eu, y liberaron Ca, Mn, Pt y Pd en los fluidos. En las condiciones del pico metamórfico, las metarrodingitas con epidota se transformaron en metarrodingitas con piralspita mediante reacciones de reducción que consumieron la epidota y liberaron Ca, Sr y Pb más allá de las condiciones de desestabilización de la antigorita. Todos los tipos de metarrodingitas experimentaron una anfibolitización tardía, desencadenada por la entrada de fluidos externos provenientes de metasedimentos, que causó enriquecimiento en Mg, Fe^{2+}, Na, K, Cs, Rb y Ba y empobrecimiento en Ca y Fe^{3+}.

Las metarrodingitas situadas en el manto serpentinizado de la losa que subduce, y en la interfaz entre la losa y la cuña de manto, pueden reducir la capacidad de oxidación de los fluidos derivados de las serpentinitas y, por lo tanto, aumentar el aporte de material oxidado al manto profundo. La allanita y la epidota de las metarrodingitas actúan como sumideros de LREE-Th y Sr-Pb-Ba, respectivamente, y mantienen estos elementos en la losa deshidratada que subduce. La retención de estos elementos puede dificultar la identificación y cuantificación del componente de subducción (ej., fluidos liberados de la corteza máfica frente a fundidos de metasedimentos) en las fuentes de los magmas de arco volcánico. Las metarrodingitas y los bordes de reacción metasomáticos asociados contribuyen a la heterogeneidad litológica y composicional de la interfaz entre la losa y la cuña del manto, e influyen en la movilidad de los elementos traza en esta porción tan crucial de las zonas de subducción. La liberación en los fluidos de Re, Pt, Pd y Ca procedentes de metarrodingitas puede enriquecer a la cuña del manto en metales preciosos, favoreciendo así la generación de yacimientos minerales, e inducir un metasomatismo de Ca que conlleve la refertilización del manto sub-arco. Sin embargo, las metarrodingitas subducidas en condiciones de facies de eclogita aún conservan alrededor de la mitad de su contenido original de Ca y, por consiguiente, su reciclaje en la astenosfera profunda puede generar reservorios ricos en Ca similares a las fuentes de los OIB.

7 Conclusions

This thesis provides new insights into the petrological and geochemical evolution of metarodingites enclosed in ultramafic rocks of the Cerro del Almirez massif (Betic Cordillera, southern Spain), from their formation at ocean floor conditions to subduction at sub-arc depth. Combined field, petrological and geochemical studies have shed new light on: (i) the metamorphic evolution of rodingites during subduction; (ii) the geochemical behavior of lithophile major and trace elements, and highly siderophile elements; (iii) the interaction of rodingites with fluids released from dehydration reactions in the enclosing serpentinites; and (iv) the general significance of metarodingites in subduction settings.

Field and textural relationships, mineral and whole-rock compositions, chemographic analyses, and thermodynamic models constrain the subduction evolution of metarodingites from Cerro del Almirez. After complete rodingitization of igneous mafic protoliths at highly reducing conditions in a seafloor setting (<2 kbar, ~150–325 °C, ~FMQ buffer), Grand-metarodingite (grossular-rich garnet (Grt-1), diopside, chlorite, and magnetite) recrystallized during subduction. Then, two generations of garnet formed in Grand-metarodingite by prograde metamorphism at high pressure (>10 kbar, ~350–650 °C). Grt-2b, which is richer in andradite and pyralspite components than Grt-1, crystallized at conditions buffered by the metarodingite whole-rock composition (fO_2 ~FMQ buffer). Grt-3, notably richer in andradite, formed during flux of oxidizing fluids (fO_2 ~HM buffer) likely released from brucite and partial antigorite breakdowns in host Atg-serpentinites.

Transformation of Grand-metarodingite into Ep-metarodingite (epidote, diopside, garnet, and titanite), was driven by the simultaneous effects of increasing μSiO_2 and decreasing μCaO gradients, triggered by the flux of high amounts of oxidizing fluids released during high-pressure final Atg-breakdown in host serpentinites. Within Chl-harzburgites produced by serpentinite dehydration, some epidote-metarodingite bodies transformed into pyralspite-metarodingites (Grt-5, tremolitic Amp-1, epidote, zoisite, chlorite and rutile) at peak metamorphic conditions (16–19 kbar, 660–684 °C) by decreasing μCaO and increasing μMgO gradients, and a strong drop in the whole-rock Fe^{3+}/Fe_{Total} ratio. The contrasting Fe^{3+}/Fe_{Total} ratios between Atg-serpentinite and Chl-harzburgite, and between the three metarodingite types enclosed in these ultramafic rocks, attest for the highly heterogeneous oxidation degree of the subducting slab, and highlight the role of metarodingites in the transfer of oxidized materials to the deep mantle beyond the Atg-out isograd in subducted serpentinites.

Metarodingites from Cerro del Almirez derive from basalts and dolerites that experienced Si, Na, K loss and Ca enrichment caused by rodingitization and concomitant serpentinization of host peridotites close to the seafloor. During rodingitization, REE remained immobile at the whole-rock scale but partitioned into the new mineral phases of Grandite-rodingites. HREE were especially incorporated into granditic Grt-1. Conversely, LILE (Cs, Rb, Ba and Sr) and Pb were remobilized into reducing fluids as result of breakdown of primary igneous minerals mainly to Grt-1 and diopside. At the seafloor and during subduction, strong gradients of chemical potentials of Mg, Ca and Al at the rodingite-serpentinite interface caused heterogeneous chloritization of the rodingite rim transformed to Chl-blackwall, and massive precipitation of diopside in serpentinites converted to Chl-Di and Chl-Ol-Di-metasomatic rims richer in REE.

Metarodingites and metasomatic reaction rims locally mixed via subduction shearing favoured by the abundance of weak chlorite at the contact between these rock types. Prograde subduction metamorphism induced iron oxidation and Re loss in Grand-metarodingites associated with partial replacement of Grt-1 by Grt-2 and Grt-3 with higher andraditic component and MREE/HREE ratios. Accessory allanite crystallized in subducting Grand-metarodingites and efficiently sequestered LREE and Th during subduction.

Due to the intense flux of oxidizing fluids produced by final antigorite breakdown in host serpentinites, Grand-metarodingites transformed into Ep-metarodingites that trapped Si, Sr, Pb, Ba and Eu mostly into epidote, and liberated Ca, Mn, Pt and Pd into fluids. At peak metamorphic conditions, Ep-metarodingites transformed to Pyrals-metarodingites by reducing reactions that consumed epidote and released Ca, Sr and Pb beyond the conditions of antigorite breakdown. All metarodingite types experienced late amphibolitization triggered by incoming external fluids from metasediments that caused enrichment in Mg, Fe^{2+}, Na, K, Cs, Rb, Ba and depletion in Ca and Fe^{3+}.

Metarodingites in subducted serpentinized slab mantle and at the slab-mantle interface may reduce the oxidizing capacity of serpentinite-derived fluids and increase the redox budget of the deep mantle. Allanite and epidote in metarodingites act as sinks of LREE-Th and Sr-Pb-Ba, respectively, and thus hold these elements in the subducting dehydrating slab. This retention may hinder the identification of the slab component (e.g., fluid from the mafic crust vs. sediment melt) and the quantification of its imprint to the sources of arc magmas. Metarodingites and related metasomatic rims contribute to the lithological and compositional heterogeneity of the slab-mantle interface and influence the mobility of trace elements in this crucial region of subduction zones. The release of Re, Pt, Pd and Ca from metarodingites in slab fluids may endow the mantle wedge with precious metals, thus favouring the generation of ore deposits, and induce Ca metasomatism and refertilization in the sub-arc mantle. However, subducted metarodingites still conserve around half of their Ca budgets at eclogite facies conditions and their recycling in the deep asthenosphere may generate Ca-rich reservoirs similar to OIB sources.

8 References

Ague, J. J., and Carlson, W. D. (2013). Metamorphism as Garnet Sees It: The Kinetics of Nucleation and Growth, Equilibration, and Diffusional Relaxation. *Elements, 9*(6), 439-445.

Alard, O., Luguet, A., Pearson, N. J., Griffin, W. L., Lorand, J.-P., Gannoun, A., Burton, K. W., and O'reilly, S. Y. (2005). In situ Os isotopes in abyssal peridotites bridge the isotopic gap between MORBs and their source mantle. *Nature, 436*(7053), 1005.

Alberti, A., Comin-Chiaramonti, P., and Moazez, S. (1976). On some rodingite occurrences in north-eastern Iran. *Neues Jahrb. Mineral. Monatsh*, 185-191.

Allen, D. E., and Seyfried Jr, W. (2005). REE controls in ultramafic hosted MOR hydrothermal systems: an experimental study at elevated temperature and pressure. *Geochimica Et Cosmochimica Acta, 69*(3), 675-683.

Alt, J. C., Garrido, C. J., Shanks III, W. C., Turchyn, A., Padrón-Navarta, J. A., López Sánchez-Vizcaíno, V., Pugnaire, M. T. G., and Marchesi, C. (2012). Recycling of water, carbon, and sulfur during subduction of serpentinites: A stable isotope study of Cerro del Almirez, Spain. *Earth and Planetary Science Letters, 327*, 50-60.

Alt, J. C., Schwarzenbach, E. M., Früh-Green, G. L., Shanks, W. C., Bernasconi, S. M., Garrido, C. J., Crispini, L., Gaggero, L., Padrón-Navarta, J. A., and Marchesi, C. (2013). The role of serpentinites in cycling of carbon and sulfur: Seafloor serpentinization and subduction metamorphism. *Lithos, 178,* 40-54.

Anders, E., and Grevesse, N. (1989). Abundances of the elements: Meteoritic and solar. *Geochimica Et Cosmochimica Acta, 53*(1), 197-214.

Andersen, D. J., and Lindsley, D. H. (1988). Internally consistent solution models for Fe-Mg-Mn-ti oxides: Fe-Ti oxides. *The American Mineralogist, 73*(7-8), 714-726.

Andreani, M., Munoz, M., Marcaillou, C., and Delacour, A. (2013). μXANES study of iron redox state in serpentine during oceanic serpentinization. *Lithos, 178*, 70-83.

Andrut, M., Wildner, M., and Beran, A. (2002). The crystal chemistry of birefringent natural uvarovites. Part IV. OH defect incorporation mechanisms in non-cubic garnets derived from polarized IR spectroscopy. *European Journal of Mineralogy, 14*(6), 1019-1026.

Anhaeusser, C. R. (1979). Rodingite occurences in some Archaean Ultramafic Complexes in the Barberton Mountain Land, South-Africa. *Precambrian Research, 8*(1-2), 49-76.

Antao, S. M., Zaman, M., Gontijo, V. L., Camargo, E. S., and Marr, R. A. (2015). Optical anisotropy, zoning, and coexistence of two cubic phases in andradites from Quebec and New York. *Contributions to Mineralogy and Petrology, 169*(2), 10.

Arshinov, V., and Merenkov, B. (1930). Petrology of the chrysotile asbestos deposits of the Krasnouralky Mine in the Ural Mountains. *Trans. Inst. Econ. Min, 45*.

Attoh, K., Evans, M. J., and Bickford, M. E. (2006). Geochernistry of an ultramafic-rodingite rock association in the Paleoproterozoic Dixcove greenstone belt, southwestern Ghana. *Journal of African Earth Sciences, 45*(3), 333-346.

Augier, R., Agard, P., Monié, P., Jolivet, L., Robin, C., and Booth-Rea, G. (2005). Exhumation, doming and slab retreat in the Betic Cordillera (SE Spain): in situ ^{40}Ar/^{39}Ar ages and P–T–d–t paths for the Nevado-Filabride complex. *Journal of Metamorphic Geology, 23*(5), 357-381.

Aumento, F., and Loubat, H. (1971). The Mid-Atlantic ridge near 45 N. XVI. Serpentinized ultramafic intrusions. *Canadian Journal of Earth Sciences, 8*(6), 631-663.

Austrheim, H., and Prestvik, T. (2008). Rodingitization and hydration of the oceanic lithosphere as developed in the Leka ophiolite, North-central Norway. *Lithos, 104*(1-4), 177-198.

Bach, W., Jöns, N., and Klein, F. (2013). Metasomatism within the ocean crust *Metasomatism and the chemical transformation of rock* (pp. 253-288): Springer.

Bach, W., and Klein, F. (2009). The petrology of seafloor rodingites: Insights from geochemical reaction path modeling. *Lithos, 112*(1-2), 103-117.

Baker, G. (1959). Rodingite in nickeliferous serpentinite, near Beaconsfield, Northern Tasmania. *Journal of the Geological Society of Australia, 6*(1), 21-35.

Banno, S. (1986). The high-pressure metamorphic belts of Japan: A review. *Geological Society of America Memoirs, 164*, 365-374.

Barnes, I., O'neil, J., and Trescases, J.-J. (1978). Present day serpentinization in New Caledonia, Oman and Yugoslavia. *Geochimica Et Cosmochimica Acta, 42*(1), 144-145.

Barnicoat, A., and Fry, N. (1986). High-pressure metamorphism of the Zermatt-Saas ophiolite zone, Switzerland. *Journal of the Geological Society, 143*(4), 607-618.

Beard, J. S., Fullagar, P. D., and Krisha Sinha, A. (2002). Gabbroic pegmatite intrusions, Iberia Abyssal Plain, ODP Leg 173, Site 1070: magmatism during a transition from non-volcanic rifting to sea-floor spreading. *Journal of Petrology, 43*(5), 885-905.

Bebout, G. E. (1991). Field-based evidence for devolatilization in subduction zones: implications for arc magmatism. *Science, 251*(4992), 413-416.

Bebout, G. E. (2014). Chemical and isotopic cycling in subduction zones *Treatise on Geochemistry: Second Edition* (pp. 703-747): Elsevier Inc.

Bebout, G. E., and Barton, M. D. (2002). Tectonic and metasomatic mixing in a high-T, subduction-zone mélange—insights into the geochemical evolution of the slab–mantle interface. *Chemical Geology, 187*(1-2), 79-106.

Bebout, G. E., and Penniston-Dorland, S. C. (2016). Fluid and mass transfer at subduction interfaces—The field metamorphic record. *Lithos, 240*, 228-258.

Becker, H. (2000). Re–Os fractionation in eclogites and blueschists and the implications for recycling of oceanic crust into the mantle. *Earth and Planetary Science Letters, 177*(3-4), 287-300.

Behr, W., and Platt, J. (2012). Kinematic and thermal evolution during two-stage exhumation of a Mediterranean subduction complex. *Tectonics, 31*(4).

Behr, W. M., and Platt, J. P. (2013). Rheological evolution of a Mediterranean subduction complex. *Journal of Structural Geology, 54*, 136-155.

Bell, J. M., de Courcy Clarke, E., and Marshall, P. (1911). *The geology of the Dun Mountain subdivision, Nelson*: J. Mackay, government printer.

Benson, W. N. (1913). *The geology and petrology of the great serpentine belt of New South Wales*.

Benson, W. N. (1914). *The geology and petrology of the great serpentine belt of New South Wales*.

Benson, W. N. (1915). *The geology and petrology of the Great Serpentine Belt of New South Wales. Part iv. The dolerites, spilites and keratophyres of the Nundle district.* Paper presented at the Proceedings of the Linnean Society of New South Wales.

Benson, W. N. (1918). *The geology and petrology of the Great Serpentine Belt of New South Wales. Part viii. The extension of the Great Serpentine Belt from the Nundle district to the coast.* Paper presented at the Proceedings of the Linnean Society of New South Wales.

Benson, W. N. (1926). *The tectonic conditions accompanying the intrusion of basic and ultrabasic igneous rocks* (Vol. 19): US Government Printing Office.

Berger, A., and Bousquet, R. (2008). Subduction-related metamorphism in the Alps: review of isotopic ages based on petrology and their geodynamic consequences. *Geological Society, London, Special Publications, 298*(1), 117-144.

Bilgrami, S., and Howie, R. (1960). The mineralogy and petrology of a rodingite dike, Hindubagh, Pakistan. *American Mineralogist, 45*(7-8), 791-801.

Birck, J. L., Barman, M. R., and Capmas, F. (1997). Re-Os Isotopic Measurements at the Femtomole Level in Natural Samples. *Geostandards Newsletter, 21*(1), 19-27.

Bloxam, T. (1954). Rodingite from the Girvan-Ballantrae complex, Ayrshire. *Mineralogical Magazine and Journal of the Mineralogical Society, 30*(227), 525-528.

Bøe, R. (1985). Rodingite from Lindås, western Norway. *Norwegian Journal of Geology, 65*, 301-320.

Boev, B., Mircovski, V., and Korikovski, S. (1999). Rondigite rocs in the Jurassic serpentinite masses from the area of 'Rzanovo, Republic of Macedonia'. *Geologica Macedonica, 13*, 75-84.

Booth-Rea, G., Azañón, J. M., Martínez-Martínez, J. M., Vidal, O., and García-Dueñas, V. (2005). Contrasting structural and P-T evolution of tectonic units in the southeastern Betics: Key for understanding the exhumation of the Alboran Domain HP/LT crustal rocks (western Mediterranean). *Tectonics, 24*(2).

Booth-Rea, G., Martínez-Martínez, J., and Giaconia, F. (2015). Continental subduction, intracrustal shortening, and coeval upper-crustal extension: PT evolution of subducted south Iberian paleomargin metapelites (Betics, SE Spain). *Tectonophysics, 663*, 122-139.

Booth-Rea, G., Ranero, C. R., Martinez-Martinez, J., and Grevemeyer, I. (2007). Crustal types and Tertiary tectonic evolution of the Alborán sea, western Mediterranean. *Geochemistry, Geophysics, Geosystems, 8*(10).

Bosch, D., Jamais, M., Boudier, F., Nicolas, A., Dautria, J.-M., and Agrinier, P. (2004). Deep and high-temperature hydrothermal circulation in the Oman ophiolite—petrological and isotopic evidence. *Journal of Petrology, 45*(6), 1181-1208.

Boschi, C., Früh-Green, G. L., Delacour, A., Karson, J. A., and Kelley, D. S. (2006). Mass transfer and fluid flow during detachment faulting and development of an oceanic core complex, Atlantis Massif (MAR 30 N). *Geochemistry, Geophysics, Geosystems, 7*(1).

Brandon, A. D., Creaser, R. A., Shirey, S. B., and Carlson, R. W. (1996). Osmium recycling in subduction zones. *Science, 272*(5263), 861-863.

Brenker, F. E., Vincze, L., Vekemans, B., Nasdala, L., Stachel, T., Vollmer, C., Kersten, M., Somogyi, A., Adams, F., and Joswig, W. (2005). Detection of a Ca-rich lithology in the Earth's deep (> 300 km) convecting mantle. *Earth and Planetary Science Letters, 236*(3-4), 579-587.

Bromiley, G. D., and Pawley, A. R. (2003). The stability of antigorite in the systems $MgO-SiO_2-H_2O$ (MSH) and $MgO-Al_2O_3-SiO_2-H_2O$ (MASH): The effects of Al^{3+} substitution on high-pressure stability. *American Mineralogist, 88*(1), 99-108.

Cannaò, E., Agostini, S., Scambelluri, M., Tonarini, S., and Godard, M. (2015). B, Sr and Pb isotope geochemistry of high-pressure Alpine metaperidotites monitors fluid-mediated element recycling during serpentinite dehydration in subduction mélange (Cima di Gagnone, Swiss Central Alps). *Geochimica Et Cosmochimica Acta, 163*, 80-100.

Cater Jr, F. W., and Wells, F. G. (1953). Geology and mineral resources of the Gasquet quadrangle, California-Oregon. *United States Geological Survey Bulletin*, 79-133.

Charlou, J., Donval, J., Fouquet, Y., Jean-Baptiste, P., and Holm, N. (2002). Geochemistry of high H 2 and CH 4 vent fluids issuing from ultramafic rocks at the Rainbow hydrothermal field (36 14′ N, MAR). *Chemical Geology, 191*(4), 345-359.

Chesterman, C. W. (1960). Intrusive ultrabasic rocks and their metamorphic relationships at Leech Lake Mountain, Mendocino County, California. *Rept Intern Geol Congr 21st Session Norden, 13*, 208-215.

Chidester, A. H. (1962). *Petrology and geochemistry of selected talc-bearing ultramafic rocks and adjacent country rocks in north-central Vermont* (2330-7102).

Cohen, A. S., and Waters, F. G. (1996). Separation of osmium from geological materials by solvent extraction for analysis by thermal ionisation mass spectrometry. *Analytica Chimica Acta, 332*(2), 269-275.

Coleman, R. G. (1963). Serpentinites, rodingites, and tectonic inclusions in Alpine-type mountain chains. *Geological Society of America, Special Papers, 73*, 130-131.

Coleman, R. G. (1966). *New Zealand serpentinites and associated metasomatic rocks*: Dept. of Scientific and Industrial Research, NZ Geological Survey.

Coleman, R. G. (1967). *Low-temperature reaction zones and alpine ultramafic rocks of California, Oregon, and Washington*.

Connolly, J. (2009). The geodynamic equation of state: what and how. *Geochemistry, Geophysics, Geosystems, 10*(10).

Conrad, C. P., and Lithgow-Bertelloni, C. (2002). How mantle slabs drive plate tectonics. *Science, 298*(5591), 207-209.

Cooper, L. B., Plank, T., Arculus, R. J., Hauri, E. H., Hall, P. S., and Parman, S. W. (2010). High-Ca boninites from the active Tonga Arc. *Journal of Geophysical Research: Solid Earth, 115*(B10).

Crossley, R. J., Evans, K. A., Reddy, S. M., and Lester, G. W. (2017). Redistribution of Iron and Titanium in High-Pressure Ultramafic Rocks. *Geochemistry, Geophysics, Geosystems*.

Dai, J., Wang, C., Liu, S., Qian, X., Zhu, D., and Ke, S. (2016). Deep carbon cycle recorded by calcium-silicate rocks (rodingites) in a subduction-related ophiolite. *Geophysical Research Letters, 43*(22), 11,635-611,643.

Dal Piaz, G. (1967). Le ‘granatiti’ (rodingiti ls) nelle serpentine delle Alpi occidentali italiane. *Memorie della Società Geologica Italiana, 6*(3), 267-307.

Dal Piaz, G. (1969). Filoni rodingitici e zone di reazione a bassa temperatura al contatto tettonico tra serpentine e rocce incassanti nelle Alpi occidentali italiane. *Rend. Soc. It. Min. Petr, 25*, 263-315.

Dale, C., Burton, K., Pearson, D., Gannoun, A., Alard, O., Argles, T., and Parkinson, I. (2009). Highly siderophile element behaviour accompanying subduction of oceanic crust: whole rock and mineral-scale insights from a high-pressure terrain. *Geochimica Et Cosmochimica Acta, 73*(5), 1394-1416.

Dale, C., Gannoun, A., Burton, K., Argles, T., and Parkinson, I. (2007). Rhenium–osmium isotope and elemental behaviour during subduction of oceanic crust and the implications for mantle recycling. *Earth and Planetary Science Letters, 253*(1-2), 211-225.

Dale, C. W., Luguet, A., Macpherson, C. G., Pearson, D. G., and Hickey-Vargas, R. (2008). Extreme platinum-group element fractionation and variable Os isotope compositions in Philippine Sea Plate basalts: Tracing mantle source heterogeneity. *Chemical Geology, 248*(3), 213-238.

Dale, J., Holland, T., and Powell, R. (2000). Hornblende–garnet–plagioclase thermobarometry: a natural assemblage calibration of the thermodynamics of hornblende. *Contributions to Mineralogy and Petrology, 140*(3), 353-362.

Damdinov, B., Zhmodik, S., Mironov, A., and Ochirov, Y. C. (2004). Noble-metal mineralization in rodingites of the southeastern East Sayans. *Geologiya i Geofizika (Russian Geology and Geophysics), 45*(5), 577-587.

Dasgupta, R., Hirschmann, M. M., and Withers, A. C. (2004). Deep global cycling of carbon constrained by the solidus of anhydrous, carbonated eclogite under upper mantle conditions. *Earth and Planetary Science Letters, 227*(1-2), 73-85.

Davidson, J. P., and Arculus, R. (2006). *The significance of Phanerozoic arc magmat ism in generating continental crust*.

Davies, G. F., and Richards, M. A. (1992). Mantle convection. *The Journal of Geology, 100*(2), 151-206.

Davies, J. H., and von Blanckenburg, F. (1995). Slab breakoff: a model of lithosphere detachment and its test in the magmatism and deformation of collisional orogens. *Earth and Planetary Science Letters, 129*(1-4), 85-102.

De, A. (1972). Petrology of dikes emplaced in the ultramafic rocks of southeastern Québec and origin of the rodingite. *Geological Society of America Memoirs, 132*, 489-502.

Debret, B., Andreani, M., Muñoz, M., Bolfan-Casanova, N., Carlut, J., Nicollet, C., Schwartz, S., and Trcera, N. (2014). Evolution of Fe redox state in serpentine during subduction. *Earth and Planetary Science Letters, 400*, 206-218.

Debret, B., Bolfan-Casanova, N., Padrón-Navarta, J. A., Martin-Hernandez, F., Andreani, M., Garrido, C. J., López Sánchez-Vizcaíno, V., Gómez-Pugnaire, M. T., Muñoz, M., and Trcera, N. (2015). Redox state of iron during high-pressure serpentinite dehydration. *Contributions to Mineralogy and Petrology, 169*(4), 36.

Debret, B., and Sverjensky, D. (2017). Highly oxidising fluids generated during serpentinite breakdown in subduction zones. *Scientific reports, 7*.

Deschamps, F., Godard, M., Guillot, S., and Hattori, K. (2013). Geochemistry of subduction zone serpentinites: A review. *Lithos, 178*, 96-127.

Desmurs, L., Müntener, O., and Manatschal, G. (2002). Onset of magmatic accretion within a magma-poor rifted margin: a case study from the Platta ocean-continent transition, eastern Switzerland. *Contributions to Mineralogy and Petrology, 144*(3), 365-382.

Dilissen, N., Garrido, C. J., López Sánchez-Vizcaíno, V., Padrón-Navarta, J. A., Jabaloy-Sánchez, A., Gerya, T., and Hidas, K. (2018). *Episodic Fluid release during High-pressure Dehydration of Antigorite-serpentinite in Subducting Slabs.* Paper presented at the EGU General Assembly Conference Abstracts.

Dilissen, N., Hidas, K., Garrido, C. J., López Sánchez-Vizcaíno, V., and Kahl, W.-A. (2019). Morphological transition during prograde olivine growth formed by high-pressure dehydration of antigorite-serpentinite to chlorite-harzburgite in a subduction setting. *Lithos*.

Dubińska, E. (1995). Rodingites of the Eastern Part of the Jordanow-Gogolow Serpentinite Massif, Lower Silesia, Poland. *Canadian Mineralogist, 33*, 585-608.

Dubińska, E. (1997). Rodingites and amphibolites from the serpentinites surrounding Sowie Góry block (Lower Silesia, Poland): Record of supra-subduction zone magmatism and serpentinization. *Neues Jahrbuch Fur Mineralogie-Abhandlungen, 171*(3), 239-279.

Dubińska, E., Bylina, P., Kozłowski, A., Dörr, W., Nejbert, K., Schastok, J., and Kulicki, C. (2004a). U–Pb dating of serpentinization: hydrothermal zircon from a metasomatic rodingite shell (Sudetic ophiolite, SW Poland). *Chemical Geology, 203*(3-4), 183-203.

Dubińska, E., Bylina, P., & Kozłowski, A. (2004b). Garnets from Lower Silesia rodingites: constraints from their chemistry. *Prace Spec. Pol. Tow. Mineral*, *24*, 135-139.

Dubińska, E., and Wiewióra, A. (1999). Layer silicates from a rodingite and its blackwall from Przemiłów (Lower Silesia, Poland): mineralogical record of metasomatic processes during serpentinization and serpentinite Recrystallization. *Mineralogy and Petrology, 67*(3-4), 223-237.

Dymkova, D., and Gerya, T. (2013). Porous fluid flow enables oceanic subduction initiation on Earth. *Geophysical Research Letters, 40*(21), 5671-5676.

Elliott, T., Plank, T., Zindler, A., White, W., and Bourdon, B. (1997). Element transport from slab to volcanic front at the Mariana arc. *Journal of Geophysical Research: Solid Earth, 102*(B7), 14991-15019.

Ernst, W. (2011). Accretion of the Franciscan Complex attending Jurassic–Cretaceous geotectonic development of northern and central California. *Geological Society of America Bulletin, 123*(9-10), 1667-1678.

Etheve, N., de Lamotte, D. F., Mohn, G., Martos, R., Roca, E., and Blanpied, C. (2016). Extensional vs contractional Cenozoic deformation in Ibiza (Balearic Promontory, Spain): Integration in the West Mediterranean back-arc setting. *Tectonophysics, 682*, 35-55.

Evans, B. W. (2004). The serpentinite multisystem revisited: chrysotile is metastable. *International Geology Review, 46*(6), 479-506.

Evans, B. W., and Trommsdorff, V. (1978). Petrogenesis of garnet lherzolite, Cima di Gagnone, Lepontine Alps. *Earth and Planetary Science Letters, 40*(3), 333-348.

Evans, B. W., Trommsdorff, V., and Goles, G. G. (1981). Geochemistry of high-grade eclogites and metarodingites from the Central Alps. *Contributions to Mineralogy and Petrology, 76*(3), 301-311.

Evans, B. W., Trommsdorff, V., and Richter, W. (1979). Petrology of an Eclogite-Metarodingite Suite at Cima Di Gagnone, Ticino, Switzerland. *American Mineralogist, 64*(1-2), 15-31.

Evans, K. (2006). Redox decoupling and redox budgets: Conceptual tools for the study of earth systems. *Geology, 34*(6), 489-492.

Evans, K. (2012). The redox budget of subduction zones. *Earth-Science Reviews, 113*(1-2), 11-32.

Evans, K., and Powell, R. (2015). The effect of subduction on the sulphur, carbon and redox budget of lithospheric mantle. *Journal of Metamorphic Geology, 33*(6), 649-670.

Evans, K., Reddy, S., Tomkins, A., Crossley, R., and Frost, B. (2017). Effects of geodynamic setting on the redox state of fluids released by subducted mantle lithosphere. *Lithos, 278*, 26-42.

Faccenda, M. (2014). Water in the slab: A trilogy. *Tectonophysics, 614*, 1-30.

Ferrando, S., Frezzotti, M. L., Orione, P., Conte, R. C., and Compagnoni, R. (2010). Late-Alpine rodingitization in the Bellecombe meta-ophiolites (Aosta Valley, Italian Western Alps): evidence from mineral assemblages and serpentinization-derived H_2-bearing brine. *International Geology Review, 52*(10-12), 1220-1243.

Forsyth, D., and Uyeda, S. (1975). On the relative importance of the driving forces of plate motion. *Geophysical Journal International, 43*(1), 163-200.

Frei, D., Liebscher, A., Franz, G., and Dulski, P. (2004). Trace element geochemistry of epidote minerals. *Reviews in Mineralogy and Geochemistry, 56*(1), 553-605.

Frost, B. R. (1975). Contact metamorphism of serpentinite, chloritic blackwall and rodingite at Paddy-Go-Easy Pass, Central Cascades, Washington. *Journal of Petrology, 16*(2), 272-313.

Frost, B. R. (1985). On the stability of sulfides, oxides, and native metals in serpentinite. *Journal of Petrology, 26*(1), 31-63.

Frost, B. R., and Beard, J. S. (2007). On silica activity and serpentinization. *Journal of Petrology, 48*(7), 1351-1368.

Frost, B. R., Beard, J. S., McCaig, A., and Condliffe, E. (2008). The formation of micro-rodingites from IODP Hole U1309D: key to understanding the process of serpentinization. *Journal of Petrology, 49*(9), 1579-1588.

Frost, B. R., Evans, K. A., Swapp, S. M., Beard, J. S., and Mothersole, F. E. (2013). The process of serpentinization in dunite from New Caledonia. *Lithos, 178*, 24-39.

Früh-Green, G. L., Kelley, D. S., Bernasconi, S. M., Karson, J. A., Ludwig, K. A., Butterfield, D. A., Boschi, C., and Proskurowski, G. (2003). 30,000 years of hydrothermal activity at the Lost City vent field. *Science, 301*(5632), 495-498.

Früh-Green, G. L., Orcutt, B. N., Green, S. L., Cotterill, C., Morgan, S., Akizawa, N., Bayrakci, G., Behrmann, J.-H., Boschi, C., Brazleton, W. J., Cannat, M., Dunkel, K. G., Escartin, J., Harris, M., Herrero-Bervera, E., Hesse, K., John, B. E., Lang, S. Q., Lilley, M. D., Liu, H.-Q., Mayhew, L. E., McCaig, A. M., Menez, B., Morono, Y., Quéméneur, M., Rouméjon, S., Sandaruwan Ratnayake, A., Schrenk, M. O., Schwarzenbach, E. M., Twing, K. I., Weis, D., Whattham, S. A., Williams, M., and Zhao, R. (2017). Expedition 357 summary. In G. L. Früh-Green, Orcutt, B.N., Green, S.L., Cotterill, C., and the Expedition 357 Scientists (Ed.), *Atlantis Massif Serpentinization and Life* (pp. 1-34). College Station: International Ocean Discovery Program.

Früh-Green, G. L., Plas, A., and Dell'Angelo, L. N. (1996). Mineralogic and stable isotope record of polyphase alteration of upper crustal gabbros of the East Pacific Rise (Hess Deep, Site 894). In C. Mevel, Gillis, K.M., Allan, J.F., Meyer, P.S. (Ed.), *Proceedings of the Ocean Drilling Program, Scientific Results, vol. 147* (pp. 235-254).

Fukuyama, M., Ogasawara, M., Dunkley, D. J., Wang, K. L., Lee, D. C., Hokada, T., Maki, K., Hirata, T., and Kon, Y. (2014). The formation of rodingite in the N agasaki metamorphic rocks at N omo P eninsula, K yushu, J apan–Z ircon U–P b and H f isotopes and trace element evidence. *Island Arc, 23*(4), 281-298.

Furukawa, Y. (1993). Depth of the decoupling plate interface and thermal structure under arcs. *Journal of Geophysical Research: Solid Earth, 98*(B11), 20005-20013.

Gannoun, A., Burton, K. W., Day, J. M., Harvey, J., Schiano, P., and Parkinson, I. (2016). Highly siderophile element and Os isotope systematics of volcanic rocks at divergent and convergent plate boundaries and in intraplate settings. *Reviews in Mineralogy and Geochemistry, 81*(1), 651-724.

Garrido, C. J., López Sánchez-Vizcaíno, V., Gómez-Pugnaire, M. T., Trommsdorff, V., Alard, O., Bodinier, J. L., and Godard, M. (2005). Enrichment of HFSE in Chlorite-Harzburgite produced by high-pressure dehydration of Antigorite-Serpentinite: implications for subduction magmatism. *Geochemistry, Geophysics, Geosystems, 6*(1).

Gasc, J., Brunet, F., Brantut, N., Corvisier, J., Findling, N., Verlaguet, A., and Lathe, C. (2016). Effect of Water Activity on Reaction Kinetics and Intergranular Transport: Insights from the $Ca(OH)_2 + MgCO_3 \rightarrow CaCO_3 + Mg(OH)_2$ Reaction at 1.8 GPa. *Journal of Petrology, 57*(7), 1389-1408.

Gaspar, M., Knaack, C., Meinert, L. D., and Moretti, R. (2008). REE in skarn systems: A LA-ICP-MS study of garnets from the Crown Jewel gold deposit. *Geochimica Et Cosmochimica Acta, 72*(1), 185-205.

Godard, M., Awaji, S., Hansen, H., Hellebrand, E., Brunelli, D., Johnson, K., Yamasaki, T., Maeda, J., Abratis, M., and Christie, D. (2009). Geochemistry of a long in-situ section of intrusive slow-spread oceanic lithosphere: Results from IODP Site U1309 (Atlantis Massif, 30 N Mid-Atlantic-Ridge). *Earth and Planetary Science Letters, 279*(1-2), 110-122.

Gómez-Pugnaire, M. T., Franz, G., and López Sánchez-Vizcaino, V. (1994). Retrograde formation of NaCl-scapolite in high pressure metaevaporites from the Cordilleras Béticas (Spain). *Contributions to Mineralogy and Petrology, 116*(4), 448-461.

Gomez-Pugnaire, M. T., Galindo-Zaldívar, J., Rubatto, D., González-Lodeiro, F., López Sánchez-Vizcaíno, V., and Jabaloy, A. (2004). A reinterpretation of the Nevado-Filábride and Alpujárride complexes (Betic Cordillera): field, petrography and U-Pb ages from orthogneisses (western Sierra Nevada, S Spain). *Schweizerische Mineralogische Und Petrographische Mitteilungen, 84*, 303-322.

Gómez-Pugnaire, M. T., Rubatto, D., Fernández-Soler, J., Jabaloy, A., López-Sánchez-Vizcaíno, V., González-Lodeiro, F., Galindo-Zaldívar, J., and Padrón-Navarta, J. (2012). Late Variscan magmatism in the Nevado-Filábride Complex: U-Pb geochronologic evidence for the pre-Mesozoic nature of the deepest Betic complex (SE Spain). *Lithos, 146*, 93-111.

Gómez-Pugnaire, M. T., Ulmer, P., and López-Sánchez-Vizcaíno, V. (2000). Petrogenesis of the mafic igneous rocks of the Betic Cordilleras: A field, petrological and geochemical study. *Contributions to Mineralogy and Petrology, 139*(4), 436-457.

Goscombe, B. D., Passchier, C. W., and Hand, M. (2004). Boudinage classification: end-member boudin types and modified boudin structures. *Journal of Structural Geology, 26*(4), 739-763.

Govindaraju, K. (1994). 1994 compilation of working values and sample description for 383 geostandards. *Geostandards Newsletter, 18*, 1-158.

Grange, L. (1927). *On the rodingite of Nelson.* Paper presented at the Trans. NZ Inst.

Grant, T. B., Harlov, D. E., and Rhede, D. (2016). Experimental formation of pyroxenite veins by reactions between olivine and Si, Al, Ca, Na, and Cl-rich fluids at 800 ºC and 800 MPa: Implications for fluid metasomatism in the mantle wedge. *American Mineralogist, 101*(4), 808-818.

Grove, T., Parman, S., Bowring, S., Price, R., and Baker, M. (2002). The role of an H 2 O-rich fluid component in the generation of primitive basaltic andesites and andesites from the Mt. Shasta region, N California. *Contributions to Mineralogy and Petrology, 142*(4), 375-396.

Haas, J. R., Shock, E. L., and Sassani, D. C. (1995). Rare earth elements in hydrothermal systems: estimates of standard partial molal thermodynamic properties of aqueous complexes of the rare earth elements at high pressures and temperatures. *Geochimica Et Cosmochimica Acta, 59*(21), 4329-4350.

Hacker, B. R. (2008). H_2O subduction beyond arcs. *Geochemistry, Geophysics, Geosystems, 9*(3).

Hacker, B. R., Abers, G. A., and Peacock, S. M. (2003). Subduction factory 1. Theoretical mineralogy, densities, seismic wave speeds, and H_2O contents. *Journal of Geophysical Research: Solid Earth, 108*(B1).

Hacker, B. R., Peacock, S. M., Abers, G. A., and Holloway, S. D. (2003). Subduction factory 2. Are intermediate-depth earthquakes in subducting slabs linked to metamorphic dehydration reactions? *Journal of Geophysical Research: Solid Earth, 108*(B1).

Hager, B. H., and O'Connell, R. J. (1981). A simple global model of plate dynamics and mantle convection. *Journal of Geophysical Research: Solid Earth, 86*(B6), 4843-4867.

Hall, A., and Ahmed, Z. (1984). Rare earth content and origin of rodingites. *Chemie der Erde, 43*, 45-56.

Handy, M. R., M. Schmid, S., Bousquet, R., Kissling, E., and Bernoulli, D. (2010). Reconciling plate-tectonic reconstructions of Alpine Tethys with the geological–geophysical record of spreading and subduction in the Alps. *Earth-Science Reviews, 102*(3), 121-158.

Hatzipanagiotou, K., and Tsikouras, B. (2001). Rodingite formation from diorite in the Samothraki ophiolite, NE Aegean, Greece. *Geological Journal, 36*(2), 93-109.

Hatzipanagiotou, K., Tsikouras, B., Migiros, G., Gartzos, E., and Serelis, K. (2003). Origin of rodingites in ultramafic rocks from Lesvos island (NE Aegean, Greece). *Ofioliti, 28*(1), 13-23.

Hermann, J. (2002). Allanite: thorium and light rare earth element carrier in subducted crust. *Chemical Geology, 192*(3-4), 289-306.

Hermann, J., Spandler, C., Hack, A., and Korsakov, A. V. (2006). Aqueous fluids and hydrous melts in high-pressure and ultra-high-pressure rocks: implications for element transfer in subduction zones. *Lithos, 92*(3-4), 399-417.

Hinsbergen, D. J., Vissers, R. L., and Spakman, W. (2014). Origin and consequences of western Mediterranean subduction, rollback, and slab segmentation. *Tectonics, 33*(4), 393-419.

Holland, T., and Powell, R. (1996). Thermodynamics of order-disorder in minerals: II. Symmetric formalism applied to solid solutions. *American Mineralogist, 81*(11-12), 1425-1437.

Holland, T., and Powell, R. (1998). An internally consistent thermodynamic data set for phases of petrological interest. *Journal of Metamorphic Geology, 16*(3), 309-343.

Holland, T., and Powell, R. (2011). An improved and extended internally consistent thermodynamic dataset for phases of petrological interest, involving a new equation of state for solids. *Journal of Metamorphic Geology, 29*(3), 333-383.

Honnorez, J., and Kirst, P. (1975). Petrology of Rodingites from Equatorial Mid-Atlantic Fracture Zones and Their Geotectonic Significance. *Contributions to Mineralogy and Petrology, 49*(3), 233-257.

Hu, C.-N., Santosh, M., Yang, Q.-Y., Kim, S., Nakagawa, M., and Maruyama, S. (2017). Magmatic and metasomatic imprints in a long-lasting subduction zone: evidence from zircon in rodingite and serpentinite of Kochi, SW Japan. *Lithos, 274*, 349-362.

Imai, N., TERASHIMA, S., ITOH, S., and ANDO, A. (1995). 1994 compilation of analytical data for minor and trace elements in seventeen GSJ geochemical reference samples, "Igneous rock series". *Geostandards Newsletter, 19*(2), 135-213.

Inoue, T. (1994). Effect of water on melting phase relations and melt composition in the system Mg_2SiO_4 - $MgSiO_3$ - H_2O up to 15 GPa. *Physics of the earth and planetary interiors, 85*(3-4), 237-263.

Ionov, D., Savoyant, L., and Dupuy, C. (1992). Application of the ICP-MS technique to trace element analysis of peridotites and their minerals. *Geostandards Newsletter, 16*(2), 311-315.

Ionov, D. A., Chazot, G., Chauvel, C., Merlet, C., and Bodinier, J.-L. (2006). Trace element distribution in peridotite xenoliths from Tok, SE Siberian craton: a record of pervasive, multi-stage metasomatism in shallow refractory mantle. *Geochimica Et Cosmochimica Acta, 70*(5), 1231-1260.

Ishikawa, A., Senda, R., Suzuki, K., Dale, C. W., and Meisel, T. (2014). Re-evaluating digestion methods for highly siderophile element and ^{187}Os isotope analysis: Evidence from geological reference materials. *Chemical Geology, 384*, 27-46.

Ishimaru, S., and Arai, S. (2011). Peculiar Mg–Ca–Si metasomatism along a shear zone within the mantle wedge: inference from fine-grained xenoliths from Avacha volcano, Kamchatka. *Contributions to Mineralogy and Petrology, 161*(5), 703-720.

Jabaloy-Sánchez, A., Gómez-Pugnaire, M. T., Padrón-Navarta, J. A., López Sánchez-Vizcaíno, V., and Garrido, C. J. (2015). Subduction-and exhumation-related structures preserved in metaserpentinites and associated metasediments from the Nevado–Filábride Complex (Betic Cordillera, SE Spain). *Tectonophysics, 644*, 40-57.

Jabaloy-Sánchez, A., Talavera, C., Gómez-Pugnaire, M. T., López Sánchez-Vizcaíno, V., Vázquez-Vílchez, M., Rodríguez-Peces, M. J., and Evans, N. J. (2018). U-Pb ages of detrital zircons from the Internal Betics: A key to deciphering paleogeographic provenance and tectono-stratigraphic evolution. *Lithos, 318*, 244-266.

Jaffé, F. (1955). *Les ophiolites et les roches connexes de la région du Col des Gets:(Chablais, Haute Savoie).* University of Geneva.

Jamtveit, B., and Andersen, T. B. (1992). Morphological instabilities during rapid growth of metamorphic garnets. *Physics and Chemistry of Minerals, 19*(3), 176-184.

Jenner, F. E., and O'Neill, H. S. C. (2012). Analysis of 60 elements in 616 ocean floor basaltic glasses. *Geochemistry, Geophysics, Geosystems, 13*(2).

Jochum, K., Seufert, H., and Thirlwall, M. (1990). Multi-element analysis of 15 international standard rocks by isotope-dilution spark source mass spectrometry. *Geostandards Newsletter, 14*(3), 469-473.

Jochum, K. P., Weis, U., Schwager, B., Stoll, B., Wilson, S. A., Haug, G. H., Andreae, M. O., and Enzweiler, J. (2016). Reference values following ISO guidelines for frequently requested rock reference materials. *Geostandards and Geoanalytical Research, 40*(3), 333-350.

Karato, S.-i., Wang, Z., Liu, B., and Fujino, K. (1995). Plastic deformation of garnets: systematics and implications for the rheology of the mantle transition zone. *Earth and Planetary Science Letters, 130*(1-4), 13-30.

Katayama, I., Terada, T., Okazaki, K., and Tanikawa, W. (2012). Episodic tremor and slow slip potentially linked to permeability contrasts at the Moho. *Nature Geoscience, 5*(10), 731.

Katoh, T., and Niida, K. (1983). Rodingites from the Kamuikotan tectonic belt, Hokkaido. *北海道大学理学部紀要= Journal of the Faculty of Science, Hokkaido University. Series 4, Geology and mineralogy, 20*(2-3), 151-169.

Kelemen, P. B., Hanghøj, K., and Greene, A. (2003). One view of the geochemistry of subduction-related magmatic arcs, with an emphasis on primitive andesite and lower crust. *Treatise on geochemistry, 3*, 659.

Kelemen, P. B., Hanghøj, K., and Greene, A. (2014). One view of the geochemistry of subduction-related magmatic arcs, with an emphasis on primitive andesite and lower crust. *Treatise on geochemistry, 749-805*, 659.

Kelemen, P. B., Shimizu, N., and Salters, V. J. (1995). Extraction of mid-ocean-ridge basalt from the upwelling mantle by focused flow of melt in dunite channels. *Nature, 375*(6534), 747.

Kendrick, M. A., Scambelluri, M., Hermann, J., and Padrón-Navarta, J. A. (2018). Halogens and noble gases in serpentinites and secondary peridotites: Implications for seawater subduction and the origin of mantle neon. *Geochimica Et Cosmochimica Acta, 235*, 285-304.

Kendrick, M. A., Scambelluri, M., Honda, M., and Phillips, D. (2011). High abundances of noble gas and chlorine delivered to the mantle by serpentinite subduction. *Nature Geoscience, 4*(11), 807.

Kirchner, K. L., Behr, W. M., Loewy, S., and Stockli, D. F. (2016). Early Miocene subduction in the western Mediterranean: Constraints from Rb-Sr multimineral isochron geochronology. *Geochemistry, Geophysics, Geosystems, 17*(5), 1842-1860.

Klein, E. (2003). Geochemistry of the igneous oceanic crust. *Treatise on geochemistry, 3*, 659.

Kodolányi, J., Pettke, T., Spandler, C., Kamber, B. S., and Gméling, K. (2012). Geochemistry of ocean floor and fore-arc serpentinites: constraints on the ultramafic input to subduction zones. *Journal of Petrology, 53*(2), 235-270.

Koutsovitis, P., Magganas, A., Ntaflos, T., and Koukouzas, N. (2018). Rodingitization and carbonation, associated with serpentinization of Triassic ultramafic cumulates and lavas in Othris, Greece. *Lithos, 320*, 35-48.

Koutsovitis, P., Magganas, A., and Pomonis, P. (2008). *Rodingites within scattered ophiolitic occurrences from the northern and eastern Othris area, Greece.* Paper presented at the Proceedings of XIII International conference on thermobarogeochemistry and IVth APIFIS.

Koutsovitis, P., Magganas, A., Pomonis, P., and Ntaflos, T. (2013). Subduction-related rodingites from East Othris, Greece: Mineral reactions and physicochemical conditions of formation. *Lithos, 172*, 139-157.

Laborda-Lopez, C., Aguirre, J., and Donovan, S. K. (2015). Surviving metamorphism: taphonomy of fossil assemblages in marble and calc-silicate schist. *Palaios, 30*(9), 668-679.

Laborda-López, C., Rodríguez, J. A., Donovan, S. K., and Navasparejo, P. (2015). Fossil assemblages and biostratigraphy of metamorphic rocks of the Nevado-Filábride Complex from the Águilas tectonic arc (SE Spain). *Spanish journal of palaeontology, 30*(2), 275-291.

Lan, C.-y. a. L. J. G. (1981). *Occurrence, Petrology and Tectonics of Serpentinites and Associated Rodingites in Central Range, Taiwan*: Mining Research and Service Organization, ITRT.

Lanari, P., Vidal, O., De Andrade, V., Dubacq, B., Lewin, E., Grosch, E. G., and Schwartz, S. (2014). XMapTools: A MATLAB©-based program for electron microprobe X-ray image processing and geothermobarometry. *Computers and Geosciences, 62*, 227-240.

Larrabee, D. M. (1969). Serpentinite and rodingite in the Hunting Hill quarry, Montgomery County, Maryland.

Leach, T., and Rodgers, K. (1978). Metasomatism in the Wairere serpentinite, King Country, New Zealand. *Mineralogical Magazine, 42*(321), 45-62.

Leblanc, M., and Lbouabi, M. (1988). Native Silver Mineralization Along a Rodingite Tectonic Contact Between Serpentinite and Quartz Diorite (Bou-Azzer, Morocco). *Economic Geology, 83*(7), 1379-1391.

Li, X.-H., Putis, M., Yang, Y.-H., Koppa, M., and Dyda, M. (2014). Accretionary wedge harzburgite serpentinization and rodingitization constrained by perovskite U/Pb SIMS age, trace elements and Sm/Nd isotopes: Case study from the Western Carpathians, Slovakia. *Lithos, 205*, 1-14.

Li, X.-P., Duan, W.-Y., Zhao, L.-Q., Schertl, H.-P., Kohn, F.-M., Shi, T.-Q., and X., Z. (2017). Rodingites from the Xigaze ophiolite, southern Tibet – new insights into the processes of rodingitization. *Eur. J. Mineral.*

Li, X.-P., Rahn, M., and Bucher, K. (2004). Metamorphic processes in rodingites of the Zermatt-Saas ophiolites. *International Geology Review, 46*(1), 28-51.

Li, X.-P., Rahn, M., and Bucher, K. (2008). Eclogite facies metarodingites - phase relations in the system SiO_2-Al_2O_3-Fe_2O_3-FeO-MgO-CaO-CO_2-H_2O: an example from the Zermatt-Saas ophiolite. *Journal of Metamorphic Geology, 26*(3), 347-364.

Li, X.-P., Zhang, L., Wei, C., Ai, Y., and Chen, J. (2007). Petrology of rodingite derived from eclogite in western Tianshan, China. *Journal of Metamorphic Geology, 25*(3), 363-382.

Li, X.-P., Zhang, L.-F., Wilde, S. A., Song, B., and Liu, X.-M. (2010). Zircons from rodingite in the Western Tianshan serpentinite complex: mineral chemistry and U–Pb ages define nature and timing of rodingitization. *Lithos, 118*(1-2), 17-34.

Lillie, R. J. (2005). *Parks and plates: The geology of our national parks, monuments, and seashores*: WW Norton.

Loader, M. A., Wilkinson, J. J., and Armstrong, R. N. (2017). The effect of titanite crystallisation on Eu and Ce anomalies in zircon and its implications for the assessment of porphyry Cu deposit fertility. *Earth and Planetary Science Letters, 472*, 107-119.

Locock, A. J. (2008). An Excel spreadsheet to recast analyses of garnet into end-member components, and a synopsis of the crystal chemistry of natural silicate garnets. *Computers and Geosciences, 34*(12), 1769-1780.

Locock, A. J. (2014). An Excel spreadsheet to classify chemical analyses of amphiboles following the IMA 2012 recommendations. *Computers and Geosciences, 62*, 1-11.

López Sánchez-Vizcaíno, V., Gómez-Pugnaire, M. T. (in press). Alpine Metamorphism. Metamorphism of the Nevado-Filábride Complex. In C. Quesada, Oliveira, J.T. (Ed.), *The Geology of Iberia: A Geodynamic Approach.*

López Sánchez-Vizcaíno, V., Gómez-Pugnaire, M. T., Garrido, C. J., Padrón-Navarta, J. A., and Mellini, M. (2009). Breakdown mechanisms of titanclinohumite in antigorite serpentinite (Cerro del Almirez massif, S. Spain): A petrological and TEM study. *Lithos, 107*(3), 216-226.

López Sánchez-Vizcaíno, V., Rubatto, D., Gómez-Pugnaire, M. T., Trommsdorff, V., and Müntener, O. (2001). Middle Miocene high-pressure metamorphism and fast exhumation of the Nevado-Filábride Complex, SE Spain. *Terra Nova, 13*(5), 327-332.

López Sánchez-Vizcaíno, V., Trommsdorff, V., Gómez-Pugnaire, M., Garrido, C., Müntener, O., and Connolly, J. (2005). Petrology of titanian clinohumite and olivine at the high-pressure breakdown of antigorite serpentinite to chlorite harzburgite (Almirez Massif, S. Spain). *Contributions to Mineralogy and Petrology, 149*(6), 627-646.

Luguet, A., Lorand, J.-P., and Seyler, M. (2003). Sulfide petrology and highly siderophile element geochemistry of abyssal peridotites: A coupled study of samples from the Kane Fracture Zone (45 W 23 20N, MARK area, Atlantic Ocean). *Geochimica Et Cosmochimica Acta, 67*(8), 1553-1570.

Malaspina, N., Langenhorst, F., Tumiati, S., Campione, M., Frezzotti, M., and Poli, S. (2017). The redox budget of crust-derived fluid phases at the slab-mantle interface. *Geochimica Et Cosmochimica Acta, 209*, 70-84.

Manatschal, G., and Müntener, O. (2009). A type sequence across an ancient magma-poor ocean–continent transition: the example of the western Alpine Tethys ophiolites. *Tectonophysics, 473*(1-2), 4-19.

Marchesi, C., Garrido, C. J., Padrón-Navarta, J. A., López Sánchez-Vizcaíno, V., and Gómez-Pugnaire, M. T. (2013). Element mobility from seafloor serpentinization to high-pressure dehydration of antigorite in subducted serpentinite: insights from the Cerro del Almirez ultramafic massif (southern Spain). *Lithos, 178*, 128-142.

Marks, M. A., Coulson, I. M., Schilling, J., Jacob, D. E., Schmitt, A. K., and Markl, G. (2008). The effect of titanite and other HFSE-rich mineral (Ti-bearing andradite, zircon, eudialyte) fractionation on the geochemical evolution of silicate melts. *Chemical Geology, 257*(1-2), 153-172.

Marschall, H., and Schumacher, J. (2012). Arc magmas sourced from mélange diapirs in subduction zones. Nat. Geosci. 5, 862–867.

Marschall, H. R., Altherr, R., Ludwig, T., Kalt, A., Gméling, K., and Kasztovszky, Z. (2006). Partitioning and budget of Li, Be and B in high-pressure metamorphic rocks. *Geochimica Et Cosmochimica Acta, 70*(18), 4750-4769.

Martínez-Martínez, J., Soto, J., and Balanyá, J. (2002). Orthogonal folding of extensional detachments: structure and origin of the Sierra Nevada elongated dome (Betics, SE Spain). *Tectonics, 21*(3).

Martínez-Martínez, J. M. (2006). Lateral interaction between metamorphic core complexes and less-extended, tilt-block domains: the Alpujarras strike-slip transfer fault zone (Betics, SE Spain). *Journal of Structural Geology, 28*(4), 602-620.

Massonne, H.-J., and Willner, A. P. (2008). Phase relations and dehydration behaviour of psammopelite and mid-ocean ridge basalt at very-low-grade to low-grade metamorphic conditions. *European Journal of Mineralogy, 20*(5), 867-879.

McInnes, B. I., McBride, J. S., Evans, N. J., Lambert, D. D., and Andrew, A. S. (1999). Osmium isotope constraints on ore metal recycling in subduction zones. *Science, 286*(5439), 512-516.

Mei, S., Bai, W., Hiraga, T., and Kohlstedt, D. (2002). Influence of melt on the creep behavior of olivine–basalt aggregates under hydrous conditions. *Earth and Planetary Science Letters, 201*(3-4), 491-507.

Menzel, M. D., Garrido, C. J., López Sánchez-Vizcaíno, V., Hidas, K., and Marchesi, C. (2019). Subduction metamorphism of serpentinite-hosted carbonates beyond antigorite-serpentinite dehydration (Nevado-Filábride Complex, Spain). *Journal of Metamorphic Geology, 0*(0), 1– 35.

Merkulova, M. V., Muñoz, M., Brunet, F., Vidal, O., Hattori, K., Vantelon, D., Trcera, N., and Huthwelker, T. (2017). Experimental insight into redox transfer by iron-and sulfur-bearing serpentinite dehydration in subduction zones. *Earth and Planetary Science Letters, 479*, 133-143.

Merkulova, M. V., Muñoz, M., Vidal, O., and Brunet, F. (2016). Role of iron content on serpentinite dehydration depth in subduction zones: Experiments and thermodynamic modeling. *Lithos, 264*, 441-452.

Miles, K. (1950). Garnetized Gabbros from the Eulaminna District, Mt. Margaret Goldfield. *Bull. geol. Surv. W. Austral, 103*, 108-130.

Mittwede, S. K., and Schandl, E. S. (1992). Rodingites from the southern Appalachian Piedmont, South-Carolina, USA. *European Journal of Mineralogy, 4*(1), 7-16.

Mogessie, A., and Rammlmair, D. (1994). Occurence of zoned uvarovite-grossular garnet in a rodingite from the Vumba Schist-Belt, Bostwana, Africa: Implications for the origin of rodingites. *Mineralogical Magazine, 58*(392), 375-386.

Müller, P. (1963). Kalksilikatfelse im serpentin des Piz Lunghin bei Maloja. *Chemie der Erde, 22*, 452-163.

Munteanu-Murgoci, G. (1900). Granat-und Vesuvianfels: aus dem serpentin von Parîngu. *Buletinul Societății de Științe din București-România/Bulletin de la Société des Sciences de Bucarest-Roumanie, 9*(5), 568-612.

Murzin, V. V., and Shanina, S. N. (2007). Fluid regime and origin of gold-bearing rodingites from the Karabash alpine-type ultrabasic massif, Southern Ural. *Geochemistry International, 45*(10), 998-1011

Newton, R., and Haselton, H. (1981). Thermodynamics of the garnet – plagioclase – Al_2SiO_5 – quartz geobarometer. Thermodynamics of minerals and melts (pp. 131-147): Springer.

Nishiyama, T., Yoshida-Shiosaki, C., Mori, Y., and Shigeno, M. (2017). Interplay of irreversible reactions and deformation: a case of hydrofracturing in the rodingite–serpentinite system. *Progress in Earth and Planetary Science, 4*(1), 1.

Niu, Y. (2004). Bulk-rock major and trace element compositions of abyssal peridotites: implications for mantle melting, melt extraction and post-melting processes beneath mid-ocean ridges. *Journal of Petrology, 45*(12), 2423-2458.

Normand, C., and Williams-Jones, A. E. (2007). Physicochemical conditions and timing of rodingite formation: evidence from rodingite-hosted fluid inclusions in the JM Asbestos mine, Asbestos, Quebec. *Geochemical Transactions, 8*, 1-19.

Nowell, G. M., Pearson, D. G., Parman, S. W., Luguet, A., and Hanski, E. (2008). Precise and accurate $^{186}Os/^{188}Os$ and $^{187}Os/^{188}Os$ measurements by Multi-collector Plasma Ionisation Mass Spectrometry, part II: Laser ablation and its application to single-grain Pt–Os and Re–Os geochronology. *Chemical Geology, 248*(3), 394-426.

O'Brien, J., and Rodgers, K. (1973). Xonotlite and rodingites from Wairere, New Zealand. *Mineralogical Magazine, 39*(302), 233-240.

O'Hanley, D. (1996). Rodingites, albitites, and other rocks formed by metasomatism *Serpentinites. Records of Tectonic and Petrological History* (pp. 112-126). New York. Oxford: Oxford University Press.

O'Hanley, D. S., Schandl, E. S., and Wicks, F. J. (1992). The Origin of Rodingites from Cassiar, British-Columbia, and Their Use to Estimate T and P (H_2O) During Serpentinization. *Geochimica Et Cosmochimica Acta, 56*(1), 97-108.

O'Neill, C., Jellinek, A., and Lenardic, A. (2007). Conditions for the onset of plate tectonics on terrestrial planets and moons. *Earth and Planetary Science Letters, 261*(1-2), 20-32.

Padrón Navarta, J. A. (2010). A coupled petrological and petrophysical study of high-pressure dehydration reactions in subduction settings. Insights from the Betic Cordillera and the Kohistan Paleo-arc.

Padrón-Navarta, J. A., Lopez Sanchez-Vizcaino, V., Garrido, C. J., and Gómez-Pugnaire, M. T. (2011). Metamorphic record of high-pressure dehydration of antigorite serpentinite to chlorite harzburgite in a subduction setting (Cerro del Almirez, Nevado–Filábride Complex, Southern Spain). *Journal of Petrology, 52*(10), 2047-2078.

Padrón-Navarta, J. A., López Sánchez-Vizcaíno, V., Hermann, J., Connolly, J. A., Garrido, C. J., Gómez-Pugnaire, M. T., and Marchesi, C. (2013). Tschermak's substitution in antigorite and consequences for phase relations and water liberation in high-grade serpentinites. *Lithos, 178,* 186-196.

Padrón-Navarta, J. A., Tommasi, A., Garrido, C. J., and López Sánchez-Vizcaíno, V. (2012). Plastic deformation and development of antigorite crystal preferred orientation in high-pressure serpentinites. *Earth and Planetary Science Letters, 349*, 75-86.

Padrón-Navarta, J. A., Tommasi, A., Garrido, C. J., López Sánchez-Vizcaíno, V., Gómez-Pugnaire, M. T., Jabaloy, A., and Vauchez, A. (2010a). Fluid transfer into the wedge controlled by high-pressure hydrofracturing in the cold top-slab mantle. *Earth and Planetary Science Letters, 297*(1), 271-286.

Padrón-Navarta, J.A., Hermann, J., Garrido, C.J., López Sánchez-Vizcaíno, V., Gómez-Pugnaire, M.T., (2010b). An experimental investigation of antigorite dehydration in natural silica-enriched serpentinite. *Contributions to Mineralogy and Petrology* 159, 25-42.

Palme, H., and Jones, A. (2003). Solar System Abundances of the Elements: Treatise on Geochemistry, Vol. 1: Oxford: Elsevier.

Palyanova, G., Murzin, V., Zhuravkova, T., and Varlamov, D. (2018). Au-Cu-Ag mineralization in rodingites and nephritoids of the Agardag ultramafic massif (southern Tuva, Russia). *Russian Geology and Geophysics, 59*(3), 238-256.

Pan, P., and Wood, S. (1994). Solubility of Pt and Pd sulfides and Au metal in aqueous bisulfide solutions. *Mineralium Deposita, 29*(5), 373-390.

Panseri, M., Fontana, E., and Tartarotti, P. (2008). Evolution of rodingitic dykes: Metasomatism and metamorphism in the Mount Avic serpentinites (Alpine ophiolites, Southern Aosta Valley). *Ofioliti, 33*(2), 165-185.

Paton, C., Hellstrom, J., Paul, B., Woodhead, J., and Hergt, J. (2011). Iolite: Freeware for the visualisation and processing of mass spectrometric data. *Journal of Analytical Atomic Spectrometry, 26*(12), 2508-2518.

Peacock, S. M. (2001). Are the lower planes of double seismic zones caused by serpentine dehydration in subducting oceanic mantle? *Geology, 29*(4), 299-302.

Pearce, J. A., and Peate, D. W. (1995). Tectonic implications of the composition of volcanic arc magmas. *Annual Review of Earth and Planetary Sciences, 23*(1), 251-285.

Pearce, J. A., Stern, R. J., Bloomer, S. H., and Fryer, P. (2005). Geochemical mapping of the Mariana arc-basin system: Implications for the nature and distribution of subduction components. *Geochemistry, Geophysics, Geosystems, 6*(7).

Pearson, D. G., and Woodland, S. J. (2000). Solvent extraction/anion exchange separation and determination of PGEs (Os, Ir, Pt, Pd, Ru) and Re–Os isotopes in geological samples by isotope dilution ICP-MS. *Chemical Geology, 165*(1), 87-107.

Penniston-Dorland, S. C., Gorman, J. K., Bebout, G. E., Piccoli, P. M., and Walker, R. J. (2014). Reaction rind formation in the Catalina Schist: Deciphering a history of mechanical mixing and metasomatic alteration. *Chemical Geology, 384*, 47-61.

Penniston-Dorland, S. C., Walker, R. J., Pitcher, L., and Sorensen, S. S. (2012). Mantle–crust interactions in a paleosubduction zone: Evidence from highly siderophile element systematics of eclogite and related rocks. *Earth and Planetary Science Letters, 319*, 295-306.

Perraki, M., Karipi, S., Rigopoulos, I., Tsikouras, B., Pomonis, P., and Hatzipanagiotou, K. (2010). *Grossular/hydrogrossular in rodingites from Othrys Ophiolite (Central Greece): Raman spectroscopy as a tool to distinguish it from vesuvianite.* Paper presented at the XIX CBGA Congress, Thessaloniki, Greece.

Peucker-Ehrenbrink, B., Bach, W., Hart, S. R., Blusztajn, J. S., and Abbruzzese, T. (2003). Rhenium-osmium isotope systematics and platinum group element concentrations in oceanic crust from DSDP/ODP Sites 504 and 417/418. *Geochemistry, Geophysics, Geosystems, 4*(7).

Platt, J. P., Anczkiewicz, R., Soto, J.-I., Kelley, S. P., and Thirlwall, M. (2006). Early Miocene continental subduction and rapid exhumation in the western Mediterranean. *Geology, 34*(11), 981-984.

Platt, J. P., Behr, W. M., and Cooper, F. J. (2015). Metamorphic core complexes: windows into the mechanics and rheology of the crust. *Journal of the Geological Society, 172*(1), 9-27.

Platt, J. P., Behr, W. M., Johanesen, K., and Williams, J. R. (2013). The Betic-Rif arc and its orogenic hinterland: a review. *Annual Review of Earth and Planetary Sciences, 41*, 313-357.

Plümper, O., John, T., Podladchikov, Y. Y., Vrijmoed, J. C., and Scambelluri, M. (2017). Fluid escape from subduction zones controlled by channel-forming reactive porosity. *Nature Geoscience, 10*(2), 150.

Polat, A. (2012). Growth of Archean continental crust in oceanic island arcs. *Geology, 40*(4), 383-384.

Poli, S., and Schmidt, M. W. (2002). Petrology of subducted slabs. *Annual Review of Earth and Planetary Sciences, 30*(1), 207-235.

Pomonis, P., Tsikouras, B., Karipi, S., and Hatzipanagiotou, K. (2008). Rodingite formation in ultramafic rocks from the Koziakas ophiolite, western Thessaly, Greece: Conditions of metasomatic alteration, geochemical exchanges and T-X(CO_2) evolutionary path. *Canadian Mineralogist, 46*, 569-581.

Puchtel, I. S., Walker, R. J., Touboul, M., Nisbet, E. G., and Byerly, G. R. (2014). Insights into early Earth from the Pt–Re–Os isotope and highly siderophile element abundance systematics of Barberton komatiites. *Geochimica Et Cosmochimica Acta, 125*, 394-413.

Puga, E., de Federico, A. D., Nieto, J., Puga, M. D., and Martínez-Conde, J. R. (2009). The Betic Ophiolitic Association: a very significant Geological Heritage that needs to be preserved. *Geoheritage, 1*(1), 11.

Puga, E., Díaz de Federico, A., Fanning, M., Nieto, J. M., Rodríguez Martínez-Conde, J. Á., Díaz Puga, M. Á., Lozano, J. A., Bianchini, G., Natali, C., and Beccaluva, L. (2017). The Betic ophiolites and the mesozoic evolution of the western Tethys. *Geosciences*, *7*(2), 31.

Puga, E., Fanning, M., Díaz de Federico, A., Nieto, J. M., Beccaluva, L., Bianchini, G., and Díaz Puga, M. A. (2011). Petrology, geochemistry and U–Pb geochronology of the Betic Ophiolites: Inferences for Pangaea break-up and birth of the westernmost Tethys Ocean. *Lithos*, *124*(3), 255-272.

Puga, E., Nieto, J. M., Díaz de Federico, A., Bodinier, J. L., and Morten, L. (1999). Petrology and metamorphic evolution of ultramafic rocks and dolerite dykes of the Betic Ophiolitic Association (Mulhacen Complex, SE Spain): evidence of eo-Alpine subduction following an ocean-floor metasomatic process. *Lithos, 49*(1-4), 23-56.

Puschnig, A. R. (2002). Metasomatic alterations at mafic-ultramaric contacts in Valmalenco (Rhetic Alps, N-Italy). *Schweizerische Mineralogische Und Petrographische Mitteilungen, 82*(3), 515-536.

Python, M., Ceuleneer, G., Ishida, Y., Barrat, J.-A., and Arai, S. (2007). Oman diopsidites: a new lithology diagnostic of very high temperature hydrothermal circulation in mantle peridotite below oceanic spreading centres. *Earth and Planetary Science Letters, 255*(3-4), 289-305.

Python, M., Ishida, Y., Ceuleneer, G., and Arai, S. (2007). Trace element heterogeneity in hydrothermal diopside: evidence for Ti depletion and Sr-Eu-LREE enrichment during hydrothermal metamorphism of mantle harzburgite. *Journal of Mineralogical and Petrological Sciences, 102*(2), 143-149.

Ravizza, G., Blusztajn, J., and Prichard, H. (2001). Re–Os systematics and platinum-group element distribution in metalliferous sediments from the Troodos ophiolite. *Earth and Planetary Science Letters, 188*(3-4), 369-381.

Reisberg, L., Rouxel, O., Ludden, J., Staudigel, H., and Zimmermann, C. (2008). Re–Os results from ODP Site 801: Evidence for extensive Re uptake during alteration of oceanic crust. *Chemical Geology, 248*(3-4), 256-271.

Rice, J. M. (1983). Metamorphism of rodingites: Part I. Phase relations in a portion of the system CaO–MgO–Al_2O_3–SiO_2–CO_2–H_2O. *American Journal of Science, 283*(A), 121-510.

Righter, K., and Hauri, E. H. (1998). Compatibility of rhenium in garnet during mantle melting and magma genesis. *Science, 280*(5370), 1737-1741.

Rodríguez-Cañero, R., Jabaloy-Sánchez, A., Navas-Parejo, P., and Martín-Algarra, A. (2018). Linking Palaeozoic palaeogeography of the Betic Cordillera to the Variscan Iberian Massif: new insight through the first conodonts of the Nevado-Filábride Complex. *International Journal of Earth Sciences*, 1-16.

Rossman, G. R., and Aines, R. D. (1991). The hydrous components in garnets: Grossular-hydrogrossular. *American Mineralogist*, *76*(7-8), 1153-1164.

Royden, L. H. (1993). Evolution of retreating subduction boundaries formed during continental collision. *Tectonics*, *12*(3), 629-638.

Rüpke, L. H., Morgan, J. P., Hort, M., and Connolly, J. A. (2004). Serpentine and the subduction zone water cycle. *Earth and Planetary Science Letters, 223*(1-2), 17-34.

Salters, V. J., and Stracke, A. (2004). Composition of the depleted mantle. *Geochemistry, Geophysics, Geosystems, 5*(5).

Santamaría-López, Á., and Sanz de Galdeano, C. (2018). SHRIMP U–Pb detrital zircon dating to check subdivisions in metamorphic complexes: a case of study in the Nevado–Filábride complex (Betic Cordillera, Spain). *International Journal of Earth Sciences*, 1-14.

Sarp, H., and Deferne, J. (1978). Le bilan chimique de la rodingitisation et l'origine de l'exces de chaux dans les rodingites. *Schweiz. Mineral. Petrogr. Mitt*, *58*(3), 315-328.

Scambelluri, M., Bottazzi, P., Trommsdorff, V., Vannucci, R., Hermann, J., Gòmez-Pugnaire, M. T., and Vizcaìno, V. L.-S. (2001). Incompatible element-rich fluids released by antigorite breakdown in deeply subducted mantle. *Earth and Planetary Science Letters, 192*(3), 457-470.

Scambelluri, M., Fiebig, J., Malaspina, N., Müntener, O., and Pettke, T. (2004). Serpentinite subduction: implications for fluid processes and trace-element recycling. *International Geology Review, 46*(7), 595-613.

Scambelluri, M., Pettke, T., and Cannaò, E. (2015). Fluid-related inclusions in Alpine high-pressure peridotite reveal trace element recycling during subduction-zone dehydration of serpentinized mantle (Cima di Gagnone, Swiss Alps). *Earth and Planetary Science Letters, 429*, 45-59.

Scambelluri, M., and Rampone, E. (1999). Mg-metasomatism of oceanic gabbros and its control on Ti-clinohumite formation during eclogitization. *Contributions to Mineralogy and Petrology, 135*(1), 1-17.

Scambelluri, M., and Tonarini, S. (2012). Boron isotope evidence for shallow fluid transfer across subduction zones by serpentinized mantle. *Geology, 40*(10), 907-910.

Schaltegger, U., Desmurs, L., Manatschal, G., Müntener, O., Meier, M., Frank, M., and Bernoulli, D. (2002). The transition from rifting to sea-floor spreading within a magma-poor rifted margin: Field and isotopic constraints. *Terra Nova, 14*(3), 156-162.

Schandl, E. S., Ohanley, D. S., and Wicks, F. J. (1989). Rodingites in Serpentinized Ultramafic Rocks of the Abitibi Greenstone-Belt, Ontario. *Canadian Mineralogist, 27*, 579-591.

Schandl, E. S., Ohanley, D. S., Wicks, F. J., and Kyser, T. K. (1990). Fluid Inclusions in Rodingite - a Geothermometer for Serpentinization. *Economic Geology and the Bulletin of the Society of Economic Geologists, 85*(6), 1273-1276.

Schiano, P., Eiler, J., Hutcheon, I., and Stolper, E. (2000). Primitive CaO-rich, silica-undersaturated melts in island arcs: Evidence for the involvement of clinopyroxene-rich lithologies in the petrogenesis of arc magmas. *Geochemistry, Geophysics, Geosystems, 1*(5).

Schlocker, J. (1960). Rodingite from Angel Island, San Francisco Bay, California. *US Geol. Surv. Prof. Pap. B, 400*, B311-B312.

Schmidt, M. W., and Poli, S. (1998). Experimentally based water budgets for dehydrating slabs and consequences for arc magma generation. *Earth and Planetary Science Letters, 163*(1-4), 361-379.

Schmidt, M. W., and Poli, S. (2014). Devolatilization during subduction. in “Treatise on geochemistry”, Holland, HD and Turekian, KK, eds: Elsevier, Oxford, UK.

Schubert, G., Turcotte, D. L., and Olson, P. (2001). *Mantle convection in the Earth and planets*: Cambridge University Press.

Schwartz, S., Guillot, S., Reynard, B., Lafay, R., Debret, B., Nicollet, C., Lanari, P., and Auzende, A. L. (2013). Pressure–temperature estimates of the lizardite/antigorite transition in high pressure serpentinites. *Lithos, 178*, 197-210.

Schwarzenbach, E. M., Caddick, M. J., Petroff, M., Gill, B. C., Cooperdock, E. H., and Barnes, J. D. (2018). Sulphur and carbon cycling in the subduction zone mélange. *Scientific reports, 8*(1), 15517.

Seki, Y. K., Sakiko. (1962). Mafic and leucocratic rocks associated with serpentinite of Kanasaki, Kanto Mountains, central Japan. *Japanese journal of geology and geography, 33*(1).

Shirey, S. B., and Walker, R. J. (1998). The Re-Os isotope system in cosmochemistry and high-temperature geochemistry. *Annual Review of Earth and Planetary Sciences, 26*(1), 423-500.

Sorensen, S. S., and Barton, M. D. (1987). Metasomatism and partial melting in a subduction complex Catalina Schist, southern California. *Geology, 15*(2), 115-118.

Spandler, C., Hermann, J., Arculus, R., and Mavrogenes, J. (2003). Redistribution of trace elements during prograde metamorphism from lawsonite blueschist to eclogite facies; implications for deep subduction-zone processes. *Contributions to Mineralogy and Petrology, 146*(2), 205-222.

Spandler, C., Hermann, J., Faure, K., Mavrogenes, J. A., and Arculus, R. J. (2008). The importance of talc and chlorite “hybrid” rocks for volatile recycling through subduction zones; evidence from the high-pressure subduction mélange of New Caledonia. *Contributions to Mineralogy and Petrology, 155*(2), 181-198.

Spandler, C., and Pirard, C. (2013). Element recycling from subducting slabs to arc crust: A review. *Lithos, 170*, 208-223.

Spence, W. (1987). Slab pull and the seismotectonics of subducting lithosphere. *Reviews of geophysics, 25*(1), 55-69.

Stern, R. J. (2002). Subduction zones. *Reviews of geophysics, 40*(4), 3-1-3-38.

Stern, R. J. (2018). The evolution of plate tectonics. *Philosophical Transactions of the Royal Society A: Mathematical, Physical and Engineering Sciences, 376*(2132), 20170406.

Sun, S.-S., and McDonough, W. F. (1989). Chemical and isotopic systematics of oceanic basalts: implications for mantle composition and processes. *Geological Society, London, Special Publications, 42*(1), 313-345.

Sun, W., Bennett, V. C., Eggins, S. M., Kamenetsky, V. S., and Arculus, R. J. (2003). Enhanced mantle-to-crust rhenium transfer in undegassed arc magmas. *Nature, 422*(6929), 294.

Suzuki, J. (1953). On the rodingitic rocks within the serpentinite masses of Hokkaido. *Journal of the Faculty of Science, Hokkaido University. Series 4, Geology and mineralogy= 北海道大學理學部紀要, 8*(4), 419-430.

Syracuse, E. M., van Keken, P. E., and Abers, G. A. (2010). The global range of subduction zone thermal models. *Physics of the earth and planetary interiors, 183*(1-2), 73-90.

Tang, Y., Zhai, Q.-G., Hu, P.-Y., Wang, J., Xiao, X.-C., Wang, H.-T., Tang, S.-H., and Lei, M. (2018). Rodingite from the Beila ophiolite in the Bangong–Nujiang suture zone, northern Tibet: New insights into the formation ofophiolite-related rodingite. *Lithos, 316*, 33-47.

Tatsumi, Y. (2005). *The subduction factory: How it operates in the evolving Earth* (Vol. 15).

Terabayashi, M., and Maruyama, S. (1998). Large pressure gap between the Coastal and Central Franciscan belts, northern and central California. *Tectonophysics, 285*(1-2), 87-101.

Thayer, T. (1966). Serpentinization considered as a constant-volume metasomatic process. *American Mineralogist: Journal of Earth and Planetary Materials, 51*(5-6), 685-710.

Tribuzio, R., Messiga, B., Vannucci, R., and Bottazzi, P. (1996). Rare earth element redistribution during high - pressure - low - temperature metamorphism in ophiolitic Fe-gabbros (Liguria, northwestern Italy): implications for light REE mobility in subduction zones. *Geology, 24*(8), 711-714.

Trommsdorff, V., and Evans, B. W. (1974). Alpine metamorphism of peridotitic rocks. *Schweizerische Mineralogische Und Petrographische Mitteilungen, 54*, 334– 352.

Trommsdorff, V., López Sánchez-Vizcaíno, V., Gomez-Pugnaire, M., and Müntener, O. (1998). High pressure breakdown of antigorite to spinifex-textured olivine and orthopyroxene, SE Spain. *Contributions to Mineralogy and Petrology, 132*(2), 139-148.

Tsikouras, B., Karipi, S., and Hatzipanagiotou, K. (2013). Evolution of rodingites along stratigraphic depth in the Iti and Kallidromon ophiolites (Central Greece). *Lithos, 175*, 16-29.

Tsikouras, B., Karipi, S., Rigopoulos, I., Perraki, M., Pomonis, P., and Hatzipanagiotou, K. (2009). Geochemical processes and petrogenetic evolution of rodingite dykes in the ophiolite complex of Othrys (Central Greece). *Lithos, 113*(3-4), 540-554.

Tumiati, S., Fumagalli, P., Tiraboschi, C., and Poli, S. (2012). An experimental study on COH-bearing peridotite up to 3.2 GPa and implications for crust–mantle recycling. *Journal of Petrology, 54*(3), 453-479.

Tumiati, S., Godard, G., Martin, S., Malaspina, N., and Poli, S. (2015). Ultra-oxidized rocks in subduction mélanges? Decoupling between oxygen fugacity and oxygen availability in a Mn-rich metasomatic environment. *Lithos, 226*, 116-130.

Turcotte, D., and Schubert, G. (2014). *Geodynamics*: Cambridge university press.

Turner, F. J. (1933). *The metamorphic and intrusive rocks of southern Westland.* Paper presented at the Transactions of the New Zealand Institute.

Ulmer, P., and Trommsdorff, V. (1995). Serpentine stability to mantle depths and subduction-related magmatism. *Science, 268*(5212), 858-861.

Ulmer, P. T., Volkmar. (1999). Phase relations of hydrous mantle subducting to 300 km. *Mantle petrology: Field observations and high-pressure experimentation*, 259-281.

van Keken, P. E., Hacker, B. R., Syracuse, E. M., and Abers, G. A. (2011). Subduction factory: 4. Depth-dependent flux of H_2O from subducting slabs worldwide. *Journal of Geophysical Research: Solid Earth, 116*(B1).

van Keken, P. E., Wada, I., Abers, G. A., Hacker, B. R., and Wang, K. (2018). Mafic High-Pressure Rocks Are Preferentially Exhumed From Warm Subduction Settings. *Geochemistry, Geophysics, Geosystems, 19*(9), 2934-2961.

Walker, R. J., Prichard, H. M., Ishiwatari, A., and Pimentel, M. (2002). The osmium isotopic composition of convecting upper mantle deduced from ophiolite chromites. *Geochimica Et Cosmochimica Acta, 66*(2), 329-345.

Walowski, K. J., Wallace, P. J., Hauri, E., Wada, I., and Clynne, M. A. (2015). Slab melting beneath the Cascade Arc driven by dehydration of altered oceanic peridotite. *Nature Geoscience, 8*(5), 404.

Watson, K. (1953). Prehnitization of albitite. *American Mineralogist: Journal of Earth and Planetary Materials, 38*(3-4), 197-206.

Weinschenk, E. (1894). Beitrage zue Petrographie der östlichen Zentralpen, speziell des Grossvenedigerstockes. I. Über die Peridotite und die aus ihnen Hervorgegangenen Serpentingestein. II. Über das granitische Zentralmassiv und die Beziehungenzwischen Granit und Gneiss: Ablandl. Bayr. Ak. Wiss., Kl. II.

Wells, F. G. (1949). *Preliminary description of the geology of the Kerby Quadrangle, Oregon*: US Dept. of the Interior, US Geological Survey.

Wenner, D. B., and Taylor, H. P. (1971). Temperatures of serpentinization of ultramafic rocks based on $^{18}O/^{16}O$ fractionation between coexisting serpentine and magnetite. *Contributions to Mineralogy and Petrology, 32*(3), 165-185.

White, R. W., Powell, R., and Holland, T. J. B. (2007). Progress relating to calculation of partial melting equilibria for metapelites. *Journal of Metamorphic Geology, 25*(5), 511-527.

Whitney, D. L., and Evans, B. W. (2010). Abbreviations for names of rock-forming minerals. *American Mineralogist, 95*(1), 185-187.

Wilson, M. (1993). Plate-moving mechanisms: constraints and controversies. *Journal of the Geological Society, 150*(5), 923-926.

Winkler, H. (1979). *Petrogenesis of metamorphic rocks.*

Wong A Ton, S. Y. M., and Wortel, M. J. R. (1997). Slab detachment in continental collision zones: An analysis of controlling parameters. *Geophysical Research Letters, 24*(16), 2095-2098.

Wunder, B., and Schreyer, W. (1997). Antigorite: High-pressure stability in the system MgO - SiO_2 - H_2O (MSH). *Lithos, 41*(1-3), 213-227.

Zack, T., Foley, S., and Rivers, T. (2002). Equilibrium and disequilibrium trace element partitioning in hydrous eclogites (Trescolmen, Central Alps). *Journal of Petrology, 43*(10), 1947-1974.

Zanoni, D., Rebay, G., and Spalla, M. I. (2016). Ocean floor and subduction record in the Zermatt-Saas rodingites, Valtournanche, Western Alps. *Journal of Metamorphic Geology, 34*, 941-961.

9 Appendices

TABLE A1 Garnet microprobe analyses, average compositions and standard deviations (σ)

Garnet Type	Grt-1	Grt-1	Grt-1	Grt-1	Grt-1		Grt-2a	Grt-2a	Grt-2a
Metarodingite Type	Grandite-metarodingite					σ	Grandite-metarodingite		
Sample	AL2000-6	AL2000-6	AL2000-6	AL2000-6	Average	n=33	AL2000-6	AL2000-6	AL14-04C
SiO_2	36.96	36.95	37.08	37.02	37.11	0.21	36.50	36.60	36.93
TiO_2	2.11	2.00	2.16	1.91	1.94	0.12	2.37	2.55	2.80
Al_2O_3	17.34	17.34	17.14	17.04	16.91	0.44	13.23	13.32	12.86
Cr_2O_3	0.00	0.00	0.01	0.02	0.01	0.01	0.02	0.02	0.00
FeO /FeO_{total}	4.61	4.79	4.92	5.64	5.68	0.74	10.13	10.12	10.52
MnO	0.27	0.26	0.24	0.25	0.26	0.02	0.23	0.21	0.18
MgO	0.07	0.10	0.09	0.14	0.13	0.04	0.22	0.18	0.17
CaO	36.10	36.09	36.29	35.75	35.60	0.36	34.13	33.51	34.60
Na_2O	0.01	0.00	0.00	0.01	0.00	0.00	0.01	0.01	0.00
H_2O^+	1.19	1.22	1.22	1.19	1.03	0.15	0.77	0.53	0.71
Total	98.67	98.76	99.16	98.96	98.69	0.27	97.61	97.04	98.77
FeO	1.78	1.76	1.79	2.02	2.06	0.27	2.92	3.60	3.29
Fe_2O_3	3.15	3.38	3.47	4.03	4.02	0.79	8.01	7.24	8.03
Total	98.99	99.11	99.50	99.37	99.09	0.29	98.41	97.76	99.56
Formula									
Si (T)	2.85	2.84	2.84	2.85	2.87	0.02	2.90	2.93	2.91
Al (T)	0.00	0.00	0.00	0.00	0.00	0.00	0.00	0.00	0.00
Fe^{3+} (T)	0.00	0.00	0.00	0.00	0.00	0.00	0.00	0.00	0.00
$4H^+$ (T)	0.15	0.16	0.16	0.15	0.13	0.02	0.10	0.07	0.09
Ti (O)	0.12	0.12	0.12	0.11	0.11	0.01	0.14	0.15	0.17
Al (O)	1.57	1.57	1.55	1.54	1.54	0.04	1.24	1.26	1.19
Cr (O)	0.00	0.00	0.00	0.00	0.00	0.00	0.00	0.00	0.00
Fe^{2+} (O)	0.11	0.11	0.11	0.11	0.11	0.01	0.14	0.15	0.17
Fe^{3+} (O)	0.18	0.20	0.20	0.23	0.23	0.05	0.48	0.44	0.48
Mg (O)	0.01	0.00	0.01	0.00	0.00	0.00	0.00	0.00	0.00
Fe^{2+} (D)	0.00	0.00	0.00	0.02	0.02	0.02	0.05	0.09	0.05
Mn^{2+} (D)	0.02	0.02	0.02	0.02	0.02	0.00	0.02	0.01	0.01
Mg (D)	0.00	0.01	0.00	0.02	0.01	0.01	0.03	0.02	0.02
Ca (D)	2.98	2.98	2.98	2.95	2.95	0.02	2.90	2.87	2.92
Na (D)	0.00	0.00	0.00	0.00	0.00	0.00	0.00	0.00	0.00
End-members									
Grossular	0.73	0.73	0.72	0.70	0.71	0.02	0.55	0.56	0.54
Andradite	0.09	0.10	0.10	0.12	0.12	0.02	0.24	0.22	0.24
Almandine	0.00	0.00	0.00	0.01	0.01	0.01	0.02	0.03	0.02
Pyrope	0.00	0.00	0.00	0.01	0.00	0.00	0.01	0.01	0.01
Spessartine	0.01	0.01	0.01	0.01	0.01	0.00	0.01	0.00	0.00
Katoite	0.05	0.05	0.05	0.05	0.04	0.01	0.03	0.02	0.03
Morimotoite	0.11	0.11	0.11	0.11	0.11	0.01	0.14	0.15	0.17
Uvarovite	0.00	0.00	0.00	0.00	0.00	0.00	0.00	0.00	0.00
Hutcheonite	0.00	0.00	0.00	0.00	0.00	0.00	0.00	0.00	0.00
NaTi garnet	0.00	0.00	0.00	0.00	0.00	0.00	0.00	0.00	0.00
Morimotoite-Mg	0.01	0.00	0.01	0.00	0.00	0.00	0.00	0.00	0.00

TABLE A1 Garnet microprobe analyses, average compositions and standard deviations (σ)

Garnet Type	Grt-2a		Grt-2b	Grt-2b	Grt-2b	Grt-2b	Grt-2b(relict)	Grt-2b	
Metarodingite Type	Grand-	σ	Grandite-metarodingite				Epidote-MR		σ
Sample	Average	n=11	AL95-36C	AL14-04C2	AL2000-6	AL2000-6	AL14-26E	Average	n=72
SiO_2	36.65	0.19	37.90	37.65	37.00	36.57	37.23	37.49	0.53
TiO_2	2.52	0.22	0.46	0.82	0.88	1.24	0.73	0.78	0.21
Al_2O_3	13.36	0.22	16.54	14.52	13.73	13.43	13.85	14.77	0.93
Cr_2O_3	0.02	0.01	0.03	0.04	0.01	0.01	0.08	0.07	0.18
FeO /FeO_{total}	9.77	0.35	12.59	14.07	13.96	13.56	14.12	13.46	0.72
MnO	0.20	0.05	0.76	0.50	0.39	0.29	0.30	0.48	0.10
MgO	0.18	0.03	1.62	1.10	1.05	1.04	0.87	1.23	0.20
CaO	34.01	0.45	28.15	30.25	30.75	31.10	30.97	29.96	0.73
Na_2O	0.01	0.00	0.00	0.01	0.00	0.01	0.06	0.01	0.01
H_2O^+	0.59	0.11	0.16	0.45	0.61	0.83	0.56	0.43	0.25
Total	97.31	0.85	98.19	99.41	98.37	98.06	98.78	98.67	0.54
FeO	3.12	0.30	6.32	5.41	4.60	4.45	4.46	5.29	0.59
Fe_2O_3	7.39	0.41	6.96	9.62	10.40	10.13	10.74	9.08	1.02
Total	98.05	0.86	98.88	100.37	99.42	99.09	99.86	99.58	0.53
Formula									
Si (T)	2.92	0.01	2.98	2.94	2.92	2.89	2.93	2.94	0.03
Al (T)	0.00	0.00	0.00	0.00	0.00	0.00	0.00	0.00	0.00
Fe^{3+} (T)	0.00	0.00	0.00	0.00	0.00	0.00	0.00	0.00	0.00
$4H^+$ (T)	0.08	0.01	0.02	0.06	0.08	0.11	0.07	0.06	0.03
Ti (O)	0.15	0.01	0.03	0.05	0.05	0.07	0.04	0.05	0.01
Al (O)	1.25	0.03	1.53	1.34	1.28	1.25	1.28	1.37	0.08
Cr (O)	0.00	0.00	0.00	0.00	0.00	0.00	0.00	0.00	0.01
Fe^{2+} (O)	0.15	0.01	0.03	0.05	0.05	0.07	0.03	0.05	0.01
Fe^{3+} (O)	0.44	0.02	0.41	0.57	0.62	0.60	0.64	0.54	0.06
Mg (O)	0.00	0.00	0.00	0.00	0.00	0.00	0.00	0.00	0.00
Fe^{2+} (D)	0.06	0.02	0.39	0.31	0.25	0.22	0.26	0.30	0.05
Mn^{2+} (D)	0.01	0.00	0.05	0.03	0.03	0.02	0.02	0.03	0.01
Mg (D)	0.02	0.00	0.19	0.13	0.12	0.12	0.10	0.14	0.02
Ca (D)	2.90	0.02	2.37	2.53	2.60	2.63	2.61	2.52	0.07
Na (D)	0.00	0.00	0.00	0.00	0.00	0.00	0.01	0.00	0.00
End-members									
Grossular	0.57	0.01	0.55	0.49	0.48	0.47	0.49	0.51	0.03
Andradite	0.22	0.01	0.21	0.28	0.31	0.30	0.32	0.27	0.03
Almandine	0.02	0.01	0.13	0.10	0.08	0.07	0.09	0.10	0.02
Pyrope	0.01	0.00	0.06	0.04	0.04	0.04	0.03	0.05	0.01
Spessartine	0.00	0.00	0.02	0.01	0.01	0.01	0.01	0.01	0.00
Katoite	0.03	0.00	0.01	0.02	0.03	0.04	0.02	0.02	0.01
Morimotoite	0.15	0.01	0.03	0.05	0.05	0.07	0.03	0.05	0.01
Uvarovite	0.00	0.00	0.00	0.00	0.00	0.00	0.00	0.00	0.01
Hutcheonite	0.00	0.00	0.00	0.00	0.00	0.00	0.00	0.00	0.00
NaTi garnet	0.00	0.00	0.00	0.00	0.00	0.00	0.00	0.00	0.00
Morimotoite-Mg	0.00	0.00	0.00	0.00	0.00	0.00	0.00	0.00	0.00

TABLE A1 Garnet microprobe analyses, average compositions and standard deviations (σ)

Garnet Type	Grt-3	Grt-3	Grt-3	Grt-3	Grt-3	Grt-3		Grt-3	Grt-3
Metarodingite Type	Grand-metarodingite						σ	Ep-MR (amphibolitized)	
Sample	AL2000-6	AL2000-6	AL2000-6	AL2000-6	AL2000-6	Average	n=84	AL14-18	AL14-18
SiO_2	36.22	36.58	36.50	36.60	36.64	36.53	0.28	36.38	36.28
TiO_2	1.48	0.81	1.13	1.00	1.26	1.23	0.28	0.79	0.76
Al_2O_3	10.27	11.71	12.20	12.68	12.81	12.05	0.78	8.84	9.23
Cr_2O_3	0.02	0.04	0.02	0.01	0.01	0.03	0.10	0.11	0.13
FeO /FeO_{total}	15.69	15.34	13.78	13.48	13.54	14.34	0.76	17.25	16.82
MnO	0.23	0.34	0.32	0.36	0.16	0.28	0.06	0.77	0.84
MgO	0.49	0.59	0.58	0.64	0.89	0.70	0.14	0.27	0.69
CaO	32.68	31.47	32.75	32.32	32.21	32.12	0.55	32.98	32.78
Na_2O	0.00	0.02	0.00	0.00	0.00	0.01	0.01	0.01	0.01
H_2O^+	0.70	0.44	0.78	0.67	0.83	0.71	0.17	0.47	0.73
Total	97.78	97.34	98.06	97.77	98.35	98.00	0.43	97.86	98.28
FeO	3.04	3.55	2.89	3.10	3.57	3.49	0.43	1.58	1.39
Fe_2O_3	14.06	13.10	12.11	11.54	11.08	12.06	0.87	17.41	17.15
Total	99.19	98.64	99.28	98.92	99.46	99.21	0.44	99.60	100.00
Formula									
Si (T)	2.91	2.94	2.90	2.91	2.89	2.91	0.02	2.94	2.90
Al (T)	0.00	0.00	0.00	0.00	0.00	0.00	0.00	0.00	0.00
Fe^{3+} (T)	0.00	0.00	0.00	0.00	0.00	0.00	0.00	0.00	0.00
$4H^+$ (T)	0.09	0.06	0.10	0.09	0.11	0.09	0.02	0.06	0.10
Ti (O)	0.09	0.05	0.07	0.06	0.08	0.07	0.02	0.05	0.05
Al (O)	0.97	1.11	1.14	1.19	1.19	1.13	0.07	0.84	0.87
Cr (O)	0.00	0.00	0.00	0.00	0.00	0.00	0.01	0.01	0.01
Fe^{2+} (O)	0.09	0.05	0.07	0.06	0.07	0.07	0.02	0.05	0.04
Fe^{3+} (O)	0.85	0.79	0.72	0.69	0.66	0.72	0.05	1.06	1.03
Mg (O)	0.00	0.00	0.00	0.00	0.00	0.00	0.00	0.00	0.00
Fe^{2+} (D)	0.11	0.19	0.12	0.15	0.16	0.16	0.03	0.06	0.05
Mn^{2+} (D)	0.02	0.02	0.02	0.02	0.01	0.02	0.00	0.05	0.06
Mg (D)	0.06	0.07	0.07	0.08	0.10	0.08	0.02	0.03	0.08
Ca (D)	2.81	2.71	2.78	2.75	2.72	2.74	0.05	2.85	2.81
Na (D)	0.00	0.00	0.00	0.00	0.00	0.00	0.00	0.00	0.00
End-members									
Grossular	0.39	0.44	0.46	0.48	0.47	0.45	0.03	0.35	0.34
Andradite	0.42	0.40	0.36	0.35	0.33	0.36	0.03	0.53	0.52
Almandine	0.04	0.06	0.04	0.05	0.05	0.05	0.01	0.02	0.02
Pyrope	0.02	0.02	0.02	0.03	0.03	0.03	0.01	0.01	0.03
Spessartine	0.01	0.01	0.01	0.01	0.00	0.01	0.00	0.02	0.02
Katoite	0.03	0.02	0.03	0.03	0.04	0.03	0.01	0.02	0.03
Morimotoite	0.09	0.05	0.07	0.06	0.07	0.07	0.02	0.05	0.04
Uvarovite	0.00	0.00	0.00	0.00	0.00	0.00	0.00	0.00	0.00
Hutcheonite	0.00	0.00	0.00	0.00	0.00	0.00	0.00	0.00	0.00
NaTi garnet	0.00	0.00	0.00	0.00	0.00	0.00	0.00	0.00	0.00
Morimotoite-Mg	0.00	0.00	0.00	0.00	0.00	0.00	0.00	0.00	0.00

TABLE A1 Garnet microprobe analyses, average compositions and standard deviations (σ)

Garnet Type	Grt-3	Grt-3		Grt-4	Grt-4	Grt-4	Grt-4		Grt-4	Grt-4
Metarodingite Type	Ep-MRa		σ	Epidote-metarodingite (amphibolitized)				σ	Ep-MR (amph)	
Sample	AL14-18	Average	n=7	AL98-19B	AL98-19B	AL14-78	Average	n=5	AL14-70	AL14-70
SiO_2	36.49	36.45	0.10	38.30	38.15	38.84	38.52	0.31	38.36	38.37
TiO_2	0.69	0.79	0.07	0.24	0.55	0.56	0.58	0.29	0.44	0.09
Al_2O_3	9.83	9.42	0.34	18.86	16.49	20.31	18.81	1.72	19.84	20.72
Cr_2O_3	0.11	0.10	0.03	0.11	0.03	0.06	0.07	0.04	0.08	0.04
FeO /FeO_{total}	16.23	16.63	0.33	13.17	13.41	11.24	12.41	0.97	11.92	15.54
MnO	0.99	0.89	0.09	2.28	0.99	1.55	1.63	0.46	4.54	2.28
MgO	0.30	0.35	0.15	2.38	1.65	0.73	1.50	0.75	3.22	5.96
CaO	33.04	32.95	0.12	23.92	27.79	26.83	26.07	1.45	20.85	15.55
Na_2O	0.03	0.02	0.01	0.00	0.00	0.00	0.01	0.01	0.00	0.00
H_2O^+	0.61	0.55	0.11	0.28	0.21	0.08	0.15	0.09	0.00	0.00
Total	98.32	98.15	0.31	99.51	99.27	100.21	99.75	0.45	99.24	98.56
FeO	1.46	1.58	0.11	9.37	6.98	9.86	9.11	1.30	9.21	13.11
Fe_2O_3	16.41	16.72	0.40	4.22	7.15	1.54	3.68	2.38	3.01	2.70
Total	99.96	99.83	0.30	99.94	99.99	100.37	100.12	0.24	99.54	98.83
Formula										
Si (T)	2.92	2.93	0.01	2.96	2.97	2.99	2.98	0.01	2.98	2.97
Al (T)	0.00	0.00	0.00	0.00	0.00	0.00	0.00	0.00	0.02	0.03
Fe^{3+} (T)	0.00	0.00	0.00	0.00	0.00	0.00	0.00	0.00	0.00	0.00
$4H^+$ (T)	0.08	0.07	0.01	0.04	0.03	0.01	0.02	0.01	0.00	0.00
Ti (O)	0.04	0.05	0.00	0.01	0.03	0.03	0.03	0.02	0.03	0.01
Al (O)	0.93	0.89	0.03	1.72	1.51	1.84	1.72	0.15	1.79	1.86
Cr (O)	0.01	0.01	0.00	0.01	0.00	0.00	0.00	0.00	0.00	0.00
Fe^{2+} (O)	0.04	0.04	0.00	0.01	0.03	0.03	0.03	0.02	0.00	0.00
Fe^{3+} (O)	0.99	1.01	0.03	0.25	0.42	0.09	0.21	0.14	0.18	0.16
Mg (O)	0.00	0.00	0.00	0.00	0.00	0.00	0.00	0.00	0.00	0.00
Fe^{2+} (D)	0.06	0.06	0.01	0.59	0.42	0.60	0.56	0.09	0.60	0.85
Mn^{2+} (D)	0.07	0.06	0.01	0.15	0.07	0.10	0.11	0.03	0.30	0.15
Mg (D)	0.04	0.04	0.02	0.27	0.19	0.08	0.17	0.09	0.37	0.69
Ca (D)	2.83	2.83	0.01	1.98	2.32	2.21	2.16	0.12	1.73	1.29
Na (D)	0.00	0.00	0.00	0.00	0.00	0.00	0.00	0.00	0.00	0.00
End-members										
Grossular	0.38	0.37	0.02	0.51	0.52	0.66	0.57	0.07	0.47	0.37
Andradite	0.49	0.50	0.01	0.12	0.21	0.04	0.11	0.07	0.09	0.06
Almandine	0.02	0.02	0.00	0.20	0.14	0.20	0.19	0.03	0.20	0.28
Pyrope	0.01	0.01	0.01	0.09	0.06	0.03	0.06	0.03	0.12	0.23
Spessartine	0.02	0.02	0.00	0.05	0.02	0.03	0.04	0.01	0.10	0.05
Katoite	0.03	0.02	0.00	0.01	0.01	0.00	0.01	0.00	0.00	0.00
Morimotoite	0.04	0.04	0.00	0.01	0.03	0.03	0.03	0.02	0.00	0.00
Uvarovite	0.00	0.00	0.00	0.00	0.00	0.00	0.00	0.00	0.00	0.00
Hutcheonite	0.00	0.00	0.00	0.00	0.00	0.00	0.00	0.00	0.01	0.00
NaTi garnet	0.00	0.00	0.00	0.00	0.00	0.00	0.00	0.00	0.00	0.00
Morimotoite-Mg	0.00	0.00	0.00	0.00	0.00	0.00	0.00	0.00	0.00	0.00

TABLE A1 Garnet microprobe analyses, average compositions and standard deviations (σ)

Garnet Type	Grt-4	Grt-4		Grt-4		Grt-5 (core)	Grt-5 (core)	Grt-5 (core)	Grt-5 (core)	
Metarodingite Type	Ep-MR (amph)		σ	All Grt-4	σ	Pyralspite-metarodingite				σ
Sample	AL14-78	Average	n=9	Average	n=14	AL96-24A	AL96-24A	AL96-24A	Average	n=19
SiO_2	39.18	38.53	0.33	38.53	0.31	37.40	38.12	38.24	37.69	0.36
TiO_2	0.12	0.17	0.13	0.32	0.28	0.15	0.28	0.15	0.17	0.13
Al_2O_3	20.79	20.55	0.45	19.93	1.33	20.93	21.25	21.19	21.02	0.17
Cr_2O_3	0.04	0.07	0.02	0.07	0.02	0.00	0.00	0.02	0.00	0.01
FeO /FeO_{total}	13.83	14.30	1.46	13.63	1.57	24.00	23.64	23.29	23.63	0.30
MnO	1.54	2.98	1.01	2.50	1.07	1.16	1.15	1.18	1.17	0.07
MgO	3.89	4.93	1.14	3.70	1.97	2.79	3.34	3.77	3.26	0.32
CaO	20.63	17.63	2.36	20.65	4.66	12.76	12.24	12.22	12.53	0.37
Na_2O	0.03	0.01	0.02	0.01	0.02	0.01	0.00	0.00	0.00	0.00
H_2O^+	0.00	0.00	0.00	0.05	0.09	0.00	0.00	0.00	0.00	0.00
Total	100.04	99.17	0.54	99.38	0.57	99.20	100.02	100.06	99.49	0.50
FeO	11.90	11.77	1.64	10.82	1.98	22.32	23.01	22.27	22.16	0.41
Fe_2O_3	2.15	2.81	0.36	3.12	1.42	1.87	0.70	1.13	1.63	0.46
Total	100.26	99.45	0.51	99.69	0.54	99.39	100.09	100.18	99.65	0.46
Formula										
Si (T)	3.00	2.97	0.01	2.98	0.01	2.96	2.98	2.98	2.97	0.01
Al (T)	0.00	0.03	0.01	0.02	0.02	0.04	0.02	0.02	0.03	0.01
Fe^{3+} (T)	0.00	0.00	0.00	0.00	0.00	0.00	0.00	0.00	0.00	0.00
$4H^+$ (T)	0.00	0.00	0.00	0.01	0.01	0.00	0.00	0.00	0.00	0.00
Ti (O)	0.01	0.01	0.01	0.02	0.02	0.01	0.02	0.01	0.01	0.01
Al (O)	1.87	1.84	0.03	1.80	0.11	1.91	1.94	1.93	1.92	0.02
Cr (O)	0.00	0.00	0.00	0.00	0.00	0.00	0.00	0.00	0.00	0.00
Fe^{2+} (O)	0.00	0.00	0.00	0.01	0.02	0.00	0.00	0.00	0.00	0.00
Fe^{3+} (O)	0.12	0.16	0.02	0.18	0.08	0.11	0.04	0.07	0.10	0.03
Mg (O)	0.00	0.00	0.00	0.00	0.00	0.00	0.00	0.00	0.00	0.00
Fe^{2+} (D)	0.76	0.76	0.10	0.69	0.14	1.48	1.51	1.45	1.46	0.02
Mn^{2+} (D)	0.10	0.20	0.07	0.16	0.07	0.08	0.08	0.08	0.08	0.00
Mg (D)	0.44	0.57	0.13	0.43	0.23	0.33	0.39	0.44	0.38	0.04
Ca (D)	1.69	1.46	0.20	1.71	0.39	1.08	1.03	1.02	1.06	0.03
Na (D)	0.00	0.00	0.00	0.00	0.00	0.00	0.00	0.00	0.00	0.00
End-members										
Grossular	0.50	0.41	0.05	0.47	0.10	0.33	0.31	0.31	0.32	0.01
Andradite	0.06	0.07	0.01	0.08	0.05	0.03	0.02	0.03	0.03	0.00
Almandine	0.25	0.25	0.03	0.23	0.05	0.49	0.50	0.48	0.49	0.01
Pyrope	0.15	0.19	0.04	0.14	0.08	0.11	0.13	0.15	0.13	0.01
Spessartine	0.03	0.07	0.02	0.05	0.02	0.03	0.03	0.03	0.03	0.00
Katoite	0.00	0.00	0.00	0.00	0.00	0.00	0.00	0.00	0.00	0.00
Morimotoite	0.00	0.00	0.00	0.01	0.02	0.00	0.00	0.00	0.00	0.00
Uvarovite	0.00	0.00	0.00	0.00	0.00	0.00	0.00	0.00	0.00	0.00
Hutcheonite	0.00	0.00	0.00	0.00	0.00	0.00	0.01	0.00	0.00	0.00
NaTi garnet	0.00	0.00	0.00	0.00	0.00	0.00	0.00	0.00	0.00	0.00
Morimotoite-Mg	0.00	0.00	0.00	0.00	0.00	0.00	0.00	0.00	0.00	0.00

TABLE A1 Garnet microprobe analyses, average compositions and standard deviations (σ)

Garnet Type	Grt-5 (rim)	Grt-5 (rim)	Grt-5 (rim)	Grt-5 (rim)	Grt-5 (rim)	
Metarodingite Type	Pyralspite-metarodingite					σ
Sample	AL96-24A	AL14-01	AL14-99-2	AL96-24A	Average	n=29
SiO_2	38.44	38.95	38.18	38.94	38.89	0.43
TiO_2	0.06	0.14	0.04	0.06	0.09	0.04
Al_2O_3	21.49	21.44	20.96	22.25	21.56	0.30
Cr_2O_3	0.00	0.00	0.09	0.00	0.01	0.02
FeO /FeO_{total}	18.77	18.95	21.34	18.37	18.99	0.85
MnO	0.44	1.13	0.60	0.52	0.54	0.29
MgO	7.44	6.22	7.84	6.67	7.04	0.37
CaO	12.32	13.60	9.81	13.04	12.55	0.89
Na_2O	0.00	0.00	0.00	0.00	0.00	0.00
H_2O^+	0.00	0.00	0.00	0.00	0.00	0.00
Total	98.97	100.44	98.87	99.85	99.68	0.55
FeO	16.50	17.06	18.54	17.49	17.41	0.68
Fe_2O_3	2.52	2.10	3.11	0.98	1.76	0.76
Total	99.22	100.65	99.18	99.95	99.86	0.50
Formula						
Si (T)	2.95	2.97	2.95	2.97	2.97	0.02
Al (T)	0.05	0.03	0.05	0.03	0.03	0.02
Fe^{3+} (T)	0.00	0.00	0.00	0.00	0.00	0.00
$4H^+$ (T)	0.00	0.00	0.00	0.00	0.00	0.00
Ti (O)	0.00	0.01	0.00	0.00	0.01	0.00
Al (O)	1.90	1.89	1.86	1.97	1.91	0.03
Cr (O)	0.00	0.00	0.01	0.00	0.00	0.00
Fe^{2+} (O)	0.00	0.00	0.00	0.00	0.00	0.00
Fe^{3+} (O)	0.15	0.12	0.18	0.06	0.10	0.04
Mg (O)	0.00	0.00	0.00	0.00	0.00	0.00
Fe^{2+} (D)	1.06	1.09	1.20	1.11	1.11	0.04
Mn^{2+} (D)	0.03	0.07	0.04	0.03	0.04	0.02
Mg (D)	0.85	0.71	0.90	0.76	0.80	0.04
Ca (D)	1.01	1.11	0.81	1.07	1.03	0.07
Na (D)	0.00	0.00	0.00	0.00	0.00	0.00
End-members						
Grossular	0.30	0.33	0.22	0.35	0.31	0.03
Andradite	0.03	0.04	0.05	0.00	0.03	0.01
Almandine	0.35	0.36	0.40	0.37	0.37	0.01
Pyrope	0.28	0.24	0.30	0.25	0.27	0.01
Spessartine	0.01	0.02	0.01	0.01	0.01	0.01
Katoite	0.00	0.00	0.00	0.00	0.00	0.00
Morimotoite	0.00	0.00	0.00	0.00	0.00	0.00
Uvarovite	0.00	0.00	0.00	0.00	0.00	0.00
Hutcheonite	0.00	0.00	0.00	0.00	0.00	0.00
NaTi garnet	0.00	0.00	0.00	0.00	0.00	0.00
Morimotoite-Mg	0.00	0.00	0.00	0.00	0.00	0.00

TABLE A2 Chlorite microprobe analyses, average compositions and standard deviations (σ)

Mineral	Chlorite	Chlorite	Chlorite	Chlorite	Chlorite		Chlorite	Chlorite	Chlorite
Rock Type	Grandite-metarodingite					σ	Epidote-metarodingite		
Sample	AL95-36C	AL95-36C	AL14-04B	AL14-04B	Average	n=24	AL14-26E-6	AL14-70	AL14-70
SiO_2	29.07	29.22	28.23	29.18	29.15	0.41	29.43	28.73	29.14
TiO_2	0.01	0.02	0.01	0.04	0.02	0.01	0.02	0.07	0.03
Al_2O_3	21.27	21.26	20.50	20.72	20.97	0.33	20.14	20.79	20.68
FeO	6.79	6.76	8.22	7.95	6.87	0.69	7.66	6.98	7.04
MnO	0.02	0.03	0.04	0.02	0.05	0.02	0.12	0.11	0.11
MgO	29.51	29.15	28.97	28.20	29.12	0.46	28.37	28.82	29.17
CaO	0.00	0.01	0.01	0.03	0.04	0.03	0.07	0.07	0.01
Na_2O	0.00	0.00	0.03	0.11	0.03	0.03	0.00	0.00	0.01
K_2O	0.01	0.01	0.01	0.03	0.02	0.01	0.03	0.00	0.01
BaO	0.00	0.00	0.00	0.00	0.00	0.00	0.10	0.02	0.00
F	0.03	0.01	0.02	0.10	0.03	0.03	0.01	0.01	0.00
Cl	0.07	0.02	0.05	0.02	0.03	0.02	0.01	0.02	0.05
Cr_2O_3	0.03	0.02	0.02	0.01	0.02	0.01	0.04	0.19	0.06
NiO	0.07	0.08	0.06	0.07	0.07	0.02	0.10	0.07	0.08
Total	86.89	86.59	86.14	86.46	86.41	0.77	86.10	85.89	86.40
Fe_2O_3	0.14	0.36	0.00	0.38	0.29	0.19	0.41	0.14	0.14
FeO	6.66	6.43	8.22	7.61	6.61	0.73	7.29	6.85	6.92
H_2O*	12.40	12.42	12.20	12.23	12.36	0.12	12.28	12.28	12.35
Total	99.30	99.04	98.34	98.73	98.80	0.88	98.42	98.18	98.77
O=F,Cl	0.03	0.01	0.02	0.04	0.02	0.01	0.01	0.01	0.01
Total	99.27	99.03	98.32	98.68	98.78	0.88	98.42	98.18	98.75
Formula 38O									
Si	5.58	5.62	5.50	5.65	5.63	0.05	5.73	5.60	5.64
Al^{iv}	2.42	2.38	2.50	2.35	2.37	0.05	2.27	2.40	2.36
Al^{vi}	2.40	2.45	2.24	2.40	2.40	0.06	2.36	2.38	2.36
Ti	0.00	0.00	0.00	0.01	0.00	0.00	0.00	0.01	0.00
Cr	0.01	0.00	0.00	0.00	0.00	0.00	0.01	0.03	0.01
Fe^{3+}	0.02	0.05	0.00	0.06	0.04	0.03	0.06	0.02	0.02
Fe^{2+}	1.07	1.03	1.43	1.23	1.07	0.13	1.19	1.12	1.12
Mn	0.00	0.01	0.01	0.00	0.01	0.00	0.02	0.02	0.02
Mg	8.45	8.36	8.42	8.14	8.38	0.12	8.24	8.37	8.42
Ni	0.01	0.01	0.01	0.01	0.01	0.00	0.02	0.01	0.01
Ca	0.00	0.00	0.00	0.01	0.01	0.01	0.01	0.01	0.00
Na	0.00	0.00	0.02	0.08	0.02	0.02	0.00	0.00	0.01
K	0.01	0.01	0.01	0.01	0.01	0.01	0.01	0.00	0.00
Ba	0.00	0.00	0.00	0.00	0.00	0.00	0.01	0.00	0.00
F	0.04	0.02	0.03	0.12	0.04	0.03	0.01	0.01	0.00
Cl	0.05	0.01	0.03	0.01	0.02	0.01	0.00	0.02	0.04
OH (calc.)	15.92	15.97	15.94	15.87	15.94	0.04	15.98	15.98	15.96
Total	35.97	35.93	36.14	35.95	35.96	0.06	35.93	35.97	35.97
Variety	sheridanite	clinochlore	sheridanite	clinochlore			clinochlore	sheridanite	clinochlore

TABLE A2 Chlorite microprobe analyses, average compositions and standard deviations (σ)

Mineral	Chlorite	Chlorite		Chlorite	Chlorite	Chlorite	Chlorite	Chlorite		Chlorite	
Rock Type	Ep-metarodingite		σ	Pyralspite-metarodingite					σ	All MR	σ
Sample	AL14-70	Average	n=34	AL14-01	AL14-99-1	AL14-99-1	AL14-99-1	Average	n=17	Average	n=75
SiO_2	28.27	29.12	0.58	28.95	28.53	29.54	28.15	28.94	0.46	29.09	0.51
TiO_2	0.05	0.04	0.03	0.06	0.09	0.04	0.05	0.04	0.01	0.04	0.02
Al_2O_3	20.57	20.72	0.57	20.26	20.37	20.56	22.16	20.69	0.62	20.79	0.53
FeO	6.99	7.34	0.46	8.67	10.17	7.38	7.66	7.66	0.80	7.26	0.68
MnO	0.10	0.10	0.03	0.06	0.11	0.07	0.05	0.05	0.03	0.07	0.04
MgO	29.18	28.79	0.55	27.36	27.18	28.86	28.75	28.85	0.72	28.91	0.58
CaO	0.06	0.05	0.03	0.03	0.07	0.03	0.02	0.02	0.02	0.04	0.03
Na_2O	0.04	0.01	0.01	0.04	0.01	0.00	0.00	0.02	0.02	0.02	0.02
K_2O	0.02	0.01	0.01	0.02	0.01	0.01	0.00	0.01	0.01	0.01	0.01
BaO	0.00	0.02	0.02	0.00	0.03	0.01	0.07	0.01	0.02	0.01	0.02
F	0.00	0.01	0.01	0.03	0.00	0.00	0.00	0.01	0.02	0.01	0.02
Cl	0.01	0.03	0.02	0.06	0.02	0.02	0.04	0.05	0.03	0.03	0.02
Cr_2O_3	0.05	0.07	0.05	0.02	0.08	0.05	0.11	0.06	0.03	0.05	0.04
NiO	0.10	0.08	0.02	0.02	0.00	0.00	0.01	0.01	0.01	0.06	0.03
Total	85.45	86.40	0.77	85.57	86.67	86.57	87.07	86.41	0.50	86.40	0.71
Fe_2O_3	0.00	0.26	0.27	0.52	0.00	0.43	0.00	0.13	0.18	0.24	0.23
FeO	6.99	7.11	0.55	8.20	10.17	6.99	7.66	7.54	0.79	7.05	0.75
H_2O*	12.21	12.34	0.12	12.10	12.20	12.40	12.41	12.31	0.10	12.34	0.12
Total	97.67	98.77	0.89	97.72	98.87	99.01	99.48	98.73	0.58	98.77	0.82
O=F,Cl	0.00	0.01	0.01	0.03	0.00	0.01	0.01	0.01	0.01	0.01	0.01
Total	97.67	98.76	0.89	97.70	98.87	99.00	99.47	98.72	0.58	98.75	0.82
Formula 38O											
Si	5.53	5.64	0.07	5.69	5.60	5.70	5.43	5.61	0.08	5.63	0.07
Al^{iv}	2.47	2.36	0.07	2.31	2.40	2.30	2.57	2.39	0.08	2.37	0.07
Al^{vi}	2.29	2.38	0.08	2.40	2.32	2.39	2.47	2.35	0.07	2.38	0.08
Ti	0.01	0.01	0.00	0.01	0.01	0.01	0.01	0.01	0.00	0.01	0.00
Cr	0.01	0.01	0.01	0.00	0.01	0.01	0.02	0.01	0.00	0.01	0.01
Fe^{3+}	0.00	0.04	0.04	0.08	0.00	0.06	0.00	0.02	0.03	0.03	0.03
Fe^{2+}	1.21	1.16	0.10	1.35	1.69	1.13	1.26	1.24	0.14	1.15	0.13
Mn	0.02	0.02	0.01	0.01	0.02	0.01	0.01	0.01	0.00	0.01	0.01
Mg	8.51	8.32	0.14	8.01	7.95	8.30	8.26	8.34	0.18	8.34	0.15
Ni	0.02	0.01	0.00	0.00	0.00	0.00	0.00	0.00	0.00	0.01	0.01
Ca	0.01	0.01	0.01	0.01	0.02	0.01	0.00	0.00	0.00	0.01	0.01
Na	0.03	0.01	0.01	0.03	0.01	0.00	0.00	0.01	0.01	0.01	0.02
K	0.01	0.01	0.00	0.01	0.00	0.01	0.00	0.00	0.00	0.01	0.01
Ba	0.00	0.00	0.00	0.00	0.00	0.00	0.01	0.00	0.00	0.00	0.00
F	0.00	0.01	0.01	0.04	0.00	0.00	0.00	0.01	0.02	0.02	0.03
Cl	0.01	0.02	0.01	0.04	0.01	0.02	0.02	0.03	0.02	0.02	0.01
OH*	15.99	15.98	0.01	15.92	15.99	15.98	15.98	15.96	0.03	15.96	0.03
Total	36.11	35.97	0.07	35.91	36.03	35.92	36.04	36.00	0.05	35.97	0.06
Variety	sheridanite			clinochlore	sheridanite	clinochlore	sheridanite				

TABLE A2 Chlorite microprobe analyses, average compositions and standard deviations (σ)

Mineral	Chlorite	Chlorite	Chlorite	Chlorite		Chlorite	Chlorite	Chlorite	Chlorite	
Rock Type	Chl-blackwall				σ	Chl-Di- and Chl-Di-Ol-metasomatic rim				σ
Sample	AL14-19	AL14-19	AL14-19	Average	n=43	AL14-20-L	AL14-20-L	AL14-20-L	Average	n=26
SiO_2	30.42	33.51	30.63	31.33	1.46	33.82	33.96	33.85	33.40	0.66
TiO_2	0.02	0.01	0.00	0.03	0.02	0.00	0.00	0.00	0.02	0.01
Al_2O_3	18.62	13.54	19.19	18.02	2.46	12.86	12.76	12.68	14.23	0.96
FeO	6.53	4.92	4.56	5.28	1.00	3.23	3.62	3.70	3.58	0.44
MnO	0.09	0.02	0.10	0.06	0.03	0.02	0.02	0.03	0.02	0.01
MgO	30.38	33.76	31.34	31.17	1.37	35.23	34.35	34.38	33.77	0.67
CaO	0.00	0.00	0.00	0.12	0.52	0.01	0.01	0.01	0.02	0.02
Na_2O	0.00	0.01	0.01	0.03	0.09	0.01	0.01	0.01	0.02	0.01
K_2O	0.01	0.01	0.01	0.03	0.05	0.01	0.01	0.02	0.01	0.01
BaO	0.00	0.00	0.00	0.01	0.02	0.00	0.00	0.00	0.01	0.01
F	0.02	0.00	0.02	0.01	0.02	0.00	0.00	0.05	0.01	0.01
Cl	0.02	0.01	0.01	0.02	0.02	0.01	0.01	0.02	0.03	0.01
Cr_2O_3	0.00	0.03	0.00	0.04	0.03	0.73	1.21	0.86	0.88	0.33
NiO	0.00	0.11	0.05	0.05	0.06	0.15	0.18	0.20	0.32	0.10
Total	86.12	85.94	85.93	86.20	1.54	86.07	86.14	85.84	86.30	0.61
Fe_2O_3	0.14	0.00	0.37	0.47	0.40	0.00	0.18	0.11	0.34	0.23
FeO	6.40	4.92	4.23	4.86	1.20	3.23	3.45	3.60	3.28	0.55
H_2O*	12.36	12.46	12.47	12.47	0.21	12.55	12.53	12.42	12.54	0.11
Total	98.49	98.41	98.43	98.71	1.72	98.62	98.69	98.27	98.88	0.72
O=F,Cl	0.01	0.00	0.01	0.01	0.01	0.00	0.00	0.03	0.01	0.01
Total	98.48	98.40	98.42	98.70	1.72	98.62	98.69	98.24	98.87	0.72
Formula 38O										
Si	5.88	6.44	5.87	6.01	0.29	6.45	6.49	6.49	6.37	0.11
Al^{iv}	2.12	1.56	2.13	1.99	0.29	1.55	1.51	1.51	1.63	0.11
Al^{vi}	2.13	1.51	2.21	2.08	0.26	1.34	1.37	1.36	1.57	0.13
Ti	0.00	0.00	0.00	0.00	0.00	0.00	0.00	0.00	0.00	0.00
Cr	0.00	0.00	0.00	0.01	0.00	0.11	0.18	0.13	0.13	0.05
Fe^{3+}	0.02	0.00	0.05	0.07	0.06	0.00	0.03	0.02	0.05	0.03
Fe^{2+}	1.04	0.81	0.68	0.79	0.20	0.56	0.55	0.58	0.53	0.09
Mn	0.02	0.00	0.02	0.01	0.00	0.00	0.00	0.01	0.00	0.00
Mg	8.76	9.67	8.95	8.91	0.37	10.01	9.79	9.83	9.60	0.17
Ni	0.00	0.02	0.01	0.01	0.01	0.02	0.03	0.03	0.05	0.02
Ca	0.00	0.00	0.00	0.02	0.11	0.00	0.00	0.00	0.00	0.00
Na	0.00	0.01	0.01	0.02	0.07	0.01	0.01	0.01	0.01	0.01
K	0.01	0.01	0.01	0.01	0.03	0.01	0.01	0.01	0.00	0.00
Ba	0.00	0.00	0.00	0.00	0.00	0.00	0.00	0.00	0.00	0.00
F	0.03	0.00	0.03	0.01	0.02	0.00	0.00	0.07	0.01	0.02
Cl	0.01	0.01	0.01	0.01	0.01	0.01	0.01	0.02	0.02	0.01
OH*	15.96	15.99	15.96	15.97	0.02	15.99	15.99	15.92	15.97	0.02
Total	35.97	36.03	35.93	35.93	0.10	36.06	35.97	35.97	35.94	0.05
Variety	clinochlore	penninite	clinochlore			penninite	penninite	penninite		

TABLE A3 Epidote microprobe analyses, average compositions and standard deviations (σ)

Mineral	Epidote	Epidote	Epidote	Epidote	Epidote	Epidote		Epidote	Epidote
Rock Type	Grandite-metarodingite Vein Grt-3						σ	Epidote-metarodingite	
Sample	AL14-04B	AL14-16-2	AL14-16-2	AL14-16-2	AL14-16-2	Average	n=15	AL14-26-E-2	AL98-19B
SiO_2	38.52	37.69	37.91	37.24	37.41	37.96	0.45	37.43	37.98
TiO_2	0.16	0.03	0.05	0.07	0.06	0.10	0.05	0.04	0.17
Al_2O_3	25.48	23.25	23.92	24.44	24.37	24.74	0.76	23.49	24.25
Cr_2O_3	0.00	0.05	0.05	0.06	0.06	0.03	0.02	0.03	0.04
FeO	9.59	11.76	10.83	9.93	10.08	10.22	0.72	11.25	10.59
MnO	0.03	0.03	0.03	0.04	0.06	0.02	0.02	0.04	0.01
MgO	0.26	0.04	0.28	0.06	0.07	0.17	0.08	0.02	0.13
CaO	23.42	23.25	23.23	23.41	23.30	23.35	0.12	23.61	22.93
Na2O	0.00	0.01	0.01	0.01	0.00	0.01	0.01	0.01	0.01
K_2O	0.01	0.01	0.00	0.00	0.00	0.01	0.00	0.00	0.01
Cl	0.18	0.03	0.00	0.00	0.00	0.10	0.07	0.00	0.09
F	0.00	0.01	0.05	0.00	0.02	0.01	0.01	0.03	0.00
BaO	0.00	0.03	0.02	0.03	0.00	0.01	0.01	0.00	0.01
NiO	0.00	0.01	0.04	0.02	0.01	0.01	0.01	0.01	0.00
Total	97.67	96.17	96.41	95.30	95.43	96.73	0.80	95.95	96.22
Fe_2O_3	10.55	12.94	11.91	10.92	11.09	11.25	0.80	12.38	11.65
Total	97.49	96.13	96.30	95.26	95.41	96.61	0.75	95.91	96.12
Formula									
Si	3.01	3.02	3.02	3.00	3.00	3.01	0.01	3.00	3.02
Al^{IV}	0.00	0.00	0.00	0.00	0.00	0.00	0.00	0.00	0.00
Z	3.01	3.02	3.02	3.00	3.00	3.01	0.01	3.00	3.02
Al^{VI}	2.35	2.19	2.24	2.31	2.31	2.31	0.05	2.22	2.27
Cr	0.00	0.00	0.00	0.00	0.00	0.00	0.00	0.00	0.00
Fe^{3+}	0.62	0.78	0.71	0.66	0.67	0.67	0.05	0.75	0.70
Y	2.97	2.98	2.96	2.98	2.98	2.98	0.01	2.97	2.97
Ti	0.01	0.00	0.00	0.00	0.00	0.01	0.00	0.00	0.01
Mg	0.03	0.00	0.03	0.01	0.01	0.02	0.01	0.00	0.02
Mn	0.00	0.00	0.00	0.00	0.00	0.00	0.00	0.00	0.00
Ni	0.00	0.00	0.00	0.00	0.00	0.00	0.00	0.00	0.00
Ca	1.96	1.99	1.98	2.02	2.00	1.98	0.02	2.03	1.95
Na	0.00	0.00	0.00	0.00	0.00	0.00	0.00	0.00	0.00
K	0.00	0.00	0.00	0.00	0.00	0.00	0.00	0.00	0.00
X	2.01	2.00	2.02	2.03	2.02	2.01	0.01	2.04	1.98
	7.99	8.00	8.00	8.01	8.00	8.00	0.01	8.01	7.98
FeO_{Total}	9.59	11.76	10.83	9.93	10.08	10.22	0.72	11.25	10.59
X_{Czs}	0.34	0.19	0.24	0.31	0.30	0.30	0.05	0.22	0.27
X_{Ep}	0.60	0.78	0.70	0.65	0.66	0.66	0.06	0.74	0.69
%Pistacite	20.91	26.21	24.12	22.23	22.51	22.52	1.77	25.17	23.46
aZo	0.36	0.22	0.28	0.34	0.33	0.32	0.05	0.26	0.29

TABLE A3 Epidote microprobe analyses, average compositions and standard deviations (σ)

Mineral	Epidote	Epidote	Epidote		Epidote	Epidote	Epidote	Epidote		Clinozoisite	Clinozoisite
Rock Type	Epidote-metarodingite			σ	Epidote-metarodingite				σ	Epidote-metarodingite	
Sample	AL14-18	AL14-18	Average	n=30	AL14-18	AL98-19B	AL14-18	Average	n=9	AL98-19B	AL98-19B
SiO_2	37.34	37.69	37.73	0.33	37.44	38.31	37.81	38.08	0.42	38.80	38.57
TiO_2	0.03	0.16	0.12	0.05	0.17	0.09	0.15	0.14	0.03	0.15	0.20
Al_2O_3	24.82	25.65	24.46	0.61	26.01	26.89	27.13	26.79	0.44	28.99	29.33
Cr_2O_3	0.03	0.01	0.02	0.02	0.05	0.00	0.00	0.01	0.02	0.02	0.00
FeO	10.20	9.44	10.49	0.48	8.64	7.83	7.39	7.93	0.44	5.17	4.71
MnO	0.01	0.05	0.06	0.04	0.02	0.15	0.07	0.10	0.06	0.11	0.12
MgO	0.12	0.13	0.12	0.04	0.14	0.05	0.05	0.08	0.03	0.06	0.05
CaO	23.53	23.15	23.27	0.41	23.13	23.33	23.62	23.41	0.20	23.73	23.95
Na2O	0.02	0.02	0.01	0.01	0.03	0.02	0.02	0.01	0.01	0.00	0.00
K_2O	0.01	0.02	0.01	0.00	0.01	0.01	0.01	0.01	0.00	0.02	0.01
Cl	0.00	0.00	0.07	0.07	0.00	0.17	0.00	0.08	0.07	0.12	0.09
F	0.00	0.00	0.00	0.01	0.00	0.01	0.00	0.01	0.01	0.00	0.01
BaO	0.00	0.00	0.00	0.01	0.00	0.00	0.00	0.00	0.01	0.00	0.00
NiO	0.15	0.09	0.06	0.07	0.15	0.00	0.14	0.06	0.07	0.00	0.00
Total	96.25	96.43	96.42	0.37	95.79	96.86	96.41	96.71	0.56	97.17	97.03
Fe_2O_3	11.22	10.38	11.54	0.53	9.50	8.61	8.13	8.72	0.48	5.69	5.18
Total	96.10	96.32	96.29	0.36	96.65	96.68	96.26	96.68	0.47	97.05	96.93
Formula											
Si	2.98	2.99	3.00	0.02	2.98	3.01	2.98	3.00	0.01	3.01	2.99
Al^{IV}	0.02	0.01	0.01	0.01	0.02	0.00	0.02	0.01	0.01	0.00	0.01
Z	3.00	3.00	3.01	0.01	3.00	3.01	3.00	3.00	0.00	3.01	3.00
Al^{VI}	2.31	2.38	2.29	0.05	2.42	2.49	2.51	2.48	0.03	2.65	2.68
Cr	0.00	0.00	0.00	0.00	0.00	0.00	0.00	0.00	0.00	0.00	0.00
Fe^{3+}	0.67	0.62	0.69	0.03	0.57	0.51	0.48	0.52	0.03	0.33	0.30
Y	2.99	3.00	2.98	0.02	3.00	3.00	2.99	2.99	0.01	2.98	2.98
Ti	0.00	0.01	0.01	0.00	0.01	0.01	0.01	0.01	0.00	0.01	0.01
Mg	0.01	0.02	0.01	0.00	0.02	0.01	0.01	0.01	0.00	0.01	0.01
Mn	0.00	0.00	0.00	0.00	0.00	0.01	0.00	0.01	0.00	0.01	0.01
Ni	0.00	0.00	0.00	0.00	0.00	0.00	0.00	0.00	0.00	0.00	0.00
Ca	2.01	1.97	1.98	0.04	1.97	1.96	2.00	1.97	0.02	1.97	1.99
Na	0.00	0.00	0.00	0.00	0.00	0.00	0.00	0.00	0.00	0.00	0.00
K	0.00	0.00	0.00	0.00	0.00	0.00	0.00	0.00	0.00	0.00	0.00
X	2.03	2.00	2.01	0.04	2.01	1.99	2.02	2.00	0.02	2.00	2.02
	8.02	8.00	8.00	0.02	8.00	7.99	8.01	8.00	0.01	7.99	8.00
FeO_{Total}	10.20	9.44	10.49	0.48	8.64	7.83	7.39	7.93	0.44	5.17	4.71
X_{Czs}	0.30	0.36	0.28	0.05	0.40	0.48	0.48	0.46	0.04	0.64	0.66
X_{Ep}	0.65	0.59	0.67	0.04	0.54	0.50	0.46	0.50	0.03	0.33	0.29
%Pistacite	22.56	20.63	23.20	1.20	19.02	16.97	16.15	17.25	1.05	11.13	10.15
aZo	0.33	0.37	0.30	0.03	0.42	0.47	0.52	0.47	0.03	0.65	0.69

TABLE A3 Epidote microprobe analyses, average compositions and standard deviations (σ)

Mineral	Clinozoisite	Clinozoisite		Epidote	Epidote	Epidote	Epidote		Epidote	Epidote	Epidote
Rock Type	Epidote-metarodingite		σ	Pyrals-metarodingite				σ	Pyralspite-metarodingite		
Sample	AL14-18	Average	n=6	AL14-01	AL14-01	AL14-01	Average	n=4	AL14-01	AL14-01	AL14-01
SiO_2	38.17	38.53	0.27	38.07	38.17	38.10	38.00	0.24	38.00	38.08	38.02
TiO_2	0.49	0.22	0.15	0.13	0.07	0.16	0.14	0.05	0.14	0.17	0.13
Al_2O_3	29.27	29.34	0.23	25.12	25.75	25.57	25.44	0.28	25.44	25.75	26.20
Cr_2O_3	0.04	0.01	0.02	0.03	0.00	0.01	0.01	0.01	0.01	0.01	0.00
FeO	4.47	4.70	0.30	9.92	9.23	9.53	9.60	0.29	9.60	9.14	8.66
MnO	0.07	0.10	0.02	0.06	0.06	0.14	0.07	0.05	0.07	0.14	0.15
MgO	0.05	0.06	0.01	0.19	0.05	0.16	0.15	0.07	0.15	0.14	0.13
CaO	24.04	23.90	0.11	22.83	22.58	23.01	22.89	0.24	22.89	23.12	23.10
Na2O	0.01	0.01	0.01	0.02	0.01	0.01	0.01	0.00	0.01	0.01	0.02
K_2O	0.01	0.01	0.00	0.01	0.01	0.01	0.01	0.00	0.01	0.01	0.01
Cl	0.00	0.06	0.06	0.12	0.13	0.11	0.13	0.02	0.13	0.11	0.15
F	0.00	0.00	0.00	0.00	0.01	0.00	0.01	0.01	0.01	0.00	0.00
BaO	0.01	0.00	0.01	0.00	0.00	0.01	0.00	0.01	0.00	0.02	0.00
NiO	0.07	0.02	0.03	0.00	0.00	0.00	0.00	0.00	0.00	0.00	0.00
Total	96.70	96.98	0.30	96.49	96.08	96.82	96.46	0.30	96.46	96.71	96.58
Fe_2O_3	4.91	5.17	0.33	10.92	10.16	10.49	10.56	0.32	10.56	10.06	9.53
Total	96.61	96.89	0.28	96.37	95.94	96.70	96.32	0.32	96.32	96.59	96.43
Formula											
Si	2.98	2.99	0.01	3.01	3.02	3.00	3.01	0.02	3.01	3.00	3.00
Al^{IV}	0.02	0.01	0.01	0.00	0.00	0.00	0.00	0.01	0.00	0.00	0.00
Z	3.00	3.00	0.00	3.01	3.02	3.00	3.01	0.01	3.01	3.00	3.00
Al^{VI}	2.67	2.68	0.02	2.34	2.40	2.38	2.37	0.03	2.37	2.39	2.44
Cr	0.00	0.00	0.00	0.00	0.00	0.00	0.00	0.00	0.00	0.00	0.00
Fe^{3+}	0.29	0.30	0.02	0.65	0.61	0.62	0.63	0.02	0.63	0.60	0.57
Y	2.96	2.98	0.01	3.00	3.01	3.00	3.00	0.01	3.00	2.99	3.00
Ti	0.03	0.01	0.01	0.01	0.00	0.01	0.01	0.00	0.01	0.01	0.01
Mg	0.01	0.01	0.00	0.02	0.01	0.02	0.02	0.01	0.02	0.02	0.02
Mn	0.00	0.01	0.00	0.00	0.00	0.01	0.00	0.00	0.00	0.01	0.01
Ni	0.00	0.00	0.00	0.00	0.00	0.00	0.00	0.00	0.00	0.00	0.00
Ca	2.01	1.99	0.01	1.94	1.92	1.94	1.94	0.02	1.94	1.95	1.95
Na	0.00	0.00	0.00	0.00	0.00	0.00	0.00	0.00	0.00	0.00	0.00
K	0.00	0.00	0.00	0.00	0.00	0.00	0.00	0.00	0.00	0.00	0.00
X	2.05	2.02	0.02	1.97	1.93	1.98	1.97	0.03	1.97	1.99	1.99
	8.01	8.00	0.01	7.98	7.97	7.99	7.98	0.01	7.98	7.99	7.99
FeO_{Total}	4.47	4.70	0.30	9.92	9.23	9.53	9.60	0.29	9.60	9.14	8.66
X_{Czs}	0.62	0.65	0.02	0.34	0.41	0.36	0.36	0.03	0.36	0.38	0.42
X_{Ep}	0.27	0.29	0.02	0.63	0.61	0.60	0.61	0.02	0.61	0.58	0.54
%Pistacite	9.76	10.14	0.61	21.72	20.12	20.75	20.97	0.69	20.97	19.96	18.84
aZo	0.72	0.69	0.03	0.33	0.36	0.36	0.35	0.02	0.35	0.38	0.41

TABLE A3 Epidote microprobe analyses, average compositions and standard deviations (σ)

Mineral	Epidote	Epidote	Epidote	Epidote	Epidote		Clinozoisite	Clinozoisite	Clinozoisite	Clinozoisite
Rock Type	Pyralspite-metarodingite					σ	Pyralspite-metarodingite			
Sample	AL14-99-2	AL14-99-2	AL14-99-1	AL14-99-2	Average	n=47	AL14-01	AL14-01	AL96-24A	AL14-01
SiO_2	37.27	37.47	37.73	38.36	37.96	0.32	38.45	38.17	38.84	38.65
TiO_2	0.11	0.14	0.16	0.13	0.16	0.03	0.12	0.07	0.09	0.11
Al_2O_3	26.48	26.11	26.62	27.71	26.35	0.58	28.27	28.38	29.51	29.64
Cr_2O_3	0.05	0.08	0.08	0.07	0.09	0.16	0.02	0.01	0.00	0.04
FeO	8.06	7.89	7.64	6.53	8.16	0.71	6.05	5.62	4.67	4.29
MnO	0.13	0.05	0.22	0.18	0.13	0.06	0.14	0.09	0.08	0.09
MgO	0.10	0.41	0.11	0.09	0.15	0.07	0.09	0.08	0.07	0.08
CaO	22.91	22.72	23.32	23.63	23.13	0.23	23.38	23.60	23.80	23.86
Na2O	0.02	0.01	0.04	0.02	0.01	0.01	0.02	0.02	0.00	0.01
K_2O	0.00	0.01	0.00	0.00	0.01	0.01	0.02	0.01	0.02	0.01
Cl	0.00	0.00	0.00	0.00	0.09	0.07	0.13	0.10	0.08	0.12
F	0.00	0.01	0.03	0.00	0.01	0.03	0.00	0.01	0.01	0.00
BaO	0.00	0.00	0.00	0.01	0.00	0.01	0.00	0.00	0.00	0.00
NiO	0.00	0.00	0.03	0.00	0.01	0.01	0.00	0.01	0.01	0.01
Total	95.14	94.89	95.99	96.71	96.26	0.50	96.69	96.17	97.18	96.92
Fe_2O_3	8.87	8.68	8.40	7.18	8.97	0.78	6.66	6.18	5.14	4.72
Total	95.14	94.88	95.93	96.71	96.15	0.46	96.56	96.07	97.09	96.80
Formula										
Si	2.98	3.00	2.99	3.00	3.00	0.01	3.00	3.00	3.01	3.00
Al^{IV}	0.02	0.00	0.01	0.00	0.00	0.01	0.00	0.00	0.00	0.00
Z	3.00	3.00	3.00	3.00	3.00	0.01	3.00	3.00	3.01	3.00
Al^{VI}	2.47	2.46	2.48	2.56	2.45	0.05	2.60	2.63	2.69	2.71
Cr	0.00	0.00	0.01	0.00	0.01	0.01	0.00	0.00	0.00	0.00
Fe^{3+}	0.53	0.52	0.50	0.42	0.53	0.05	0.39	0.37	0.30	0.28
Y	3.01	2.99	2.98	2.98	2.99	0.01	3.00	2.99	2.99	2.99
Ti	0.01	0.01	0.01	0.01	0.01	0.00	0.01	0.00	0.01	0.01
Mg	0.01	0.05	0.01	0.01	0.02	0.01	0.01	0.01	0.01	0.01
Mn	0.01	0.00	0.01	0.01	0.01	0.00	0.01	0.01	0.01	0.01
Ni	0.00	0.00	0.00	0.00	0.00	0.00	0.00	0.00	0.00	0.00
Ca	1.96	1.95	1.98	1.98	1.96	0.02	1.96	1.99	1.97	1.98
Na	0.00	0.00	0.01	0.00	0.00	0.00	0.00	0.00	0.00	0.00
K	0.00	0.00	0.00	0.00	0.00	0.00	0.00	0.00	0.00	0.00
X	1.99	2.01	2.02	2.01	2.00	0.02	1.99	2.01	2.00	2.01
	8.00	8.00	8.01	8.00	7.99	0.01	7.99	8.00	7.99	8.00
FeO_{Total}	8.06	7.89	7.64	6.53	8.16	0.71	6.05	5.62	4.67	4.29
X_{Czs}	0.45	0.43	0.45	0.54	0.44	0.05	0.59	0.61	0.68	0.69
X_{Ep}	0.51	0.49	0.47	0.41	0.51	0.04	0.38	0.36	0.29	0.27
%Pistacite	17.74	17.52	16.83	14.20	17.88	1.57	13.07	12.21	10.00	9.23
aZo	0.45	0.45	0.49	0.57	0.45	0.05	0.58	0.63	0.68	0.71

TABLE A3 Epidote microprobe analyses, average compositions and standard deviations (σ)

Mineral	Clinozoisite		Zoisite	Zoisite	Zoisite	Zoisite	
Rock Type	Pyrals-MR	σ	Pyralspite-metarodingite				σ
Sample	Average	n=7	AL96-24A	AL96-24A	AL96-24A	Average	n=3
SiO_2	38.53	0.29	39.42	39.22	39.31	39.32	0.10
TiO_2	0.10	0.02	0.03	0.04	0.06	0.04	0.01
Al_2O_3	28.95	0.73	32.07	31.74	31.88	31.90	0.17
Cr_2O_3	0.02	0.02	0.02	0.01	0.01	0.01	0.01
FeO	5.16	0.82	1.70	1.83	1.85	1.79	0.08
MnO	0.10	0.03	0.03	0.04	0.05	0.04	0.01
MgO	0.08	0.01	0.06	0.06	0.07	0.06	0.01
CaO	23.66	0.22	24.00	23.78	23.81	23.87	0.12
Na2O	0.01	0.01	0.00	0.00	0.00	0.00	0.00
K_2O	0.01	0.00	0.02	0.01	0.01	0.01	0.00
Cl	0.11	0.02	0.10	0.09	0.09	0.09	0.00
F	0.00	0.00	0.01	0.00	0.01	0.00	0.00
BaO	0.00	0.00	0.00	0.00	0.01	0.00	0.01
NiO	0.01	0.00	0.00	0.00	0.00	0.00	0.00
Total	96.74	0.43	97.47	96.84	97.16	97.16	0.31
Fe_2O_3	5.67	0.90	1.86	2.01	2.03	1.97	0.09
Total	96.63	0.43	97.36	96.75	97.05	97.05	0.31
Formula							
Si	3.00	0.00	3.01	3.02	3.01	3.01	0.00
Al^{IV}	0.00	0.00	0.00	0.00	0.00	0.00	0.00
Z	3.00	0.00	3.01	3.02	3.01	3.01	0.00
Al^{VI}	2.66	0.05	2.89	2.88	2.88	2.88	0.01
Cr	0.00	0.00	0.00	0.00	0.00	0.00	0.00
Fe^{3+}	0.33	0.05	0.11	0.12	0.12	0.11	0.01
Y	2.99	0.00	3.00	3.00	3.00	3.00	0.00
Ti	0.01	0.00	0.00	0.00	0.00	0.00	0.00
Mg	0.01	0.00	0.01	0.01	0.01	0.01	0.00
Mn	0.01	0.00	0.00	0.00	0.00	0.00	0.00
Ni	0.00	0.00	0.00	0.00	0.00	0.00	0.00
Ca	1.98	0.01	1.97	1.96	1.96	1.96	0.00
Na	0.00	0.00	0.00	0.00	0.00	0.00	0.00
K	0.00	0.00	0.00	0.00	0.00	0.00	0.00
X	2.00	0.01	1.98	1.97	1.97	1.97	0.00
	8.00	0.01	7.99	7.98	7.98	7.99	0.00
FeO_{Total}	5.16	0.82	1.70	1.83	1.85	1.79	0.08
X_{Czs}	0.64	0.05	0.89	0.88	0.88	0.88	0.01
X_{Ep}	0.33	0.05	0.11	0.12	0.12	0.11	0.01
%Pistacite	11.13	1.81	3.58	3.89	3.91	3.79	0.19
aZo	0.65	0.06	0.86	0.85	0.84	0.85	0.01

TABLE A4 Diopside microprobe analyses, average compositions and standard deviations (σ)

Mineral	Diopside	Diopside	Diopside	Diopside	Diopside	Diopside	Diopside	Diopside	
Rock Type	Grandite-metarodingite								σ
Sample	AL2000-6	AL14-04C	AL14-04C-2	AL14-04C-2	AL14-04C-2	AL14-16-2	AL14-127	Average	n=55
SiO_2	54.25	53.25	53.23	54.03	53.71	53.67	53.99	53.99	0.43
TiO_2	0.02	0.02	0.05	0.03	0.06	0.10	0.04	0.06	0.03
Al_2O_3	0.40	0.83	1.05	0.43	1.19	0.80	0.50	0.85	0.33
Cr_2O_3	0.03	0.44	0.03	0.01	0.01	0.04	0.04	0.03	0.09
FeO	5.87	6.80	6.17	5.06	3.47	2.16	1.27	3.21	1.13
MnO	0.11	0.07	0.10	0.15	0.04	0.04	0.01	0.05	0.04
MgO	14.87	14.02	14.79	15.55	16.23	17.11	17.69	16.49	0.71
CaO	24.82	24.43	24.55	24.52	25.25	25.68	25.86	25.19	0.37
Na_2O	0.11	0.26	0.32	0.20	0.10	0.05	0.00	0.12	0.09
K_2O	0.01	0.01	0.02	0.01	0.01	0.00	0.00	0.01	0.01
F	0.00	0.17	0.15	0.07	0.12	0.00	0.00	0.09	0.05
Cl	0.11	0.01	0.00	0.03	0.00	0.00	0.00	0.01	0.02
BaO	0.00	0.00	0.00	0.00	0.00	0.06	0.00	0.00	0.01
NiO	0.00	0.01	0.01	0.00	0.00	0.01	0.03	0.02	0.02
Total	100.60	100.31	100.47	100.08	100.19	99.73	99.42	100.12	0.33
Fe_2O_3	0.00	0.76	2.17	0.75	1.11	1.75	1.41	0.99	0.54
FeO	5.87	6.11	4.22	4.38	2.47	0.58	0.00	2.31	1.24
newTotal	100.49	100.22	100.54	100.06	100.19	99.84	99.56	100.12	0.29
Formula 4C 6O									
Si	2.00	1.97	1.96	1.99	1.96	1.96	1.97	1.97	0.01
Al^{IV}	0.00	0.03	0.04	0.01	0.04	0.03	0.02	0.03	0.01
T	2.00	2.00	2.00	2.00	2.00	1.99	1.99	2.00	0.00
Al^{VI}	0.01	0.01	0.00	0.01	0.01	0.00	0.00	0.01	0.01
Ti	0.00	0.00	0.00	0.00	0.00	0.00	0.00	0.00	0.00
Cr	0.00	0.01	0.00	0.00	0.00	0.00	0.00	0.00	0.00
Fe^{3+}	0.00	0.02	0.06	0.02	0.03	0.05	0.04	0.03	0.01
Fe^{2+}	0.18	0.19	0.13	0.13	0.08	0.02	0.00	0.07	0.04
Mn	0.00	0.00	0.00	0.00	0.00	0.00	0.00	0.00	0.00
Mg	0.82	0.77	0.81	0.85	0.88	0.93	0.96	0.90	0.04
Ni	0.00	0.00	0.00	0.00	0.00	0.00	0.00	0.00	0.00
M1	1.01	1.01	1.01	1.02	1.00	1.00	1.00	1.01	0.01
Ca	0.98	0.97	0.97	0.97	0.99	1.00	1.01	0.98	0.01
Na	0.01	0.02	0.02	0.01	0.01	0.00	0.00	0.01	0.01
K	0.00	0.00	0.00	0.00	0.00	0.00	0.00	0.00	0.00
M2	0.99	0.99	0.99	0.98	1.00	1.01	1.01	0.99	0.01
SUM	2.00	2.00	2.00	2.00	2.00	2.01	2.01	2.00	0.00
Al^{IV}	0.00	0.03	0.04	0.01	0.04	0.03	0.02	0.03	0.01
Al^{VI}	0.01	0.01	0.00	0.01	0.01	0.00	0.00	0.01	0.01
Altot	0.02	0.04	0.05	0.02	0.05	0.03	0.02	0.04	0.01
Fetot	5.87	6.80	6.17	5.06	3.47	2.16	1.27	3.21	1.13
X_{Mg}	0.82	0.80	0.86	0.86	0.92	0.98	1.00	0.93	0.04
Diopside	0.80	0.76	0.79	0.82	0.88	0.94	0.98	0.89	0.04
Hedembergite	0.18	0.18	0.13	0.13	0.07	0.02	0.00	0.07	0.04

TABLE A4 Diopside microprobe analyses, average compositions and standard deviations (σ)

Mineral	Diopside	Diopside	Diopside	Diopside	Diopside	Diopside	Diopside	Diopside	Diopside
Rock Type	Epidote-metarodingite								σ
Sample	AL98-19B	AL98-19B	AL14-26E	AL14-26E	AL14-26E	AL14-70	AL14-70	Average	n=32
SiO_2	53.47	53.61	53.79	53.27	53.18	53.10	53.60	53.55	0.43
TiO_2	0.03	0.03	0.04	0.12	0.06	0.00	0.02	0.05	0.03
Al_2O_3	0.71	0.66	1.06	1.26	1.23	0.36	0.46	0.85	0.34
Cr_2O_3	0.02	0.00	0.05	0.04	0.06	0.08	0.05	0.04	0.02
FeO	6.58	5.75	3.53	2.94	4.25	6.29	2.66	4.02	1.41
MnO	0.05	0.07	0.04	0.06	0.09	0.19	0.28	0.10	0.08
MgO	14.68	15.27	16.08	16.56	15.46	14.82	16.92	15.89	0.80
CaO	23.99	24.17	25.39	25.50	24.51	24.62	25.24	24.97	0.49
Na_2O	0.43	0.46	0.18	0.25	0.50	0.11	0.13	0.27	0.15
K_2O	0.01	0.01	0.01	0.01	0.00	0.00	0.00	0.00	0.00
F	0.13	0.06	0.00	0.01	0.00	0.00	0.00	0.02	0.04
Cl	0.01	0.01	0.00	0.01	0.03	0.03	0.00	0.01	0.01
BaO	0.00	0.00	0.00	0.00	0.01	0.00	0.00	0.01	0.02
NiO	0.02	0.00	0.03	0.00	0.02	0.00	0.01	0.01	0.01
Total	100.13	100.11	100.20	100.02	99.41	99.60	99.37	99.79	0.52
Fe_2O_3	1.80	2.26	1.43	2.86	2.20	1.64	2.15	1.83	0.70
FeO	4.95	3.71	2.25	0.36	2.27	4.81	0.73	2.37	1.65
newTotal	100.17	100.26	100.34	100.30	99.59	99.73	99.59	99.93	0.48
Formula 4C 6O									
Si	1.97	1.97	1.96	1.94	1.96	1.97	1.96	1.96	0.01
Al^{IV}	0.03	0.03	0.04	0.05	0.04	0.02	0.02	0.03	0.01
T	2.00	2.00	2.00	1.99	2.00	1.99	1.98	2.00	0.01
Al^{VI}	0.01	0.00	0.01	0.00	0.01	0.00	0.00	0.00	0.01
Ti	0.00	0.00	0.00	0.00	0.00	0.00	0.00	0.00	0.00
Cr	0.00	0.00	0.00	0.00	0.00	0.00	0.00	0.00	0.00
Fe^{3+}	0.05	0.06	0.04	0.08	0.06	0.05	0.06	0.05	0.02
Fe^{2+}	0.15	0.11	0.07	0.01	0.07	0.15	0.02	0.07	0.05
Mn	0.00	0.00	0.00	0.00	0.00	0.01	0.01	0.00	0.00
Mg	0.81	0.84	0.87	0.90	0.85	0.82	0.92	0.87	0.04
Ni	0.00	0.00	0.00	0.00	0.00	0.00	0.00	0.00	0.00
M1	1.02	1.02	0.99	0.99	1.00	1.02	1.02	1.00	0.01
Ca	0.95	0.95	0.99	0.99	0.97	0.98	0.99	0.98	0.02
Na	0.03	0.03	0.01	0.02	0.04	0.01	0.01	0.02	0.01
K	0.00	0.00	0.00	0.00	0.00	0.00	0.00	0.00	0.00
M2	0.98	0.99	1.01	1.01	1.00	0.99	1.00	1.00	0.01
SUM	2.00	2.00	2.00	2.01	2.00	2.01	2.02	2.00	0.01
Al^{IV}	0.03	0.03	0.04	0.05	0.04	0.02	0.02	0.03	0.01
Al^{VI}	0.01	0.00	0.01	0.00	0.01	0.00	0.00	0.00	0.01
Altot	0.03	0.03	0.05	0.05	0.05	0.02	0.02	0.04	0.01
Fetot	6.58	5.75	3.53	2.94	4.25	6.29	2.66	4.02	1.41
X_{Mg}	0.84	0.88	0.93	0.99	0.92	0.85	0.98	0.92	0.05
Diopside	0.79	0.82	0.88	0.92	0.84	0.80	0.93	0.87	0.05
Hedembergite	0.15	0.11	0.07	0.01	0.07	0.15	0.02	0.07	0.05

TABLE A4 Diopside microprobe analyses, average compositions and standard deviations (σ)

Mineral	Diopside	Diopside	Diopside	Diopside	Diopside	Diopside	Diopside		Diopside	
Rock Type	Pyralspite-metarodingite							σ		σ
Sample	AL96-24A	AL14-01	AL14-01	AL14-01	AL14-01	AL14-01	Average	n=12	Average	n=99
SiO_2	53.85	53.56	53.43	53.61	53.94	53.98	53.74	0.30	53.82	0.46
TiO_2	0.05	0.09	0.04	0.04	0.05	0.03	0.05	0.02	0.06	0.03
Al_2O_3	1.26	1.34	1.22	1.08	1.10	1.00	1.13	0.31	0.88	0.34
Cr_2O_3	0.00	0.00	0.01	0.02	0.01	0.00	0.02	0.03	0.03	0.07
FeO	3.66	3.96	4.66	4.51	3.99	4.24	4.17	0.54	3.59	1.24
MnO	0.01	0.05	0.10	0.07	0.05	0.07	0.08	0.03	0.07	0.06
MgO	16.08	15.96	15.48	15.69	15.90	15.74	15.80	0.37	16.21	0.77
CaO	23.99	24.17	24.11	24.24	24.23	24.19	24.17	0.42	24.99	0.53
Na_2O	0.51	0.54	0.52	0.45	0.47	0.43	0.47	0.15	0.21	0.17
K_2O	0.02	0.02	0.01	0.01	0.01	0.01	0.01	0.00	0.01	0.01
F	0.08	0.09	0.15	0.11	0.12	0.12	0.11	0.02	0.07	0.05
Cl	0.01	0.00	0.00	0.01	0.01	0.00	0.01	0.01	0.01	0.02
BaO	0.00	0.01	0.00	0.00	0.00	0.00	0.00	0.00	0.01	0.01
NiO	0.00	0.01	0.00	0.00	0.00	0.01	0.01	0.01	0.01	0.02
Total	99.51	99.81	99.73	99.85	99.90	99.82	99.76	0.20	99.97	0.42
Fe_2O_3	1.15	2.07	1.95	1.78	1.24	0.90	1.46	0.50	1.32	0.70
FeO	2.62	2.10	2.90	2.90	2.87	3.43	2.85	0.40	2.40	1.32
newTotal	99.54	99.91	99.77	99.90	99.89	99.79	99.79	0.17	100.02	0.37
Formula 4C 6O										
Si	1.97	1.96	1.96	1.97	1.97	1.98	1.97	0.01	1.97	0.01
Al^{IV}	0.03	0.04	0.04	0.03	0.03	0.02	0.03	0.01	0.03	0.01
T	2.00	2.00	2.00	2.00	2.00	2.00	2.00	0.00	2.00	0.00
Al^{VI}	0.03	0.02	0.02	0.01	0.02	0.02	0.02	0.01	0.01	0.01
Ti	0.00	0.00	0.00	0.00	0.00	0.00	0.00	0.00	0.00	0.00
Cr	0.00	0.00	0.00	0.00	0.00	0.00	0.00	0.00	0.00	0.00
Fe^{3+}	0.03	0.06	0.05	0.05	0.03	0.02	0.04	0.01	0.04	0.02
Fe^{2+}	0.08	0.06	0.09	0.09	0.09	0.11	0.09	0.01	0.07	0.04
Mn	0.00	0.00	0.00	0.00	0.00	0.00	0.00	0.00	0.00	0.00
Mg	0.88	0.87	0.85	0.86	0.87	0.86	0.86	0.02	0.88	0.04
Ni	0.00	0.00	0.00	0.00	0.00	0.00	0.00	0.00	0.00	0.00
M1	1.02	1.01	1.01	1.01	1.02	1.02	1.02	0.01	1.01	0.01
Ca	0.94	0.95	0.95	0.95	0.95	0.95	0.95	0.01	0.98	0.02
Na	0.04	0.04	0.04	0.03	0.03	0.03	0.03	0.01	0.02	0.01
K	0.00	0.00	0.00	0.00	0.00	0.00	0.00	0.00	0.00	0.00
M2	0.98	0.99	0.99	0.99	0.98	0.98	0.98	0.01	1.00	0.01
SUM	2.00	2.00	2.00	2.00	2.00	2.00	2.00	0.00	2.00	0.00
Al^{IV}	0.03	0.04	0.04	0.03	0.03	0.02	0.03	0.01	0.03	0.01
Al^{VI}	0.03	0.02	0.02	0.01	0.02	0.02	0.02	0.01	0.01	0.01
Altot	0.05	0.06	0.05	0.05	0.05	0.04	0.05	0.01	0.04	0.01
Fetot	3.66	3.96	4.66	4.51	3.99	4.24	4.17	0.54	3.59	1.24
X_{Mg}	0.92	0.93	0.90	0.91	0.91	0.89	0.91	0.01	0.92	0.04
Diopside	0.84	0.84	0.82	0.83	0.84	0.83	0.83	0.03	0.87	0.05
Hedembergite	0.08	0.06	0.09	0.09	0.08	0.10	0.08	0.01	0.07	0.04

TABLE A4 Diopside microprobe analyses, average compositions and standard deviations (σ)

Mineral	Diopside	Diopside	Diopside	Diopside	Diopside	Diopside	Diopside	Diopside	
Rock Type	Chl-Di-metasomatic rim		Chl-blackwall				Chl-Di-Ol-R		σ
Sample	AL14-24-BWD	AL14-24-BWD	AL14-19	AL14-19	AL14-54	AL14-79	AL14-134-L	Average	n=50
SiO_2	54.68	54.81	54.93	54.46	54.88	54.83	55.57	55.08	0.57
TiO_2	0.02	0.01	0.01	0.02	0.03	0.02	0.00	0.02	0.02
Al_2O_3	0.01	0.00	0.02	0.36	0.34	0.50	0.07	0.14	0.17
Cr_2O_3	0.05	0.03	0.03	0.00	0.04	0.02	0.06	0.03	0.02
FeO	0.84	0.70	1.27	1.39	2.33	2.88	1.45	1.72	1.09
MnO	0.13	0.04	0.09	0.03	0.12	0.16	0.04	0.09	0.04
MgO	18.01	18.07	17.79	17.66	17.20	16.63	18.08	17.53	0.79
CaO	25.74	25.78	25.45	25.80	25.93	25.64	25.49	25.69	0.22
Na_2O	0.02	0.03	0.04	0.04	0.06	0.05	0.10	0.05	0.05
K_2O	0.01	0.02	0.01	0.01	0.01	0.01	0.01	0.01	0.01
F	0.00	0.00	0.00	0.00	0.00	0.00	0.00	0.00	0.01
Cl	0.00	0.00	0.00	0.00	0.00	0.03	0.00	0.04	0.18
BaO	0.00	0.00	0.00	0.00	0.00	0.02	0.01	0.01	0.02
NiO	0.00	0.00	0.01	0.02	0.00	0.01	0.00	0.01	0.02
Total	99.51	99.50	99.64	99.79	100.94	100.80	100.88	100.93	0.38
Fe_2O_3	0.87	0.71	0.20	1.16	1.07	0.25	0.47	0.51	0.45
FeO	0.06	0.06	1.08	0.34	1.36	2.66	1.03	1.26	1.23
newTotal	99.60	99.57	99.66	99.91	101.04	100.78	100.92	100.42	0.73
Formula 4C 6O									
Si	1.99	1.99	2.00	1.98	1.98	1.99	2.00	1.99	0.01
Al^{IV}	0.00	0.00	0.00	0.02	0.01	0.01	0.00	0.00	0.01
T	1.99	1.99	2.00	1.99	1.99	2.00	2.00	2.00	0.01
Al^{VI}	0.00	0.00	0.00	0.00	0.00	0.01	0.00	0.00	0.00
Ti	0.00	0.00	0.00	0.00	0.00	0.00	0.00	0.00	0.00
Cr	0.00	0.00	0.00	0.00	0.00	0.00	0.00	0.00	0.00
Fe^{3+}	0.02	0.02	0.01	0.03	0.03	0.01	0.01	0.01	0.01
Fe^{2+}	0.00	0.00	0.03	0.01	0.04	0.08	0.03	0.04	0.04
Mn	0.00	0.00	0.00	0.00	0.00	0.00	0.00	0.00	0.00
Mg	0.98	0.98	0.96	0.96	0.92	0.90	0.97	0.94	0.04
Ni	0.00	0.00	0.00	0.00	0.00	0.00	0.00	0.00	0.00
M1	1.01	1.00	1.01	1.00	1.00	1.00	1.01	1.00	0.01
Ca	1.00	1.00	0.99	1.00	1.00	1.00	0.98	1.00	0.01
Na	0.00	0.00	0.00	0.00	0.00	0.00	0.01	0.00	0.00
K	0.00	0.00	0.00	0.00	0.00	0.00	0.00	0.00	0.00
M2	1.00	1.01	0.99	1.01	1.01	1.00	0.99	1.00	0.01
SUM	2.01	2.01	2.00	2.01	2.01	2.00	2.00	2.00	0.01
Al^{IV}	0.00	0.00	0.00	0.02	0.01	0.01	0.00	0.00	0.01
Al^{VI}	0.00	0.00	0.00	0.00	0.00	0.01	0.00	0.00	0.00
Altot	0.00	0.00	0.00	0.02	0.01	0.02	0.00	0.01	0.01
Fetot	0.84	0.70	1.27	1.39	2.33	2.88	1.45	1.72	1.09
X_{Mg}	1.00	1.00	0.97	0.99	0.96	0.92	0.97	0.96	0.04
Diopside	0.99	0.99	0.96	0.97	0.94	0.90	0.95	0.95	0.04
Hedembergite	0.00	0.00	0.03	0.01	0.04	0.08	0.03	0.04	0.04

TABLE A5 Amphibole microprobe analyses, average compositions and standard deviations (σ)

Amphibole Type	Amp1	Amp-1	Amp-1	Amp-1	Amp-1	Amp-1	Amp-1		Amp-2	Amp-2
Rock Type	Pyralspite-metarodingite							σ	Grandite-metarodingite	
Sample	AL96-24A	AL96-24A	AL96-24A	AL96-24A	AL14-01	AL14-99-1	Average	n=74	AL2000-6	AL95-36-C
SiO_2	54.67	55.63	50.56	53.47	48.73	49.50	50.93	2.29	41.37	40.53
TiO_2	0.06	0.24	0.15	0.10	0.21	0.22	0.17	0.09	0.18	0.31
Al_2O_3	2.67	1.90	7.12	4.36	8.17	6.78	6.17	1.89	14.77	15.70
Cr_2O_3	0.01	0.00	0.00	0.00	0.00	0.05	0.04	0.02	0.04	0.02
MnO	0.09	0.05	0.08	0.03	0.06	0.09	0.07	0.04	0.02	0.06
FeO	9.08	4.39	5.93	4.60	7.32	6.67	5.98	1.17	8.86	9.18
NiO	0.00	0.00	0.00	0.00	0.03	0.00	0.01	0.01	0.00	0.03
MgO	18.72	21.18	18.40	20.19	17.90	18.79	19.29	1.16	15.86	15.20
CaO	12.01	12.70	12.78	12.86	12.24	12.19	12.41	0.30	12.53	12.44
Na_2O	0.72	0.53	1.14	0.73	1.77	1.45	1.25	0.37	3.41	3.33
K_2O	0.12	0.06	0.36	0.22	0.39	0.39	0.31	0.13	0.56	0.55
F	0.00	0.00	0.00	0.00	0.07	0.01	0.01	0.02	0.07	0.09
Cl	0.01	0.00	0.00	0.00	0.00	0.04	0.04	0.04	0.11	0.17
Initial Total	98.16	96.69	96.51	96.56	96.89	96.16	96.63	0.49	97.73	97.53
$Fe^{3+}/\Sigma Fe$ used	0.23	0.19	0.10	0.14	0.26	0.40	0.33	0.15	0.52	0.50
FeO	6.97	3.54	5.32	3.97	5.42	4.00	3.99	1.04	4.29	4.61
Fe_2O_3	2.34	0.94	0.68	0.71	2.12	2.97	2.22	1.03	5.08	5.08
H_2O^+	2.13	2.17	2.14	2.16	2.07	2.12	2.13	0.03	2.01	1.98
Total	100.52	98.95	98.72	98.79	99.17	98.57	98.98	0.50	100.25	100.02
Formula										
Si (T)	7.66	7.77	7.19	7.51	6.96	7.08	7.21	0.25	5.98	5.88
Al (T)	0.35	0.24	0.81	0.49	1.04	0.92	0.79	0.25	2.03	2.12
Ti (C)	0.01	0.03	0.02	0.01	0.02	0.02	0.02	0.01	0.02	0.03
Al (C)	0.10	0.08	0.39	0.24	0.34	0.22	0.24	0.09	0.49	0.56
Cr (C)	0.00	0.00	0.00	0.00	0.00	0.01	0.01	0.00	0.01	0.00
Fe^{3+} (C)	0.25	0.10	0.07	0.07	0.23	0.32	0.24	0.11	0.55	0.56
Ni (C)	0.00	0.00	0.00	0.00	0.00	0.00	0.00	0.00	0.00	0.00
Mn^{2+} (C)	0.00	0.00	0.00	0.00	0.00	0.00	0.00	0.00	0.00	0.00
Fe^{2+} (C)	0.74	0.39	0.62	0.45	0.60	0.43	0.43	0.13	0.52	0.55
Mg (B)	3.91	4.41	3.90	4.23	3.81	4.01	4.07	0.20	3.42	3.29
Mn^{2+} (B)	0.01	0.01	0.01	0.00	0.01	0.01	0.01	0.00	0.00	0.01
Fe^{2+} (B)	0.07	0.02	0.01	0.02	0.05	0.05	0.04	0.02	0.00	0.01
Ca (B)	1.80	1.90	1.95	1.94	1.87	1.87	1.88	0.04	1.94	1.93
Na (B)	0.12	0.07	0.03	0.04	0.07	0.07	0.06	0.02	0.06	0.05
Na (A)	0.08	0.07	0.28	0.16	0.42	0.33	0.28	0.10	0.90	0.88
K (A)	0.02	0.01	0.07	0.04	0.07	0.07	0.06	0.02	0.10	0.10
OH (W)	2.00	2.00	2.00	2.00	1.96	1.99	1.99	0.01	1.94	1.92
F (W)	0.00	0.00	0.00	0.00	0.03	0.00	0.01	0.01	0.03	0.04
Cl (W)	0.00	0.00	0.00	0.00	0.01	0.01	0.01	0.01	0.03	0.04
O (non-W)	22.00	22.00	22.00	22.00	22.00	22.00	22.00	0.00	22.00	22.00
Sum T, C, B&A	15.10	15.08	15.35	15.20	15.49	15.40	15.34	0.12	16.00	15.99
X_{Mg}	0.83	0.91	0.86	0.90	0.85	0.89	0.90	0.03	0.87	0.85
C(AlVI+Fe3+)	0.34	0.18	0.46	0.31	0.57	0.54	0.48	0.13	1.04	1.12
A(Na+K)	0.10	0.08	0.35	0.20	0.49	0.40	0.34	0.12	1.00	0.99

TABLE A5 Amphibole microprobe analyses, average compositions and standard deviations (σ)

Amphibole Type	Amp-2	Amp-2	Amp-2	Amp-2	Amp-2	Amp-2	Amp-2	Amp-2	Amp-2	
Rock Type	Grand-metarodingite		Epidote-metarodingite			Pyralspite -metarodingite				σ
Sample	AL14-16-2	AL14-127	AL14-70	AL14-78	AL14-18	AL14-99-1	AL-96-24A	AL14-01	Average	n=175
SiO_2	39.88	40.24	40.48	41.34	44.57	46.02	44.11	41.38	43.60	2.07
TiO_2	0.28	0.44	0.32	0.24	0.45	0.30	0.30	0.32	0.29	0.09
Al_2O_3	15.00	15.29	14.81	14.48	11.62	10.31	12.57	14.41	12.83	1.50
Cr_2O_3	0.04	0.07	0.08	0.06	0.00	0.06	0.00	0.02	0.03	0.03
MnO	0.07	0.08	0.22	0.19	0.10	0.03	0.04	0.09	0.06	0.05
FeO	8.90	8.38	9.88	10.43	10.75	7.17	7.34	10.10	8.40	1.49
NiO	0.00	0.07	0.02	0.02	0.03	0.00	0.00	0.01	0.02	0.02
MgO	15.50	15.52	14.39	14.13	14.16	17.70	16.15	14.60	15.77	1.09
CaO	12.53	12.51	12.29	12.49	10.40	12.25	12.18	12.41	12.16	0.45
Na_2O	3.15	3.07	3.02	2.66	3.49	2.15	2.32	2.78	2.55	0.53
K_2O	0.55	0.59	0.66	0.56	1.12	0.46	0.87	0.55	0.82	0.27
F	0.03	0.00	0.00	0.01	0.12	0.00	0.00	0.15	0.11	0.06
Cl	0.14	0.21	0.52	0.56	0.03	0.17	0.00	0.80	0.26	0.26
Initial Total	96.04	96.42	96.58	97.05	96.78	96.59	95.87	97.38	96.65	0.59
$Fe^{3+}/\Sigma Fe$ used	0.55	0.52	0.37	0.36	0.10	0.46	0.21	0.39	0.28	0.14
FeO	3.97	4.02	6.26	6.68	9.71	3.86	5.81	6.18	5.99	1.20
Fe_2O_3	5.48	4.84	4.02	4.17	1.16	3.68	1.70	4.36	2.68	1.56
H_2O^+	2.02	2.02	1.92	1.91	1.99	2.06	2.09	1.78	2.02	0.09
Total	98.61	98.92	98.91	99.38	98.89	99.01	98.13	99.60	98.94	0.60
Formula										
Si (T)	5.87	5.89	5.98	6.07	6.56	6.61	6.44	6.06	6.35	0.26
Al (T)	2.13	2.11	2.02	1.93	1.44	1.39	1.56	1.94	1.65	0.26
Ti (C)	0.03	0.05	0.04	0.03	0.05	0.03	0.03	0.04	0.03	0.01
Al (C)	0.47	0.53	0.56	0.58	0.58	0.36	0.60	0.55	0.55	0.06
Cr (C)	0.01	0.01	0.01	0.01	0.00	0.01	0.00	0.00	0.00	0.00
Fe^{3+} (C)	0.61	0.53	0.45	0.46	0.13	0.40	0.19	0.48	0.29	0.17
Ni (C)	0.00	0.01	0.00	0.00	0.00	0.00	0.00	0.00	0.00	0.00
Mn^{2+} (C)	0.00	0.00	0.00	0.01	0.00	0.00	0.00	0.00	0.01	0.00
Fe^{2+} (C)	0.48	0.49	0.78	0.82	1.13	0.42	0.67	0.74	0.70	0.15
Mg (B)	3.40	3.39	3.17	3.09	3.11	3.79	3.51	3.19	3.42	0.21
Mn^{2+} (B)	0.01	0.01	0.03	0.02	0.01	0.00	0.00	0.01	0.01	0.01
Fe^{2+} (B)	0.01	0.01	0.00	0.00	0.06	0.05	0.04	0.01	0.03	0.02
Ca (B)	1.98	1.96	1.95	1.97	1.64	1.89	1.91	1.95	1.90	0.07
Na (B)	0.01	0.02	0.03	0.02	0.29	0.06	0.05	0.03	0.07	0.06
Na (A)	0.89	0.85	0.84	0.74	0.71	0.54	0.60	0.76	0.66	0.13
K (A)	0.10	0.11	0.13	0.11	0.21	0.09	0.16	0.10	0.15	0.05
OH (W)	1.95	1.95	1.87	1.86	1.94	1.96	2.00	1.73	1.94	0.08
F (W)	0.01	0.00	0.00	0.00	0.06	0.00	0.00	0.07	0.06	0.03
Cl (W)	0.04	0.05	0.13	0.14	0.01	0.04	0.00	0.20	0.06	0.06
O (non-W)	22.00	22.00	22.00	22.00	22.00	22.00	22.00	22.00	22.00	0.00
Sum T, C, B&A	15.99	15.96	15.96	15.84	15.92	15.62	15.77	15.86	15.81	0.13
X_{Mg}	0.87	0.87	0.80	0.79	0.72	0.89	0.83	0.81	0.82	0.04
C(AlVI+Fe3+)	1.08	1.06	1.01	1.04	0.71	0.76	0.78	1.03	0.84	0.16
A(Na+K)	0.99	0.96	0.96	0.84	0.92	0.62	0.77	0.87	0.81	0.13

TABLE A5 Amphibole microprobe analyses, average compositions and standard deviations (σ)

Amphibole Type	Amp-3	Amp-3	Amp-3	Amp-3	Amp-3	
Rock Type	Pyralspite-Metarodingite					σ
Sample	AL96-24A	AL14-99-1	AL96-24A	AL96-24A	Average	n=17
SiO_2	43.74	39.28	39.79	40.50	40.61	1.45
TiO_2	0.29	0.22	0.40	0.34	0.39	0.12
Al_2O_3	13.79	17.28	16.98	16.59	16.06	1.31
Cr_2O_3	0.00	0.09	0.00	0.00	0.10	0.05
MnO	0.07	0.11	0.11	0.11	0.10	0.02
FeO	8.19	10.40	10.34	10.43	9.71	0.77
NiO	0.00	0.01	0.00	0.00	0.01	0.01
MgO	18.10	12.70	12.91	12.80	14.09	1.82
CaO	11.18	12.40	11.92	12.35	12.16	0.41
Na_2O	2.88	2.56	2.63	2.48	2.64	0.16
K_2O	0.87	0.67	0.73	0.90	0.68	0.17
F	0.00	0.00	0.00	0.00	0.03	0.07
Cl	0.00	0.73	0.00	0.00	0.71	0.26
Initial Total	99.12	96.28	95.82	96.49	96.76	1.02
$Fe^{3+}/\Sigma Fe$ used	0.00	0.00	0.00	0.00	0.00	0.00
FeO	1.79	7.09	7.32	9.03	6.01	2.08
Fe_2O_3	7.11	3.68	3.35	1.55	4.11	1.58
H_2O^+	2.10	1.86	2.06	2.05	1.97	0.13
Total	101.93	98.51	98.22	98.69	99.14	1.17
Formula						
Si (T)	6.13	5.83	5.90	5.99	5.95	0.11
Al (T)	1.87	2.17	2.11	2.01	2.05	0.11
Ti (C)	0.03	0.03	0.05	0.04	0.04	0.01
Al (C)	0.40	0.86	0.86	0.88	0.72	0.18
Cr (C)	0.00	0.01	0.00	0.00	0.01	0.01
Fe^{3+} (C)	0.75	0.41	0.38	0.17	0.45	0.16
Ni (C)	0.00	0.00	0.00	0.00	0.00	0.00
Mn^{2+} (C)	0.00	0.00	0.00	0.00	0.00	0.00
Fe^{2+} (C)	0.04	0.88	0.87	1.09	0.71	0.31
Mg (B)	3.78	2.81	2.85	2.82	3.07	0.33
Mn^{2+} (B)	0.01	0.01	0.01	0.01	0.01	0.00
Fe^{2+} (B)	0.17	0.00	0.04	0.03	0.04	0.05
Ca (B)	1.68	1.97	1.89	1.96	1.91	0.09
Na (B)	0.14	0.01	0.06	0.00	0.05	0.04
Na (A)	0.64	0.72	0.70	0.71	0.71	0.04
K (A)	0.16	0.13	0.14	0.17	0.13	0.03
OH (W)	2.00	1.82	2.00	2.00	1.91	0.12
F (W)	0.00	0.00	0.00	0.00	0.05	0.02
Cl (W)	0.00	0.18	0.00	0.00	0.18	0.10
O (non-W)	22.00	22.00	22.00	22.00	22.00	0.00
Sum T, C, B&A	15.80	15.85	15.84	15.88	15.83	0.04
X_{Mg}	0.95	0.76	0.76	0.72	0.80	0.07
$C(Al^{VI}+Fe^{3+})$	1.15	1.27	1.24	1.06	1.17	0.07
A(Na+K)	0.80	0.85	0.84	0.88	0.83	0.04

TABLE A6 Olivine microprobe analyses, average compositions and standard deviations (σ)

Mineral	Olivine	Olivine	Olivine	Olivine	Olivine	Olivine	Olivine	
Rock Type	Chl-Di-Ol-metasomatic rim							
Domain	Atg-serpentinites							σ
Sample	AL14-20	AL14-20	AL14-20	AL14-20	AL14-20	AL14-20	Average	n=6
SiO_2	40.57	40.17	40.05	40.10	40.06	40.36	40.22	0.21
TiO_2	0.01	0.00	0.00	0.01	0.00	0.02	0.01	0.01
Al_2O_3	0.00	0.00	0.00	0.00	0.00	0.00	0.00	0.00
Cr_2O_3	0.00	0.02	0.00	0.00	0.01	0.00	0.01	0.01
FeO	8.41	8.82	9.04	9.06	8.93	7.58	8.64	0.57
MnO	0.25	0.24	0.23	0.25	0.22	0.26	0.24	0.01
MgO	50.55	50.18	50.02	49.70	50.23	50.93	50.27	0.43
CaO	0.00	0.00	0.01	0.00	0.00	0.00	0.00	0.00
Na_2O	0.01	0.00	0.00	0.01	0.00	0.01	0.01	0.00
K_2O	0.01	0.01	0.00	0.01	0.01	0.01	0.01	0.00
F	0.06	0.09	0.07	0.05	0.07	0.07	0.07	0.01
Cl	0.03	0.00	0.00	0.00	0.01	0.00	0.01	0.01
BaO	0.00	0.00	0.00	0.00	0.00	0.00	0.00	0.00
NiO	0.31	0.25	0.26	0.26	0.35	0.31	0.29	0.04
Total	100.22	99.80	99.69	99.46	99.89	99.56	99.77	0.27
H_2O (calc.)								
O=Cl	0.01	0.00	0.00	0.00	0.00	0.00	0.00	0.00
O=F	0.03	0.04	0.03	0.02	0.03	0.03	0.03	0.01
Total	100.19	99.76	99.66	99.44	99.86	99.53	99.74	0.27
Formula	3.00	3.00	3.00	3.00	3.00	3.00	3.00	0.00
Si	0.99	0.98	0.98	0.98	0.98	0.98	0.98	0.00
Ti	0.00	0.00	0.00	0.00	0.00	0.00	0.00	0.00
Al	0.00	0.00	0.00	0.00	0.00	0.00	0.00	0.00
Cr	0.00	0.00	0.00	0.00	0.00	0.00	0.00	0.00
Fe^{2+}	0.17	0.18	0.19	0.19	0.18	0.15	0.18	0.01
Mn	0.01	0.01	0.00	0.01	0.00	0.01	0.00	0.00
Mg	1.83	1.83	1.82	1.82	1.83	1.85	1.83	0.01
Ni	0.01	0.00	0.01	0.01	0.01	0.01	0.01	0.00
Ca	0.00	0.00	0.00	0.00	0.00	0.00	0.00	0.00
Na	0.00	0.00	0.00	0.00	0.00	0.00	0.00	0.00
K	0.00	0.00	0.00	0.00	0.00	0.00	0.00	0.00
F	0.00	0.01	0.01	0.00	0.01	0.01	0.01	0.00
Cl	0.00	0.00	0.00	0.00	0.00	0.00	0.00	0.00
OH								
Sum cations	3.00	3.00	3.00	3.00	3.00	3.00	3.00	0.00
X_{Fe}								
X_F								
X_{Ti}								
Factor								
X_{Mg}	0.91	0.91	0.91	0.91	0.91	0.92	0.91	0.01

TABLE A6 Olivine microprobe analyses, average compositions and standard deviations (σ)

Mineral	Olivine	Olivine	Olivine	Olivine	Olivine	Olivine	Olivine	Olivine	
Rock Type	Chl-Di-Ol-metasomatic rim								
Domain	Chl-harzburgites								σ
Sample	AL14-134-L	AL14-134-L	AL14-134-L	AL14-134-L	AL14-134-L	AL14-134-L	AL14-134-L	Average	n=7
SiO_2	40.76	40.88	41.06	40.74	40.96	40.57	40.79	40.82	0.16
TiO_2	0.00	0.03	0.00	0.00	0.01	0.00	0.00	0.01	0.01
Al_2O_3	0.00	0.00	0.02	0.00	0.01	0.03	0.00	0.01	0.01
Cr_2O_3	0.02	0.02	0.04	0.04	0.05	0.04	0.04	0.04	0.01
FeO	9.18	8.51	8.61	8.54	8.41	8.98	8.98	8.74	0.30
MnO	0.13	0.15	0.14	0.12	0.14	0.16	0.15	0.14	0.01
MgO	49.39	50.15	49.99	49.68	50.31	49.62	49.39	49.79	0.37
CaO	0.01	0.00	0.00	0.00	0.00	0.00	0.01	0.00	0.00
Na_2O	0.00	0.00	0.02	0.02	0.00	0.00	0.00	0.01	0.01
K_2O	0.00	0.00	0.01	0.01	0.00	0.00	0.00	0.00	0.00
F	0.00	0.01	0.00	0.00	0.00	0.00	0.00	0.00	0.00
Cl	0.00	0.00	0.01	0.00	0.00	0.00	0.01	0.00	0.01
BaO	0.02	0.00	0.08	0.01	0.00	0.00	0.00	0.02	0.03
NiO	0.71	0.70	0.69	0.74	0.68	0.69	0.70	0.70	0.02
Total	100.20	100.45	100.60	99.89	100.57	100.09	100.07	100.27	0.27
H_2O (calc.)									
O=Cl	0.00	0.00	0.00	0.00	0.00	0.00	0.00	0.00	0.00
O=F	0.00	0.00	0.00	0.00	0.00	0.00	0.00	0.00	0.00
Total	100.20	100.44	100.60	99.89	100.57	100.09	100.07	100.27	0.27
Formula	3.00	3.00	3.00	3.00	3.00	3.00	3.00	3.00	0.00
Si	1.00	0.99	1.00	1.00	0.99	0.99	1.00	0.99	0.00
Ti	0.00	0.00	0.00	0.00	0.00	0.00	0.00	0.00	0.00
Al	0.00	0.00	0.00	0.00	0.00	0.00	0.00	0.00	0.00
Cr	0.00	0.00	0.00	0.00	0.00	0.00	0.00	0.00	0.00
Fe^{2+}	0.19	0.17	0.17	0.17	0.17	0.18	0.18	0.18	0.01
Mn	0.00	0.00	0.00	0.00	0.00	0.00	0.00	0.00	0.00
Mg	1.80	1.82	1.81	1.81	1.82	1.81	1.80	1.81	0.01
Ni	0.01	0.01	0.01	0.01	0.01	0.01	0.01	0.01	0.00
Ca	0.00	0.00	0.00	0.00	0.00	0.00	0.00	0.00	0.00
Na	0.00	0.00	0.00	0.00	0.00	0.00	0.00	0.00	0.00
K	0.00	0.00	0.00	0.00	0.00	0.00	0.00	0.00	0.00
F	0.00	0.00	0.00	0.00	0.00	0.00	0.00	0.00	0.00
Cl	0.00	0.00	0.00	0.00	0.00	0.00	0.00	0.00	0.00
OH									
Sum cations	3.00	3.00	3.00	3.00	3.00	3.00	3.00	3.00	0.00
X_{Fe}									
X_F									
X_{Ti}									
Factor									
X_{Mg}	0.91	0.91	0.91	0.91	0.91	0.91	0.91	0.91	0.00

TABLE A6 Ti-clinohumite microprobe analyses, average compositions and standard deviations (σ)

Mineral	Ti-Chu	Ti-Chu	Ti-Chu	Ti-Chu	Ti-Chu	Ti-Chu	Ti-Chu	Ti-Chu	Ti-Chu	
Rock Type	Chl-Di-Ol-metasomatic rim									
Domain	Atg-serpentinites									σ
Sample	AL14-20	AL14-20	AL14-20	AL14-20	AL14-20	AL14-20	AL14-20	AL14-20	Average	n=8
SiO_2	36.93	34.51	35.99	36.31	36.48	36.07	36.85	36.00	36.14	0.75
TiO_2	5.15	7.33	5.31	5.21	5.31	5.52	4.24	5.41	5.44	0.86
Al_2O_3	0.00	0.00	0.00	0.00	0.00	0.00	0.00	0.00	0.00	0.00
Cr_2O_3	0.01	0.01	0.02	0.00	0.01	0.01	0.00	0.01	0.01	0.01
FeO	7.40	8.49	7.58	7.03	6.23	7.81	7.81	7.02	7.42	0.68
MnO	0.27	0.27	0.26	0.25	0.30	0.30	0.26	0.28	0.28	0.02
MgO	48.34	45.90	47.89	48.84	48.70	47.49	48.43	48.07	47.96	0.94
CaO	0.01	0.00	0.02	0.01	0.02	0.00	0.01	0.04	0.01	0.01
Na_2O	0.02	0.02	0.04	0.01	0.00	0.00	0.01	0.01	0.01	0.01
K_2O	0.01	0.01	0.02	0.01	0.01	0.01	0.01	0.01	0.01	0.00
F	0.10	0.14	0.09	0.11	0.16	0.13	0.12	0.06	0.11	0.03
Cl	0.02	0.01	0.11	0.00	0.00	0.01	0.05	0.02	0.03	0.04
BaO	0.06	0.10	0.05	0.06	0.06	0.06	0.05	0.07	0.06	0.02
NiO	0.26	0.21	0.24	0.25	0.21	0.22	0.24	0.25	0.23	0.02
Total	98.57	97.02	97.63	98.09	97.50	97.63	98.08	97.24	97.72	0.51
H_2O (calc.)	0.83	0.28	0.75	0.80	0.75	0.71	1.01	0.76	0.74	0.21
O=Cl	0.00	0.00	0.02	0.00	0.00	0.00	0.01	0.00	0.01	0.01
O=F	0.04	0.06	0.04	0.05	0.07	0.05	0.05	0.02	0.05	0.01
Total	99.30	97.13	98.27	98.79	98.12	98.23	98.99	97.91	98.34	0.68
Formula	14.00	14.00	14.00	14.00	14.00	14.00	14.00	14.00	14.00	0.00
Si	5.42	5.18	5.34	5.36	5.41	5.35	5.43	5.36	5.36	0.08
Ti	0.57	0.83	0.59	0.58	0.59	0.62	0.47	0.61	0.61	0.10
Al	0.00	0.00	0.00	0.00	0.00	0.00	0.00	0.00	0.00	0.00
Cr	0.00	0.00	0.00	0.00	0.00	0.00	0.00	0.00	0.00	0.00
Fe^{2+}	0.91	1.07	0.94	0.87	0.77	0.97	0.96	0.87	0.92	0.09
Mn	0.06	0.06	0.06	0.06	0.07	0.07	0.06	0.06	0.06	0.00
Mg	6.01	5.83	6.02	6.10	6.12	5.97	6.04	6.06	6.02	0.09
Ni	0.03	0.03	0.03	0.03	0.02	0.03	0.03	0.03	0.03	0.00
Ca	0.00	0.00	0.00	0.00	0.00	0.00	0.00	0.01	0.00	0.00
Na	0.00	0.00	0.01	0.00	0.00	0.00	0.00	0.00	0.00	0.00
K	0.00	0.00	0.00	0.00	0.00	0.00	0.00	0.00	0.00	0.00
F	0.05	0.07	0.04	0.05	0.07	0.06	0.05	0.03	0.05	0.01
Cl	0.00	0.00	0.03	0.00	0.00	0.00	0.01	0.00	0.01	0.01
OH	0.81	0.28	0.74	0.79	0.74	0.71	0.99	0.76	0.73	0.20
Sum cations	13.86	13.34	13.81	13.84	13.81	13.77	14.06	13.79	13.78	0.20
X_{Fe}	0.94	0.95	0.94	0.94	0.92	0.94	0.94	0.93	0.94	0.01
X_F	0.02	0.03	0.02	0.03	0.04	0.03	0.03	0.01	0.03	0.01
X_{Ti}	0.57	0.83	0.59	0.58	0.59	0.62	0.47	0.61	0.61	0.10
Factor	8.81	9.02	8.92	8.87	8.92	8.91	8.85	8.94	8.91	0.06
X_{Mg}	0.87	0.85	0.86	0.88	0.89	0.86	0.86	0.87	0.87	0.01

TABLE A7 Antigorite microprobe analyses, average compositions and standard deviations (σ)

Mineral	Antigorite	Antigorite	Antigorite	Antigorite	Antigorite	Antigorite	
Rock Type	Chl-Di-Ol-metasomatic rim						σ
Sample	AL14-20	AL14-20	AL14-21	AL14-22	AL14-23	Average	n=5
SiO_2	41.53	41.31	41.32	41.62	41.73	41.50	0.19
TiO_2	0.03	0.01	0.01	0.02	0.02	0.02	0.01
Al_2O_3	3.87	3.98	3.51	3.53	3.26	3.63	0.29
Cr_2O_3	0.25	0.30	0.31	0.31	0.35	0.30	0.04
FeO	3.21	3.26	3.43	3.54	3.28	3.34	0.14
MnO	0.06	0.03	0.05	0.04	0.02	0.04	0.01
MgO	38.12	38.14	37.69	37.81	38.24	38.00	0.24
CaO	0.00	0.00	0.01	0.00	0.00	0.00	0.00
Na_2O	0.01	0.02	0.01	0.01	0.01	0.01	0.00
K_2O	0.01	0.01	0.01	0.01	0.01	0.01	0.00
NiO	0.15	0.15	0.16	0.15	0.15	0.15	0.01
F	0.01	0.01	0.00	0.06	0.01	0.02	0.02
Cl	0.07	0.04	0.04	0.06	0.08	0.06	0.02
BaO	0.00	0.00	0.00	0.00	0.00	0.00	0.00
Total	87.31	87.25	86.55	87.17	87.18	87.09	0.31
O=F	0.01	0.00	0.00	0.03	0.01	0.01	0.01
O=Cl	0.01	0.01	0.01	0.01	0.02	0.01	0.00
Total	87.29	87.24	86.54	87.13	87.15	87.07	0.30
Formula							
Nº oxygens	6.82	6.82	6.82	6.82	6.82	6.82	0.00
Si	1.89	1.88	1.90	1.90	1.90	1.90	0.01
Al	0.21	0.21	0.19	0.19	0.18	0.20	0.02
Ti	0.00	0.00	0.00	0.00	0.00	0.00	0.00
Mg	2.59	2.59	2.58	2.57	2.60	2.59	0.01
Fe^{2+}	0.12	0.12	0.13	0.14	0.13	0.13	0.01
Mn	0.00	0.00	0.00	0.00	0.00	0.00	0.00
Ca	0.00	0.00	0.00	0.00	0.00	0.00	0.00
Na	0.00	0.00	0.00	0.00	0.00	0.00	0.00
K	0.00	0.00	0.00	0.00	0.00	0.00	0.00
Ni	0.01	0.01	0.01	0.01	0.01	0.01	0.00
Cr	0.01	0.01	0.01	0.01	0.01	0.01	0.00
F	0.00	0.00	0.00	0.01	0.00	0.00	0.00
Cl	0.01	0.00	0.00	0.00	0.01	0.00	0.00

TABLE A8 Titanite microprobe analyses, average compositions and standard deviations (σ)

Mineral	Titanite	Titanite	Titanite	Titanite		Titanite	Titanite	Titanite	Titanite	Titanite	
Rock Type	Grandite-metarodingite				σ	Epidote-metarodingite					σ
Sample	AL2000-6	AL95-36-C	AL14-127	Average	n=7	AL14-18	AL14-26-E-2	AL14-78	AL14-70	Average	n=23
SiO_2	30.38	30.14	29.93	30.36	0.28	29.98	30.18	30.43	30.41	29.22	5.68
TiO_2	36.68	37.16	37.65	36.82	1.72	36.77	38.94	38.11	38.58	35.63	7.69
Al_2O_3	1.39	0.79	1.71	1.55	0.51	1.38	1.41	1.30	1.29	1.85	1.89
Cr_2O_3	0.00	0.00	0.03	0.01	0.02	0.00	0.05	0.05	0.06	0.04	0.03
FeO	0.66	0.56	0.42	0.74	0.38	0.99	0.50	0.60	0.46	0.72	0.91
MgO	0.13	0.12	0.00	0.06	0.05	0.05	0.00	0.00	0.06	0.13	0.44
MnO	0.00	0.02	0.01	0.01	0.01	0.04	0.01	0.01	0.02	0.02	0.01
NiO	0.01	0.00	0.00	0.00	0.00	0.00	0.00	0.00	0.01	0.00	0.01
CaO	27.98	27.79	28.28	28.25	0.30	28.24	28.82	28.46	28.03	27.21	5.35
Na_2O	0.00	0.00	0.00	0.01	0.01	0.04	0.00	0.00	0.00	0.01	0.02
K_2O	0.01	0.02	0.00	0.01	0.01	0.02	0.01	0.00	0.00	0.01	0.01
F	0.20	0.20	0.00	0.14	0.10	0.24	0.00	0.04	0.00	0.05	0.08
Cl	0.00	0.02	0.01	0.01	0.01	0.14	0.01	0.00	0.04	0.06	0.09
BaO	0.50	0.52	0.16	0.39	0.21	0.46	0.14	0.03	0.08	0.25	0.22
O=F	0.09	0.08	0.00	0.06	0.04	0.10	0.00	0.02	0.00	0.02	0.03
Total	97.37	96.72	98.04	97.91	1.36	97.65	99.93	98.99	98.94	94.80	18.40
FeO											
Fe_2O_3											
newTotal											
factor	7.91	7.98	8.03	7.92	0.07	8.02	7.96	7.90	7.90	7.66	1.49
(S)											
Si	4.00	4.00	4.00	4.00	0.00	4.00	4.00	4.00	4.00	3.86	0.00
Ti	3.63	3.71	3.78	3.65	0.17	3.69	3.88	3.77	3.82	3.54	0.76
Al	0.22	0.12	0.27	0.24	0.08	0.22	0.22	0.20	0.20	0.29	0.30
Cr	0.00	0.00	0.00	0.00	0.00	0.00	0.01	0.01	0.01	0.00	0.00
Fe^{3+}											
Fe^{2+}	0.07	0.06	0.05	0.08	0.04	0.11	0.06	0.07	0.05	0.08	0.10
Mg	0.03	0.02	0.00	0.01	0.01	0.01	0.00	0.00	0.01	0.03	0.09
Ni	0.00	0.00	0.00	0.00	0.00	0.00	0.00	0.00	0.00	0.00	0.00
Mn	0.00	0.00	0.00	0.00	0.00	0.00	0.00	0.00	0.00	0.00	0.00
Ca	3.95	3.95	4.05	3.99	0.04	4.04	4.09	4.01	3.95	3.85	0.76
Na	0.00	0.00	0.00	0.00	0.00	0.01	0.00	0.00	0.00	0.00	0.00
K	0.00	0.00	0.00	0.00	0.00	0.00	0.00	0.00	0.00	0.00	0.00
F	0.09	0.08	0.00	0.06	0.04	0.10	0.00	0.02	0.00	0.02	0.03
Cl	0.00	0.00	0.00	0.00	0.00	0.03	0.00	0.00	0.01	0.01	0.02
P											
OH											
Al+F	0.29	0.19	2.36	0.61	0.78	0.33	0.28	0.31	0.32	0.41	0.40
Sum											
FeO_{Total}											

TABLE A8 Titanite microprobe analyses, average compositions and standard deviations (σ)

Mineral	Titanite	Titanite	Titanite	Titanite		Titanite	Titanite	Titanite	
Rock Type	Pyralspite-metarodingite				σ	Chl-blackwall			σ
Sample	AL96-24A	AL14-01	AL14-99-1	Average	n=15	AL14-19	AL14-54	Average	n=2
SiO_2	30.13	30.11	29.99	30.09	0.44	29.95	30.69	30.32	0.52
TiO_2	37.10	37.49	39.34	38.03	2.22	36.81	38.33	37.57	1.07
Al_2O_3	1.12	1.12	1.13	1.28	0.83	2.20	1.67	1.93	0.38
Cr_2O_3	0.01	0.00	0.00	0.02	0.02	0.07	0.04	0.05	0.02
FeO	0.31	1.11	0.57	0.73	0.97	0.65	0.46	0.55	0.13
MgO	0.06	0.05	0.00	0.07	0.16	0.01	0.00	0.00	0.00
MnO	0.01	0.05	0.08	0.06	0.07	0.00	0.02	0.01	0.01
NiO	0.01	0.00	0.00	0.00	0.01	0.03	0.00	0.01	0.02
CaO	28.02	28.11	28.48	28.13	0.73	28.17	28.81	28.49	0.45
Na_2O	0.02	0.02	0.01	0.02	0.01	0.00	0.00	0.00	0.00
K_2O	0.03	0.02	0.10	0.02	0.02	0.00	0.01	0.00	0.00
F	0.00	0.01	0.03	0.01	0.01	0.00	0.00	0.00	0.00
Cl	0.17	0.19	0.14	0.14	0.09	0.01	0.00	0.01	0.01
BaO	0.58	0.56	0.10	0.40	0.21	0.01	0.14	0.07	0.09
O=F	0.00	0.00	0.01	0.00	0.00	0.00	0.00	0.00	0.00
Total	96.82	98.09	99.72	98.45	0.89	97.89	100.03	98.96	1.51
FeO									
Fe_2O_3									
newTotal									
factor (S)	7.98	7.98	8.01	7.99	0.11	8.03	7.83	7.93	0.14
Si	4.00	4.00	4.00	4.00	0.00	4.00	4.00	4.00	0.00
Ti	3.70	3.75	3.95	3.81	0.27	3.70	3.76	3.73	0.04
Al	0.17	0.18	0.18	0.20	0.12	0.35	0.26	0.30	0.06
Cr	0.00	0.00	0.00	0.00	0.00	0.01	0.00	0.01	0.00
Fe^{3+}									
Fe^{2+}	0.03	0.12	0.06	0.08	0.10	0.07	0.05	0.06	0.02
Mg	0.01	0.01	0.00	0.01	0.03	0.00	0.00	0.00	0.00
Ni	0.00	0.00	0.00	0.00	0.00	0.00	0.00	0.00	0.00
Mn	0.00	0.01	0.01	0.01	0.01	0.00	0.00	0.00	0.00
Ca	3.99	4.00	4.07	4.01	0.15	4.03	4.02	4.03	0.01
Na	0.01	0.00	0.00	0.00	0.00	0.00	0.00	0.00	0.00
K	0.01	0.00	0.02	0.00	0.00	0.00	0.00	0.00	0.00
F	0.00	0.00	0.01	0.00	0.00	0.00	0.00	0.00	0.00
Cl	0.04	0.04	0.03	0.03	0.02	0.00	0.00	0.00	0.00
P									
OH									
Al+F	0.21	0.30	0.24	0.28	0.22	0.42	0.31	0.36	0.08
Sum									
FeO_{Total}									

TABLE A9 Magnetite microprobe analyses, average compositions and standard deviations (σ)

Mineral	Magnetite	Magnetite	Magnetite	Magnetite		Magnetite	Magnetite	Magnetite	Magnetite	
Rock Type	Grandite-metarodingite				σ	Epidote-metarodingite				σ
Sample	AL2000-6	AL2000-6	AL14-127	Average	n=6	AL98-19B	AL14-26E-2	AL14-26E-2	Average	n=6
SiO_2	0.07	0.05	0.06	0.07	0.05	0.06	1.18	0.03	0.23	0.42
TiO_2	0.20	0.19	0.06	0.29	0.40	0.46	0.06	0.03	0.16	0.19
Al_2O_3	0.48	0.52	0.13	0.30	0.19	0.24	0.64	0.05	0.21	0.20
Cr_2O_3	4.85	5.15	0.04	2.21	2.47	0.10	0.27	0.07	0.09	0.08
FeO	87.67	87.14	93.87	90.70	3.07	92.17	89.97	94.05	92.68	1.45
MgO	0.29	0.32	0.17	0.19	0.13	0.16	0.50	0.01	0.16	0.16
MnO	0.19	0.22	0.09	0.12	0.08	0.08	0.10	0.05	0.07	0.02
NiO	0.00	0.01	0.30	0.05	0.12	0.00	0.23	0.10	0.10	0.12
CaO	0.04	0.08	0.03	0.07	0.10	0.26	0.11	0.07	0.16	0.13
Na_2O	0.00	0.00	0.00	0.00	0.00	0.00	0.42	0.02	0.07	0.16
K_2O	0.00	0.00	0.00	0.00	0.00	0.00	0.08	0.00	0.01	0.03
F	0.00	0.00	0.00	0.00	0.00	0.32	0.00	0.00	0.14	0.18
Cl	0.31	0.31	0.01	0.27	0.13	0.00	0.11	0.00	0.02	0.04
BaO	0.00	0.00	0.03	0.00	0.01	0.00	0.02	0.00	0.01	0.01
O=F										
Total	94.09	93.99	94.81	94.30	0.33	93.85	93.71	94.47	94.12	0.46
FeO	30.82	30.61	31.05	31.15	0.63	31.06	29.59	31.23	30.85	0.56
Fe_2O_3	63.18	62.82	69.81	66.19	3.01	67.91	67.10	69.82	68.71	1.12
newTotal	100.10	99.97	101.75	100.64	0.68	100.33	100.29	101.46	100.82	0.70
factor	2.97	2.97	3.02	3.00	0.03	3.04	2.98	3.04	3.03	0.03
(S)										
Si	0.00	0.00	0.00	0.00	0.00	0.00	0.04	0.00	0.01	0.02
Ti	0.01	0.01	0.00	0.01	0.01	0.01	0.00	0.00	0.00	0.01
Al	0.02	0.02	0.01	0.01	0.01	0.01	0.03	0.00	0.01	0.01
Cr	0.15	0.16	0.00	0.07	0.07	0.00	0.01	0.00	0.00	0.00
Fe^{3+}	1.82	1.81	1.98	1.90	0.08	1.95	1.91	1.99	1.97	0.03
Fe^{2+}	0.98	0.98	0.98	0.99	0.02	0.99	0.93	0.99	0.98	0.02
Mg	0.02	0.02	0.01	0.01	0.01	0.01	0.03	0.00	0.01	0.01
Ni	0.00	0.00	0.01	0.00	0.00	0.00	0.01	0.00	0.00	0.00
Mn	0.01	0.01	0.00	0.00	0.00	0.00	0.00	0.00	0.00	0.00
Ca	0.00	0.00	0.00	0.00	0.00	0.01	0.00	0.00	0.01	0.01
Na	0.00	0.00	0.00	0.00	0.00	0.00	0.03	0.00	0.00	0.01
K	0.00	0.00	0.00	0.00	0.00	0.00	0.00	0.00	0.00	0.00
F										
Cl										
P										
OH										
Al+F										
Sum	3.00	3.00	3.00	3.00	0.00	3.00	3.00	3.00	3.00	0.00
FeO_{Total}										

TABLE A9 Magnetite microprobe analyses, average compositions and standard deviations (σ)

Mineral	Magnetite	Magnetite	Magnetite	Magnetite		Magnetite	Magnetite	Magnetite	Magnetite	
Rock Type	Chl-blackwall				σ	Chl-Di-metasomatic rim		Chl-Di-Ol-M rim		σ
Sample	AL14-54	AL14-79	AL14-79	Average	n=13	AL14-20	AL14-134 D	AL14-134 L	Average	n=11
SiO_2	0.06	0.03	0.02	0.03	0.02	0.03	0.02	0.01	0.02	0.02
TiO_2	0.07	0.27	0.17	0.29	0.54	0.24	0.16	0.48	0.32	0.12
Al_2O_3	0.05	0.20	0.14	0.15	0.05	0.02	0.21	0.66	0.31	0.17
Cr_2O_3	0.07	0.07	0.09	0.08	0.01	3.55	1.40	6.94	4.53	2.04
FeO	90.65	91.25	91.86	91.17	0.57	88.61	89.22	81.75	85.46	2.73
MgO	0.03	0.47	0.28	0.20	0.13	1.44	0.00	0.00	0.13	0.43
MnO	0.04	0.07	0.06	0.07	0.03	0.22	0.64	0.91	0.74	0.20
NiO	0.05	0.04	0.08	0.05	0.02	0.38	0.00	0.04	0.06	0.11
CaO	0.47	0.01	0.00	0.07	0.13	0.00	0.06	0.24	0.13	0.08
Na_2O	0.19	0.00	0.00	0.03	0.06	0.01	1.02	1.56	1.21	0.49
K_2O	0.00	0.00	0.00	0.00	0.00	0.00	0.00	0.01	0.01	0.01
F	0.00	0.00	0.00	0.00	0.00	0.32	0.00	0.00	0.32	0.00
Cl	0.00	0.01	0.04	0.01	0.01	0.01	0.00	0.00	0.01	0.00
BaO	0.01	0.01	0.06	0.01	0.02	0.02	0.01	0.00	0.01	0.01
O=F										
Total	91.69	92.43	92.79	92.17	0.73	94.84	92.74	92.61	92.96	0.65
FeO	29.18	30.27	30.52	30.37	0.78	28.84	28.83	27.56	28.20	0.52
Fe_2O_3	68.31	67.77	68.17	67.56	0.85	66.42	67.11	60.22	63.63	2.53
newTotal	98.53	99.20	99.52	98.91	0.70	101.15	99.45	98.64	99.29	0.69
factor	3.12	3.08	3.08	3.10	0.03	2.95	3.04	2.94	2.98	0.04
(S)										
Si	0.00	0.00	0.00	0.00	0.00	0.00	0.00	0.00	0.00	0.00
Ti	0.00	0.01	0.00	0.01	0.02	0.01	0.00	0.01	0.01	0.00
Al	0.00	0.01	0.01	0.01	0.00	0.00	0.01	0.03	0.01	0.01
Cr	0.00	0.00	0.00	0.00	0.00	0.11	0.04	0.21	0.14	0.06
Fe^{3+}	2.00	1.97	1.98	1.97	0.03	1.88	1.94	1.73	1.83	0.07
Fe^{2+}	0.95	0.98	0.98	0.99	0.02	0.91	0.93	0.88	0.90	0.02
Mg	0.00	0.03	0.02	0.01	0.01	0.08	0.06	0.09	0.08	0.02
Ni	0.00	0.00	0.00	0.00	0.00	0.01	0.02	0.03	0.02	0.00
Mn	0.00	0.00	0.00	0.00	0.00	0.01	0.00	0.01	0.00	0.00
Ca	0.02	0.00	0.00	0.00	0.01	0.00	0.00	0.00	0.00	0.00
Na	0.01	0.00	0.00	0.00	0.00	0.00	0.00	0.00	0.00	0.00
K	0.00	0.00	0.00	0.00	0.00	0.00	0.00	0.00	0.00	0.00
F										
Cl										
P										
OH										
Al+F										
Sum	3.00	3.00	3.00	3.00	0.00	3.00	3.00	3.00	3.00	0.00
FeO_{Total}										

TABLE A10 Rutile and Apatite microprobe analyses, average compositions and standard deviations (σ)

Mineral	Rutile	Rutile	Rutile	Rutile		Apatite	Apatite	Apatite	Apatite		Apatite
Rock Type	Pyralspite-metarodingite				σ	Grandite-metarodingite				σ	Ep-MR
Sample	AL96-24A	AL14-99-1	AL14-99-2	Average	n=10	AL14-04-C	AL14-04-C	AL14-04-C2	Average	n=7	Al 14-18
SiO_2	0.03	0.03	0.04	0.05	0.05	0.02	0.03	0.01	0.02	0.02	0.01
TiO_2	97.99	98.76	100.38	98.75	1.32	0.00	0.01	0.00	0.00	0.00	0.00
Al_2O_3	0.04	0.03	0.02	0.03	0.01	0.00	0.00	0.00	0.00	0.00	0.00
Cr_2O_3	0.00	0.15	0.15	0.10	0.07	0.00	0.00	0.00	0.00	0.00	0.00
FeO	0.48	2.80	0.25	1.14	0.92	0.01	0.03	0.02	0.03	0.02	0.04
MgO	0.01	0.10	0.01	0.03	0.04	0.07	0.07	0.07	0.07	0.00	0.05
MnO	0.01	0.03	0.04	0.03	0.02	0.02	0.00	0.00	0.01	0.01	0.01
NiO	0.07	0.00	0.02	0.06	0.10	0.00	0.01	0.00	0.00	0.01	0.00
CaO	0.01	0.04	0.25	0.25	0.37	54.03	53.85	53.87	53.80	0.28	53.53
Na_2O	0.02	0.00	0.01	0.01	0.02	0.00	0.00	0.00	0.00	0.00	0.00
K_2O	0.15	0.01	0.01	0.06	0.08	0.01	0.01	0.01	0.01	0.00	0.02
F	0.00	0.00	0.00	0.00	0.00	1.17	1.07	1.03	1.05	0.07	0.87
Cl	1.38	0.00	0.04	0.42	0.67	1.04	1.47	1.37	1.35	0.16	3.43
BaO	0.01	0.23	0.20	0.16	0.11	0.00	0.00	0.00	0.00	0.00	0.02
O=F						56.39	56.54	56.39	56.35	0.26	57.97
Total	98.80	101.95	101.17	100.51	1.76						
FeO	0.53	3.11	0.28	1.26	1.02						
Fe_2O_3	0.00	0.00	0.00	0.00	0.00						
newTotal	98.86	102.26	101.20	100.64	1.82						
factor	0.81	0.79	0.79	0.80	0.01						
(S)	1.01	1.02	1.00	1.01	0.00						
Si	0.00	0.00	0.00	0.00	0.00	0.00	0.01	0.00	0.00	0.00	0.00
Ti	0.99	0.96	0.99	0.98	0.01						
Al	0.00	0.00	0.00	0.00	0.00						
Cr	0.00	0.00	0.00	0.00	0.00						
Fe^{3+}	0.01	0.03	0.00	0.01	0.01	0.00	0.01	0.00	0.00	0.00	0.01
Fe^{2+}	0.00	0.00	0.00	0.00	0.00						
Mg	0.00	0.00	0.00	0.00	0.00						
Ni	0.00	0.00	0.00	0.00	0.00						
Mn	0.00	0.00	0.00	0.00	0.00	0.00	0.00	0.00	0.00	0.00	0.00
Ca	0.00	0.00	0.00	0.00	0.01	9.60	9.77	9.75	9.72	0.07	9.69
Na	0.00	0.00	0.00	0.00	0.00						0.00
K	0.00	0.00	0.00	0.00	0.00						
F						0.51	0.58	0.57	0.56	0.04	0.46
Cl						0.36	0.37	0.42	0.38	0.05	0.98
P						5.87	6.00	5.99	5.96	0.06	5.94
OH						0.13	0.05	0.01	0.06	0.04	0.00
Al+F											
Sum						16.47	16.78	16.75	16.69	0.13	16.64
FeO_{Total}	0.48	2.80	0.25	1.14	0.92						

TABLE A10 Apatite microprobe analyses, average compositions and standard deviations (σ)

Mineral	Apatite	Apatite	Apatite		Apatite	Apatite	Apatite	Apatite		Apatite	Apatite	Apatite	Apatite	
Rock Type	Ep-metarodingite			σ	Pyralspite-metarodingite				σ	Chl-blackwall				σ
Sample	AL14-26E2	AL14-70	Average	n=9	AL14-01	AL14-99-1	AL14-99-2	Average	n=7	AL14-79	AL14-79	AL14-79	Average	n=6
SiO_2	0.47	0.05	0.08	0.15	0.09	0.03	0.04	0.04	0.04	0.05	0.08	0.10	0.09	0.03
TiO_2	0.03	0.02	0.01	0.01	0.01	0.00	0.00	0.01	0.01	0.00	0.00	0.01	0.00	0.00
Al_2O_3	0.00	0.02	0.01	0.01	0.05	0.00	0.00	0.01	0.02	0.00	0.00	0.00	0.00	0.00
Cr_2O_3	0.04	0.04	0.03	0.02	0.00	0.03	0.04	0.03	0.01	0.04	0.05	0.05	0.04	0.01
FeO	0.08	0.10	0.05	0.03	0.45	0.30	0.05	0.18	0.14	0.06	0.07	2.54	0.49	1.00
MgO	0.09	0.00	0.04	0.04	0.10	0.03	0.00	0.02	0.04	0.00	0.00	0.00	0.00	0.00
MnO	0.03	0.04	0.03	0.01	0.07	0.06	0.01	0.03	0.03	0.00	0.00	0.00	0.01	0.01
NiO	0.00	0.00	0.01	0.01	0.00	0.01	0.01	0.00	0.00	0.02	0.00	0.00	0.00	0.01
CaO	48.83	52.94	53.08	1.62	53.93	53.65	52.89	51.84	2.88	52.74	52.52	51.74	52.52	0.64
Na_2O	1.62	0.00	0.18	0.54	0.00	0.01	0.02	0.01	0.01	0.12	0.00	0.11	0.04	0.06
K_2O	0.01	0.01	0.01	0.01	0.01	0.00	0.00	0.00	0.00	0.00	0.00	0.03	0.01	0.01
F	3.31	3.93	2.54	1.71	1.02	4.15	3.98	3.52	1.11	3.75	4.04	3.79	3.92	0.13
Cl	1.08	7.33	3.08	1.81	3.64	0.26	8.09	5.89	2.90	7.82	7.52	7.36	7.69	0.22
BaO	0.00	0.00	0.01	0.02	0.00	0.00	0.03	0.00	0.01	0.03	0.02	0.00	0.02	0.02
O=F	55.60	64.49	59.14	2.54	59.36	58.53	65.16	61.58	3.59	64.64	64.30	65.72	64.84	0.79
Total														
FeO														
Fe_2O_3														
newTotal														
factor														
(S)														
Si	0.08	0.01	0.01	0.03	0.00	0.00	0.01	0.00	0.01	0.01	0.01	0.02	0.02	0.00
Ti														
Al														
Cr														
Fe^{3+}	0.01	0.01	0.01	0.00	0.00	0.04	0.01	0.02	0.01	0.01	0.01	0.36	0.07	0.14
Fe^{2+}														
Mg														
Ni														
Mn	0.00	0.01	0.00	0.00	0.00	0.01	0.00	0.00	0.00	0.00	0.00	0.00	0.00	0.00
Ca	8.84	9.59	9.61	0.29	9.76	9.72	9.58	9.39	0.52	9.55	9.51	9.37	9.51	0.12
Na	0.53	0.00	0.06	0.18	0.00	0.01	0.00	0.00	0.00	0.00	0.00		0.01	0.02
K														
F	1.77	2.10	1.36	0.92	0.55	2.22	2.13	1.88	0.59	2.00	2.16	2.03	2.09	0.07
Cl	0.31	2.10	0.88	0.52	0.39	0.08	2.32	1.59	0.94	2.24	2.15	2.11	2.20	0.06
P	5.27	5.86	5.88	0.23	5.99	5.96	5.85	5.70	0.41	5.83	5.80	5.68	5.80	0.09
OH	0.00	0.00	0.00	0.00	0.06	0.00	0.00	0.01	0.02	0.00	0.00	0.00	0.00	0.00
Al+F														
Sum	15.74	16.47	16.57	0.33	16.75	16.73	16.45	16.11	0.94	16.44	16.33	16.47	16.41	0.17
FeO_{Total}														

TABLE A11 Ilmenite microprobe analyses, average compositions and standard deviations (σ)

Mineral	Ilmenite	Ilmenite	Ilmenite	Ilmenite	Ilmenite	Ilmenite	
Rock Type	Grand-MR	Ep-metarodingite		Pyrals-metarodingite			σ
Sample	AL2000-6	AL198-19B	AL14-78	AL14-01	AL14-99-1	Average	n=11
SiO_2	0.03	0.05	0.04	0.01	0.00	0.02	0.02
TiO_2	49.30	48.64	47.36	46.19	52.93	48.44	3.46
Al_2O_3	0.03	0.04	0.03	0.02	0.01	0.02	0.01
Cr_2O_3	0.02	0.02	0.06	0.02	0.06	0.05	0.02
FeO	44.08	44.12	48.28	50.49	44.80	45.60	4.45
MgO	0.64	1.11	1.07	0.31	1.60	1.05	0.40
MnO	4.11	3.75	2.17	2.31	1.44	2.18	0.92
NiO	0.00	0.00	0.04	0.00	0.00	0.01	0.01
CaO	0.05	0.13	0.30	0.02	0.00	0.07	0.09
Na_2O	0.01	0.00	0.04	0.00	0.01	0.01	0.02
K_2O	0.00	0.00	0.00	0.00	0.00	0.00	0.00
F	0.27	0.25	0.00	0.25	0.00	0.07	0.12
Cl	0.00	0.00	0.01	0.00	0.00	0.00	0.01
BaO	0.76	0.74	0.12	0.68	0.18	0.27	0.29
TOTAL	99.31	98.85	99.51	100.30	101.04	97.80	6.55
FeO	36.30	35.81	37.08	37.10	43.34	38.46	3.30
Fe_2O_3	8.65	9.24	12.44	14.88	1.62	7.93	5.45
newTotal	99.14	98.79	100.63	100.86	101.02	98.24	6.69
factor	1.53	1.54	1.55	1.56	1.49	1.57	0.12
(S)	2.06	2.06	2.08	2.10	2.01	2.05	0.04
Si	0.00	0.00	0.00	0.00	0.00	0.00	0.00
Ti	0.92	0.91	0.88	0.86	0.98	0.92	0.05
Al	0.00	0.00	0.00	0.00	0.00	0.00	0.00
Cr	0.00	0.00	0.00	0.00	0.00	0.00	0.00
Fe^{3+}	0.16	0.17	0.23	0.28	0.03	0.15	0.10
Fe^{2+}	0.75	0.75	0.77	0.77	0.90	0.82	0.06
Mg	0.15	0.14	0.08	0.09	0.05	0.08	0.03
Ni	0.00	0.00	0.00	0.00	0.00	0.00	0.00
Mn	0.01	0.02	0.02	0.01	0.03	0.02	0.01
Ca	0.00	0.00	0.01	0.00	0.00	0.00	0.00
Na	0.00	0.00	0.00	0.00	0.00	0.00	0.00
K	0.00	0.00	0.00	0.00	0.00	0.00	0.00
Sum	2.00	2.00	2.00	2.00	2.00	2.00	0.00
XI_{lm}	0.75	0.75	0.77	0.77	0.90	0.82	0.06
X_{Hem}	0.08	0.09	0.13	0.14	0.02	0.08	0.05
Pyrophanite	1.46	2.58	2.57	0.76	3.42	2.43	0.82
Hematite	14.91	15.95	20.78	24.35	2.97	13.45	8.99
Geikielite	16.54	15.33	9.19	9.90	5.40	8.98	3.73
a(Ilm)	0.69	0.68	0.68	0.66	0.88	0.76	0.10

TABLE A11 Ilmenite microprobe analyses, average compositions and standard deviations (σ)

Mineral	Ilmenite	Ilmenite	Ilmenite	Ilmenite		Ilmenite	Ilmenite	Ilmenite	Ilmenite	
Rock Type	Chl-blackwall				σ	Chl-Di-Ol-metasomatic rim				σ
Sample	AL14-19	AL14-144	AL14-79	Average	n=8	AL14-134 L	AL14-134 L	AL14-134 L	Average	n=3
SiO_2	0.03	0.00	0.02	0.01	0.01	0.01	0.04	0.00	0.02	0.02
TiO_2	49.63	52.55	49.30	49.89	1.34	49.69	54.54	54.00	52.74	2.66
Al_2O_3	0.02	0.01	0.01	0.01	0.01	0.06	0.00	0.02	0.03	0.03
Cr_2O_3	0.00	0.06	0.09	0.05	0.03	0.07	0.52	0.39	0.33	0.23
FeO	41.40	45.96	45.58	43.52	1.98	43.54	31.74	32.35	35.88	6.64
MgO	4.80	1.56	1.49	3.52	1.34	3.28	11.25	10.31	8.28	4.36
MnO	2.47	1.46	1.97	2.05	0.37	1.94	1.75	1.80	1.83	0.10
NiO	0.01	0.04	0.03	0.02	0.02	0.02	0.12	0.09	0.08	0.05
CaO	0.04	0.01	0.01	0.03	0.03	0.06	0.01	0.01	0.03	0.03
Na_2O	0.00	0.00	0.00	0.01	0.02	0.00	0.00	0.00	0.00	0.00
K_2O	0.01	0.00	0.01	0.00	0.01	0.00	0.00	0.00	0.00	0.00
F	0.27	0.00	0.00	0.10	0.14	0.00	0.00	0.00	0.00	0.00
Cl	0.00	0.00	0.01	0.00	0.00	0.00	0.00	0.00	0.00	0.00
BaO	0.76	0.13	0.12	0.33	0.32	0.04	0.04	0.09	0.06	0.03
TOTAL	99.46	101.78	98.63	99.56	1.00	98.72	100.02	99.06	99.27	0.67
FeO	35.28	43.03	39.27	37.55	2.59	37.82	31.74	32.35	33.97	3.35
Fe_2O_3	6.80	3.26	7.02	6.64	2.01	6.36	0.00	0.00	2.12	3.67
newTotal	99.10	101.98	99.21	99.79	0.91	99.31	99.98	98.97	99.42	0.51
factor	1.54	1.49	1.55	1.53	0.02	1.54	1.48	1.50	1.51	0.03
(S)	2.04	2.02	2.05	2.04	0.01	2.04	1.98	1.98	2.00	0.03
Si	0.00	0.00	0.00	0.00	0.00	0.00	0.00	0.00	0.00	0.00
Ti	0.94	0.97	0.93	0.94	0.02	0.94	1.02	1.02	0.99	0.05
Al	0.00	0.00	0.00	0.00	0.00	0.00	0.00	0.00	0.00	0.00
Cr	0.00	0.00	0.00	0.00	0.00	0.00	0.01	0.01	0.01	0.00
Fe^{3+}	0.13	0.06	0.13	0.13	0.04	0.12	0.00	0.00	0.04	0.07
Fe^{2+}	0.74	0.88	0.83	0.78	0.05	0.79	0.66	0.68	0.71	0.07
Mg	0.09	0.05	0.07	0.08	0.01	0.07	0.06	0.07	0.07	0.00
Ni	0.00	0.00	0.00	0.00	0.00	0.00	0.00	0.00	0.00	0.00
Mn	0.10	0.03	0.03	0.07	0.03	0.07	0.24	0.22	0.18	0.09
Ca	0.00	0.00	0.00	0.00	0.00	0.00	0.00	0.00	0.00	0.00
Na	0.00	0.00	0.00	0.00	0.00	0.00	0.00	0.00	0.00	0.00
K	0.00	0.00	0.00	0.00	0.00	0.00	0.00	0.00	0.00	0.00
Sum	2.00	2.00	2.00	2.00	0.00	2.00	2.00	2.00	2.00	0.00
XI_{lm}	0.74	0.88	0.83	0.78	0.05	0.79	0.66	0.68	0.71	0.07
X_{Hem}	0.07	0.03	0.07	0.07	0.02	0.06	0.04	0.03	0.04	0.02
Pyrophanite	10.91	3.34	3.40	7.97	3.06	7.45	24.57	22.66	18.23	9.39
Hematite	12.05	5.83	12.44	11.71	3.41	11.32	0.00	0.00	3.77	6.54
Geikielite	9.88	5.51	7.92	8.18	1.54	7.75	6.73	6.96	7.14	0.54
a(Ilm)	0.69	0.86	0.77	0.73	0.06	0.74	0.68	0.70	0.71	0.04

Table A12: Stable assemblages in the number labelled fields of the pseudosections in Figures 4.11, 4.12 and 4.13

Stable assemblages
1 Ol Spl Ilm Grt Cpx H_2O; **2** Ol Spl Ilm Mag Grt Cpx H_2O; **3** Chl Ilm Grt Cpx Ttn H_2O; **4** Ep Chl Ilm Mag Grt Rt; **5** Ep Chl Ilm Grt Rt; **6** Ep Chl Ilm Grt Ttn Rt; **7**) Chl Ilm Grt Cpx Ttn; **8** Ep Chl Ilm Grt Cpx Rt; **9** Ep Chl Ilm Grt Cpx Ttn; **10** Chl Ilm Mag Grt Cpx Ttn; **11** Chl Spl Ilm Mag Grt Cpx Ttn H_2O ; **12** Ep Chl Ilm Mag Grt Cpx Ttn Rt; **13** Chl Spl Ilm Mag Grt Cpx Ttn; **14** Ep Chl Amp Ilm Mag Grt Ttn Rt; **15** Ep Chl Sp Ilm Mag Grt Cpx Ttn; **16** Ep Chl Spl Mag Grt Cpx Ttn; **17** Chl Spl Mag Grt Cpx Ttn H_2O; **18** Chl Sp Mag Grt Cpx Ttn An; **19** Chl Spl Ilm Mag Grt Cpx Ttn An; **20** Chl Ilm Mag Grt Cpx Ttn An
1 Chl Ol Spl Ilm Cpx Ves; **2** Chl Spl Ilm Mag Grt Cpx Ves; **3** Chl Spl Ilm Grt Cpx; **4** Chl Ilm Grt Cpx; **5** Ep Chl Ilm Grt Cpx Ttn; **6** Ep Chl Ilm Grt Cpx; **7** Chl Ol Ilm Mag Grt Cpx; **8** Ep Chl Ilm Mag Grt Cpx; **9** Ep Chl Ilm Mag Grt Cpx Ttn; **10** Ep Chl Amp Mag Grt Cpx Ttn; **11** Ep Chl Amp Mag Grt Ttn; **12** Ep Chl Amp Grt Ttn Rt Hem; **13** Chl Ilm Mag Grt Oam; **14** Ep Chl Mag Grt Oam Ttn
1 Spl Ilm Mag Grt Cpx H_2O; **2** Chl Ol Spl Ilm Mag Cpx Ves H_2O; **3** Chl Ilm Grt Cpx H_2O **4** Ep Chl Mag Grt Ttn **5** Ep Chl Ilm Grt Ttn; **6** Ep Chl Ilm Mag Grt Ttn; **7** Ep Chl Mag Grt Ttn Rt; **8** Ep Chl Ilm Mag Grt Rt; **9** Chl Ilm Grt Cpx Rt; **10** Chl Mag Grt Cpx Rt; **11** Ep Spl Mag Grt Cpx Ttn H_2O
1 Ep Amp Mica Grt Rt; **2** Ep Amp Mica Grt Ttn; **3** Ep Mica Grt Cpx Ttn; **4** Ep Tlc Grt Rt; **5** Ep Amp Grt Rt; **6** Ep Chl Grt Rt; **7** Ep Grt Cpx Rt; **8** Ep Chl Grt Rt Hem; **9** Ep Chl Mag Grt Rt Hem; **10** Chl St Grt Ky Rt Hem; **11** Chl St Rt Hem; **12** Chl St Cld Rt Crn Hem; **13** Chl Cld Rt Crn Hem; **14** Chl Mag Rt Crn Hem; **15** Ep Chl Grt Ttn; **16** Chl Mag Rt Crn; **17** Chl Mag Grt Rt Crn; **18** Chl Grt Rt; **19** Chl Ilm Grt Rt; **20** Chl Ilm Grt; **21** Chl Ilm Grt Ves Ttn; **22** Ilm Grt Cpx Ves Ttn; **23** Chl Ilm Grt Ves; **24** Ilm Grt Cpx Ves
1 Chl Amp Cpx Rt Hem; **2** Ep Chl Grt Cpx Rt Hem; **3** Ep Chl Amp Cpx Rt Hem; **4** Ep Chl Tlc Cpx Rt Hem; **5** Ep Chl Tlc Grt Cpx Rt Hem; **6** Ep Chl Amp Grt Cpx Rt; **7** Ep Chl Tlc Sud Grt Cpx Rt; **8** Ep Tlc Sud Grt Cpx Rt; **9** Ep Tlc Grt Cpx Rt; **10** Ep Amp Grt Cpx Rt
1 Chl Amp Grt Lws Ttn; **2** Chl Amp Grt Lws Ttn Hem; **3** Ep Chl Amp Grt Lws Ttn Rt; **4** Ep Chl Amp Grt Lws Rt; **5** Ep Tlc Grt Cpx Qz Rt; **6** Ep Tlc Grt Cpx Ky Qz Rt; **7** Chl Amp Grt Lws Ttn Qz; **8** Ep Amp Grt Cpx Rt; **9** Ep Amp Grt Cpx Ky; **10** Ep Chl Amp Grt Cpx Lws Ttn Qz; **11** Ep Chl Amp Grt Cpx Ttn Qz; **12** Ep Amp Mica Grt Cpx Rt

Table A13 Whole-rock major and trace element compositions of Cerro del Almirez samples.

Domain	**Atg-serpentinites**					
Lithology	**Grandite-metarodingite**					
Sample	AL14-16	AL 00-6	AL14-16B	AL14-25	AL14-63	AL14-64
Features					Slightly amphibolitized	slightly amphibolitized
SiO_2 (wt. %)	37.66	36.25	37.76	39.39	34.93	35.24
TiO_2	1.81	2.22	1.80	1.75	2.19	2.52
Al_2O_3	13.96	16.09	13.96	13.91	16.16	16.49
Fe_2O_3t	9.39	8.48	9.36	7.72	10.16	10.01
MnO	0.20	0.22	0.20	0.14	0.19	0.17
MgO	6.32	6.04	6.31	5.71	5.80	6.97
CaO	28.55	28.17	28.53	30.03	26.48	25.72
Na_2O	*bdl*	0.04	*bdl*	*bdl*	0.13	0.09
K_2O	*bdl*	0.01	*bdl*	*bdl*	0.02	0.02
P_2O_5	0.21	0.35	0.21	0.21	0.35	0.40
LOI	1.87	2.15	1.84	1.13	3.68	2.31
Total	99.95	100.01	99.98	99.98	100.08	99.96
FeO	2.15	3.12	2.15	1.91	3.43	3.68
V (ppm)	266	261	266	229	249	279
Cr	200	178	190	181	167	157
Co	39	29	39	36	45	47
Ni	74	100	73	147	108	110
Zn	4	68	2	2	102	111
Ga	29	26	29	21	39	31
Rb	0.054	*n.a.*	*n.a.*	0.022	0.11	0.095
Sr	22	*n.a.*	*n.a.*	14	19	17
Y	36	*n.a.*	*n.a.*	27	38	37
Zr	113	*n.a.*	*n.a.*	137	163	196
Nb	8.3	*n.a.*	*n.a.*	7.2	15	15
Cs	0.027	*n.a.*	*n.a.*	0.011	0.015	0.013
Ba	0.91	*n.a.*	*n.a.*	0.66	2.0	1.9
La	11	*n.a.*	*n.a.*	7.1	11	16
Ce	25	*n.a.*	*n.a.*	18	27	37
Pr	3.2	*n.a.*	*n.a.*	2.6	3.7	4.9
Nd	14	*n.a.*	*n.a.*	13	18	23
Sm	4.1	*n.a.*	*n.a.*	3.9	4.9	5.8
Eu	1.7	*n.a.*	*n.a.*	1.5	1.8	1.8
Gd	5.0	*n.a.*	*n.a.*	5.4	5.7	6.8
Tb	0.88	*n.a.*	*n.a.*	0.81	0.98	1.1
Dy	5.7	*n.a.*	*n.a.*	5.4	6.2	7.3
Ho	1.1	*n.a.*	*n.a.*	1.1	1.1	1.4
Er	3.0	*n.a.*	*n.a.*	3.1	3.2	4.1
Tm	0.44	*n.a.*	*n.a.*	0.43	0.46	0.57
Yb	2.8	*n.a.*	*n.a.*	2.6	2.9	3.6
Lu	0.45	*n.a.*	*n.a.*	0.39	0.44	0.54
Hf	3.2	*n.a.*	*n.a.*	3.1	4.3	4.7
Ta	0.69	*n.a.*	*n.a.*	0.63	1.2	0.69
Pb	1.9	*n.a.*	*n.a.*	*n.a.*	0.85	0.41
Th	0.56	*n.a.*	*n.a.*	0.51	0.87	1.2
U	0.28	*n.a.*	*n.a.*	0.19	0.32	0.40

Atg = Antigorite; Chl = Chlorite; Di = Diopside; Ol = Olivine; Ti-Chu = Titanclinohumite; Tl = Talc; Tr = Tremolite; Opx = Orthopyroxene; LOI = loss on ignition; bdl = below detection limit; n.a. = not analysed.

Table A13 Whole-rock major and trace element compositions of Cerro del Almirez samples.

Domain	**Chl-harzburgites**	**Atg-serpentinites**	**Atg-serpentinites**		**Chl-harzburgites**	
Lithology	**Grandite-metarodingite**	**Amphibolitized Grandite-metarodingite**	**Epidote-metarodingite**		**Epidote-metarodingite**	
Sample	AL14-127	AL14-30	AL14-17	AL14-26E	AL14-53	AL14-86
Features	Diopside-rich	Amphibolitized				
SiO2 (wt. %)	42.20	39.50	44.13	43.18	39.66	44.01
TiO2	1.45	1.78	1.77	1.86	2.01	1.51
Al2O3	11.72	14.74	14.57	14.85	16.81	15.44
Fe2O3t	7.25	9.22	7.38	8.01	9.96	7.25
MnO	0.16	0.21	0.07	0.06	0.09	0.09
MgO	6.14	6.33	6.36	6.75	6.71	6.45
CaO	30.30	26.43	24.92	24.23	22.74	24.52
Na2O	0.07	0.54	0.20	0.16	0.17	0.18
K2O	0.01	0.09	*bdl*	0.01	0.02	0.02
P2O5	0.17	0.22	0.20	0.24	0.23	0.19
LOI	0.50	0.93	0.39	0.63	1.57	0.33
Total	99.99	99.99	99.99	99.98	99.97	99.99
FeO	1.65	3.91	1.63	1.44	2.86	1.92
V (ppm)	217	257	240	232	263	226
Cr	186	221	231	206	216	151
Co	30	39	61	38	44	29
Ni	117	86	279	211	147	139
Zn	3	11	41	15	177	11
Ga	19	25	52	40	31	22
Rb	0.064	0.34	0.063	*n.a.*	0.086	0.17
Sr	35	24	1031	921	366	953
Y	20	28	29	28	30	23
Zr	104	135	124	138	149	121
Nb	5.7	6.6	8.4	9.5	9.7	9.7
Cs	0.0024	0.0059	0.0075	0.0044	*n.a.*	0.013
Ba	1.1	3.0	10	5.8	7.8	12
La	6.1	8.9	7.1	8.4	8.1	6.9
Ce	14	21	17	21	21	17
Pr	1.9	2.8	2.3	2.9	3.0	2.4
Nd	9.1	14	11	14	15	12
Sm	2.6	4.2	3.4	4.2	4.4	3.2
Eu	1.1	2.0	1.3	1.7	1.8	1.9
Gd	3.6	5.8	4.3	5.0	5.6	3.8
Tb	0.58	0.87	0.73	0.85	0.90	0.71
Dy	3.7	5.8	4.7	5.2	6.0	4.4
Ho	0.78	1.2	0.91	1.0	1.2	0.83
Er	2.2	3.2	2.5	2.8	3.4	2.6
Tm	0.33	0.45	0.35	0.40	0.46	0.35
Yb	2.1	2.8	2.3	2.3	3.0	2.3
Lu	0.30	0.43	0.35	0.33	0.47	0.33
Hf	2.4	3.2	3.1	3.2	3.6	2.9
Ta	0.34	0.53	0.62	0.52	0.56	0.47
Pb	0.61	*n.a.*	14	*n.a.*	6.7	*n.a.*
Th	0.32	0.48	0.46	0.50	0.55	0.42
U	0.20	0.31	0.17	0.41	0.27	0.31

Atg = Antigorite; Chl = Chlorite; Di = Diopside; Ol = Olivine; Ti-Chu = Titanclinohumite; Tl = Talc; Tr = Tremolite; Opx = Orthopyroxene; LOI = loss on ignition; bdl = below detection limit; n.a. = not analysed.

Table A13 Whole-rock major and trace element compositions of Cerro del Almirez samples.

Domain	**Atg-serpentinites**		**Chl-harzburgites**			**Transitional serpentinites**
Lithology	**Amphibolitized Epidote-metarodingite**					
Sample	AL14-18	AL14-26EA	AL14-70	AL14-78	AL14-87	AL14-143
Features	Amphibolitized	Amphibolitized	Amphibolitized	Amphibolitized	Amphibolitized	Amphibolitized
SiO2 (wt. %)	40.85	40.90	40.34	39.96	42.97	42.13
TiO2	2.15	2.10	1.74	2.44	1.92	1.94
Al2O3	16.97	17.10	17.40	16.41	17.90	15.42
Fe2O3t	9.68	10.65	7.10	8.68	6.55	9.48
MnO	0.08	0.11	0.21	0.13	0.07	0.12
MgO	9.55	7.25	11.46	9.97	8.15	9.17
CaO	17.52	19.50	18.42	19.68	20.63	19.25
Na2O	1.77	1.26	0.39	0.18	0.87	1.21
K2O	0.63	0.59	0.09	0.02	0.42	0.33
P2O5	0.18	0.20	0.19	0.32	0.24	0.24
LOI	0.60	0.34	2.61	2.19	0.26	0.69
Total	99.98	99.99	99.96	99.99	99.99	99.98
FeO	3.28	3.34	2.97	3.58	2.45	4.02
V (ppm)	224	291	293	317	257	285
Cr	222	243	306	74	204	221
Co	70	65	47	49	50	38
Ni	223	123	179	149	365	60
Zn	7	36	18	18	31	10
Ga	75	89	38	38	27	79
Rb	3.3	5.2	0.42	0.23	2.6	0.97
Sr	718	970	744	489	853	690
Y	26	34	32	36	27	29
Zr	135	166	130	180	155	143
Nb	9.9	9.0	5.0	11	10	10
Cs	0.017	0.020	0.017	0.036	0.010	0.028
Ba	27	48	4.5	7.8	18	112
La	10.0	8.4	8.1	11	8.7	7.9
Ce	24	22	19	26	23	20
Pr	3.3	3.1	2.6	3.6	3.0	2.8
Nd	17	16	13	18	15	14
Sm	5.2	4.7	3.9	4.8	3.9	3.9
Eu	2.6	1.8	2.8	2.1	1.5	1.8
Gd	6.4	6.7	4.8	6.1	4.6	4.7
Tb	0.91	1.0	0.88	1.0	0.81	0.82
Dy	4.7	6.7	5.6	6.7	4.9	5.2
Ho	0.82	1.4	1.1	1.3	0.98	1.0
Er	2.2	3.7	3.5	3.9	2.9	3.0
Tm	0.30	0.52	0.51	0.54	0.40	0.43
Yb	1.9	3.2	3.2	3.5	2.6	2.7
Lu	0.29	0.52	0.49	0.51	0.40	0.41
Hf	3.8	3.8	3.1	4.3	3.5	3.3
Ta	0.74	0.89	0.11	0.40	0.56	0.51
Pb	14	*n.a.*	*n.a.*	5.2	*n.a.*	*n.a.*
Th	0.56	0.60	0.37	0.79	0.54	0.54
U	0.70	0.25	0.20	0.26	0.25	0.38

Atg = Antigorite; Chl = Chlorite; Di = Diopside; Ol = Olivine; Ti-Chu = Titanclinohumite; Tl = Talc; Tr = Tremolite; Opx = Orthopyroxene; LOI = loss on ignition; bdl = below detection limit; n.a. = not analysed.

Table A13 Whole-rock major and trace element compositions of Cerro del Almirez samples.

Domain	**Chl-harzburgites**		**Atg-serpentinites**				
Lithology	**Pyralspite-metarodingite**		**Chl-Blackwall**				
Sample	AL14-95	AL 96-24B	AL14-19	AL14-31	AL14-41	AL14-54	AL14-66
Features	Amphibolitized	Amphibolitized		Amph.		Amph.	
SiO2 (wt. %)	40.28	42.55	37.82	38.75	36.47	38.08	33.77
TiO2	2.37	1.98	1.20	1.60	1.74	1.88	2.33
Al2O3	15.16	17.70	12.13	9.56	12.30	10.50	13.40
Fe2O3t	10.24	8.96	5.55	8.30	8.27	11.03	8.07
MnO	0.23	0.14	0.09	0.11	0.08	0.09	0.10
MgO	12.73	9.31	26.97	23.11	24.58	20.01	27.55
CaO	15.37	17.36	8.25	11.84	9.14	12.90	5.71
Na2O	1.72	0.97	*bdl*	0.06	*bdl*	0.32	*bdl*
K2O	0.39	0.44	0.01	0.02	*bdl*	0.04	*bdl*
P2O5	0.37	0.20	0.23	0.18	0.20	0.23	0.37
LOI	1.12	0.40	8.24	6.45	7.45	4.92	8.99
Total	99.95	99.99	100.49	99.98	100.22	100.00	100.29
FeO	5.23	4.97	3.26	4.71	4.22	5.20	4.68
V (ppm)	327	304	*n.a.*	*n.a.*	207	178	184
Cr	202	308	*n.a.*	*n.a.*	420	208	117
Co	48	57	*n.a.*	*n.a.*	96	67	90
Ni	161	256	*n.a.*	*n.a.*	419	230	820
Zn	34	7	*n.a.*	*n.a.*	5	1	7
Ga	89	34	*n.a.*	*n.a.*	80	60	117
Rb	2.5	*n.a.*	0.11	0.11	0.18	0.25	0.05
Sr	238	*n.a.*	5.8	5.4	7.2	8.0	4.9
Y	33	*n.a.*	7.7	7.2	28	37	5.9
Zr	211	*n.a.*	107	93	69	85	158
Nb	16	*n.a.*	7.5	4.2	5.6	5.1	12
Cs	0.026	*n.a.*	0.081	0.054	0.034	0.024	0.026
Ba	13	*n.a.*	1.4	1.6	1.4	3.3	1.2
La	14	*n.a.*	1.7	0.99	19	19	0.6
Ce	34	*n.a.*	4.1	3.5	40	38	2.3
Pr	4.4	*n.a.*	0.53	0.61	4.6	4.5	0.40
Nd	21	*n.a.*	2.5	3.3	19	20	2.5
Sm	5.3	*n.a.*	0.85	1.1	4.6	5.0	0.92
Eu	2.2	*n.a.*	0.29	0.47	2.5	2.5	0.15
Gd	6.1	*n.a.*	1.2	1.6	5.5	6.1	1.3
Tb	1.0	*n.a.*	0.21	0.25	0.86	1.0	0.21
Dy	6.2	*n.a.*	1.5	1.7	5.5	6.8	1.3
Ho	1.2	*n.a.*	0.29	0.32	1.1	1.3	0.23
Er	3.6	*n.a.*	0.84	0.80	3.1	4.1	0.62
Tm	0.50	*n.a.*	0.11	0.11	0.42	0.60	0.08
Yb	3.3	*n.a.*	0.63	0.56	2.6	4.0	0.48
Lu	0.49	*n.a.*	0.092	0.063	0.35	0.60	0.057
Hf	4.7	*n.a.*	3.2	2.2	1.7	2.3	3.7
Ta	0.74	*n.a.*	0.81	0.36	0.41	0.27	1.1
Pb	*n.a.*	*n.a.*	0.41	*n.a.*	*n.a.*	0.39	0.17
Th	1.1	*n.a.*	0.10	0.11	0.52	0.71	0.14
U	0.62	*n.a.*	0.04	0.059	0.11	0.19	0.022

Atg = Antigorite; Chl = Chlorite; Di = Diopside; Ol = Olivine; Ti-Chu = Titanclinohumite; Tl = Talc; Tr = Tremolite; Opx = Orthopyroxene; LOI = loss on ignition; bdl = below detection limit; n.a. = not analysed.

Table A13 Whole-rock major and trace element compositions of Cerro del Almirez samples.

Domain	**Chl-harzburgites**							**Transitional serpentinites**	
Lithology	**Chl-Blackwall**							**Chl-Blackwall**	
Sample	AL14-71	AL14-75	AL14-79	AL14-88	AL14-96	AL14-128	AL14-134	AL14-144	AL14-147
Features				Amph.	Amph.			Amph.	Amph.
SiO_2 (wt. %)	36.06	37.53	35.94	39.16	36.29	35.78	39.09	38.95	33.27
TiO_2	1.54	1.68	1.87	1.67	2.29	1.15	0.95	1.87	2.16
Al_2O_3	14.69	11.19	12.61	13.22	12.71	14.15	9.12	12.64	15.34
Fe_2O_3t	5.59	6.52	6.82	5.75	7.48	6.09	6.20	10.24	9.98
MnO	0.10	0.11	0.12	0.07	0.11	0.04	0.06	0.18	0.15
MgO	26.23	27.61	27.69	21.86	25.34	26.77	22.83	20.57	24.80
CaO	7.24	7.12	6.39	21.86	8.14	7.50	11.75	9.42	5.81
Na_2O	*bdl*	*bdl*	*bdl*	0.19	0.04	*bdl*	*bdl*	0.97	0.11
K_2O	0.01	*bdl*	*bdl*	0.05	0.01	0.01	*bdl*	0.23	0.03
P_2O_5	0.17	0.17	0.23	0.23	0.35	0.12	0.14	0.23	0.31
LOI	8.76	8.52	8.60	6.42	7.58	8.74	10.71	4.74	8.51
Total	100.38	100.45	100.28	100.16	100.34	100.35	100.85	100.04	100.48
FeO	4.34	4.27	4.49	4.50	5.08	3.10	3.67	6.10	6.31
V (ppm)	320	239	208	233	293	106	154	305	348
Cr	452	374	53	231	274	392	1131	253	158
Co	103	87	76	77	87	244	99	71	137
Ni	939	693	300	491	522	962	940	81	494
Zn	16	9	6	8	23	10	14	37	54
Ga	111	90	84	72	126	162	114	120	166
Rb	0.05	0.073	0.14	0.38	0.042	0.11	0.051	1.1	0.41
Sr	14	20	8.6	70	21	3.8	7.6	30	12
Y	28	11	8.3	26	8.4	5.1	2.7	49	20
Zr	84	91	118	118	150	34	42	139	133
Nb	6.3	5.7	8.1	8.8	18	5.2	4.1	10	16
Cs	0.035	0.022	0.046	0.033	0.018	0.073	0.020	0.28	0.14
Ba	0.73	2.0	4.9	2.4	0.48	2.4	*n.a.*	3.6	3.1
La	2.5	0.79	1.1	11	0.92	1.0	0.24	13	17
Ce	11	3.2	3.6	26	3.1	4.8	0.80	31	41
Pr	1.9	0.59	0.58	3.4	0.54	0.90	0.14	4.2	5.1
Nd	10	3.6	3.3	16	3.0	4.9	0.79	20	23
Sm	3.3	1.4	1.1	3.8	1.0	1.4	0.32	5.4	5.1
Eu	1.6	0.23	0.18	1.7	0.16	0.51	0.07	2.0	0.88
Gd	4.2	2.0	1.6	4.5	1.4	1.4	0.48	6.7	4.9
Tb	0.76	0.36	0.26	0.77	0.26	0.20	0.09	1.2	0.77
Dy	5.0	2.5	1.8	4.8	1.6	1.2	0.58	8.1	4.3
Ho	1.0	0.47	0.34	0.97	0.33	0.21	0.12	1.7	0.77
Er	3.2	1.3	0.97	2.8	0.98	0.54	0.31	5.5	2.1
Tm	0.45	0.17	0.13	0.39	0.13	0.07	0.04	0.81	0.29
Yb	2.9	0.91	0.79	2.5	0.79	0.37	0.25	5.3	1.7
Lu	0.38	0.13	0.12	0.38	0.11	0.039	0.035	0.76	0.23
Hf	2.2	2.3	2.9	2.8	3.6	0.95	0.95	3.3	3.1
Ta	0.32	0.36	0.55	0.45	0.91	0.33	0.22	0.46	0.83
Pb	*n.a.*	0.09	0.12	*n.a.*	*n.a.*	0.52	0.95	*n.a.*	*n.a.*
Th	0.22	0.096	0.18	0.56	0.21	0.056	0.053	0.69	1.4
U	0.10	0.043	0.058	0.30	0.063	0.032	0.015	0.26	0.13

Atg = Antigorite; Chl = Chlorite; Di = Diopside; Ol = Olivine; Ti-Chu = Titanclinohumite; Tl = Talc; Tr = Tremolite; Opx = Orthopyroxene; LOI = loss on ignition; bdl = below detection limit; n.a. = not analysed.

Table A13 Whole-rock major and trace element compositions of Cerro del Almirez samples.

Domain	**Atg-serpentinites**			**Atg-serpentinites**		
Lithology	**Chl-Di-reaction rim**			**Chl-Di-Ol-reaction rim**		
Sample	AL14-24D-BW	AL14-20D-BW	AL14-24D-BW B	AL14-20L-V	AL14-24L-V	AL14-23
Features				Atg. remains	Atg. remains	Atg. remains
SiO2 (wt. %)	44.08	43.86	43.73	41.97	42.90	42.53
TiO2	0.18	0.32	0.18	0.15	0.17	0.45
Al2O3	4.64	4.34	4.58	3.77	3.33	4.82
Fe2O3t	8.76	9.93	8.83	7.93	9.12	7.44
MnO	0.08	0.09	0.08	0.12	0.12	0.11
MgO	22.74	22.09	22.84	30.01	27.53	27.68
CaO	15.19	15.52	15.25	9.21	11.09	10.39
Na2O	*bdl*	*bdl*	*bdl*	*bdl*	*bdl*	*bdl*
K2O	*bdl*	*bdl*	*bdl*	0.01	*bdl*	*bdl*
P2O5	*bdl*	*bdl*	*bdl*	*bdl*	*bdl*	0.02
LOI	4.30	3.91	4.30	6.90	5.77	6.74
Total	99.97	100.05	99.80	100.06	100.02	100.17
FeO	2.95	3.20	2.95	2.40	2.79	2.34
V (ppm)	108	106	109	66	94	132
Cr	2979	2787	2965	2735	2613	5174
Co	73	67	74	86	87	56
Ni	1695	1763	1725	1848	1693	1064
Zn	46	16	46	36	49	51
Ga	29	26	28	37	39	38
Rb	0.046	0.045	*n.a.*	0.030	0.025	0.050
Sr	9.8	9.7	*n.a.*	6.6	7.0	7.4
Y	6.5	5.7	*n.a.*	3.5	4.0	3.9
Zr	0.68	0.35	*n.a.*	0.20	0.72	1.5
Nb	0.17	1.2	*n.a.*	0.43	0.23	1.4
Cs	0.043	0.025	*n.a.*	0.021	0.017	0.037
Ba	2.1	2.0	*n.a.*	2.4	3.2	2.5
La	0.39	0.39	*n.a.*	0.26	0.29	0.51
Ce	1.5	1.3	*n.a.*	0.91	1.0	1.6
Pr	0.28	0.24	*n.a.*	0.17	0.18	0.26
Nd	1.7	1.4	*n.a.*	0.91	1.0	1.4
Sm	0.68	0.57	*n.a.*	0.35	0.42	0.50
Eu	0.19	0.17	*n.a.*	0.11	0.12	0.13
Gd	1.1	0.93	*n.a.*	0.52	0.68	0.71
Tb	0.20	0.17	*n.a.*	0.10	0.12	0.13
Dy	1.4	1.2	*n.a.*	0.70	0.82	0.87
Ho	0.31	0.26	*n.a.*	0.15	0.19	0.19
Er	0.82	0.71	*n.a.*	0.44	0.51	0.52
Tm	0.11	0.094	*n.a.*	0.062	0.069	0.073
Yb	0.63	0.53	*n.a.*	0.37	0.40	0.44
Lu	0.071	0.060	*n.a.*	0.045	0.051	0.059
Hf	0.038	0.025	*n.a.*	0.016	0.035	0.079
Ta	0.015	0.091	*n.a.*	0.022	0.016	0.077
Pb	0.75	0.76	*n.a.*	0.75	0.54	0.50
Th	0.092	0.11	*n.a.*	0.092	0.076	0.082
U	0.020	0.032	*n.a.*	0.021	0.017	0.048

Atg = Antigorite; Chl = Chlorite; Di = Diopside; Ol = Olivine; Ti-Chu = Titanclinohumite; Tl = Talc; Tr = Tremolite; Opx = Orthopyroxene; LOI = loss on ignition; bdl = below detection limit; n.a. = not analysed.

Table A13 Whole-rock major and trace element compositions of Cerro del Almirez samples.

Domain	**Atg-serpentinites**									
Lithology	**Atrg-Serpentinites Close**					**Atg-Serpentinites Far**				
Sample	AL14-32	AL14-51	AL14-55	AL14-67	AL14-68	AL14-46	AL14-49	AL14-52	AL14-56	AL14-69
Features		Ti-Chu								
SiO2 (wt. %)	42.84	42.17	42.27	41.35	40.47	41.22	40.82	41.54	40.99	41.41
TiO2	0.15	0.22	0.13	0.13	0.32	0.13	0.14	0.14	0.13	0.13
Al2O3	2.08	2.76	2.85	3.00	3.00	2.27	2.45	1.95	2.33	2.24
Fe2O3t	8.01	6.79	7.84	8.19	7.85	8.35	8.17	8.19	8.48	8.37
MnO	0.09	0.10	0.09	0.07	0.09	0.13	0.13	0.12	0.12	0.13
MgO	32.11	34.98	32.91	34.47	35.81	35.61	35.92	36.44	36.59	35.77
CaO	7.43	4.56	5.31	3.19	2.67	3.19	2.80	2.68	2.43	1.77
Na2O	*bdl*	*bdl*	*bdl*	*bdl*	*bdl*	*bdl*	*bdl*	*bdl*	*bdl*	*bdl*
K2O	*bdl*	*bdl*	*bdl*	*bdl*	*bdl*	*bdl*	*bdl*	0.01	*bdl*	*bdl*
P2O5	*bdl*	*bdl*	*bdl*	*bdl*	*bdl*	*bdl*	*bdl*	*bdl*	*bdl*	*bdl*
LOI	7.18	8.48	9.08	9.83	9.86	9.51	9.86	9.00	9.30	10.62
Total	99.89	100.06	100.48	100.23	100.07	100.43	100.29	100.08	100.38	100.46
FeO	2.89	2.62	2.42	2.57	2.60	2.75	2.63	2.81	2.93	2.56
V (ppm)	64	55	69	66	60	63	64	51	61	73
Cr	2025	2587	2188	2332	2219	2405	2443	2142	2260	2697
Co	96	66	83	91	89	87	86	93	87	97
Ni	1686	1520	1748	1801	1766	1727	1725	1935	1700	2090
Zn	57	5	17	99	73	22	11	10	11	22
Ga	39	36	36	40	44	49	40	42	43	47
Rb	0.022	0.030	0.021	0.059	0.033	0.034	0.027	0.029	0.036	0.028
Sr	5.2	2.5	2.8	2.0	1.7	2.3	4.7	2.1	1.8	2.4
Y	2.0	2.7	2.3	1.2	0.90	1.9	1.9	2.1	1.6	1.4
Zr	0.50	0.31	0.22	0.22	0.41	0.19	0.18	0.17	0.22	0.25
Nb	0.14	0.85	0.14	0.09	1.7	0.24	0.26	0.18	0.21	0.094
Cs	0.010	0.025	0.016	0.061	0.032	0.022	0.023	0.019	0.021	0.022
Ba	1.4	0.51	1.9	4.4	1.4	2.0	1.1	13	1.0	4.1
La	0.21	0.42	0.13	0.055	0.057	0.24	0.21	0.36	0.22	0.10
Ce	0.65	1.2	0.37	0.18	0.21	0.62	0.65	0.93	0.57	0.30
Pr	0.11	0.17	0.067	0.039	0.038	0.089	0.10	0.12	0.073	0.046
Nd	0.62	0.90	0.38	0.25	0.25	0.45	0.53	0.59	0.35	0.26
Sm	0.23	0.29	0.19	0.12	0.088	0.16	0.19	0.18	0.13	0.11
Eu	0.067	0.090	0.053	0.018	0.018	0.061	0.058	0.068	0.050	0.030
Gd	0.35	0.47	0.32	0.20	0.13	0.27	0.28	0.28	0.21	0.18
Tb	0.065	0.081	0.063	0.037	0.029	0.051	0.051	0.055	0.041	0.035
Dy	0.42	0.57	0.46	0.26	0.18	0.37	0.36	0.41	0.29	0.26
Ho	0.094	0.12	0.11	0.055	0.037	0.083	0.083	0.092	0.067	0.058
Er	0.26	0.36	0.30	0.15	0.12	0.25	0.24	0.28	0.20	0.19
Tm	0.037	0.051	0.047	0.023	0.017	0.042	0.036	0.044	0.033	0.028
Yb	0.22	0.32	0.29	0.16	0.12	0.25	0.26	0.29	0.23	0.22
Lu	0.032	0.047	0.042	0.032	0.024	0.037	0.037	0.036	0.036	0.037
Hf	0.022	0.014	0.020	0.018	0.021	0.019	0.014	*n.a.*	*n.a.*	0.020
Ta	0.0078	0.058	0.014	0.011	0.239	0.011	0.016	0.0066	0.014	0.0060
Pb	0.27	0.13	0.27	0.13	0.16	0.37	0.28	0.10	0.22	0.16
Th	0.068	0.11	0.084	0.054	0.030	0.027	0.055	0.018	0.044	0.010
U	0.015	0.026	0.010	0.0053	0.0046	0.031	0.017	0.013	0.028	0.0056

Atg = Antigorite; Chl = Chlorite; Di = Diopside; Ol = Olivine; Ti-Chu = Titanclinohumite; Tl = Talc; Tr = Tremolite; Opx = Orthopyroxene; LOI = loss on ignition; bdl = below detection limit; n.a. = not analysed.

Table A13 Whole-rock major and trace element compositions of Cerro del Almirez samples.

Domain	**Transitional serpentinites**			
Lithology	**Chl-serpentinite Close**	**Atg–Chl–Opx (Tl)–Ol rock Close**	**Atg–Chl–Opx(Tl)–Ol rock Far**	
Sample	AL14-145	AL14-148	AL14-146	AL14-149
Features	Chl-serpentinite (incipient)	Tl Ol (altered to chryisotile)	Si-rich, Tl, Ol	Si-rich, Tr-rich, Tl, Ol
SiO2 (wt. %)	42.72	44.39	41.08	44.17
TiO2	0.13	0.13	0.14	0.13
Al2O3	2.97	2.17	2.42	2.07
Fe2O3t	7.18	8.35	8.02	6.88
MnO	0.09	0.13	0.11	0.12
MgO	35.97	37.99	37.75	38.18
CaO	1.53	0.10	0.14	1.80
Na2O	*bdl*	*bdl*	*bdl*	*bdl*
K2O	0.01	0.01	0.01	0.01
P2O5	*bdl*	*bdl*	0.02	0.03
LOI	9.88	6.65	10.87	6.75
Total	100.48	99.92	100.56	100.14
FeO	3.00	4.06	3.12	3.60
V (ppm)	67	46	57	58
Cr	2803	2527	2475	2685
Co	83	103	92	93
Ni	1473	2013	1840	2033
Zn	226	67	17	45
Ga	38	68	74	58
Rb	0.12	0.12	0.45	0.11
Sr	1.9	3.0	5.2	4.1
Y	0.38	0.32	0.54	1.3
Zr	0.44	0.40	0.21	0.49
Nb	0.64	0.68	0.93	0.92
Cs	0.23	0.043	0.57	0.085
Ba	0.94	3.2	1.5	1.5
La	0.011	0.029	0.040	0.10
Ce	0.031	0.075	0.11	0.33
Pr	0.0053	0.011	0.014	0.054
Nd	0.044	0.054	0.068	0.31
Sm	0.016	0.015	0.027	0.12
Eu	0.0019	0.0021	0.0034	0.019
Gd	0.032	0.023	0.035	0.18
Tb	0.0073	0.0053	0.0087	0.034
Dy	0.055	0.044	0.070	0.24
Ho	0.015	0.011	0.019	0.053
Er	0.061	0.055	0.086	0.18
Tm	0.014	0.014	0.018	0.027
Yb	0.11	0.13	0.17	0.20
Lu	0.022	0.029	0.035	0.038
Hf	0.013	0.013	0.009	0.018
Ta	0.16	0.058	0.097	0.091
Pb	0.62	0.14	0.23	0.23
Th	0.091	0.065	0.064	0.076
U	0.017	0.022	0.019	0.036

Atg = Antigorite; Chl = Chlorite; Di = Diopside; Ol = Olivine; Ti-Chu = Titanclinohumite; Tl = Talc; Tr = Tremolite; Opx = Orthopyroxene; LOI = loss on ignition; bdl = below detection limit; n.a. = not analysed.

Table A13 Whole-rock major and trace element compositions of Cerro del Almirez samples.

Domain	**Chl-harzburgites**							
Lithology	**Chl-harzburgites Close**							
Sample	AL14-72	AL14-76	AL14-80	AL14-89	AL14-97	AL14-101	AL14-129	AL14-135
Features								
SiO2 (wt. %)	43.83	43.78	43.00	45.76	45.69	42.68	41.12	41.89
TiO2	0.19	0.12	0.15	0.16	0.11	0.37	0.22	0.15
Al2O3	3.01	3.57	2.99	3.09	1.48	3.70	1.95	2.73
Fe2O3t	8.62	8.22	7.97	7.91	9.72	9.04	8.15	7.77
MnO	0.12	0.15	0.13	0.11	0.11	0.09	0.12	0.12
MgO	37.94	36.86	39.34	37.49	38.76	37.80	35.39	36.19
CaO	0.10	0.21	0.12	1.34	0.22	0.09	0.27	2.10
Na2O	*bdl*	*bdl*	*bdl*	*bdl*	*bdl*	*bdl*	*bdl*	*bdl*
K2O	*bdl*	0.01	*bdl*	0.01	0.01	0.01	0.01	0.01
P2O5	0.02	0.02	0.02	*bdl*	0.03	0.04	0.02	0.02
LOI	6.15	7.11	6.28	3.98	3.79	6.14	13.83	9.36
Total	99.98	100.05	100.00	99.85	99.92	99.96	101.08	100.34
FeO	5.06	4.39	5.07	5.43	5.69	5.37	1.80	3.70
V (ppm)	76	97	*n.a.*	103	46	74	*n.a.*	66
Cr	2981	3198	*n.a.*	3210	2086	2454	*n.a.*	2946
Co	111	105	*n.a.*	90	108	83	*n.a.*	97
Ni	2023	2020	*n.a.*	1914	2164	1734	*n.a.*	2087
Zn	210	149	*n.a.*	190	107	9	*n.a.*	36
Ga	60	59	*n.a.*	52	70	66	*n.a.*	84
Rb	0.065	0.096	0.073	0.086	0.11	0.11	0.044	0.032
Sr	2.6	3.0	1.6	2.5	3.8	4.0	2.0	4.1
Y	1.1	1.1	0.88	2.4	1.0	1.2	0.59	1.3
Zr	0.48	0.09	0.29	0.19	0.22	3.1	0.24	0.40
Nb	0.68	0.37	0.80	1.1	0.54	2.6	1.1	0.55
Cs	0.046	0.074	0.014	0.037	0.033	0.038	0.014	0.019
Ba	42	2.5	1.4	6.6	4.8	2.1	3.0	1.7
La	0.077	0.076	0.11	0.089	0.12	0.16	0.097	0.069
Ce	0.22	0.23	0.29	0.26	0.32	0.45	0.18	0.26
Pr	0.032	0.035	0.038	0.056	0.045	0.062	0.026	0.045
Nd	0.16	0.19	0.18	0.38	0.23	0.29	0.12	0.29
Sm	0.061	0.070	0.056	0.21	0.072	0.10	0.032	0.10
Eu	0.0082	0.012	0.010	0.025	0.012	0.017	0.0091	0.022
Gd	0.090	0.11	0.075	0.33	0.10	0.12	0.051	0.16
Tb	0.021	0.022	0.016	0.069	0.019	0.022	0.010	0.032
Dy	0.16	0.19	0.13	0.51	0.15	0.17	0.081	0.22
Ho	0.039	0.043	0.031	0.098	0.038	0.038	0.020	0.046
Er	0.15	0.16	0.13	0.30	0.16	0.19	0.083	0.17
Tm	0.027	0.029	0.029	0.043	0.035	0.037	0.015	0.028
Yb	0.21	0.23	0.26	0.27	0.32	0.28	0.13	0.18
Lu	0.039	0.043	0.046	0.046	0.059	0.053	0.027	0.032
Hf	0.019	0.007	0.016	0.012	0.010	0.086	0.010	0.015
Ta	0.088	0.047	0.049	0.14	0.050	0.42	0.12	0.086
Pb	0.11	0.19	0.33	0.58	0.74	0.26	0.24	0.21
Th	0.22	0.12	0.11	0.15	0.42	0.39	0.13	0.092
U	0.088	0.019	0.087	0.079	0.073	0.086	0.049	0.018

Atg = Antigorite; Chl = Chlorite; Di = Diopside; Ol = Olivine; Ti-Chu = Titanclinohumite; Tl = Talc; Tr = Tremolite; Opx = Orthopyroxene; LOI = loss on ignition; bdl = below detection limit; n.a. = not analysed.

Table A13 Whole-rock major and trace element compositions of Cerro del Almirez samples.

Domain	**Chl-harzburgites**							
Lithology	**Chl-Harzburgites Far**							
Sample	AL14-73	AL14-77	AL14-81	AL14-90	AL14-98	AL14-102	AL14-130	AL14-136
Features							Recryst.	Recryst.
SiO2 (wt. %)	43.78	44.81	43.44	44.13	42.61	44.11	42.10	42.46
TiO2	0.16	0.14	0.17	0.14	0.11	0.13	0.11	2.91
Al2O3	2.57	2.52	2.60	2.98	0.94	1.91	1.93	0.13
Fe2O3t	8.63	8.23	8.13	7.79	9.73	9.54	7.40	8.54
MnO	0.10	0.14	0.13	0.12	0.11	0.12	0.11	0.11
MgO	38.41	39.18	39.64	39.15	39.51	39.21	37.94	37.21
CaO	0.10	0.08	0.09	1.97	0.13	0.08	0.10	0.71
Na2O	*bdl*	*bdl*	*bdl*	*bdl*	*bdl*	*bdl*		*bdl*
K2O	*bdl*	0.01	*bdl*	0.01	*bdl*	0.01	0.01	0.01
P2O5	*bdl*	*bdl*	0.02	0.02	0.02	0.03	*bdl*	*bdl*
LOI	6.18	4.83	5.65	3.64	6.64	4.95	11	8.28
Total	99.93	99.94	99.87	99.95	99.80	100.09	100.70	100.37
FeO	4.88	5.50	5.09	5.51	4.88	5.81	3.09	4.38
V (ppm)	80	*n.a.*	*n.a.*	83	*n.a.*	67	44	62
Cr	2889	*n.a.*	*n.a.*	3486	*n.a.*	2257	2295	2771
Co	96	*n.a.*	*n.a.*	92	*n.a.*	99	103	90
Ni	1658	*n.a.*	*n.a.*	2042	*n.a.*	2025	2265	2005
Zn	162	*n.a.*	*n.a.*	5	*n.a.*	11	2	2
Ga	71	*n.a.*	*n.a.*	58	*n.a.*	77	69	88
Rb	0.089	0.080	0.058	0.094	0.056	0.075	0.20	0.033
Sr	3.1	2.5	3.9	3.8	2.6	3.7	1.8	2.0
Y	1.5	0.65	0.68	2.9	1.1	0.94	0.57	0.95
Zr	0.33	0.15	0.24	0.26	0.29	0.84	0.62	0.22
Nb	0.34	0.28	0.65	1.1	0.41	0.66	0.70	0.40
Cs	0.11	0.006	0.021	0.041	0.014	0.021	0.052	0.015
Ba	1.3	2.0	0.91	2.0	2.1	1.2	2.7	0.97
La	0.073	0.047	0.11	0.166	0.134	0.119	0.139	0.11
Ce	0.23	0.11	0.29	0.58	0.39	0.30	0.34	0.26
Pr	0.036	0.013	0.036	0.10	0.056	0.039	0.045	0.036
Nd	0.19	0.060	0.17	0.63	0.31	0.18	0.18	0.15
Sm	0.069	0.021	0.049	0.30	0.10	0.052	0.053	0.055
Eu	0.0094	0.0048	0.010	0.061	0.020	0.0079	0.012	0.016
Gd	0.10	0.042	0.058	0.42	0.12	0.071	0.068	0.080
Tb	0.022	0.010	0.012	0.089	0.023	0.013	0.012	0.017
Dy	0.18	0.091	0.097	0.63	0.16	0.11	0.093	0.14
Ho	0.052	0.029	0.025	0.12	0.038	0.030	0.021	0.032
Er	0.22	0.12	0.11	0.35	0.15	0.16	0.082	0.13
Tm	0.043	0.028	0.022	0.051	0.032	0.037	0.014	0.026
Yb	0.32	0.22	0.19	0.33	0.27	0.33	0.11	0.20
Lu	0.057	0.036	0.037	0.053	0.051	0.063	0.021	0.041
Hf	0.020	0.010	0.010	0.018	0.012	0.034	0.015	0.012
Ta	0.050	0.014	0.036	0.059	0.037	0.053	0.11	0.039
Pb	0.093	0.13	0.28	0.28	0.24	0.22	0.30	0.14
Th	0.15	0.086	0.090	0.065	0.29	0.19	0.070	0.072
U	0.072	0.032	0.083	0.094	0.052	0.060	0.13	0.042

Atg = Antigorite; Chl = Chlorite; Di = Diopside; Ol = Olivine; Ti-Chu = Titanclinohumite; Tl = Talc; Tr = Tremolite; Opx = Orthopyroxene; LOI = loss on ignition; bdl = below detection limit; n.a. = not analysed.

Table A14 XRF and ICP-MS results for international reference materials used in the analyses

	Reference materials							
	PM-S	RSD (%)	*Jochum et al. (2016)*	BIR-1	RSD (%)	*Jochum et al. (2016)*	UM-2	RSD (%)
	n = 4			*n = 8*			*n = 8*	
SiO2 (wt. %)	47.27	0	47.24	47.56	0	47.79	40.63	0
TiO2	1.23	0	1.1	1.04	1	0.9587	0.33	2
Al2O3	17.28	0	17.16	15.62	1	15.51	7.36	0
Fe2O3t	9.72	0	10.12	10.99	1	11.4	14.28	0
MnO	0.16	0	0.158	0.17	1	0.1731	0.08	5
MgO	9.03	0	9.39	9.22	1	9.689	25.26	1
CaO	12.85	0	12.6	13.56	0	13.29	4.87	1
Na2O	2.01	0	2.06	1.78	0	1.832	0.28	3
K2O	0.15	0	0.137	0.03	12	0.029	0.07	1
P2O5	0.03	0	0.038	0.02	19	0.03	0.02	1
LOI	0.27	0	-	0.40	0	-	6.72	1
Total	99.99	0	100.00	100.40	0	100.70	99.91	0
FeO								
V (ppm)	182	1	186.4	294	1	320.6	149	1
Cr	291	0	319	340	1	392.9	7975	0
Co	47	2	49	46	1	52.22	149	1
Ni	103	0	117.8	144	1	168.9	2946	1
Zn	57	1	60	62	1	70.4	46	1
Ga	*n.a.*			16	3	15.46	7	0
	n = 7			*n = 5*				
Rb	0.86	3	0.978	0.20	5	0.21	*n.a.*	
Sr	261	2	279.2	106	4	108.6	*n.a.*	
Y	10	4	11.31	15	4	15.6	*n.a.*	
Zr	35	3	38.2	14	2	14.8	*n.a.*	
Nb	2.4	7	2.44	0.56	8	0.553	*n.a.*	
Cs	0.33	4	0.372	0.0055	0	0.00646	*n.a.*	
Ba	138	3	148.1	6.3	2	6.75	*n.a.*	
La	2.5	3	2.683	0.61	7	0.627	*n.a.*	
Ce	6.4	5	6.87	1.9	5	1.92	*n.a.*	
Pr	0.97	5	1.069	0.37	3	0.3723	*n.a.*	
Nd	5.3	4	5.52	2.4	6	2.397	*n.a.*	
Sm	1.7	4	1.784	1.1	5	1.113	*n.a.*	
Eu	1.0	5	1.069	0.52	6	0.5201	*n.a.*	
Gd	2.2	9	2.04	1.9	8	1.809	*n.a.*	
Tb	0.33	5	0.338	0.36	6	0.3623	*n.a.*	
Dy	2.1	7	2.095	2.6	6	2.544	*n.a.*	
Ho	0.41	8	0.428	0.58	5	0.5718	*n.a.*	
Er	1.1	5	1.14	1.7	6	1.68	*n.a.*	
Tm	0.15	4	0.169	0.25	6	0.2558	*n.a.*	
Yb	0.97	5	0.997	1.7	6	1.631	*n.a.*	
Lu	0.14	7	0.151	0.25	7	0.2484	*n.a.*	
Hf	1.1	6	1.1	0.59	3	0.5822	*n.a.*	
Ta	0.18	9	0.19	0.038	7	0.0414	*n.a.*	
Pb	2.4	17	2.47	2.6	7	3.037	*n.a.*	
Th	0.044	10	0.053	0.032	9	0.0328	*n.a.*	
U	0.013	12	0.019	0.0090	8	0.01051	*n.a.*	

RSD (%) = Relative standard deviation (percentage) of “n" analyses. Reference values of UM-2 from the GeoReM database (http://georem.mpch-mainz.gwdg.de/sample_query.asp)

Table A14 XRF and ICP-MS results for international reference materials used in the analyses

	Reference materials						
	GeoReM database	UB-N	RSD (%)	*Govindaraju (1994)*	JP-1	RSD (%)	*Imai et al. (1995)*
		n = 6			*n = 2*		
SiO2 (wt. %)	39.2	40.59	1	39.43	42.80	0	42.38
TiO2	0.24	0.18	3	0.11	0.09	0	0.006
Al2O3	7.23	2.95	1	2.9	0.68	0	0.66
Fe2O3t	15.1	8.20	1	8.34	8.18	0	8.37
MnO	0.08	0.13	1	0.12	0.12	0	0.121
MgO	25.45	35.21	0	35.21	43.63	0	44.6
CaO	4.68	1.26	1	1.2	0.56	0	0.55
Na2O	0.32	0.09	6	0.1	*b.d.l.*	-	0.021
K2O	0.08	0.02	3	0.02	0.01	0	0.003
P2O5	0.02	0.01	3	0.04	*b.d.l.*	-	0.002
LOI	6.27	12.17	1	12.06	3.89	0	3.77
Total	98.67	100.80	0	99.53	99.95	0	100.48
FeO							
V (ppm)	-	70	2	75	*n.a.*		
Cr	-	2478	0	2421	*n.a.*		
Co	120	105	1	102	*n.a.*		
Ni	2900	2093	0	2000	*n.a.*		
Zn	-	88	0	85	*n.a.*		
Ga	-	2	0	3	*n.a.*		
		n = 4		*Godard et al. (2009)*	*n = 4*		*Ionov et al. (2006)*
Rb		3.3	4	3.3	0.30	3	0.27
Sr		7.2	1	7.7	0.53	3	0.66
Y		2.4	3	2.5	0.10	7	0.1
Zr		3.4	3	3.8	5.0	3	5.57
Nb		0.048	4	0.060	0.042	7	0.044
Cs		11	6	11	0.038	6	0.042
Ba		21	1	27	9.2	1	9.7
La		0.30	1	0.31	0.027	4	0.03
Ce		0.76	2	0.83	0.062	4	0.076
Pr		0.11	4	0.12	0.0073	6	0.006
Nd		0.59	3	0.62	0.031	3	0.04
Sm		0.21	4	0.22	0.0083	9	0.01
Eu		0.081	6	0.080	0.0027	0	0.003
Gd		0.33	7	0.33	0.013	1	0.013
Tb		0.061	9	0.060	0.0021	7	0.0021
Dy		0.43	8	0.44	0.016	3	0.017
Ho		0.092	6	0.100	0.0031	4	0.004
Er		0.29	4	0.29	0.014	6	0.013
Tm		0.045	2	0.040	0.0023	10	0.0023
Yb		0.30	5	0.30	0.021	3	0.021
Lu		0.048	6	0.049	0.0045	4	0.0041
Hf		0.13	3	0.14	0.12	7	0.12
Ta		0.024	11	0.024	0.0049	0	0.004
Pb		11	2	13	0.081	4	0.07
Th		0.062	8	0.084	0.012	8	0.013
U		0.046	6	0.057	0.012	5	0.012

RSD (%) = Relative standard deviation (percentage) of “n" analyses. Reference values of UM-2 from the GeoReM database (http://georem.mpch-mainz.gwdg.de/sample_query.asp)

Table A15 Representative LA-ICP-MS analyses of garnet, allanite, epidote, diopside and amphibole-2 from Cerro del Almirez metarodingites.

Lithology	**Grandite-metarodingite**																
Domain	Atg-serpentinite																
Sample	AL00-6																
Phase	*Garnet-1*								*Garnet-2*								
Rb (ppm)	0.05	*b.d.l.*	0.006	0.021	0.031	0.02	0.02	*b.d.l.*	*b.d.l.*	*b.d.l.*	0.007	*b.d.l.*	*b.d.l.*	0.038	0.074	0.042	0.01
Sr	1.91	1.34	1.53	1.56	3.04	3.67	1.13	1.75	0.176	0.197	0.48	0.176	0.246	0.111	0.373	0.192	0.194
Y	130	61.1	92	50.5	150	137	57.5	107	68	94	68	56.3	32.7	42	26.2	49.1	85
Zr	28.6	23.2	22.8	17.6	27.3	27.6	28.6	28.6	40.9	38.3	44.4	35.6	19	31.5	24.1	40.1	37.2
Nb	*b.d.l.*	0.002	0.003	*b.d.l.*	*b.d.l.*	0.008	0.002	0.012	*b.d.l.*	*b.d.l*	0.009	0.006	0.0072	0.02	0.004	0.013	*b.d.l.*
Cs	2.81	4.36	4.14	5.07	4.92	6.08	9.61	7.77	1.59	2.77	4.21	10.4	14	11.9	7.4	1.02	1.29
Ba	0.93	0.87	0.62	0.93	1.31	1.32	0.6	0.88	0.1	0.153	0.92	0.066	0.31	0.08	0.09	0.59	0.089
La	0.037	0.037	0.02	0.043	0.036	0.064	0.032	0.03	0.055	0.053	0.092	0.046	0.044	0.05	0.054	0.005	0.023
Ce	0.73	0.489	0.471	0.364	0.215	0.319	0.26	0.264	0.175	0.207	0.356	0.433	0.437	0.332	0.572	0.117	0.075
Pr	0.237	0.351	0.163	0.212	0.137	0.147	0.179	0.201	0.09	0.162	0.186	0.365	0.35	0.321	0.327	0.07	0.057
Nd	4.38	3.85	3.19	2.44	2.14	2.23	3.37	3.01	1.86	2.27	4.06	7.93	9.2	9.8	5.93	1.69	1.55
Sm	4.7	3.68	3.45	2.98	3.32	2.94	3.69	3.97	4.41	5.22	6.63	12	15.2	18	10.6	5.94	4
Eu	1.88	1.39	1.33	1.24	1.93	1.78	1.42	1.91	2.19	2.36	2.53	2.84	2.63	2.9	1.47	1.78	1.62
Gd	11.3	6.9	8.37	5.6	9.9	10.1	7.3	10	11	11.9	12.3	14.2	18.3	11.3	8	8	7.5
Tb	2.97	1.72	2.11	1.56	2.88	2.53	1.32	2.22	2.42	2.45	2.55	1.99	1.93	1.74	0.98	1.67	1.84
Dy	26.1	14	15.1	10.8	22.4	18.3	9.7	14.7	14.4	17.4	15.5	11.6	8.14	10.2	3.83	9.3	11.3
Ho	5.2	2.95	2.8	2.23	5.26	4.68	2.03	3.19	2.54	3.41	2.83	2.05	1.19	1.62	0.502	1.57	2.18
Er	14.1	7.12	5.9	5.16	17.9	15.1	5.4	9.6	7.3	9.1	7.4	5.7	2.82	4.1	1.2	4.08	5.1
Tm	1.76	0.965	0.83	0.82	2.28	1.96	0.65	1.38	1.01	1.1	1	0.82	0.323	0.63	0.196	0.598	0.78
Yb	12	6.03	5.4	5.17	15.2	11.5	4.44	10.1	5.36	6.9	5.31	4.02	1.88	3.2	1.06	2.49	3.7
Lu	1.42	0.748	0.68	0.74	2.05	1.53	0.57	1.98	0.74	1.11	0.76	0.58	0.21	0.34	0.15	0.29	0.5
Hf	1.58	1.09	1.07	1.04	1.19	1.04	1.32	1.63	1.46	1.41	1.72	1.99	1.86	2.5	1.91	1.11	1.25
Ta	0.077	0.142	0.111	0.208	0.099	0.173	0.271	0.255	0.078	0.168	0.213	0.567	0.82	0.79	0.271	0.025	0.049
Pb	0.153	0.079	0.075	0.118	0.143	0.12	0.056	0.11	0.069	0.036	0.28	0.158	0.054	0.048	0.041	0.067	0.075
Th	0.042	0.072	0.031	0.077	0.134	0.097	0.045	0.065	0.011	0.011	0.0051	0.0139	0.0083	0.012	0.032	0.004	0.0094
U	0.394	0.251	0.143	0.182	0.262	0.238	0.186	0.259	0.344	0.273	0.43	0.299	0.06	0.23	0.143	0.25	0.176

Atg = Antigorite; Chl = Chlorite; b.d.l. = below detection limit. RSD (%) = Relative standard deviations (percentage) of "n" analyses. Preferred values of BHVO-2G from the GeoReM database (http://georem.mpch-mainz.gwdg.de/sample_query_pref.asp)

Table A15 Representative LA-ICP-MS analyses of garnet, allanite, epidote, diopside and amphibole-2 from Cerro del Almirez metarodingites.

Lithology	**Grandite-metarodingite**						
Domain	Atg-serpentinite						
Sample	AL00-6						
Phase	*Garnet-3*						
Rb (ppm)	0.028	*b.d.l.*	0.03	0.01	*b.d.l.*	*b.d.l.*	0.011
Sr	0.139	0.106	0.09	0.12	0.12	0.12	0.131
Y	11.3	14	13.1	13.1	14.7	19.2	14.9
Zr	32.8	32.3	31	33.3	41.1	42.5	48.4
Nb	0.017	*b.d.l.*	0.025	0.012	0.0023	*b.d.l.*	0.001
Cs	0.6	0.598	0.57	0.57	0.82	0.816	0.866
Ba	0.02	*b.d.l.*	*b.d.l.*	*b.d.l.*	*b.d.l.*	*b.d.l.*	0.012
La	0.0065	0.0107	0.006	0.0139	0.035	0.027	0.016
Ce	0.272	0.348	0.26	0.313	0.42	0.509	0.416
Pr	0.194	0.265	0.194	0.187	0.235	0.285	0.272
Nd	3.04	4.02	3.1	3.95	3.66	4.39	4.01
Sm	3.59	4.11	3.6	3.7	3.67	3.58	3.36
Eu	1.27	1.26	1.14	1.32	1.79	1.66	1.83
Gd	2.88	2.66	2.5	1.86	3.99	3.89	3.79
Tb	0.44	0.49	0.42	0.366	0.594	0.568	0.515
Dy	1.77	2.68	2.3	1.76	3.34	3.43	3.02
Ho	0.281	0.49	0.32	0.264	0.58	0.66	0.51
Er	0.5	1.26	0.77	0.58	1.46	1.94	1.26
Tm	0.077	0.215	0.119	0.102	0.209	0.265	0.18
Yb	0.48	0.91	0.62	0.49	1.16	1.65	0.87
Lu	0.064	0.136	0.077	0.067	0.19	0.208	0.108
Hf	1.05	1.04	1.06	0.89	1.49	1.55	1.41
Ta	0.011	0.023	0.0086	0.024	0.019	0.043	0.0255
Pb	*b.d.l.*	0.0059	0.012	0.007	*b.d.l.*	0.009	0.01
Th	0.006	0.0014	0.014	0.0014	0.0057	0.0062	0.0051
U	0.21	0.24	0.25	0.22	0.463	0.461	0.496

Atg = Antigorite; Chl = Chlorite; b.d.l. = below detection limit. RSD (%) = Relative standard deviations (percentage) of "n" analyses. Preferred values of BHVO-2G from the GeoReM database (http://georem.mpch-mainz.gwdg.de/sample_query_pref.asp)

Table A15 Representative LA-ICP-MS analyses of garnet, allanite, epidote, diopside and amphibole-2 from Cerro del Almirez metarodingites.

Lithology	**Epidote-metarodingite**												
Domain	Atg-serpentinite												
Sample	AL14-26E												
Phase	*Garnet-2 relic*												
Rb (ppm)	0.011	0.065	0.02	0.018	0.025	0.035	0.015	0.064	0.019	0.018	0.025	0.037	0.015
Sr	1.5	0.48	3.3	2.21	3	21	0.67	0.47	3.3	2.19	3	19	0.66
Y	73	78	56.9	51.5	57.3	49.8	56.2	79	57.4	52.1	58.1	48.8	57.3
Zr	22.2	15.8	23.8	20.6	24.2	21.8	23.7	15.8	23.8	20.7	24.2	20.9	23.8
Nb	0.022	0.014	0.036	0.034	0.021	0.028	0.014	0.014	0.036	0.034	0.021	0.027	0.014
Cs	0.121	0.043	0.1	0.131	0.093	0.122	0.09	0.043	0.101	0.131	0.093	0.118	0.09
Ba	0.32	0.51	1.5	0.48	2	2	0.138	0.51	1.5	0.48	2	1.8	0.138
La	*b.d.l.*	*b.d.l.*	*b.d.l.*	*b.d.l.*	*b.d.l.*	*b.d.l.*	*b.d.l.*	*b.d.l.*	*b.d.l.*	*b.d.l.*	*b.d.l.*	*b.d.l.*	*b.d.l.*
Ce	*b.d.l.*	*b.d.l.*	*b.d.l.*	*b.d.l.*	*b.d.l.*	*b.d.l.*	*b.d.l.*	*b.d.l.*	*b.d.l.*	*b.d.l.*	*b.d.l.*	*b.d.l.*	*b.d.l.*
Pr	*b.d.l.*	*b.d.l.*	*b.d.l.*	*b.d.l.*	*b.d.l.*	*b.d.l.*	*b.d.l.*	*b.d.l.*	*b.d.l.*	*b.d.l.*	*b.d.l.*	*b.d.l.*	*b.d.l.*
Nd	0.019	0.045	0.005	0.005	0.018	0.012	0.029	0.044	0.005	0.005	0.017	0.01	0.029
Sm	0.094	0.026	0.089	0.066	0.133	0.018	0.05	0.026	0.088	0.065	0.132	0.016	0.05
Eu	0.154	0.105	0.157	0.142	0.163	0.22	0.185	0.104	0.154	0.139	0.16	0.203	0.182
Gd	0.56	0.5	1.28	0.98	1.31	0.9	0.85	0.49	1.27	0.97	1.3	0.9	0.84
Tb	0.42	0.283	0.613	0.63	0.626	0.52	0.57	0.281	0.609	0.62	0.622	0.525	0.57
Dy	4.65	5.43	7.1	7.6	6.9	6.13	6.3	5.43	7	7.6	6.89	6.15	6.29
Ho	1.55	2.32	1.99	2.11	1.84	1.78	1.87	2.32	1.99	2.11	1.84	1.82	1.87
Er	6.94	13.4	6.2	7.1	5.82	7.2	6.56	13.4	6.2	7.1	5.82	7.19	6.56
Tm	1.35	3.17	0.86	0.97	0.96	1.04	1.05	3.16	0.86	0.97	0.96	1.06	1.05
Yb	10.2	24	5.56	5.7	4.97	6.23	6.55	23.9	5.55	5.7	4.96	6.35	6.53
Lu	1.59	3.55	0.67	0.82	0.71	0.79	0.94	3.56	0.67	0.82	0.71	0.77	0.94
Hf	0.75	0.276	0.62	0.71	0.639	0.59	0.716	0.291	0.66	0.75	0.68	0.59	0.76
Ta	0.0017	0.0017	*b.d.l.*	0.0121	0.0005	0.0022	0.004	0.0017	*b.d.l.*	0.0119	0.001	0.0018	0.0039
Pb	0.122	0.58	1.87	0.042	0.57	1.23	0.046	0.57	1.85	0.042	0.56	1.07	0.045
Th	*b.d.l.*	*b.d.l.*	*b.d.l.*	*b.d.l.*	*b.d.l.*	*b.d.l.*	0.0012	*b.d.l.*	*b.d.l.*	*b.d.l.*	*b.d.l.*	*b.d.l.*	0.0012
U	0.0072	0.027	0.0233	0.0168	0.019	0.013	0.0199	0.027	0.0232	0.0167	0.019	0.011	0.0198

Atg = Antigorite; Chl = Chlorite; b.d.l. = below detection limit. RSD (%) = Relative standard deviations (percentage) of "n" analyses. Preferred values of BHVO-2G from the GeoReM database (http://georem.mpch-mainz.gwdg.de/sample_query_pref.asp)

Table A15 Representative LA-ICP-MS analyses of garnet, allanite, epidote, diopside and amphibole-2 from Cerro del Almirez metarodingites.

Lithology	**Epidote-metarodingite**						**Pyralspite-metarodingite**					
Domain	Chl-harzburgite						Chl-harzburgite					
Sample	AL98-19B						AL96-24A					
Phase	*Garnet-4*						*Garnet-5*					
Rb (ppm)	0.061	0.044	0.027	0.005	0.046	*b.d.l.*	0.0196	0.011	0.008	0.027	0.0266	0.0064
Sr	0.38	0.307	0.164	0.178	1.65	0.189	0.023	0.04	0.025	0.043	0.029	0.23
Y	45.3	42.5	55.1	54.4	55	73	41.5	22.1	20.2	31.8	44	34
Zr	14.2	12.8	20.8	13	20.1	15.3	1.81	2.63	3.53	2.66	5.6	3.49
Nb	0.011	*b.d.l.*	0.005	0.0083	*b.d.l.*	*b.d.l.*	0.021	*b.d.l.*	*b.d.l.*	0.0008	0.01	0.0014
Cs	0.064	0.049	0.046	0.072	0.14	*b.d.l.*	*bdl*	0.015	0.009	0.013	0.003	0.081
Ba	0.6	0.49	0.49	0.18	0.159	0.14	0.019	0.015	*b.d.l.*	*b.d.l.*	*b.d.l.*	0.038
La	*b.d.l.*	*b.d.l.*	*b.d.l.*	*b.d.l.*	*b.d.l.*	*b.d.l.*	*b.d.l.*	*b.d.l.*	*b.d.l.*	*b.d.l.*	*b.d.l.*	*b.d.l.*
Ce	*b.d.l.*	*b.d.l.*	*b.d.l.*	*b.d.l.*	*b.d.l.*	*b.d.l.*	*b.d.l.*	*b.d.l.*	*b.d.l.*	*b.d.l.*	*b.d.l.*	*b.d.l.*
Pr	*b.d.l.*	*b.d.l.*	*b.d.l.*	*b.d.l.*	*b.d.l.*	*b.d.l.*	*b.d.l.*	*b.d.l.*	*b.d.l.*	*b.d.l.*	*b.d.l.*	*b.d.l.*
Nd	0.18	0.027	0.033	0.031	0.031	0.033	*bdl*	*b.d.l.*	0.02	*b.d.l.*	0.012	0.027
Sm	0.012	0.032	*b.d.l.*	0.06	0.111	0.067	0.033	*b.d.l.*	*b.d.l.*	*b.d.l.*	0.062	0.013
Eu	0.13	0.059	0.04	0.065	0.082	0.04	0.031	0.008	0.024	0.006	0.048	0.024
Gd	0.652	0.56	0.276	0.44	0.55	0.34	0.167	0.23	0.1	0.3	0.43	0.18
Tb	0.267	0.232	0.191	0.229	0.307	0.245	0.126	0.049	0.046	0.148	0.159	0.099
Dy	4.3	3.54	3.12	4.91	4.74	4.13	2.23	1.43	1.27	2.13	2.65	2.08
Ho	2.44	1.86	2	2.54	1.76	2.05	1.47	0.93	0.85	1.47	1.81	1.65
Er	11.16	7	11.1	11.6	9.2	15.7	9.81	4.85	4.81	6.77	6.74	7.1
Tm	2.77	1.394	3.72	2.99	2.12	4.19	2.47	1.56	1.39	1.92	2.13	2.26
Yb	24.4	10.73	46.5	28.7	20.4	42	22.1	16.9	15.8	20.3	21.2	25.3
Lu	4.1	1.59	10.5	4.64	4.17	8.26	3.58	3.3	3.11	3.28	4	4.91
Hf	0.318	0.18	0.39	0.267	0.4	0.26	0.012	0.015	0.028	0.031	0.018	0.04
Ta	0.0046	*b.d.l.*	0.01	0.0017	0.0074	*b.d.l.*	*b.d.l.*	*b.d.l.*	*b.d.l.*	0.0031	0.0035	0.0025
Pb	0.081	0.47	0.36	0.074	0.119	0.132	0.0116	0.081	0.0149	0.049	0.025	0.067
Th	*b.d.l.*	*b.d.l.*	*b.d.l.*	*b.d.l.*	0.0028	*b.d.l.*	*b.d.l.*	*b.d.l.*	*b.d.l.*	*b.d.l.*	*b.d.l.*	0.006
U	0.018	*b.d.l.*	0.0135	0.017	0.0059	0.0054	*b.d.l.*	*b.d.l.*	*b.d.l.*	*b.d.l.*	*b.d.l.*	*b.d.l.*

Atg = Antigorite; Chl = Chlorite; b.d.l. = below detection limit. RSD (%) = Relative standard deviations (percentage) of "n" analyses. Preferred values of BHVO-2G from the GeoReM database (http://georem.mpch-mainz.gwdg.de/sample_query_pref.asp)

Table A15 Representative LA-ICP-MS analyses of garnet, allanite, epidote, diopside and amphibole-2 from Cerro del Almirez metarodingites.

Lithology	**Grandite-metarodingite**					
Domain	Atg-serpentinite					
Sample	AL00-6					
Phase	*Allanite*					
Rb (ppm)	0.042	*b.d.l.*	*b.d.l.*	*b.d.l.*	*b.d.l.*	0.034
Sr	414	537	618	486	1138	500
Y	5.8	6.1	6.43	13.1	8.6	12.3
Zr	27.3	16.7	24	29.3	21.6	25.1
Nb	1.91	0.01	5.8	*b.d.l.*	0.01	0.046
Cs	*b.d.l.*	*b.d.l.*	0.011	0.0073	0.023	0.01
Ba	0.94	0.57	1.02	0.76	1.55	0.71
La	27000	21500	21000	7660	10180	7560
Ce	65500	49200	46100	15110	17900	14150
Pr	8980	5970	6020	1900	2080	1650
Nd	28100	20200	20300	7230	6180	5530
Sm	876	709	690	599	359	492
Eu	68.3	56.8	53.4	68.3	39.2	60.2
Gd	203	158	146	131	90.6	115
Tb	7.01	5.47	4.57	5.49	3.58	4.69
Dy	7.08	6.5	4.77	10.3	5.58	8.5
Ho	0.507	0.46	0.33	0.67	0.441	0.59
Er	4.92	3.64	2.97	1.71	1.24	1.52
Tm	0.052	0.035	0.031	0.026	0.034	0.099
Yb	0.099	0.06	0.13	0.086	0.19	0.39
Lu	0.019	0.0065	0.0151	0.0031	0.0107	0.05
Hf	2.29	0.6	0.81	1.41	1	1.32
Ta	0.146	*b.d.l.*	0.39	*b.d.l.*	0.0018	0.0015
Pb	5.66	8.75	7.4	17.8	16.8	15.48
Th	1070	1220	950	732	441	533
U	15.49	28.8	27.4	25.5	20.4	22

Atg = Antigorite; Chl = Chlorite; b.d.l. = below detection limit. RSD (%) = Relative standard deviations (percentage) of "n" analyses. Preferred values of BHVO-2G from the GeoReM database (http://georem.mpch-mainz.gwdg.de/sample_query_pref.asp)

Table A15 Representative LA-ICP-MS analyses of garnet, allanite, epidote, diopside and amphibole-2 from Cerro del Almirez metarodingites

Lithology	**Epidote-metarodingite**											
Domain	Atg-serpentinite											
Sample	AL14-26E											
Phase	*Epidote*											
Rb (ppm)	0.079	0.18	0.071	0.044	0.002	*b.d.l.*	0.046	0.08	0.041	0.024	0.091	0.033
Sr	1790	1840	1740	4090	1000	1000	1340	1241	1186	957	900	1200
Y	45.7	44	36.7	64	23.5	41.7	43.6	32.8	43.3	30	27	11.9
Zr	42	26	17.7	10.9	48.4	48	45.6	47.7	55.7	31.1	27.9	48.9
Nb	5.7	5.8	4.03	*b.d.l.*	*b.d.l.*	*b.d.l.*	*b.d.l.*	*b.d.l.*	*b.d.l.*	*b.d.l.*	*b.d.l.*	0.003
Cs	0.006	0.018	0.006	0.006	*b.d.l.*	0.08	*b.d.l.*	*b.d.l.*	0.001	0.063	0.041	*bdl*
Ba	12.47	12.6	11.4	24.1	4.36	3.09	4.31	3.96	4.06	11.1	10.4	11.94
La	10.8	6.98	11.85	17.7	13.24	28.8	30.2	51.9	28.8	2.99	3.3	3.32
Ce	25.5	19	27.9	46	31.6	63	66.9	110.8	58.6	7.1	7.79	7.3
Pr	3.83	3.14	4.36	7.21	4.7	8.6	9	14.9	8.11	0.99	1.1	0.96
Nd	19.1	15.7	20.2	32.9	24.2	48.1	45.9	71.4	41.9	4.39	5.2	4.73
Sm	6.6	5.77	6.6	12.2	10.28	61	15.6	23.4	15.9	1.65	1.71	1.74
Eu	3.19	3.28	3.38	3.88	8.32	40	10	15.1	11.41	0.95	0.9	1.25
Gd	7.72	7.41	8.3	13.4	12.8	80	17.7	22.1	18.8	2.2	1.75	2.08
Tb	1.45	1.3	1.23	2.16	1.72	9	2.67	2.61	2.59	0.44	0.299	0.269
Dy	9.1	8.1	7.46	12.6	7	33	13.6	11.1	13.1	3.3	2.52	2.32
Ho	1.73	1.65	1.38	2.29	0.86	5.7	1.62	1.2	1.67	0.99	0.71	0.451
Er	5.43	4.9	4.32	6.2	1.13	9	2.91	2.15	3.01	3.84	3.21	1.64
Tm	0.74	0.63	0.465	0.618	0.09	1.3	0.279	0.144	0.2	0.75	0.6	0.272
Yb	3.86	3.36	2.85	2.61	0.27	2.4	0.84	0.54	0.85	4.38	4.3	2.36
Lu	0.507	0.37	0.323	0.215	0.047	0.21	0.075	0.052	0.087	0.638	0.59	0.266
Hf	0.91	1.09	0.67	0.45	1.45	6.4	1.72	1.35	1.9	1.01	0.9	1.07
Ta	0.37	0.32	0.232	0.003	0.004	*b.d.l.*	*b.d.l.*	0.0012	0.0024	*b.d.l.*	0.0059	*b.d.l.*
Pb	32.8	23.1	24.6	107	26.7	310	31.3	21.9	29.3	34.9	30.5	37.1
Th	0.33	0.119	0.596	0.283	0.022	3.5	0.341	1.04	0.192	0.071	0.07	0.052
U	0.505	0.352	0.713	0.38	1.82	34	4.53	5.8	3.37	0.219	0.099	0.398

Atg = Antigorite; Chl = Chlorite; b.d.l. = below detection limit. RSD (%) = Relative standard deviations (percentage) of "n" analyses. Preferred values of BHVO-2G from the GeoReM database (http://georem.mpch-mainz.gwdg.de/sample_query_pref.asp)

Table A15 Representative LA-ICP-MS analyses of garnet, allanite, epidote, diopside and amphibole-2 from Cerro del Almirez metarodingites.

Lithology	**Epidote-metarodingite**		**Pyralspite-metarodingite**			**Grandite-metarodingite**					
Domain	Chl-harzburgite		Chl-harzburgite			Atg-serpentinite					
Sample	AL98-19B		AL96-24A			AL00-6					
Phase	*Epidote*		*Epidote*			*Diopside*					
Rb (ppm)	0.047	0.003	0.069	0.038	0.065	0.017	0.042	0.028	0.041	0.017	0.0259
Sr	550	1150	2980	2000	1850	6.99	8.03	6.82	7.47	7.1	6.91
Y	13	12.2	32.5	54.7	79	0.081	0.062	0.096	0.047	0.061	0.087
Zr	52	14.5	12.4	17.6	13.8	1.89	1.98	2.19	2.02	1.81	1.71
Nb	*b.d.l.*	*b.d.l.*	1.62	2.92	0.38	0.034	0.059	0.0462	0.041	0.0284	0.0329
Cs	*b.d.l.*	*b.d.l.*	0.017	0.016	0.033	0.014	0.011	0.0053	0.0095	0.0076	0.0057
Ba	2.78	60.5	5.03	4.83	5.21	0.01	0.017	0.013	0.013	0.035	0.013
La	2.37	1.54	6.35	15.8	33	0.0128	0.033	0.0115	0.0171	0.0164	0.0134
Ce	4.57	2.97	15.6	37.8	72.2	0.053	0.113	0.0542	0.101	0.066	0.059
Pr	0.7	0.45	2.55	5.81	10.04	0.0181	0.034	0.0206	0.0322	*b.d.l.*	0.0241
Nd	3.65	2.3	12.6	28.4	46.1	0.154	0.256	0.207	0.252	0.153	0.196
Sm	0.87	0.83	3.24	9	13	0.096	0.132	0.129	0.119	0.068	0.104
Eu	0.93	0.83	1.68	4.77	7.56	0.0291	0.038	0.028	0.034	0.022	0.029
Gd	1.4	1.28	3.9	7.9	13.5	0.061	0.083	0.096	0.077	0.058	0.058
Tb	0.224	0.32	0.74	1.56	2.3	0.0048	0.007	0.0026	0.0043	0.006	0.0038
Dy	1.74	2.01	5.2	9.37	14.2	0.029	0.015	0.0165	0.023	0.022	0.02
Ho	0.45	0.435	1.07	1.75	2.57	*b.d.l.*	*b.d.l.*	*b.d.l.*	*b.d.l.*	*b.d.l.*	*b.d.l.*
Er	1.49	1.01	2.79	4.53	6.7	0.01	0.0026	0.0084	0.0044	0.0105	0.0076
Tm	0.198	0.119	0.41	0.71	0.84	*b.d.l.*	*b.d.l.*	*b.d.l.*	*b.d.l.*	0.001	0.001
Yb	1.04	0.8	2.09	4.14	4.54	*b.d.l.*	*b.d.l.*	0.0046	0.0044	0.0015	0.0049
Lu	0.101	0.135	0.28	0.556	0.55	0.00049	*b.d.l.*	0.001	*b.d.l.*	*b.d.l.*	*b.d.l.*
Hf	1.19	0.84	0.65	0.71	0.52	0.203	0.25	0.195	0.189	0.194	0.185
Ta	0.0044	*b.d.l.*	0.097	0.184	0.034	0.00041	0.0022	0.0026	0.0014	0.0014	0.0011
Pb	17.6	27.5	21.6	24.6	22.2	0.446	0.49	0.36	0.34	0.37	0.39
Th	0.043	0.0112	0.33	0.372	0.84	*b.d.l.*	0.0012	*b.d.l.*	*b.d.l.*	0.0013	*b.d.l.*
U	0.24	0.125	0.133	0.21	0.461	0.0009	0.0003	0.0005	*b.d.l.*	0.001	0.0003

Atg = Antigorite; Chl = Chlorite; b.d.l. = below detection limit. RSD (%) = Relative standard deviations (percentage) of "n" analyses. Preferred values of BHVO-2G from the GeoReM database (http://georem.mpch-mainz.gwdg.de/sample_query_pref.asp)

Table A15 Representative LA-ICP-MS analyses of garnet, allanite, epidote, diopside and amphibole-2 from Cerro del Almirez metarodingites.

Lithology	**Epidote-metarodingite**											
Domain	Atg-serpentinite											
Sample	AL14-26E											
Phase	*Diopside*											
Rb (ppm)	0.13	0.017	0.033	0.028	0.024	0.022	0.026	0.0164	0.47	0.122	0.052	0.024
Sr	14.6	13.74	14.4	14.8	15.5	15.2	14.04	14.8	22.8	16.9	14.6	17.7
Y	0.111	0.076	0.097	0.099	0.073	0.105	0.118	0.101	0.08	0.093	0.071	0.062
Zr	1.31	1.28	1.44	1.16	1.37	1.33	1.36	1.195	1.2	2.5	1.24	2.01
Nb	0.041	0.04	0.032	0.04	0.038	0.036	0.037	0.0276	0.038	0.036	0.0245	0.027
Cs	0.023	0.0089	0.0083	0.0054	0.008	0.0054	0.0098	0.0058	0.084	0.0201	0.0091	0.0091
Ba	0.28	0.15	0.065	0.091	0.092	0.13	0.083	0.018	5.7	1.08	0.3	0.045
La	0.0072	0.0019	0.0079	0.0053	0.0054	0.003	0.0027	0.0029	0.0063	0.0075	0.0022	0.0053
Ce	*b.d.l.*	*b.d.l.*	*b.d.l.*	*b.d.l.*	*b.d.l.*	*b.d.l.*	*b.d.l.*	*b.d.l.*	*b.d.l.*	*b.d.l.*	*b.d.l.*	*b.d.l.*
Pr	0.0037	0.0042	0.0044	0.0058	0.0024	0.0033	0.0037	0.0051	0.0025	0.0042	0.0053	0.0041
Nd	*b.d.l.*	*b.d.l.*	*b.d.l.*	*b.d.l.*	*b.d.l.*	*b.d.l.*	*b.d.l.*	*b.d.l.*	*b.d.l.*	*b.d.l.*	*b.d.l.*	*b.d.l.*
Sm	0.01	*b.d.l.*	0.014	*b.d.l.*	*b.d.l.*	*b.d.l.*	0.009	0.011	0.0066	0.0085	*bdl*	0.005
Eu	0.0049	0.0066	0.0082	0.006	0.0038	0.0072	0.0067	0.0047	0.0043	0.0087	0.0043	0.0062
Gd	0.023	0.014	0.0287	0.0247	0.0166	0.012	0.02	0.02	0.022	0.0158	0.011	0.015
Tb	*b.d.l.*	*b.d.l.*	*b.d.l.*	*b.d.l.*	*b.d.l.*	*b.d.l.*	*b.d.l.*	*b.d.l.*	*b.d.l.*	*b.d.l.*	*b.d.l.*	*b.d.l.*
Dy	*b.d.l.*	*b.d.l.*	0.018	*b.d.l.*	0.02	0.014	0.0135	0.0163	0.0129	*b.d.l.*	0.022	*b.d.l.*
Ho	0.0069	0.0071	0.006	0.0056	0.0053	0.0055	*bdl*	0.0058	0.0039	0.0051	0.0049	0.0033
Er	0.023	0.026	0.034	0.02	*b.d.l.*	0.024	0.0224	*bdl*	0.0101	*b.d.l.*	0.0042	*b.d.l.*
Tm	0.0055	0.0041	0.0052	*b.d.l.*	0.0016	0.0034	*bdl*	0.0022	*b.d.l.*	0.0023	*b.d.l.*	0.0005
Yb	0.041	0.046	0.032	0.034	*b.d.l.*	*b.d.l.*	0.029	0.02	0.0061	*b.d.l.*	0.0024	0.0026
Lu	0.0081	0.0092	0.0063	0.0061	0.0021	0.0048	0.0076	0.0039	0.00069	0.0019	0.00031	*b.d.l.*
Hf	0.082	0.094	0.091	0.077	0.071	0.077	0.083	0.053	0.081	0.174	0.08	0.146
Ta	0.0024	0.0025	0.00028	*b.d.l.*	0.00058	0.0013	0.0013	0.00054	0.00036	0.0019	0.002	0.00062
Pb	0.64	0.718	0.59	0.51	0.49	0.53	0.6	0.51	0.72	0.71	0.55	0.61
Th	*b.d.l.*	*b.d.l.*	*b.d.l.*	0.0008	*b.d.l.*	*b.d.l.*	*b.d.l.*	*b.d.l.*	*b.d.l.*	*b.d.l.*	*b.d.l.*	*b.d.l.*
U	0.001	*b.d.l.*	*b.d.l.*	0.00028	0.00086	0.00046	0.00022	*b.d.l.*	0.00027	0.0022	*b.d.l.*	*b.d.l.*

Atg = Antigorite; Chl = Chlorite; b.d.l. = below detection limit. RSD (%) = Relative standard deviations (percentage) of "n" analyses. Preferred values of BHVO-2G from the GeoReM database (http://georem.mpch-mainz.gwdg.de/sample_query_pref.asp)

Table A15 Representative LA-ICP-MS analyses of garnet, allanite, epidote, diopside and amphibole-2 from Cerro del Almirez metarodingites

Lithology	**Pyralspite-metarodingite**				**Grandite-metarodingite**						
Domain	Chl-harzburgite				Atg-serpentinite						
Sample	AL96-24A				AL00-6						
Phase	*Diopside*				*Amphibole-2*						
Rb (ppm)	0.083	0.054	0.15	0.044	2.68	3.44	3.72	3.23	1.922	2.37	2.59
Sr	76	60.8	70	58.2	12.3	13.2	14.1	13	17.3	15.4	15.3
Y	3.97	3.02	6.5	2.08	0.43	0.52	0.49	0.39	0.345	0.332	0.334
Zr	1.33	1	1.37	1.09	12.1	13.9	11.6	12.87	14.13	14	15
Nb	0.034	0.0264	0.036	0.043	0.084	0.083	0.134	0.139	0.066	0.082	0.05
Cs	0.0084	0.0136	0.0089	0.0063	0.006	0.0036	0.031	0.008	0.01	0.07	0.017
Ba	4	1.7	0.49	0.29	17.9	16.7	20.2	19	18.7	19.3	18.9
La	0.0246	0.0278	0.037	0.0185	0.008	0.0112	0.044	*b.d.l.*	0.014	0.025	0.036
Ce	0.089	0.077	0.116	0.093	0.128	0.099	0.152	0.089	0.173	0.119	0.137
Pr	0.031	0.0285	0.031	0.0212	0.039	*bdl*	0.048	0.059	0.044	0.0521	0.049
Nd	0.219	0.217	0.27	0.157	0.3	0.43	0.48	0.375	*b.d.l.*	0.35	0.28
Sm	0.287	0.286	0.41	0.152	0.224	0.226	0.23	0.288	0.162	0.216	0.27
Eu	0.064	0.056	0.103	0.049	0.096	0.067	0.09	0.104	0.052	0.057	0.072
Gd	0.57	0.51	0.98	0.41	0.22	*b.d.l.*	0.27	*b.d.l.*	0.18	0.2	*b.d.l.*
Tb	0.158	0.144	0.213	0.107	0.03	0.041	0.027	0.037	0.022	0.026	0.021
Dy	0.99	0.88	1.61	0.59	0.098	*b.d.l.*	*b.d.l.*	*b.d.l.*	*b.d.l.*	*b.d.l.*	*b.d.l.*
Ho	0.185	0.13	0.31	0.076	0.0169	0.041	0.027	0.033	*b.d.l.*	0.026	0.02
Er	0.4	0.252	0.96	0.179	0.018	*b.d.l.*	0.048	*b.d.l.*	0.034	0.075	*b.d.l.*
Tm	0.048	0.03	0.14	0.0207	*b.d.l.*	0.0123	0.0062	*b.d.l.*	0.0017	0.0068	0.0084
Yb	0.216	0.123	0.54	0.071	0.012	0.061	0.021	*b.d.l.*	0.007	0.026	0.019
Lu	0.0226	0.0106	0.063	0.011	0.0019	*b.d.l.*	*b.d.l.*	0.0013	0.0003	*b.d.l.*	*b.d.l.*
Hf	0.095	0.072	0.14	0.091	1.64	1.54	1.09	1.5	0.83	1.1	1.05
Ta	0.0006	*b.d.l.*	0.0031	0.0015	0.0044	0.0014	0.0024	0.0036	0.0029	0.0021	*b.d.l.*
Pb	0.57	0.47	1.3	0.63	0.188	0.224	0.87	0.279	0.225	0.76	0.242
Th	0.0005	0.0015	*b.d.l.*	0.003	0.0028	0.0001	0.0001	0.0001	0.0001	0.00003	0.00002
U	0.0033	0.002	0.0037	0.0044	*b.d.l.*	*b.d.l.*	0.018	*b.d.l.*	0.008	0.006	0.018

Atg = Antigorite; Chl = Chlorite; b.d.l. = below detection limit. RSD (%) = Relative standard deviations (percentage) of "n" analyses. Preferred values of BHVO-2G from the GeoReM database (http://georem.mpch-mainz.gwdg.de/sample_query_pref.asp)

Table A15 Representative LA-ICP-MS analyses of garnet, allanite, epidote, diopside and amphibole-2 from Cerro del Almirez metarodingites. LA-ICP-MS results for international reference material (BHVO-2G) run as unknown at the IACT laboratory are also shown

Lithology	**Pyralspite-metarodingite**						**LA-ICP-MS reference material**		
Domain	Chl-harzburgite								
Sample	AL96-24A						BHVO-2G (n = 41)	RSD (%)	GeoReM database
Phase	*Amphibole-2*								
Rb (ppm)	3.36	4.11	3.61	2.68	2.76	3.01	9.3	5	9.2
Sr	66	56.1	59	63.4	68.3	74	402	5	396
Y	3	5.1	4.5	4.79	4.8	5.4	26	7	26
Zr	3.3	6.6	4.55	3.28	3.61	3.22	170	7	170
Nb	0.31	0.069	*b.d.l.*	0.045	0.04	0.031	18	4	18.3
Cs	0.025	0.012	0.009	0.009	0.002	0.007	0.10	8	0.1
Ba	15.9	17.5	16.3	11.37	10.88	14.6	131	4	131
La	0.017	0.011	0.004	0.004	0.006	0.029	15	6	15.2
Ce	*b.d.l.*	0.026	0.017	*bdl*	0.027	*b.d.l.*	38	3	37.6
Pr	*b.d.l.*	0.011	0.009	0.005	0.009	0.015	5.3	6	5.35
Nd	*b.d.l.*	0.064	0.106	0.051	0.094	0.12	25	5	24.5
Sm	*b.d.l.*	0.04	0.12	0.06	0.101	0.097	6.1	7	6.1
Eu	0.041	0.058	0.079	0.082	0.078	0.054	2.1	7	2.07
Gd	*b.d.l.*	0.42	0.26	0.22	0.262	0.14	6.1	7	6.16
Tb	0.051	0.096	0.104	0.1	0.07	0.093	0.92	9	0.92
Dy	0.39	0.751	0.84	0.95	0.695	0.69	5.2	6	5.28
Ho	0.092	0.179	0.162	0.143	0.141	0.166	0.97	8	0.98
Er	0.33	0.42	0.48	0.47	0.58	0.45	2.5	7	2.56
Tm	0.036	0.043	0.038	0.077	0.073	0.055	0.35	8	0.34
Yb	0.28	0.143	0.211	0.284	0.46	0.287	2.0	6	2.01
Lu	0.021	0.008	0.01	0.034	0.042	0.034	0.28	8	0.279
Hf	0.24	0.65	0.38	0.33	0.28	0.207	4.3	8	4.32
Ta	0.015	0.012	*b.d.l.*	0.002	*bdl*	0.003	1.1	7	1.15
Pb	0.152	0.113	0.117	0.308	0.488	0.468	1.7	7	1.7
Th	*b.d.l.*	*b.d.l.*	*b.d.l.*	*bdl*	0.001	*b.d.l.*	1.3	9	1.22
U	*b.d.l.*	*b.d.l.*	*b.d.l.*	*b.d.l.*	0.001	*b.d.l.*	0.40	8	0.403

Atg = Antigorite; Chl = Chlorite; b.d.l. = below detection limit. RSD (%) = Relative standard deviations (percentage) of "n" analyses. Preferred values of BHVO-2G from the GeoReM database (http://georem.mpch-mainz.gwdg.de/sample_query_pref.asp)

Table A16 Whole-rock compositions of PGE-Re and Os isotopes of Cerro del Almirez metarodingites, metasomatic reaction rims and host ultramafic rocks.

Lithology	**Grandite-metarodingite**		**Epidote-metarodingite**	**Amphibolitized Epidote-metarodingite**			**Amph. Pyralspite-metarodingite**	**Chl-blackwall**	
Domain	Atg-serpentinite		Atg-serpentinite	Atg-serpentinite	Chl-harzburgite		Chl-harzburgite	Atg-serpentinite	
Sample	AL14-16	AL14-63	AL14-17	AL14-18	AL14-70	AL14-87	AL14-95	AL14-19	AL14-66
Os (ppb)	0.133	0.016	0.002	0.003	0.024	0.004	0.033	0.013	0.002
Ir	0.005	0.012	*b.d.l.*	0.004	*b.d.l.*	0.004	0.021	0.008	0.001
Ru	*b.d.l.*	0.021	0.064	*b.d.l.*	0.051	*b.d.l.*	*b.d.l.*	0.025	0.036
Pt	0.058	0.087	0.031	0.051	0.053	0.059	0.112	0.076	*b.d.l.*
Pd	0.654	*b.d.l.*	*b.d.l.*	0.120	*b.d.l.*	0.243	0.286	0.108	*b.d.l.*
Re	0.021	0.067	0.042	0.011	*b.d.l.*	0.022	0.113	0.008	0.029
^{187}Os/^{188}Os	0.1993	0.6589	1.072	0.9463	0.2768	0.3966	0.3940	0.2479	1.139
2sd	0.0006	0.0005	0.050	0.0009	0.0006	0.0006	0.0005	0.0003	0.010

Lithology	**Chl-blackwall**			**Chl-diopsidite metasomatic rim**	**Chl-Ol-diopsidite metasomatic rim**		**Atg-serpentinite close to metarodingite**
Domain	Chl-harzburgite			Atg-serpentinite	Atg-serpentinite		Atg-serpentinite
Sample	AL14-71	AL14-88	AL14-96	AL14-20D-BW	AL14-20L-V	AL14-23	AL14-68
Os (ppb)	0.003	0.002	*n.a.*	3.37	4.08	1.10	2.89
Ir	0.001	0.001	0.007	3.51	3.59	0.709	3.85
Ru	0.065	*b.d.l.*	0.024	6.17	6.75	1.98	5.21
Pt	*b.d.l.*	0.018	0.032	7.15	7.74	9.45	7.44
Pd	*b.d.l.*	*b.d.l.*	*b.d.l.*	4.44	6.03	11.1	4.51
Re	*b.d.l.*	0.003	0.013	0.110	0.138	0.083	0.228
187Os/188Os	0.248	0.298	*n.a.*	0.1251	0.1248	0.1341	0.1219
2sd	0.005	0.007		0.0001	0.0001	0.0002	0.0001

Lithology	**Atg-serpentinite far from metarodingite**			**Chl-harzburgite close to metarodingite**			**Chl-harzburgite far from metarodingite**			
Domain	Atg-serpentinite			Chl-harzburgite			Chl-harzburgite			
Sample	AL14-46	AL14-46 replicate	AL14-69	AL14-72	AL14-89	AL14-97	AL14-73	AL14-73 replicate	AL14-90	AL14-98
Os (ppb)	4.10	3.71	3.80	5.28	3.25	3.39	3.60	3.54	3.79	6.93
Ir	2.52	3.30	4.11	3.42	2.40	2.53	2.84	3.46	3.50	5.41
Ru	6.21	6.13	6.49	7.92	5.71	*b.d.l.*	6.26	6.07	6.54	12.2
Pt	7.18	6.93	8.46	4.99	4.34	6.23	6.38	8.43	9.67	9.15
Pd	5.55	5.56	5.16	3.32	2.81	1.48	4.27	4.15	7.54	11.6
Re	0.189	0.226	0.160	0.705	0.330	0.675	0.375	0.387	*b.d.l.*	0.435
187Os/188Os	0.1253	0.1256	0.1257	0.1189	0.1229	0.1204	0.1231	0.1225	0.1258	0.1219
2sd	0.0001	0.0001	0.0001	0.0001	0.0001	0.0001	0.0001	0.0001	0.0001	0.0001

Lithology	**Strongly chalcophile elements reference materials**					
Domain						
Sample	TDB-1 *(n = 2)*	RSD (%)	*Ishikawa et al. (2014)*	UB-N *(n = 2)*	RSD (%)	*Puchtel et al. (2014)*
Os (ppb)	0.152	4	0.150	3.79	10	3.79
Ir	0.095	2	0.077	3.57	5	3.55
Ru	0.288	10	0.236	6.45	9	6.88
Pt	5.71	6	4.8	8.09	11	7.71
Pd	23.4	1	23.1	5.82	2	6.10
Re	0.925	22	0.99	0.177	3	0.211
^{187}Os/^{188}Os	0.8712	12	0.88	0.1265	0	0.1271
2sd	0.0006		0.33	0.0001		0.0001

Table A17 Mass balance calculations of trace element partitioning between minerals in metarodingites from the Almirez massif. The table displays the average compositions of minerals used in calculations, their estimated modal abundances, the percentage deviations between the calculated and real whole-rock compositions, and the element percentages of whole-rock budget hosted in minerals

Lithology	**Grandite-metarodingite**									
Sample	AL00-6	AL00-6	AL00-6	AL00-6	AL14-64	Deviations (%)	Garnet-1 budget (%)	Garnet-2 budget (%)	Garnet-3 budget (%)	Allanite budget (%)
Phase	Garnet-1	Garnet-2	Garnet-3	Allanite	Whole-rock					
Modal abundances (%)	30	20	22	0.11						
Sr (ppm)	*n.d.*	*n.d.*	*n.d.*	*n.d.*	*n.d.*	*n.d.*	*n.d.*	*n.d.*	*n.d.*	*n.d.*
Ba	*n.d.*	*n.d.*	*n.d.*	*n.d.*	*n.d.*	*n.d.*	*n.d.*	*n.d.*	*n.d.*	*n.d.*
La	0.037	0.050	0.016	15817	16	8	0	0	0	100
Ce	0.39	0.33	0.36	34660	37	3	0	0	0	99
Pr	0.20	0.23	0.23	4433	4.9	3	1	1	1	97
Nd	3.1	5.3	3.7	14590	23	-18	5	6	4	85
Sm	3.6	9.8	3.7	621	5.8	-22	24	43	18	15
Eu	1.6	2.3	1.5	58	1.8	-26	36	35	24	5
Gd	8.7	12	3.1	141	6.8	-15	45	41	12	3
Tb	2.2	2.0	0.48	5.1	1.1	4	56	34	9	0
Dy	16	11	2.6	7.1	7.3	6	63	29	7	0
Ho	3.5	2.0	0.44	0.50	1.4	12	68	25	6	0
Er	10.0	5.2	1.1	2.7	4.1	5	70	24	6	0
Tm	1.3	0.71	0.17	0.046	0.57	1	69	25	6	0
Yb	8.7	3.8	0.88	0.16	3.6	-2	73	21	5	0
Lu	1.2	0.52	0.12	0.017	0.54	-8	73	21	5	0
Pb	*n.d.*	*n.d.*	*n.d.*	*n.d.*	*n.d.*	*n.d.*	*n.d.*	*n.d.*	*n.d.*	*n.d.*
Th	0.070	0.012	0.006	824	1.2	-20	2	0	0	97

Lithology	**Epidote-metarodingite**							
Sample	AL14-26E	AL14-26E	AL14-26E	AL14-26E	Deviations (%)	Garnet-2 budget (%)	Epidote budget (%)	Diopside budget (%)
Phase	Garnet-2	Epidote	Diopside	Whole-rock				
Modal abundances (%)	13	49	38					
Sr (ppm)	4.7	1524	16	921	-18	0	99	1
Ba	1.0	9.5	0.67	5.8	-13	3	92	5
La	*b.d.l.*	17	0.005	8.4	2	0	100	0
Ce	*b.d.l.*	39	*b.d.l.*	21	-8	0	100	0
Pr	*b.d.l.*	5.6	0.004	2.9	-5	0	100	0
Nd	0.019	28	*b.d.l.*	14	-5	0	100	0
Sm	0.066	9.2	0.009	4.2	8	0	100	0
Eu	0.16	5.6	0.006	1.7	67	1	99	0
Gd	0.93	10	0.019	5.0	4	2	98	0
Tb	0.53	1.5	*b.d.l.*	0.85	-4	8	92	0
Dy	6.4	8.2	0.017	5.2	-7	17	83	0
Ho	2.0	1.3	0.005	1.0	-10	28	72	0
Er	7.7	4.0	0.020	2.8	5	34	66	0
Tm	1.3	0.51	0.003	0.40	6	41	59	0
Yb	8.9	2.4	0.024	2.3	0	50	50	0
Lu	1.3	0.28	0.005	0.33	-9	54	45	1
Pb	0.66	29	0.60	14	7	1	98	2
Th	*n.d.*	*n.d.*	*n.d.*	*n.d.*	*n.d.*	*n.d.*	*n.d.*	*n.d.*

n.d. = not determined; b.d.l. = below detection limit

Table A17 Mass balance calculations of trace element partitioning between minerals in metarodingites from the Almirez massif. The table displays the average compositions of minerals used in calculations, their estimated modal abundances, the percentage deviations between the calculated and real whole-rock compositions, and the element percentages of whole-rock budget hosted in minerals

Lithology	**Pyralspite-metarodingite**							
Sample	AL96-24A	AL96-24A	AL96-24A	AL14-95	Deviations (%)	Garnet-5 budget (%)	Epidote budget (%)	Diopside budget (%)
Phase	Garnet-5	Epidote	Diopside	Whole-Rock				
Modal abundances (%)	4	64	32					
Sr (ppm)	*n.d.*	*n.d.*	*n.d.*	*n.d.*	*n.d.*	*n.d.*	*n.d.*	*n.d.*
Ba	*n.d.*	*n.d.*	*n.d.*	*n.d.*	*n.d.*	*n.d.*	*n.d.*	*n.d.*
La	*b.d.l.*	18	0.027	14	-15	0	100	0
Ce	*b.d.l.*	42	0.094	34	-21	0	100	0
Pr	*b.d.l.*	6.1	0.028	4.4	-11	0	100	0
Nd	0.020	29	0.22	21	-10	0	100	0
Sm	0.036	8.4	0.24	5.3	4	0	99	1
Eu	0.024	4.7	0.056	2.2	37	0	99	1
Gd	0.23	8.4	0.50	6.1	-8	0	97	3
Tb	0.10	1.5	0.14	1.0	1	0	95	4
Dy	2.0	9.6	0.82	6.2	4	1	95	4
Ho	1.4	1.8	0.13	1.2	2	4	92	3
Er	6.7	4.7	0.28	3.6	-8	8	89	3
Tm	2.0	0.65	0.033	0.50	1	15	82	2
Yb	20	3.6	0.14	3.3	-4	26	73	1
Lu	3.7	0.46	0.015	0.49	-8	33	66	1
Pb	*n.d.*	*n.d.*	*n.d.*	*n.d.*	*n.d.*	*n.d.*	*n.d.*	*n.d.*
Th	*n.d.*	*n.d.*	*n.d.*	*n.d.*	*n.d.*	*n.d.*	*n.d.*	*n.d.*

n.d. = not determined; b.d.l. = below detection limit

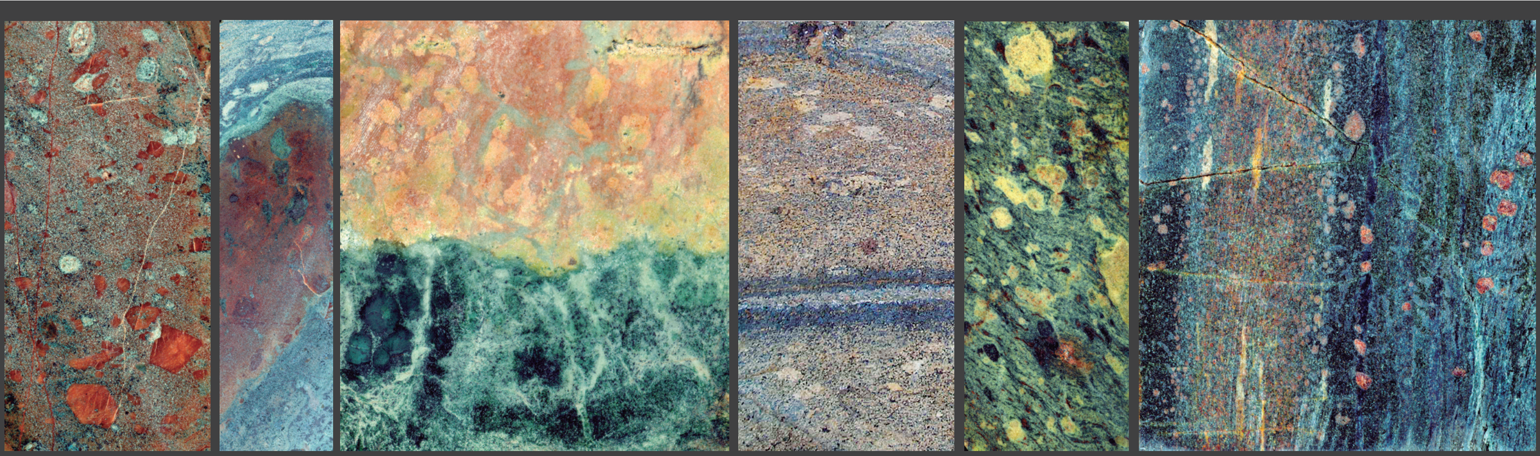

Subduction zones are the main settings of water and mass recycling on Earth. Rodingites are common metasomatic rocks in the oceanic lithosphere and they always occur associated with serpentinized ultramafic rocks, with which they may share prograde metamorphic evolution during subduction. The dehydration of antigorite serpentinite is the most important fluid-releasing reaction that takes place in subduction zones at high-pressure conditions. Interaction with these fluids may importantly affect the mineralogy and composition of accompanying (meta)rodingites.

The main aim of this Ph.D. Thesis is to constrain the significance of rodingites and their metamorphic and geochemical evolution during subduction to intermediate depths after an exhaustive field, petrological, and geochemical study of metarodingites from the Cerro del Almirez ultramafic massif (Betic Cordillera, southern Spain). This massif exceptionally preserves both the reactants and products of dehydration of antigorite serpentinite to chlorite harzburgite. Rodingite bodies are hosted in both ultramafic rock types. Three types of metarodingites have been identified: grandite-, epidote- and pyralspite-metarodingite. They represent the successive transformations of these rocks from their formation on the ocean floor to their subduction to "sub-arc" conditions (16-19 kbar - 660-684 °C). During this evolution, metarodingites underwent changes in pressure and temperature, gradients of chemical potentials, redox transformations and interaction with fluids produced by dehydration of the enclosing serpentinites. The associated geochemical variations show that during subduction metarodingites concentrate Ca, Fe3+, Sr, Pb and Ba and can contribute to the oxidation of the deep mantle and the origin of deep reservoirs rich in Ca. The fluids released from metarodingites, rich in Ca, Re, Pt and Pd, may contribute to the refertilization of the "sub-arc" mantle and the generation of deposits of economic interest.